

1-1-2007

## Modeling of the protective oxide layer growth in non-isothermal lead-alloys coolant systems

Taide Tan

*University of Nevada, Las Vegas*

Follow this and additional works at: <https://digitalscholarship.unlv.edu/rtds>

---

### Repository Citation

Tan, Taide, "Modeling of the protective oxide layer growth in non-isothermal lead-alloys coolant systems" (2007). *UNLV Retrospective Theses & Dissertations*. 2750.

<http://dx.doi.org/10.25669/j8zr-1yt4>

This Dissertation is protected by copyright and/or related rights. It has been brought to you by Digital Scholarship@UNLV with permission from the rights-holder(s). You are free to use this Dissertation in any way that is permitted by the copyright and related rights legislation that applies to your use. For other uses you need to obtain permission from the rights-holder(s) directly, unless additional rights are indicated by a Creative Commons license in the record and/or on the work itself.

This Dissertation has been accepted for inclusion in UNLV Retrospective Theses & Dissertations by an authorized administrator of Digital Scholarship@UNLV. For more information, please contact [digitalscholarship@unlv.edu](mailto:digitalscholarship@unlv.edu).

MODELING OF THE PROTECTIVE OXIDE LAYER GROWTH  
IN NON-ISOTHERMAL LEAD-ALLOYS  
COOLANT SYSTEMS

by

Taide Tan

Bachelor of Science  
Nanchang University  
1996

Master of Science  
University of Nevada, Las Vegas  
2004

A dissertation submitted in partial fulfillment  
of the requirement for the

**Doctor of Philosophy Degree in Mechanical Engineering  
Department of Mechanical Engineering  
Howard R. Hughes College of Engineering**

**Graduate College  
University of Nevada, Las Vegas  
August 2007**

UMI Number: 3282013

### INFORMATION TO USERS

The quality of this reproduction is dependent upon the quality of the copy submitted. Broken or indistinct print, colored or poor quality illustrations and photographs, print bleed-through, substandard margins, and improper alignment can adversely affect reproduction.

In the unlikely event that the author did not send a complete manuscript and there are missing pages, these will be noted. Also, if unauthorized copyright material had to be removed, a note will indicate the deletion.

**UMI<sup>®</sup>**

---

UMI Microform 3282013

Copyright 2007 by ProQuest Information and Learning Company.

All rights reserved. This microform edition is protected against unauthorized copying under Title 17, United States Code.

ProQuest Information and Learning Company  
300 North Zeeb Road  
P.O. Box 1346  
Ann Arbor, MI 48106-1346



## Dissertation Approval

The Graduate College  
University of Nevada, Las Vegas

June 20, 2007

The Dissertation prepared by

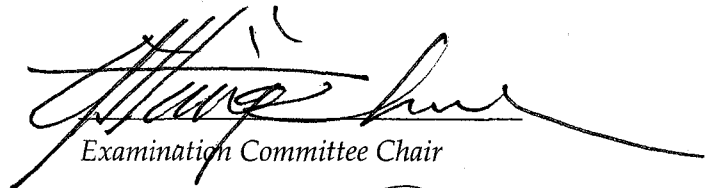
Taide Tan

Entitled

Modeling of the Protective Oxide Layer Growth in Non-isothermal Lead-  
Alloys Coolant Systems

is approved in partial fulfillment of the requirements for the degree of

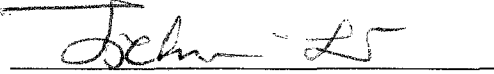
Doctor of Philosophy in Mechanical Engineering

  
Examination Committee Chair

  
Dean of the Graduate College

  
Examination Committee Member

  
Examination Committee Member

  
Graduate College Faculty Representative

  
Examination Committee Member

  
Examination Committee Member

## ABSTRACT

### **Modeling of the Protective Oxide Layer Growth in Non-Isothermal Lead-Alloys Coolant Systems**

by

Taide Tan

Dr. Yitung Chen, Examination Committee Chair  
Associate Professor of Mechanical Engineering  
University of Nevada, Las Vegas

Lead alloys have been determined to be potential coolant candidates in advanced reactors and accelerator driven systems (ADS) because of their favorable thermal-physical and chemical properties. However, the corrosiveness of the lead-alloys is a critical obstacle and challenge for safe applications in reactors and ADS. Furthermore, the selective dissolution of materials into lead alloys would destroy the structure and contaminate the coolant rapidly, and the deposition of corrosion product may lead to severe flow-path restrictions. One of the effective ways to protect the material is to form and maintain a protective oxide film along the structural material surface by active oxygen control technology.

The goal of this research is to provide basic understanding of the protective oxide layer behaviors and to develop oxide layer growth models of steels in non-isothermal lead-alloys coolant systems in order to provide useful information for active oxygen control technique.

First, a theoretical kinetic model based on the boundary layer theory was developed to investigate the corrosion/precipitation in non-isothermal lead alloy coolant systems. The analytical expressions of the local corrosion/precipitation rate and the bulk concentration of the corrosion products were obtained by considering a turbulent core region and a laminar sub-layer. Numerical solutions were also accomplished together with considering the effect of the eddy mass diffusivity in lead alloy systems. Second, a diffusion controlling oxide layer growth model with scale removal was built in oxygen containing lead alloys. Scale removal effect was considered and the formation mechanism of duplex oxide layer structure was investigated in the model. Finally, the oxide layer growth process, together with the transport of oxygen and ionic metal, was studied at a mesoscopic level based on an improved stochastic cellular automaton (CA) model.

Results from the developed models were compared with the available experimental data and previous work, and good agreement was attained. Moreover, the extended applications of the developed models were analyzed.

## TABLE OF CONTENTS

ABSTRACT .....	iii
TABLE OF CONTENTS.....	v
LIST OF FIGURES .....	vii
ACKNOWLEDGEMENTS.....	xii
CHAPTER 1 INTRODUCTION AND BACKGROUND .....	1
1.1 Lead and LBE.....	1
1.2 Corrosion on Stainless Steel by Lead and LBE.....	7
1.2.1 Mechanisms of Liquid Metal/alloy Corrosion .....	8
1.2.2 Factors Affecting Structural Materials Corrosion in LBE .....	15
1.3 Oxidation of Stainless Steels in Lead/LBE .....	20
1.3.1 Chemical and Chemical Thermodynamics Basis.....	21
1.3.2 The Oxide Structure from Experimental Results .....	24
1.3.3 The Mechanism of the Oxide Layer Growth .....	33
1.3.4 Oxygen Control Technique .....	42
1.4 DELTA Loop.....	45
1.5 Transmutation Research Program .....	50
1.6 Purpose of Study.....	51
CHAPTER 2 CORROSION AND PRECIPITATION IN NON-ISOTHERMAL LIQUID LEAD OR LBE SYSTEMS .....	54
2.1 Introduction .....	54
2.2 Literature Survey .....	55
2.3 Theory.....	58
2.3.1 Assumptions and Governing Equations .....	58
2.3.2 Boundary Conditions and Oxygen Control Technology.....	62
2.4 Methodology.....	66
2.5 Analytical Solutions .....	67
2.5.1 Analytical Solutions for Open Pipe Flow .....	67
2.5.2 Analytical Solution for Closed Loop Flow .....	69
2.6 Numerical Model.....	70
2.7 Parameter Identification .....	71
2.8 Results and Discussion .....	75
2.9 Conclusions .....	92
CHAPTER 3 A DIFFUSION CONTROLLING OXIDATION MODEL WITH SCALE REMOVAL IN OXYGEN-CONTAINING LIQUID FLOW.....	95

3.1 Introduction .....	95
3.2 Literature Survey .....	95
3.3 Theory.....	98
3.4 Methodology.....	108
3.5 Results and Discussions .....	109
3.5.1 Benchmark 1: Oxidation of Pure Zirconium without Scale Removal .....	109
3.5.2 Benchmark 2: Oxidation of Pure Titanium .....	111
3.5.3 Benchmark 3: Oxidation of Stainless Steel in LBE .....	112
3.5.4 Parametric Study .....	113
3.5.5 Duplex Oxidation Simulation.....	119
3.6 Conclusions .....	123
 CHAPTER 4 AN IMPROVED MESOSCOPIC OXIDATION MODEL OF METALS IN MOLTEN LEAD OR LBE.....	125
4.1 Introduction .....	125
4.2 Literature Survey .....	126
4.3 Methodology.....	128
4.4 An Improved CA Oxidation Model.....	130
4.5 Results and Discussions .....	140
4.5.1 Benchmark the Pure Diffusion Process without Reaction .....	141
4.5.2 Oxidation Process with Transport of Oxygen and Metal.....	143
4.5.3 Mapping between the Mesoscopic Model and the Experimental Data .....	149
4.5.4 Parametric Study .....	150
4.6 Conclusions .....	172
 CHAPTER 5 CONCLUSIONS AND RECOMMENDATIONS .....	174
5.1 Conclusions .....	174
5.2 Recommendations for future work.....	176
 APPENDIX NOMENCLATURE.....	177
 REFERENCES .....	182
 VITA.....	191



## LIST OF FIGURES

Figure 1. Pb-Bi phase diagram obtained by IPPE, Obninsk, Russia. ( $\alpha$ is Pb, $\beta$ is $Pb_7Bi_3$ and $\gamma$ is Bi.) [11] .....	2
Figure 2. Density of the molten lead and LBE as a function of temperature at the normal pressure [13]. .....	4
Figure 3. Dynamic viscosity of molten lead and LBE at the normal pressure as a function of temperature. [13] .....	5
Figure 4. Comparison of the kinematic viscosities of molten lead, LBE and experimental data. ....	6
Figure 5. The mass diffusivity as a function of temperature. ....	7
Figure 6. The microstructure of severe corrosion in 316L steel [17]. ....	8
Figure 7. Uniform corrosion and local corrosion. ....	9
Figure 8. Diffusion of LBE along the grain boundaries of 316L steel after 5000 h of exposure time. [23] .....	10
Figure 9. Representation of the four main types of flow affected corrosion. ....	11
Figure 10. Interactions of a flowing liquid with a solid boundary. ....	13
Figure 11. Velocity effects on the corrosion rate. [31] .....	17
Figure 12. Comparison of solubility of Fe in LBE and Pb, solubility of Cr and Ni in LBE, with the experimental data [38] of solubility of Fe in LBE. ....	20
Figure 13. (SEM) of cross-section of OPTIFER specimen after 3000 hours at 550°C [42]. ....	25
Figure 14. (SEM) of cross-section of 1.4970 specimen after 3000 hours at 550°C [42]. ..	26
Figure 15. SEM micrograph of the oxide layer structure of the T91 steel at 470 °C after 3000 h exposure. [43]. ....	27
Figure 16. Cross-section of HT-9 (tube) after being exposed to flowing LBE for 2000 h at T = 460 °C. [17] .....	28
Figure 17. Cross-section of HT-9 (tube) after being exposed to flowing LBE for 3000 h at T = 550 °C. [17] .....	29
Figure 18. SEM micrograph of the oxide layer structure of the 1.4970 steel at 470 °C after 3000 h exposure. [43]. ....	30
Figure 19. Cross-section of 316 (tube) after being exposed to flowing LBE for 2000 h at T = 460 °C. [17] .....	31
Figure 20. Slot corrosion of 316L steel at T = 460 °C for 2000 h. [17] .....	31
Figure 21. Cross-section of 316 (tube) after being exposed to flowing LBE for 2000 h at T = 550 °C. [17] .....	32
Figure 22. Dissolution corrosion in unsaturated static lead or LBE. ....	33
Figure 23. Corrosion ceases when dissolution is in balance with deposition. ....	34
Figure 24. Deposition induces a single layer of (Fe,Cr) <sub>3</sub> O <sub>4</sub> . ....	34
Figure 25. Duplex-layer structure without oxygen transported into the stainless steel. ....	35
Figure 26. Duplex-layer structure oxide controlled by transports of iron and oxygen. ....	36

Figure 27. Single layer structure oxide induced by surface reaction in clean static lead/LBE. ....	37
Figure 28. Duplex layer structure of oxide with oxygen transported in. ....	38
Figure 29. Dissolution corrosion in unsaturated flowing lead or LBE. ....	39
Figure 30. Dissolution is in balance with deposition (with scale removal). ....	40
Figure 31. Corrosion and oxidation in an non-isothermal lead/LBE system with balance of dissolution and deposition in total quantity. ....	40
Figure 32. Typical oxygen control range in non-isothermal liquid lead and LBE flow systems. [36] ....	44
Figure 33. The schematic sketch of DELTA Loop. [51] ....	46
Figure 34. The DELTA Loop. Sump tank is visible on the left, heat exchanger next to sump tank, calibration tank is at the right top corner, and recuperator is underneath calibration tank, in the shadow. [51] ....	47
Figure 35. Scheme of the turbulent core region and laminar sub-layer near the wall. ....	60
Figure 36. Temperature profile of the open pipe/DELTA loop, ( $T_{\max} = 823.15K$ , $T_{\text{int}} = (T_{\min} + T_{\max})/2$ ). ....	72
Figure 37. Wall concentration profile of the open pipe/DELTA loop. ....	73
Figure 38. Cosine axial temperature profile of the pipe/loop. ....	74
Figure 39. Wall concentration profile of a pipe/loop with a cosine axial temperature profile. ....	74
Figure 40. Corrosion/precipitation rates of an open pipe. ....	76
Figure 41. Corrosion/precipitation rates of a closed loop. ....	76
Figure 42. Corrosion/precipitation rates of an open pipe with a cosine axial temperature profile. ....	77
Figure 43. Corrosion/precipitation rates of a closed loop with a cosine axial temperature profile. ....	78
Figure 44. Corrosion/precipitation rates vs. inlet velocities of an open pipe with $\Delta T=50$ K. ....	79
Figure 45. Corrosion/precipitation rates vs. inlet velocities of an open pipe with $\Delta T=200$ K. ....	80
Figure 46. Corrosion/precipitation rates vs. inlet velocities of an open pipe with $\Delta T=350$ K. ....	80
Figure 47. Corrosion/precipitation rates vs. inlet velocities of a closed loop with $\Delta T=50$ K. ....	81
Figure 48. Corrosion/precipitation rates vs. inlet velocities of a closed loop with $\Delta T=200$ K. ....	81
Figure 49. Corrosion/precipitation rates vs. inlet velocities of a closed loop with $\Delta T=350$ K. ....	82
Figure 50. Comparison of analytical solution and numerical solutions for $\Delta T=50$ K. ....	84
Figure 51. Comparison of analytical solution and numerical solutions for $\Delta T=200$ K. ....	84
Figure 52. Comparison of analytical solution and numerical solutions for $\Delta T=350$ K. ....	85
Figure 53. Sherwood number variations at the test leg for an open pipe, $T_{\max} = 823.15K$ , $\Delta T = 50K$ . ....	86
Figure 54. Sherwood number variations at the test leg for an open pipe, $T_{\max} = 823.15K$ , $\Delta T = 200K$ . ....	86

Figure 55. Sherwood number variations at the test leg for an open pipe, $T_{\max} = 823.15K, \Delta T = 350K$ .....	87
Figure 56. Sherwood number variations at the test leg for a closed loop, $T_{\max} = 823.15K, \Delta T = 50K$ .....	87
Figure 57. Sherwood number variations at the test leg for a closed loop, $T_{\max} = 823.15K$ , $\Delta T = 200K$ .....	88
Figure 58. Sherwood number variations at the test leg for a closed loop, $T_{\max} = 823.15K, \Delta T = 350K$ .....	88
Figure 59. Wall temperature distribution and the wall concentration of iron of the experiment of the pure lead loop.....	90
Figure 60. Comparisons between the experiment data [72], numerical and analytical results from the model for the pure lead loop. ....	91
Figure 61. Illustration of the oxygen-controlling oxidation process.....	101
Figure 62. The function $Z(C^*)$ with unphysical interval of $D^* = 0$ .....	107
Figure 63. The weight gain with time for the oxidation of pure zirconium without scale removal.....	110
Figure 64. Distribution of the oxygen concentration at time $t=0.5h$ ( $Kr=2 \times 10^{-9}$ m/s for the scale removal model). ....	111
Figure 65. Benchmark with the experimental data. ....	113
Figure 66. The impact of $K_r^*$ ( $D_{Ox}^* = 0.5$ and $m=1.5$ ). ....	114
Figure 67. The impact of $m$ ( $K_r^* = 0.2$ and $D_{Ox}^* = 0.5$ ) .....	115
Figure 68. The impact of $D_{Ox}^*$ ( $K_r^* = 0.2$ and $m=1.5$ ). ....	116
Figure 69. Total oxide layer thickness for $r=1$ .....	117
Figure 70. Total oxide layer thickness for $r=0.6$ .....	118
Figure 71. Net change in the total volume for $r=1$ .....	118
Figure 72. Net change in the total volume for $r=0.6$ .....	119
Figure 73. The thickness of the total oxide layer, the inner oxide layer and the outer oxide layer for different values of $w$ ( $p=0.8$ ). ....	121
Figure 74. The thickness of the total oxide layer, the inner oxide layer and the outer oxide layer for different values of $p$ ( $w=0.9$ ). ....	123
Figure 75. Schematic of CA model of corrosion/oxidation of metal in LBE.....	132
Figure 76. The Von Neumann neighborhood. ....	134
Figure 77. The Moore neighborhood. ....	134
Figure 78. The extended Moore neighborhood.....	135
Figure 79. The neighbor lattices $\{Lat_{i,j}^{Nb}(t)\}$ and interstitial sites $\{Inte_{i,j}^{Nb}(t)\}$ for lattice $Lat_{i,j}(t)$ .....	136
Figure 80. The neighbor lattices $\{Lat_{i,j}^{Nb}(t)\}$ and interstitial sites $\{Inte_{i,j}^{Nb}(t)\}$ for interstitial site $Inte_{i,j}(t)$ .....	136
Figure 81. Particle concentration distributions for different time steps.....	142
Figure 82. Benchmark of the results form the present model with the analytical solution and Brieger's result [98].....	142

Figure 83. The snapshot of the simulated mesoscopic structure after $N_t = 10,000$ steps.	144
Figure 84. The zoom in view of the simulated mesoscopic structure of oxide layer after $N_t = 10,000$ steps.	145
Figure 85. The walker concentration in the oxide layer.	146
Figure 86. The oxygen concentration for different calculating steps.	147
Figure 87. The oxide layer growth vs. time steps.	148
Figure 88. Values of $(\delta_{N,in})^2$ , $(\delta_{N,out})^2$ , and $(\delta_{N,tot})^2$ vs. time steps.	149
Figure 89. The snapshot of the mesoscopic structure for $N_t = 200,000$ , with $K_d = 1$ , $C_{oxy} = 0.2$ and $P_{act} = 0.0005$ .	151
Figure 90. The snapshot of the mesoscopic structure for $N_t = 200,000$ , with $K_d = 1$ , $C_{oxy} = 0.2$ and $P_{act} = 0.3$ .	152
Figure 91. The snapshot of the mesoscopic structure for $N_t = 200,000$ , with $K_d = 1$ , $C_{oxy} = 0.2$ and $P_{act} = 0.5$ .	153
Figure 92. The snapshot of the mesoscopic structure for $N_t = 200,000$ , with $K_d = 1$ , $C_{oxy} = 0.2$ and $P_{act} = 0.8$ .	154
Figure 93. The comparison of the oxide layer thickness of cases with $P_{act} = 0.0005$ and $P_{act} = 0.5$ at $N_t = 200,000$ , with $K_d = 1$ , $C_{oxy} = 0.2$ .	154
Figure 94. The comparison of the oxide layer thickness of cases with $P_{act} = 0.3$ and $P_{act} = 0.8$ at $N_t = 200,000$ , with $K_d = 1$ , $C_{oxy} = 0.2$ .	155
Figure 95. The comparison of the oxide layer thickness of cases with $P_{act} = 0.3$ and $P_{act} = 0.8$ at the initial stage, with $K_d = 1$ , $C_{oxy} = 0.2$ .	155
Figure 96. The walker distributions for $N_t = 200,000$ , with $K_d = 1$ , $C_{oxy} = 0.2$ and $P_{act} = 0.0005$ .	156
Figure 97. The walker distributions for $N_t = 200,000$ , with $K_d = 1$ , $C_{oxy} = 0.2$ and $P_{act} = 0.3$ .	156
Figure 98. The walker distributions for $N_t = 200,000$ , with $K_d = 1$ , $C_{oxy} = 0.2$ and $P_{act} = 0.5$ .	157
Figure 99. The walker distributions for $N_t = 200,000$ , with $K_d = 1$ , $C_{oxy} = 0.2$ and $P_{act} = 0.8$ .	157
Figure 100. The oxygen distributions for $N_t = 200,000$ , with $K_d = 1$ , $C_{oxy} = 0.2$ and $P_{act} = 0.0005$ .	158
Figure 101. The oxygen distributions for $N_t = 200,000$ , with $K_d = 1$ , $C_{oxy} = 0.2$ and $P_{act} = 0.3$ .	158
Figure 102. The oxygen distributions for $N_t = 200,000$ , with $K_d = 1$ , $C_{oxy} = 0.2$ and $P_{act} = 0.5$ .	159

Figure 103. The oxygen distributions for $N_t = 200,000$ , with $K_d = 1$ , $C_{oxy} = 0.2$ and $P_{act} = 0.8$ .....	159
Figure 104. Snapshot of the mesoscopic structure with $K_d = 2$ , $C_{oxy} = 0.2$ and $P_{act} = 0.0005$ at $N_t = 200,000$ .....	161
Figure 105. Snapshot of the mesoscopic structure with $K_d = 2$ , $C_{oxy} = 0.2$ and $P_{act} = 0.5$ at $N_t = 200,000$ .....	162
Figure 106. Comparison of the oxide layer thicknesses for cases $P_{act} = 0.0005$ and $P_{act} = 0.5$ (both with $K_d = 2$ , $C_{oxy} = 0.2$ ). .....	162
Figure 107. The oxygen distributions for $N_t = 200,000$ , with $K_d = 2$ , $C_{oxy} = 0.2$ and $P_{act} = 0.0005$ .....	163
Figure 108. The oxygen distributions for $N_t = 200,000$ , with $K_d = 2$ , $C_{oxy} = 0.2$ and $P_{act} = 0.5$ .....	164
Figure 109. The walker distributions for $N_t = 200,000$ , with $K_d = 2$ , $C_{oxy} = 0.2$ and $P_{act} = 0.0005$ .....	164
Figure 110. The walker distributions for $N_t = 200,000$ , with $K_d = 2$ , $C_{oxy} = 0.2$ and $P_{act} = 0.5$ .....	165
Figure 111. Snapshot of the mesoscopic structure with $K_d = 4$ , $C_{oxy} = 0.2$ and $P_{act} = 0.0005$ at $N_t = 200,000$ .....	166
Figure 112. Snapshot of the mesoscopic structure with $K_d = 4$ , $C_{oxy} = 0.2$ and $P_{act} = 0.5$ at $N_t = 200,000$ .....	167
Figure 113. Comparison of the oxide layer thicknesses for cases $P_{act} = 0.0005$ and $P_{act} = 0.5$ (both with $K_d = 4$ , $C_{oxy} = 0.2$ ). .....	167
Figure 114. The walker distributions for $N_t = 200,000$ , with $K_d = 4$ , $C_{oxy} = 0.2$ and $P_{act} = 0.0005$ .....	168
Figure 115. The walker distributions for $N_t = 200,000$ , with $K_d = 4$ , $C_{oxy} = 0.2$ and $P_{act} = 0.5$ .....	169
Figure 116. The oxygen distributions for $N_t = 200,000$ , with $K_d = 4$ , $C_{oxy} = 0.2$ and $P_{act} = 0.0005$ .....	169
Figure 117. The oxygen distributions for $N_t = 200,000$ , with $K_d = 4$ , $C_{oxy} = 0.2$ and $P_{act} = 0.5$ .....	170
Figure 118. Comparison of thickness for different value of $K_d$ , with $C_{oxy} = 0.2$ , $P_{act} = 0.0005$ .....	170
Figure 119. Comparison of thickness for different value of $K_d$ , with $C_{oxy} = 0.2$ , $P_{act} = 0.5$ .....	171

## ACKNOWLEDGEMENTS

I wish to express my appreciation to those who have supported me in this endeavor. First, I would like to thank my advisor, Dr. Yitung Chen for his sage advise, encouragement, and direction. I would also like to thank Dr. Robert Boehm, Dr. Samir Moujaes, Dr. Hsuan-Tsung (Sean) Hsieh, Dr. Jichun Li and Dr. Huajun Chen for taking the time to serve on my committee. I would also like to thank Dr. Jinsuo Zhang from Los Alamos National Laboratory and all the people from Dr. Yitung Chen's research group in University of Nevada, Las Vegas, for their assistance and encouragement. Finally, I wish to thank my family for their love, patience and support, without which none of this would have been possible.

The financial support by the U.S. Department of Energy through the University of Nevada, Las Vegas, Transmutation Research Program (TRP) (Grant No. DE-FG04-2001AL67358) is highly appreciated.

## CHAPTER 1

### INTRODUCTION AND BACKGROUND

#### 1.1 Lead and LBE

Lead bismuth eutectic (LBE) is an efficient heat transfer media in nuclear power systems because of its high thermal conductivity, high heat capacity and other favorable thermal-physical properties such as low melting point, wide margin to boiling, high boiling points and low vapor pressure. Moreover, LBE is chemically inert and does not react violently with air and water [1-4]. LBE offers the advantage of a much lower melting point (123.5°C vs. 327°C) compared to pure lead. Therefore, LBE, thermodynamically near the ideal solution, has been determined from previous experimental studies to be a potential coolant candidate in advanced nuclear reactors and accelerator driven systems (ADS) [1, 5, 6].

However, lead and lead alloys are very corrosive to many structural materials if the materials are exposed to lead or lead alloys directly. The corrosion results in significant wall thinning and/or loss of mechanical integrity [3, 4, 7]. More seriously, the selective dissolution of materials into lead alloys would destroy the structure rapidly and contaminate the lead alloys coolant. Furthermore, the subsequent deposition of corrosion product may lead to severe flow-path restrictions that can eventually block the flow. Therefore, corrosion and precipitation in lead and lead alloys coolant systems are becoming the most critical obstacle and challenge for safe application of lead and lead

alloys as ideal nuclear coolant candidates for ADS and advanced reactors, especially at medium and high temperature conditions [2, 7-9]. Hence, full knowledge of the important characteristics in flow-induced and/or enhanced corrosion is necessary in proper system design and safe operations of lead and lead alloys (mainly LBE) coolant systems.

Full knowledge of the important characteristics of the flow-induced and/or enhanced corrosion is essential in the proper design and safe operation of LBE heat transfer circuits. Currently, a lack of systematic understanding of the scientific basis is limiting many R&D efforts to testing and impeding the development of material and technologies. Several efforts are underway to remedy this deficiency, including the preparation of an LBE materials handbook by an international expert group. [10]

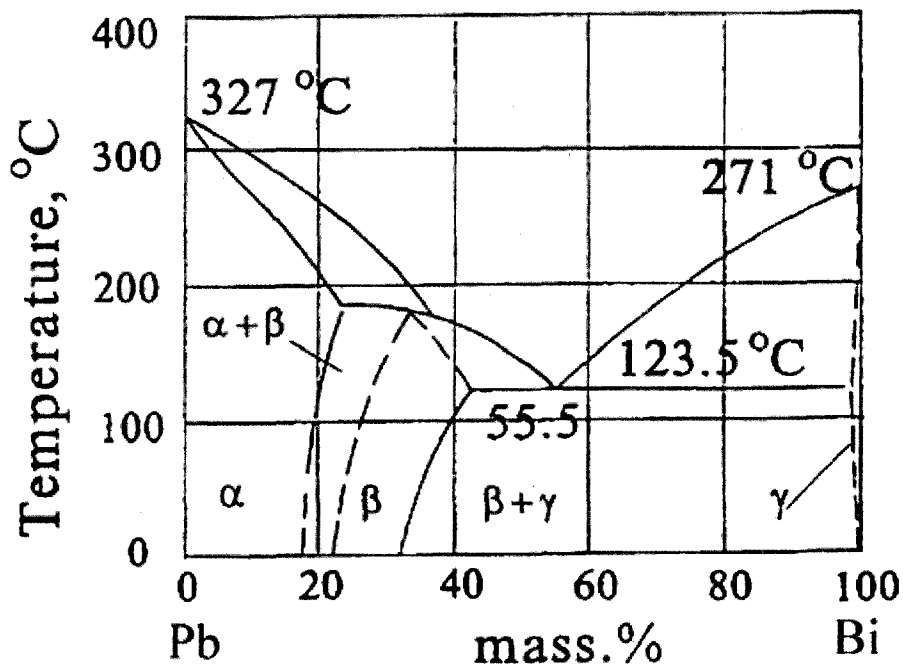


Figure 1. Pb-Bi phase diagram obtained by IPPE, Obninsk, Russia. ( $\alpha$  is Pb,  $\beta$  is  $Pb_7Bi_3$  and  $\gamma$  is Bi.) [11]



The phase diagram of lead bismuth alloy is shown in Figure 1, which was updated by the Institute of Physics and Power Engineering (IPPE) in Obninsk, Russia, for the purpose of using lead-bismuth alloy as a nuclear coolant [11]. It indicates that the eutectic point is 123.5°C at 44.8 wt% of lead.

All heavy liquid metals (HLM) are believed to be Newtonian liquids. [12, 13] Some of the physical properties of Lead and LBE are available from the previous work [10, 12, and 13]. As shown in the phase diagram (Figure 1) and

Table 1, the pure lead melting point is higher than that of LBE. A higher operation temperature is needed if liquid lead is used as a nuclear coolant. As will be discussed later, a higher temperature is difficult to manipulate because of the greatly increased corrosion rate, and many other consequent difficulties.

Table 1 Melting and Boiling Points of Lead and LBE

	Melting Point(°C)	Boiling Point(°C)
Lead	327	1725
LBE	123.5	1670

Density ( $\rho$ ) is an important physical property of molten lead and LBE as a nuclear coolant. From the previous study [10, 13], the linear regressions of the lead and LBE density values presented in Figure 2 yields

$$\rho(T)[kg / m^3] = A_{\rho} - B_{\rho}T[K] \quad (1-1)$$

where  $A_{\rho}$ ,  $B_{\rho}$ , are constants which can be found from

Table 2. The densities of lead and LBE decrease when the temperature increases.

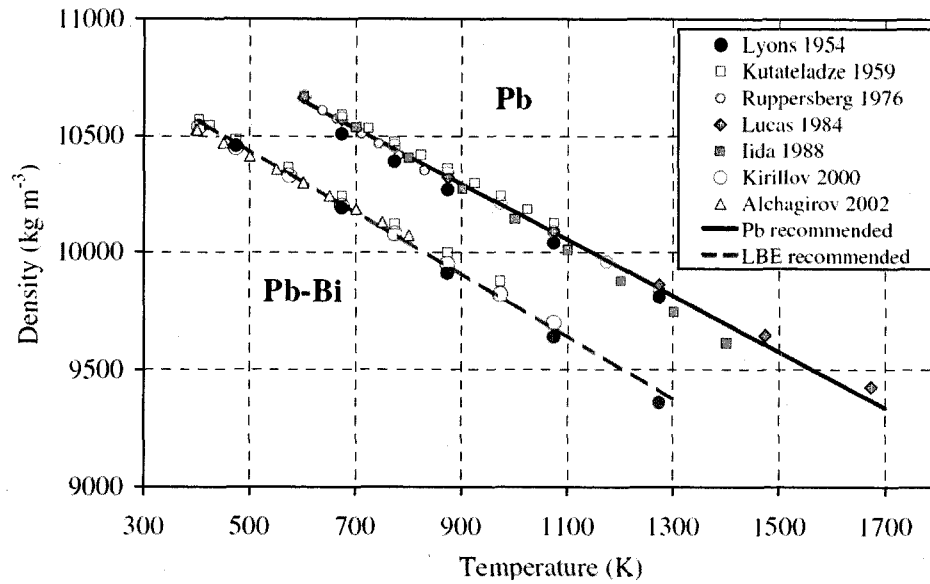


Figure 2. Density of the molten lead and LBE as a function of temperature at the normal pressure [13].

Table 2 The Constants for Calculating Density and Viscosity

	$A_p$ (kg/m <sup>3</sup> )	$B_p$ (kg/K·m <sup>3</sup> )	$A_\mu$ (10 <sup>-4</sup> kg/m·s)	$E$ (J/mol)
Lead	11,367	1.1944	4.55	8,888
LBE	11,096	1.3236	4.94	6,270

The temperature dependence of the dynamic viscosity ( $\mu$ ) of HLM is usually described by an Arrhenius type formula [13]:

$$\mu(T)[Pa \cdot s] = A_\mu \exp(E/R_g T[K]) \quad (1-2)$$

where  $R_g = 8.314 \text{ kg/m}^3$  is the gas constant,  $A_\mu$  is a coefficient and  $E$  is the activation energy of motion of viscous flow. A reliable choice of an empirical equation to describe the temperature dependence of the dynamic viscosity of molten lead and LBE can be obtained by fitting the previous data as show in Figure 3. The fitting data for  $A_\mu$  and  $E$  are reported in Ref. [13] which are listed in

Table 2.

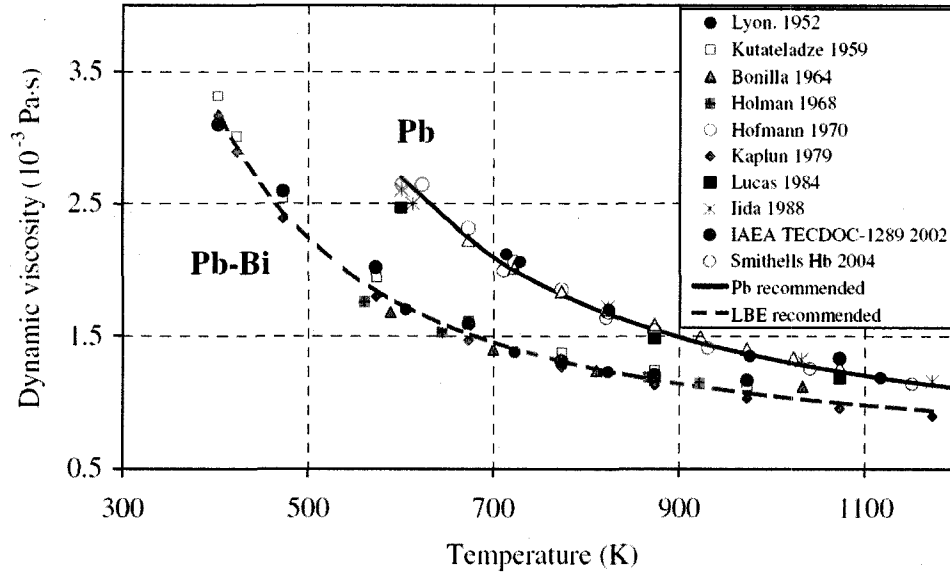


Figure 3. Dynamic viscosity of molten lead and LBE at the normal pressure as a function of temperature. [13]

It is shown that pure liquid lead has a larger dynamic viscosity than LBE at the same temperature, and especially at lower temperatures. Both dynamic viscosities decrease with increasing temperature. At a relatively lower temperature, the dynamic viscosities decrease much faster for both lead and LBE with the temperature increases. The kinematic viscosity  $\nu$  is calculated from  $\nu = \mu / \rho$ . The Reynolds number of a flow in a pipe is expressed by  $Re = VD / \nu$ . The calculated kinematic viscosities of molten lead and LBE from Eqs. (1-1) and (1-2) are compared with the experimental data in Ref [14]. The comparison shown in Figure 4 depicts that molten lead has a larger kinematic viscosity than LBE, and the calculated results for LBE agree very well with the experimental results reported by IPPE [14]. Since a smaller kinematic viscosity results in a higher

Reynolds number, the decreasing kinematic viscosity with increasing temperature results in higher corrosion rates in the mass diffusion controlled situations. [10]

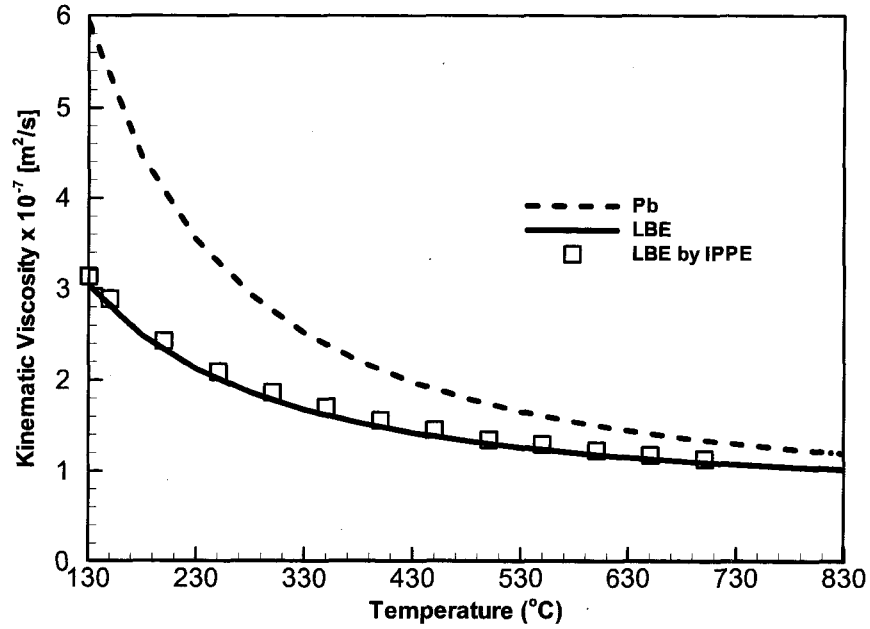


Figure 4. Comparison of the kinematic viscosities of molten lead, LBE and experimental data.

The molecular diffusivities of iron in molten lead and LBE are assumed to be equal [15] and can be approximated from an equation developed by Robertson [16]

$$D_m [m^2 / s] = 4.9 \times 10^{-7} \exp\left(\frac{-Q}{R_g T [K]}\right) \quad (1-3)$$

where  $Q = 44,100 \pm 6,300 J / mole$ . Thus the molecular diffusivity is a function of temperature as well, and the calculated molecular diffusivities are in a range between the upper limit and the lower limit according to the manipulating temperature, which is shown in Figure 5. Obviously, the mass diffusivities of molten lead and LBE increase with increase of temperature. A higher mass diffusivity results in a higher diffusing

efficiency for the corrosion products, therefore, causes a higher corrosion rate in the mass diffusion controlled corrosion, too. [10]

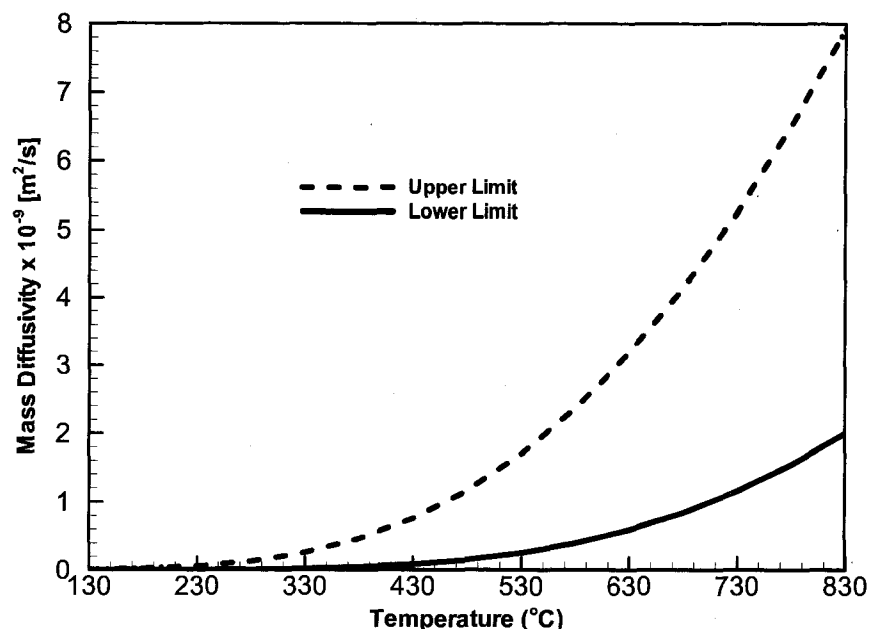


Figure 5. The mass diffusivity as a function of temperature.

## 1.2 Corrosion on Stainless Steel by Lead and LBE

LBE corrosion has long been recognized as a leading obstacle to its nuclear applications. The corrosion of stainless steel could be very severe in a flowing LBE environment, especially at a high temperature. For example, experimental tests show that the local liquid metal corrosion depth could reach 220  $\mu\text{m}$  after 3000 h of exposure time, for an austenitic steel specimen 316L (“L” stands for the low carbon version of steel), at 550  $^{\circ}\text{C}$ , with flowing velocity 1.9 m/s, as shown in Figure 6 [17].

Besides the global corrosion, severe intergranular attack was also observed for American Iron and Steel Institute (AISI) 316 steel in liquid lead. [18] Corrosion of steels in pure liquid Pb or LBE occurs primarily through dissolution of steel components into

the liquid metals/alloys. The main driving force for liquid metal corrosion is the chemical potential for dissolution of all solid surfaces in contact with liquid metals [10, 19]. More seriously, the compositional and microstructural changes due to selective dissolution and intergranular corrosion can lead to material failures and destroy the structure rapidly, which may be difficult to observe [7, 20, 21]. It is necessary to review and understand the mechanisms of the LBE corrosion and the dependence of the LBE corrosion.

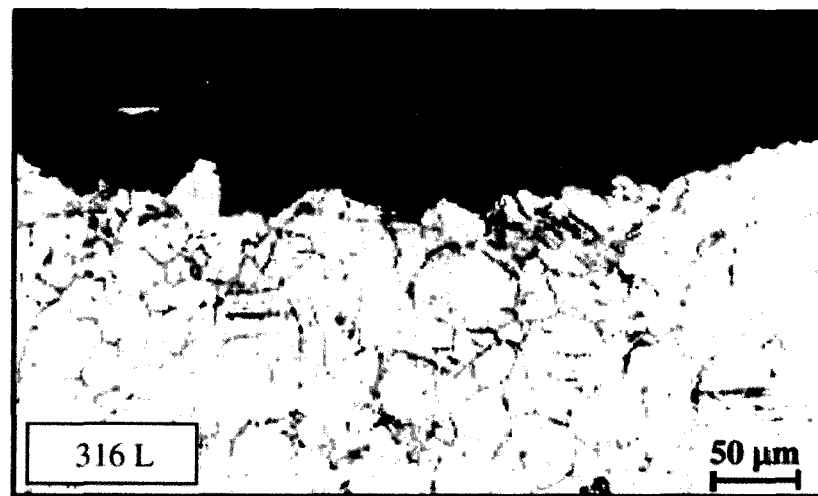


Figure 6. The microstructure of severe corrosion in 316L steel [17].

#### 1.2.1 Mechanisms of Liquid Metal/alloy Corrosion

The corrosion of steels in a liquid metal environment is divided into uniform corrosion and local corrosion, according to their damages to the structure (Figure 7) [22].

In a uniform corrosion (Figure 7 a), the corrosive liquid metal corrodes the material uniformly along the surface of the solid phase structure material. Therefore, a uniform corrosion is easy to observe, since the damage is of a same thickness at any point on the surface. However, in a local corrosion (Figure 7 b-f), the liquid metal penetrates into the solid material along the grain boundaries and some other crystal structural defects which

reach the surface of the structure. Figure 7 b, c, and d illustrates the penetration of liquid metal along the specific crystallographic directions, along the grain boundaries, and along vacancies and pores, respectively. The penetration of the corrosive liquid metal will cause deep corrossions, and the corrossions will develop along the previously formed defects, such as in Figure 7 e and Figure 7 f. The local corrosion can cause very severe damage to the structural material, and it is more difficult to observe.

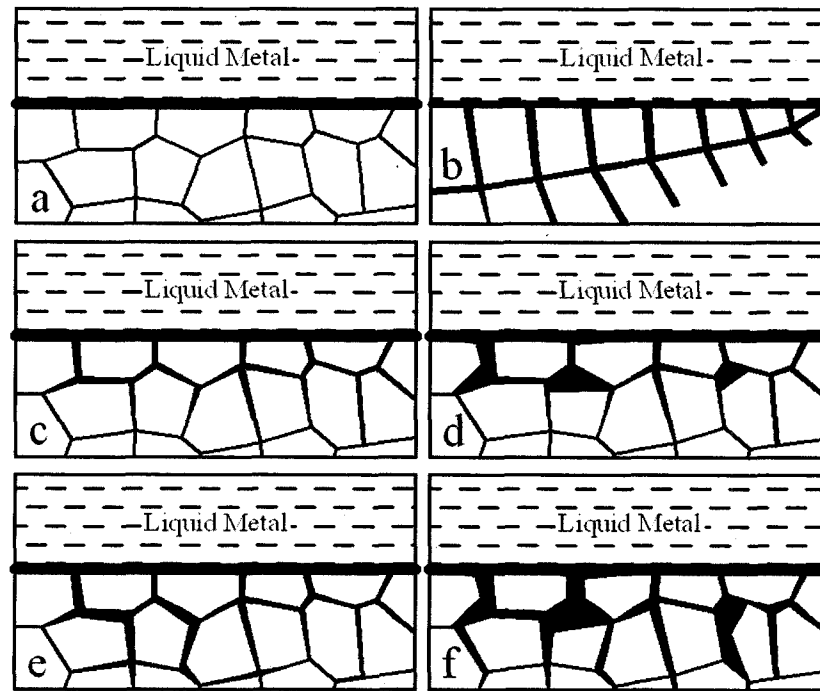


Figure 7. Uniform corrosion and local corrosion.

The quick diffusion of LBE along the boundaries and consequent local corrosion on stainless steels has been demonstrated and reported from experiments by Glasbrenner. LBE can reach to over 50  $\mu\text{m}$  inside the material of 316L steel after 5000 hours of exposure, while, in spite of that, uniform corrosion occurs at the same time (Figure 8). [23]

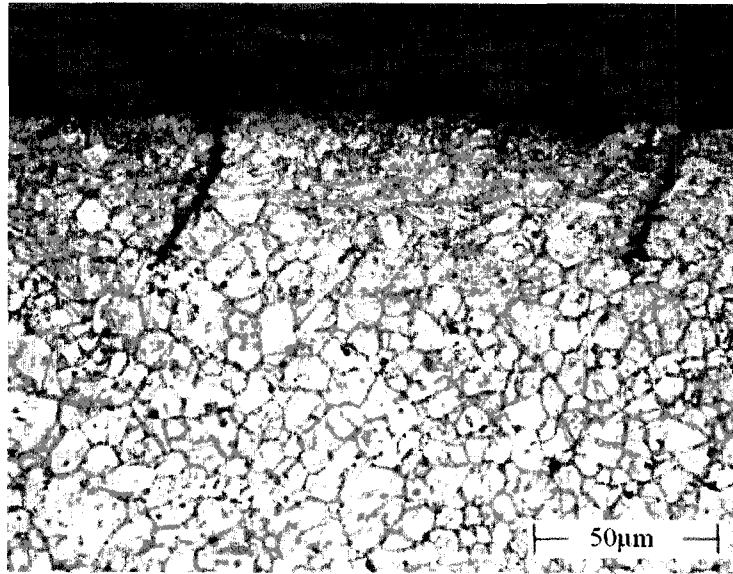


Figure 8. Diffusion of LBE along the grain boundaries of 316L steel after 5000 h of exposure time. [23]

The flow conditions affect corrosion to a great extent, especially for the corrosion in a liquid metal environment at a high temperature. The flowing velocity of liquid metals accelerates corrosion on the solid structural material, which is called flow accelerated corrosion (FAC) [24]. At a very low flow velocity which is close to zero, natural convection alone is involved in mass transfer and presents no mechanical flow effects. For a moderate velocity flow, mass transfer is accelerated by forced convection, and mechanical flow effect is still assumed to be absent. Under the influence of a high velocity, especially in a turbulent flow, mass transfer increases greatly, and mechanical flow effect becomes important. The oxide layer, and even the metal structural material, may suffer mechanically induced damage. [25]

When liquid metal flows over solid metal/alloy structural surfaces with a moderate velocity, corrosion occurs by direct dissolution, and the corrosion mechanism can be



divided into two steps: (i) the dissolution reaction at the surface of the solid structure, and (ii) the mass transport by convection and diffusion of the dissolved metal from the solid-liquid interface to the bulk flow. A number of mechanisms of combined actions of flow and corrosion results in four main types of FAC (Figure 9 a-d): mass transport-controlled corrosion, phase transport-controlled corrosion, erosion-corrosion and cavitation-corrosion [15, 26].

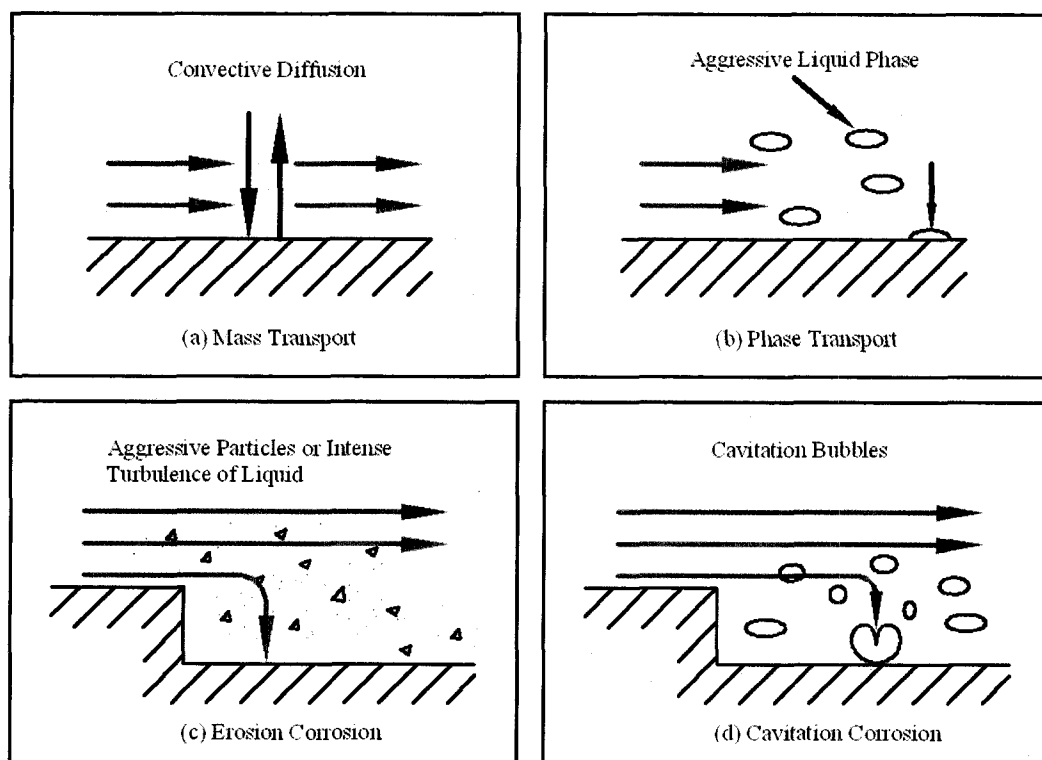


Figure 9. Representation of the four main types of flow affected corrosion.

When the flow velocity is low, the combined mass transport rate of convection and diffusion is less than the dissolution rate of the solid metal into the liquid metal (Figure 9 a). In such cases, the corrosion rate is controlled completely or partially by the combined mass transfer rate. And, the corrosion product concentration at the solid/liquid interface

equals the saturation or equilibrium concentration. Phase transport-controlled corrosion (Figure 9 b) was manifested during the transport of multi-phase systems, such as water droplets containing hydrocarbon with dissolved corrosive components. If these droplets contact the metal surface, they adhere to and corrode the surface. For multi-phase flows with aggressive particles or intense turbulence, the oxide layer can be stripped and worn away and erosion corrosions occur. [10, 26] Cavitation corrosion is the mechanical damage in cavitating liquids, which is caused by collapsing cavitation bubbles.

The main interactions between a flowing liquid and a solid surface are synthesized in Figure 10. In single-phase flow (Figure 10 a, b), shear stress and pressure variation dominate in various kinds of interaction of a flowing liquid with a solid wall. A relatively high roughness of the solid surface, a high flowing velocity, and a high turbulence all may cause the increase of shear stress. A high shear stress can lead to the onset of erosion-corrosion. In disturbed flow and in flows on a surface with the roughness greater than the thickness of the laminar sub-layer, pressure variations reach the surface and may produce mechanical damage. On the liquid/solid surface, such pressure variations are finally converted into local shear stresses, which in turn add to the overall shear stresses discussed previously. In a flow with solid particles, interactions between particles and the solid/liquid surface will cause transports of energy and deformations of the surface. The liquid or the aggressive particles are thrown against the surface of solid metals, which results in a higher wear rate. Local mechanical damage takes place as another kind of erosion (as shown in Figure 10 c). In the areas where the flow changes its direction sharply, such as sudden expansions or elbows, this erosion takes place more frequently. In the cavitation-corrosion (as shown in Figure 10 d), the cavitating bubbles collapse on

solid metal surfaces, and create micro-jets of the liquid metal to the solid metal surface, producing high local pressure and destroying the surface. This behavior can lead to brief high stress in the solid metal, causing localized corrosion fatigue damage and environmentally assisted micro-fractures of the solid metal. [26] For the mass transfer and heat transfer, convective diffusion and convective heat transfer dominate respectively.

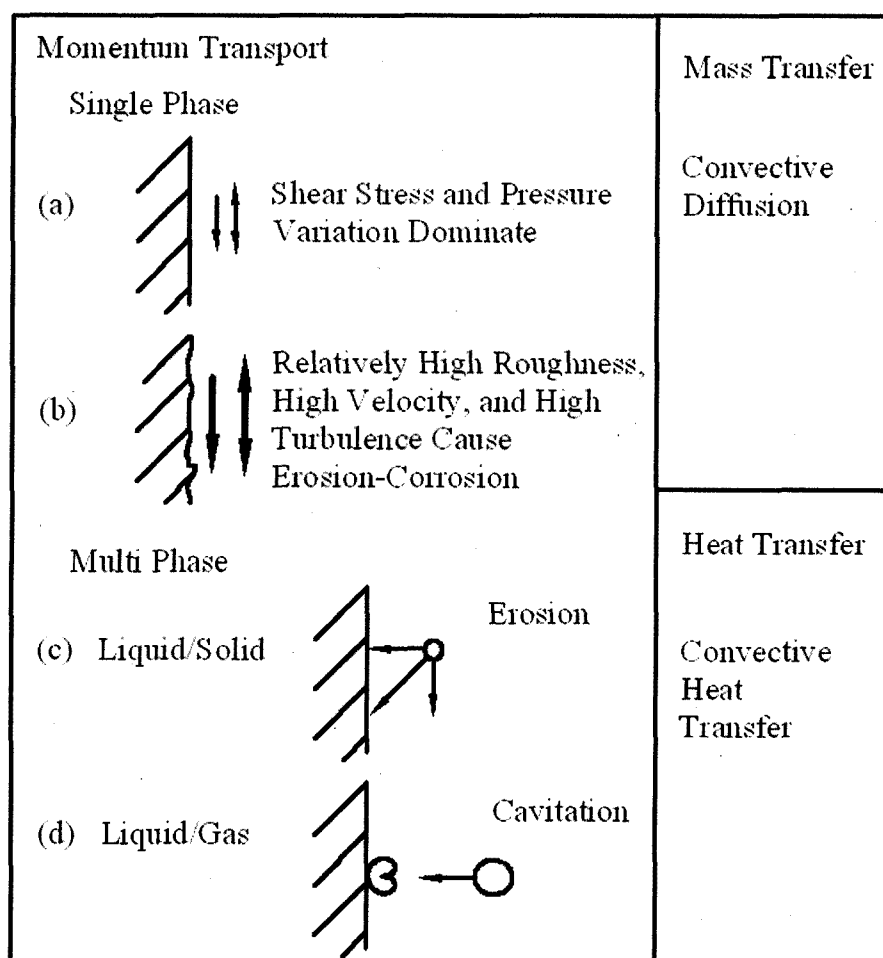


Figure 10. Interactions of a flowing liquid with a solid boundary.

From a physico-chemical point of view, corrosion reactions are heterogeneous reactions in which the reactants have to be transported towards the metal surface and the

corrosion products are transported away. Mass transfer is inherently correlated with liquid flow. [26] Basically, the mass transfer in the corrosion process of metal/alloys in liquid metal media includes: the molecular diffusion of metallic ions from the structural material to its surface with liquid as a result of a concentration gradient, the convection or diffusion of oxygen in the liquid media, the inward molecular transport of oxygen inside the material and the oxide layer, and transport of corrosion products from surfaces to bulk liquid metals.

The diffusion of metal and the transport of oxygen in the oxide layer and metal/alloys are very complex. The diffusion of iron in oxide layer can be explained by point defect theory [28], and is influenced by the oxygen pressure and temperature and point defects. The transport mechanism of oxygen in oxide layer is not well understood at present. The oxygen self-diffusion coefficient in oxide layer is very small. However, there must be some fast paths for oxygen to arrive at the inner layer at sufficiently high rates to account for the observed inner oxide growth. [27]

According to the oxygen control technique, the corrosion of structural materials, such as steel, in molten LBE, occurs via dissolution at very low oxygen concentrations, and through surface oxidation and reduction of surface oxides at higher oxygen concentrations. No matter which way the corrosion proceeds, it is usually sufficiently fast and the corrosion is limited by the mass transfer process. [21]

Corrosion products dissolved into LBE at surfaces are transported in LBE for sustained corrosion or stops when the concentrations reach the saturation limits. In a static isothermal system, the transport process is mostly diffusion that depends on the corrosion product concentration gradient, and the corrosion product diffusion coefficient

in LBE. The corrosion process stops when the liquid is saturated with the corrosion products. Since the diffusion coefficients in liquids are very small, the resulting reaction rate in a stagnant solution is very small. When the dissolution rate is less than the diffusion rate, diffusion is fast enough to take all the dissolved species away, thus the corrosion rate is determined by the dissolution rate. When the dissolution rate is greater than the diffusion rate, the concentration at the interface is always at saturation and the corrosion rate is determined by the diffusion rate. In liquid metal systems there is good evidence that both cases which were described above occur [29], depending on the solution and solute. Note that the diffusion coefficient is a function of temperature.

The situation is quite different in a flowing system. Corrosion products can be transported by both diffusion and convection. The mass transport rate is increased considerably since the convective mass transfer is much more efficient than the molecular diffusion. Moreover, in a non-isothermal flowing system, as analyzed earlier, the flowing liquid takes corrosion products from dissolution locations to other places, where the corrosion products may deposit.

### 1.2.2 Factors Affecting Structural Materials Corrosion in LBE

Liquid metal corrosion process may involve the following four processes [22]:

- (1) dissolution of the solid materials into the liquid metal;
- (2) thermal and concentration gradients assisted mass transfer;
- (3) redistribution of the interstitial impurities between the solid and liquid metals; and
- (4) diffusion penetration of liquid metals into solid metals with formation of solid solutions or new phases.

The operating conditions determine which process dominates. Factors affecting one of the above processes should affect the corrosion rate. These factors are divided into three groups [22]: corrosion, metallurgical, and technological.

The corrosion factors include the chemical composition of the liquid metal and its impurity contents, the flowing conditions (the pressure and the flow velocity), the temperature and its profile, the exposure time, etc.

The metallurgical factors include the purity of the solid metals, alloying, and the structural state and microstructure of solid materials.

The technological factors include the stress state, formation of new phases associated with machining, welding, assembling of structures, and the loading conditions [10, 22].

The main factors affecting the corrosion process are analyzed below.

(a) Flow velocity

The flow velocity is the most important factor to influence corrosion among all of the external factors [30]. The mechanism of the flow velocity affecting the corrosion is analyzed previously. As a summarization, the effects of the flow velocity for single-phase flow are as follows [10, 15, 31] (Figure 11):

(a.1) At low velocities, the corrosion is controlled or partially controlled by mass transfer. In such cases, the thickness of the laminar mass transfer layer becomes thinner with increasing velocity and, as a result, the corrosion rate increases.

(a.2) When the velocity exceeds a critical value, the mass transfer rate becomes high enough to transport all the corrosion products away from the interface. Then the

corrosion rate is determined by the dissolution/reaction rate, and independent of the flow velocity. The corrosion is activation controlled.

(a.3) For very high velocities, the high shear stress at the interface can strip the protective film on the surface of the structure. Some cavities appear at the interface and the corrosion rate increases sharply with the flow velocity. For heavy liquid metals/alloys such as LBE, erosion-corrosion is likely to occur at moderately high velocities due to their high densities.

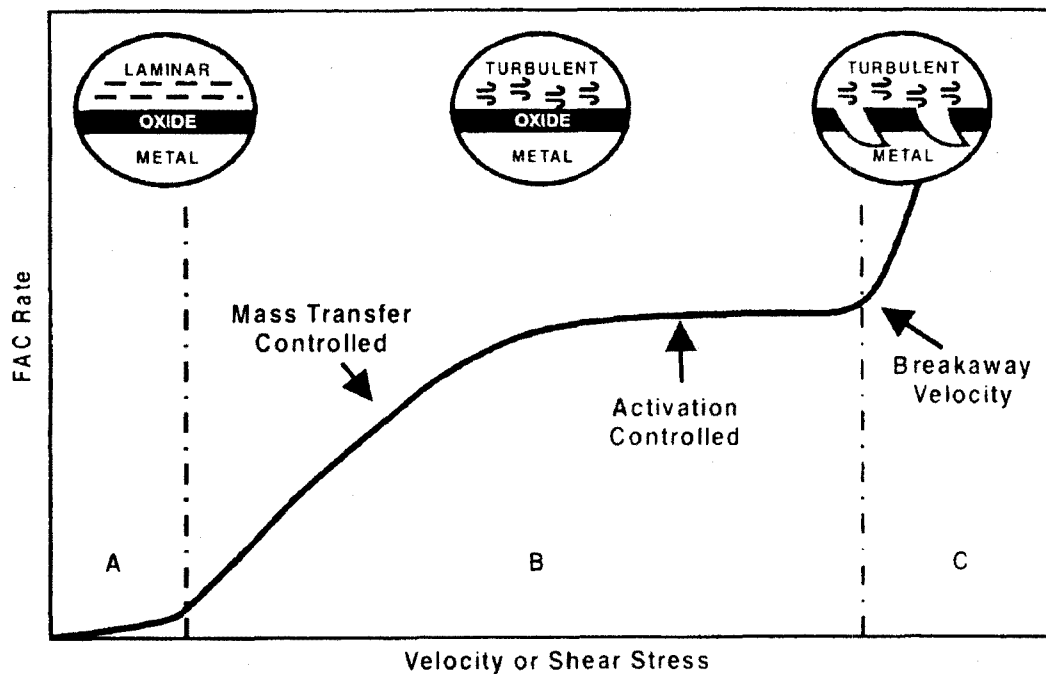


Figure 11. Velocity effects on the corrosion rate. [31]

In practical nuclear coolant system designs, conditions (2) and (3) should be avoided due to rapid and nonuniform corrosion and erosion-corrosion. Therefore, most of the corrosion studies performed for liquid metals/alloys are in the mass transfer controlled regime.

### (b) Temperature

The dissolution/chemical reaction rates, the corrosion product diffusion coefficients in solid and liquid alloys, and the liquid metal viscosity are all functions of temperature. Increasing temperature results in higher dissolution rates, higher solubility, higher diffusion coefficients, and smaller viscosities. These changes all lead to higher corrosion rates. A sustained corrosion process can only occur in a non-isothermal system such as nuclear coolant systems [32]. In a closed loop system, without temperature gradients, species concentration would eventually reach a homogeneous distribution and no further corrosion would occur. With temperature gradients, steel elements will be dissolved from the hot legs, transported to locations with lower temperatures, and precipitate. As the temperature gradient increases, attacks in hot sections of loops become more severe [30]. Precipitation in the cold areas can accelerate corrosion in the hot sections [7]. Even for loops having the same maximum temperature and other hydraulic parameters, the corrosion rates can be different if the loops are operated under different stream-wise temperature profiles [33].

### (c) Solubility of metals in Bi, Pb, and LBE

As analyzed previously, the first step of the corrosion process is the dissolution of the structural materials to the liquid metal media. The dissolution rate depends on the liquid media, the ratio of the surface area of the solid metal to the volume of the liquid metal, the conditions of the surface, the content of interstitial impurities, such as oxygen and nitrogen in the liquid metal/alloy, and the compositions of the solid materials [15]. As it was mentioned previously, the corrosion on steels in molten LBE occurs via dissolution at very low oxygen concentrations, and through surface oxidation and reduction of



surface oxides at higher oxygen concentrations. The corrosion is controlled by the mass transfer process since the reaction usually sufficiently fast. Thus, the corrosion products' concentrations are always at their saturated or equilibrium levels at the solid-liquid interface. [21, 34, 35, 36] Therefore, solubility of iron, chromium, and nickel in molten lead and LBE plays an important role in corrosion phenomena when using such liquid metals/alloys as nuclear coolants. Generally, the saturation solubility ( $c_s$ ) of a metal in LBE, lead and bismuth can be written as:

$$\log c_s [\text{wppm}] = A_1 + B_1 / T[K] \quad (1-4)$$

where  $A_1$  and  $B_1$  are constant coefficients, and the values for Fe, Cr, and Ni in liquid LBE, and lead are given in

Table 3. [10, 37, 38].

Table 3 Solubility Coefficients of Ni, Fe, and Cr in LBE [37] and Pb [38] (Temperatures are in the Unit of Kelvin)

		Fe		Cr		Ni	
		$A_1$	$B_1$	$A_1$	$B_1$	$A_1$	$B_1$
Lead	(673<T<873)	4.34	-3450				
	(873<T<1020)	5.82	-4860				
LBE		6.10	-4380	5.08	-2280	7.53	-843

The comparison of solubility of Fe, Cr and Ni in LBE and Pb is shown in Figure 12. The solubility is compared with the experimental data of solubility of Fe in LBE as well. The comparison shows the empirical equation agrees very well with the experimental data from Ref. [38] All the solubility increases quickly with an increasing temperature. The solubility of Ni in LBE is much higher than that of Fe and Cr, indicating that Ni content in steels used for containments of LBE needs to be reduced or protected to

increase the corrosion resistance. The solubility of a metal in liquid lead-bismuth alloys depends on the compositions of the liquid alloy. The Fe solubility in pure liquid lead is lower than the Fe solubility in LBE, indicating that the pure liquid lead is less corrosive than LBE.

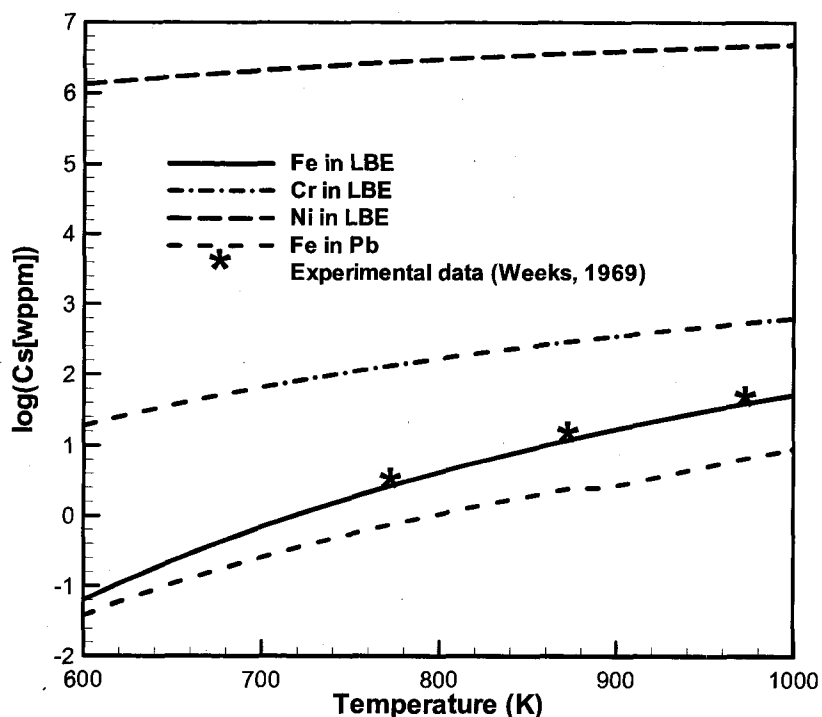


Figure 12. Comparison of solubility of Fe in LBE and Pb, solubility of Cr and Ni in LBE, with the experimental data [38] of solubility of Fe in LBE.

### 1.3 Oxidation of Stainless Steels in Lead/LBE

The oxidation of stainless steel in LBE or lead alloys, which is a high temperature chemical reaction problem, is very complex. Knowledge and understanding of the basic principles and mechanisms of oxidation of stainless steel are essential to analyze any lead or lead alloys coolant systems in which lead or lead alloys is the working medium. In

order to understand the oxidation mechanism, a simpler case with pure iron is analyzed first. In the oxidation process for pure iron, the dissolution of oxygen into the alloys is involved, together with the ionization of iron, migration of iron ions and electrons through the formed oxide film. Moreover, the chemical reactions between metal atoms and atomic oxygen take place on the oxide/metal interface, on the oxide/liquid interface and inside the oxide simultaneously, in high temperature lead or lead alloy flows. The chemical and chemical thermodynamics basis, oxide layer structure, and the oxide layer forming mechanism will be discussed one by one. The oxide layer structure of stainless steel depends on the material composition, the oxygen concentration, the flow temperature and other flow conditions.

### 1.3.1 Chemical and Chemical Thermodynamics Basis

The oxygen in high temperature metal flow is in atomic phase instead of molecular phase. [39] The dissolution of oxygen into LBE can be expressed as the following reaction,



During the oxidation, the chemical reactions are much faster than mass transfer. Thus it is reasonable to assume all the chemical reactions are at their local equilibrium states. [27] In studying thermodynamics, it is important to take the attitude that all reactions are reversible. In a practical LBE coolant system or an LBE test facility, the flow is fully turbulent and it can mix the corrosion product quickly, thus the mass transfer rate in the boundary layer dominates the transport in the liquid. It was commonly accepted that the mass transport in the oxide layer dominates the whole oxide process. [27]

The oxidation reaction can be divided into three parts: inner interface action, outer interface reaction, and reaction in the oxide layer.

At the inner interface reaction (oxide/metal interface), the oxygen atoms, which were transported to the inner interface, react with the iron atoms at the inner interface following the Eq (1-6).



At a high temperature, this reaction induces the growth of an inner oxide layer easily. Also, at the inner interface between oxide layer and iron, iron ionizes according to



The iron ions and electrons are transported outwards through the oxide layer. At a high temperature, iron ions can form new iron atoms any time by reacting with the electrons.



The reactants, atomic irons, react with the oxygen which was transported in the oxide via Eq. (1-6). This part of reactions occur whenever iron atoms meet enough oxygen atoms during the transport, and cause the redistribution of oxide layer and the volume expansion of the oxide layer.

At the outer interface (oxide/liquid interface), surface reactions take place following the Eqs (1-8) and (1-6). This part of oxidation accounts for the outward growth of the oxide layer. The migration processes of oxygen and iron ions and the oxide layer growth, in both sides of inward and outward, were also analyzed in Ref. [18]

Simply, the overall equation for the chemical reaction involved in the oxidation can be expressed in a general form,



The driving force for this reaction is, of course, the free energy change associated with the formation of oxide from the reactants and can be calculated if the pertinent thermochemical data are available. Though, as needed to keep in mind, the rate of a thermodynamically possible reaction is a kinetic problem instead of a thermodynamical problem. [40]

The transport of steel components and oxygen in the oxide layer is very complex and not well understood. Among which, the diffusion of iron in oxide layer can be explained by point defect theory. The diffusion rate of iron is influenced by the oxygen pressure, temperature and point defects (such as, vacancies and interstitials). [28] The oxygen is assumed to migrate through the oxide film by some unclear mechanisms. [27] It is reasonable to assume that the transport rates (not only the diffusion) of iron and oxygen are of the same order, and both the transport rates of iron and oxygen control the oxidation rates. The transport of electrons is comparatively fast. [27]

The oxidation of real stainless steel becomes more complex because of the added alloying components, impurities and other defects. With different temperature and flow conditions, the oxide film for a particular material can be different. The mechanism of the oxide layer growth of stainless steel in lead or lead alloys is studied based on the observation of oxidation experiments. A brief review of the identification of oxide structure will be summarized before the mechanism analysis.

### 1.3.2 The Oxide Structure from Experimental Results

The existence of the added alloying elements, impurity and other defects in the stainless steel will increase the complexity in the oxidation process. The oxide layer structure of steel in liquid lead-alloy with oxygen control, in principle, depends on steel compositions, temperature and hydraulic factors.

The most important added alloying element for improving the anticorrosiveness is chrome. The addition of element chrome can protect the stainless steel by enhancing the electrode potential of iron, obviously. The possible stainless steels in LBE systems are martensitic stainless steels and austenitic stainless steels. The chrome contents in martensitic stainless steels usually are between 13% to 18 wt%, which ensure a good corrosion resistance. Moreover, the martensitic stainless steels have a relatively high content of carbon, 0.1% to 1.0 wt%. Therefore, the martensitic stainless steels have very good mechanical properties such as, hardness, mechanical strength, abrasion resistance, and machinability. The austenitic stainless steels are the most popular stainless steels used in industry. The chrome contents in austenitic stainless steels usually are 17 wt% and above. Moreover, element nickel is added in until around 17 wt%. Titanium, niobium, molybdenum, and copper are often added as well. Therefore, the austenitic stainless steels have excellent corrosion resistance. [41]

#### (a). Oxide layer of stainless steel in pure molten lead

G. Muller et al [42] conducted corrosion experiments in pure molten lead using plate specimens of martensitic steel OPTIFER IVc (Fe9Cr) and of austenitic steel 1.4970 (16Cr15Ni), with and without surface treatment. The specimens were small plates of  $115 \times 10 \times 2 \text{ mm}^3$  dimension. The test temperature was set at 550 °C and the oxygen

concentration was controlled at  $8 \times 10^{-6}$  at% in the molten lead. The scanning electron microscope (SEM) of cross-section of OPTIFER specimen after 3000 hours is shown in Figure 13. A brittle outer layer with low Cr concentration and a Cr rich spinel inner layer are pronounced in the SEM. Below the oxide layer, a oxygen transport zone can be observed in which oxides precipitate along the grain boundaries.

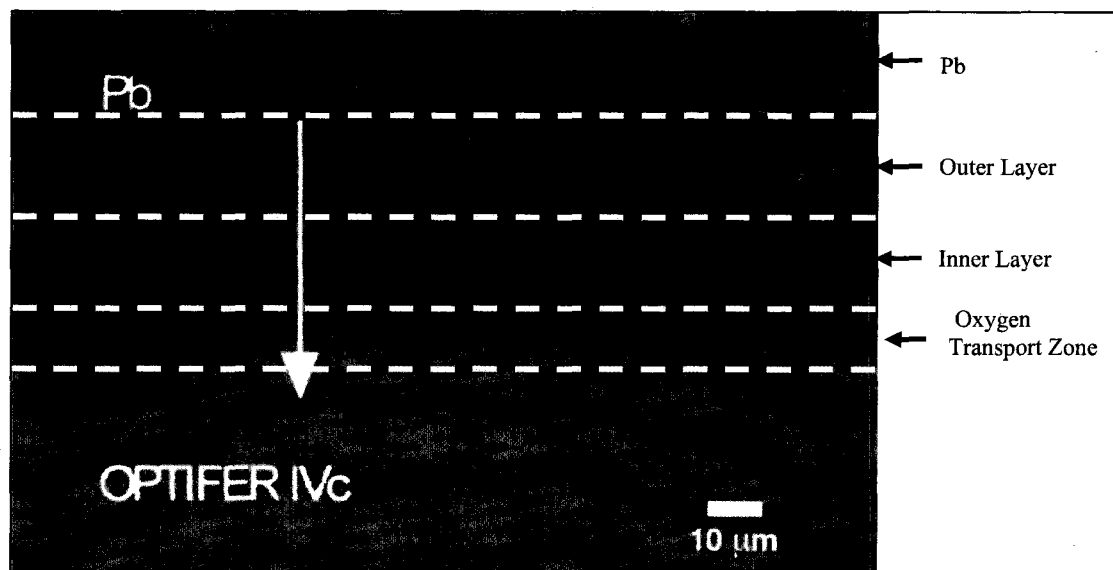


Figure 13. (SEM) of cross-section of OPTIFER specimen after 3000 hours at 550°C [42].

The scanning electron microscope (SEM) of a cross-section of a 1.4970 specimen after 3000 hours is shown in Figure 14. The oxide structure is similar to that on OPTIFER steel with layers of magnetite and Fe-Cr spinel and an oxygen diffusion substrate in the interior. Because the higher content of Cr and the presentation of Ni, the corrosion/oxidation resistance is higher in austenitic stainless steels. The oxide layer is much thinner in the steel 1.4970 than that in the steel OPTIFER, with the same conditions. It was reported that the spinel zone contains Pb and oxygen penetrates along grain boundaries up to 20  $\mu\text{m}$  deep into the metal matrix. The experiments demonstrate

that the steel 1.4970 (austenitic stainless steel) has better oxidation resistance in liquid lead than OPTIFER (martensitic stainless steel) under controlling of oxygen. However, this slow oxidation rate may lead to penetration of lead into the material since a thin oxide layer may not be able to protect the structure efficiently. The author also showed that the surface treatment can improve the corrosion/oxidation resistance of the stainless steel.

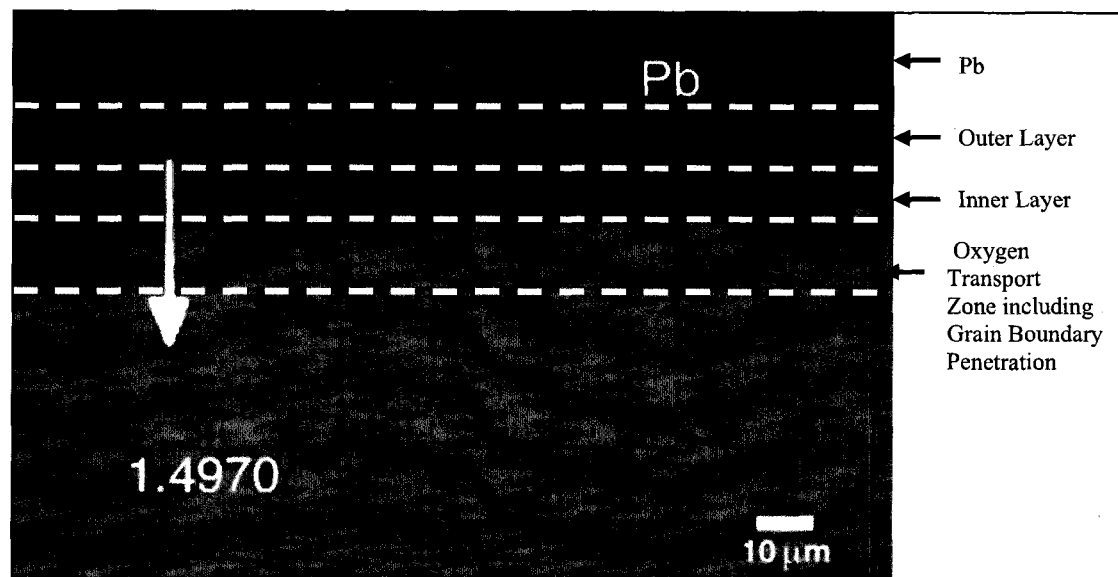


Figure 14. (SEM) of cross-section of 1.4970 specimen after 3000 hours at 550°C [42].

#### (b). Oxide layer of stainless steel in LBE

Compatibility tests of eight kinds of stainless steels in flowing LBE were performed in the non-isothermal experimental facility of IPPE-Obninsk by Barbier et al. [43] Two austenitic stainless steels AISI 316L and 1.4970, and six martensitic steels, Optifer IVc, T91, Batman 27, Batman 28, EP823, and EM10 are exposed to flowing LBE for 1000, 2000 and 3000 h and at two temperatures 300 °C and 470 °C. The experiments are under



a controlled oxygen level at  $10^{-6}$  wt% . The flowing velocity of LBE is set at  $1.9 \pm 0.1$  m/s . The results were reported in Ref. [43].

With the same facilities of IPPE-Obninsk, tube and rod specimens of austenitic steels 316/316L, D-9, and martensitic steels HT-9, T410, were tested in the flowing LBE by J. S. Zhang et al. The experiments were carried out at 460 °C and 550 °C for exposure times of 1000, 2000, and 3000 h. The flow velocity at the test section was set at 1.9 m/s and the oxygen concentration in LBE was controlled in the range of 0.03-0.05 wppm. [17]

Generally, there are three possible structures for martensitic steels, according to existing experimental results [44]:

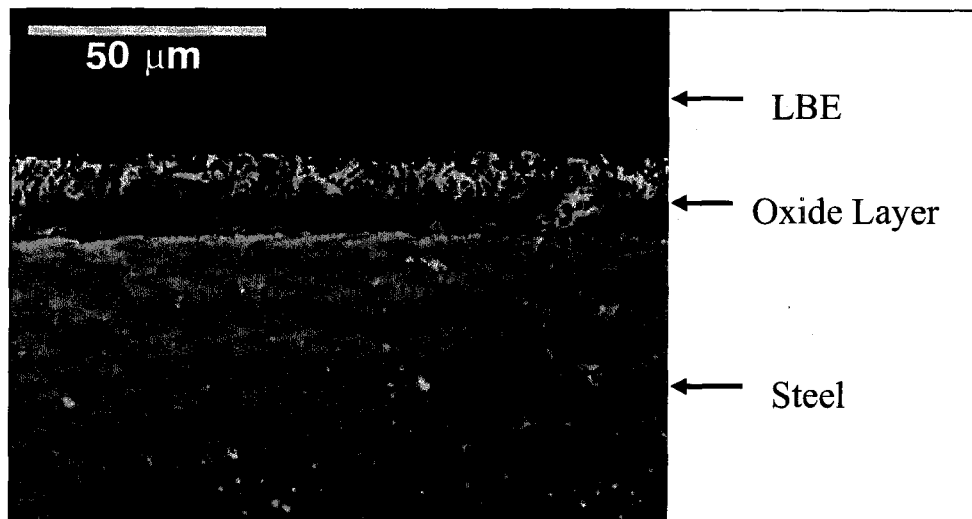


Figure 15. SEM micrograph of the oxide layer structure of the T91 steel at 470 °C after 3000 h exposure. [43]

For temperature at 300°C, the total thickness is usually very thin and sometimes too thin to measure, such as T91 steel. And the oxide scale may not be distributed uniformly.

The martensitic stainless steels show a good corrosion resistance, and the thin oxide films formed on the surfaces lead to protection against liquid metal corrosion.

For temperature at 460-470 °C, typically a duplex-layer structure can be observed, for example, in specimens Batman 27 after 1000 h exposure, Batman 28 after 1000 h exposure, EM10 steel, T91 steel, Optifer IVc, and EP823. The oxide layer is composed of an external magnetite layer,  $\text{Fe}_3\text{O}_4$  and a compact internal Fe-Cr spinel oxide layer. The SEM micrograph of T91 steel after 3000 h exposure is shown in Figure 15.

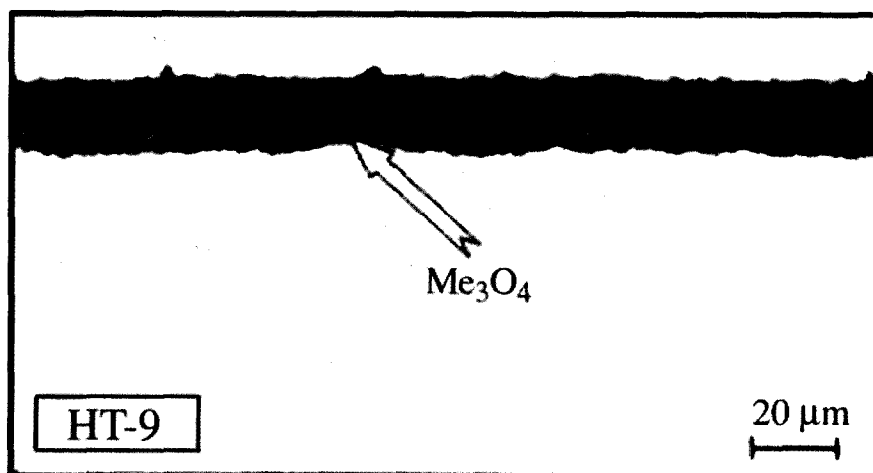


Figure 16. Cross-section of HT-9 (tube) after being exposed to flowing LBE for 2000 h at  
 $T = 460\text{ }^{\circ}\text{C}$ . [17]

In some cases, the external magnetite layer is not observed. The duplex-layer can protect the steel from dissolution. Penetrations of lead are sometimes observed in the outer layer. While, after 2000 h and 3000 h of exposure, an internal oxidation zone (third layer), with oxide precipitates along the grain boundaries, is observed below the Fe-Cr spinel layer in steels Batman 27 and Batman 28. [43] The presence of LBE was observed between the inner layer and outer layer in EM 10 steel and the penetration in the outer

layer was more evident with longer test time. The duplex-layer oxide film was also reported by Zhang [17] for HT-9 steel at 460 °C (as shown in Figure 16). No liquid metal corrosion was observed in either the experiments by Barbier [43] or Zhang [17]. However, a non-uniform single oxide layer of Cr-rich spinel was observed in a rod specimen of T410, and local damage was observed after 2000 h [17]. From Figure 15 and Figure 16, the oxide layer thicknesses are very close, which confirms the consistency of the two experiments conducted by Barbier [43] and Zhang [17].

For temperature above 550°C, an oxygen diffusion layer underneath the oxide layer after 3000 h of exposure at 550 °C, was observed by Zhang [17] for HT-9 steel at 550 °C (as shown in Figure 17). For T-410 steel, the rod specimen was subjected to heavy liquid metal corrosion.

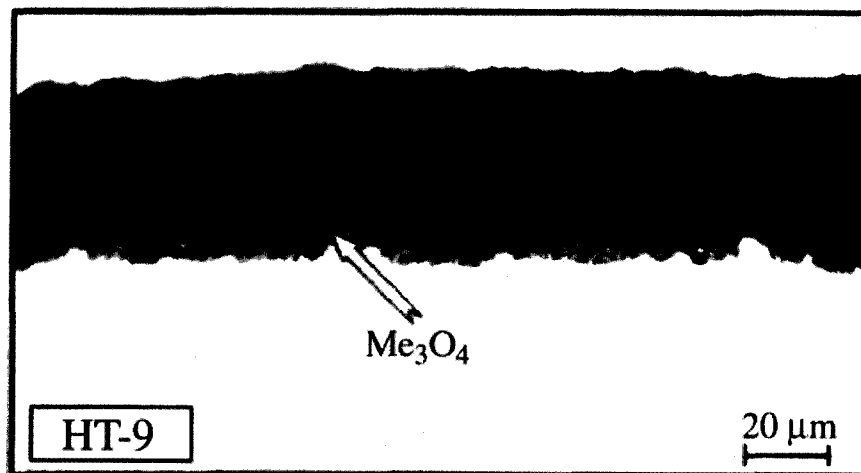


Figure 17. Cross-section of HT-9 (tube) after being exposed to flowing LBE for 3000 h at  
 $T = 550\text{ }^{\circ}\text{C}$ . [17]

Since the austenitic stainless steels have more Cr and Ni than martensitic stainless steels, the oxide layer formed on austenitic steels has the following possible structures [27]:

For temperature below 500°C, the oxide layer is very thin and is composed of the single-layer Fe-Cr spinel, which can prevent direct dissolution (316L, 1.4970 specimens in Barbier's test [43], and tube specimen of 316 in Zhang's test [17]). The SEM micrograph of 1.4970 steel after 3000 h exposure is shown in Figure 18. The Cross-section of tube specimen 316, after being exposed to flowing LBE for 2000 h at  $T = 460^{\circ}\text{C}$  from Zhang's experiment [17], is shown in Figure 19. Also, Figure 18 and Figure 19 show agreement of Barbier's [43] and Zhang's [17] experimental results in the total oxide structure and thickness.

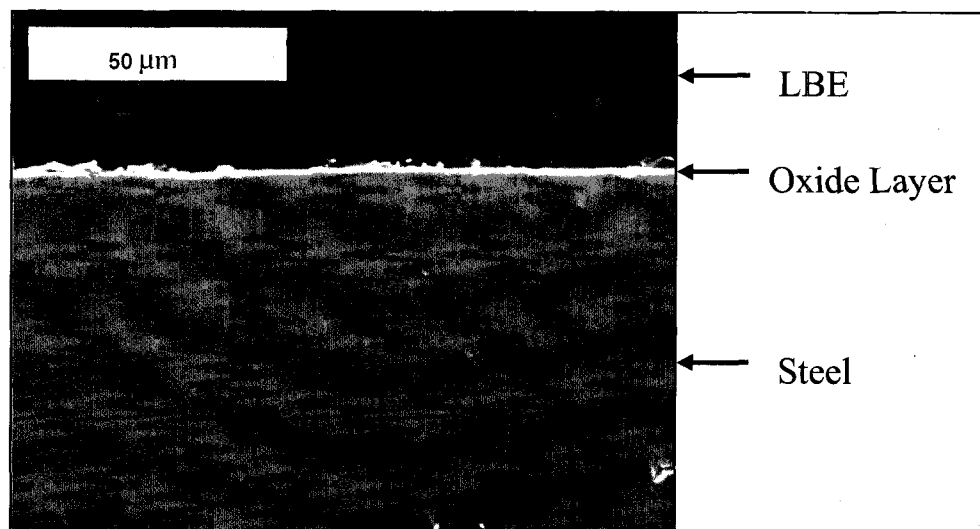


Figure 18. SEM micrograph of the oxide layer structure of the 1.4970 steel at 470 °C after 3000 h exposure. [43]

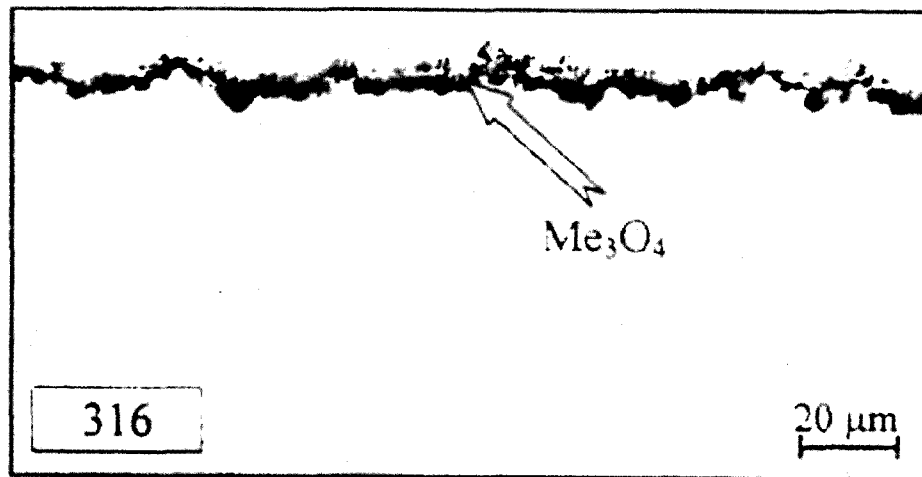


Figure 19. Cross-section of 316 (tube) after being exposed to flowing LBE for 2000 h at  $T = 460^\circ\text{C}$ . [17]

Slot corrosion was detected on the surface of rod specimen of 316L steel after 2000 h of tests at  $460^\circ\text{C}$  (as shown in Figure 20). The thickness of oxide film in steel D-9 is very thin even after 3000 h. [17]



Figure 20. Slot corrosion of 316L steel at  $T = 460^\circ\text{C}$  for 2000 h. [17]

Typically, the oxide layer has a duplex-layer structure for a temperature at  $550^\circ\text{C}$ , such as tube specimens made of tube specimens of 316 and D-9 steels [17]. The duplex-layer oxide can prevent steel component dissolution efficiently. The cross-section of steel

316 (tube), with a duplex-layer after being exposed to flowing LBE for 2000 h at  $T = 550$  °C, is shown in Figure 21.

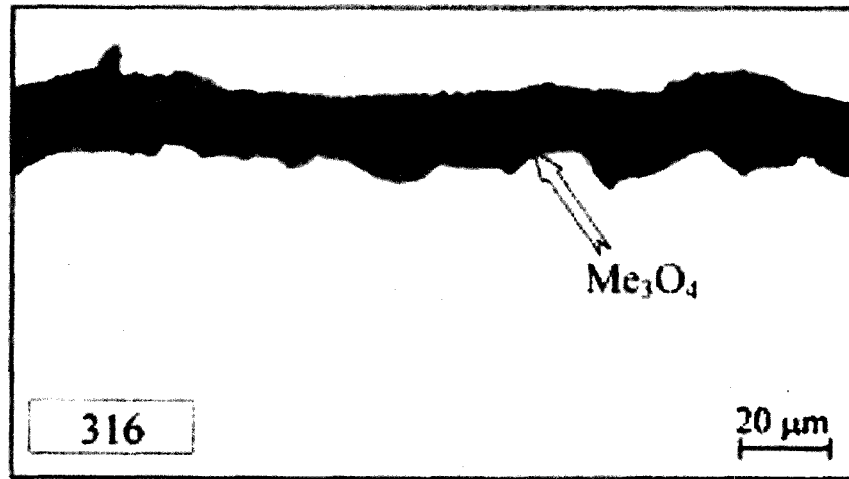


Figure 21. Cross-section of 316 (tube) after being exposed to flowing LBE for 2000 h at  $T = 550$  °C. [17]

As analyzed above, the structure of the oxide layer strongly depends on surface treatments, manufacturing technology, and flow conditions, as well. For instance, a single-layer structure oxide layer was observed by Zhang [17] in a rod specimen of steel 316L. However, a duplex-layer oxide film was reported by Muller in Ref [9]. Both liquid metal corrosion and slot corrosion were observed in austenitic stainless steel 316L at 550 °C. [17]

In the cases with the only single layer structure at such a high temperature, heavy dissolution corrosion was observed and the material could not be well protected. For temperature above 550 °C, more severe dissolution corrosion and local damage occurs, which should be avoided in real manipulation. [17] For these cases, the oxygen

concentration may need to be controlled at a higher level, as long as it will not exceed the saturation concentration.

### 1.3.3 The Mechanism of the Oxide Layer Growth

Based on the observations in Refs. [17, 42, 43], the mechanism of the oxide layer growth of stainless steel in liquid lead and leady alloys can be summarized, together with the consideration of alloying elements in the steels. The possible oxide structures of martensitic or austenitic steels in liquid lead and lead-alloys with oxygen control can be outlined as the following cases.

#### (a) For static molten lead or LBE

The flow conditions' influence on the oxidation process can be ignored for a case in static lead or LBE environment. The steel components can be dissolved to the molten lead and lead alloys since most of the steel components have high solubility in liquid lead and lead alloys [17]. If the oxygen concentration is too low to form the protective oxide layer, heavy dissolution corrosion occurs (as shown in Figure 22). Such corrosion can also occur at a high temperature if the forming oxide layer cannot prevent steel components from dissolution. [45]

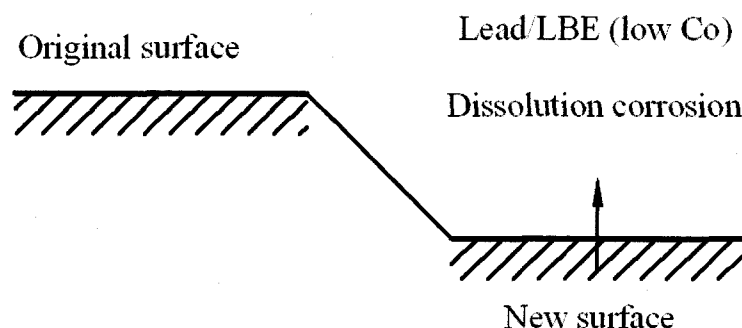


Figure 22. Dissolution corrosion in unsaturated static lead or LBE.

When the liquid is saturated with the steel components, and if the steel components which were released to the solution are in equilibrium with the components deposited on the structural surface, the corrosion will cease (as shown in Figure 23). This is a case with pre-corrosion and no change will be observed on the stainless steel surface.

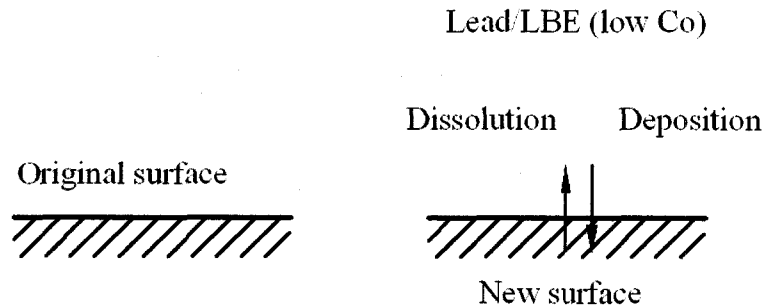


Figure 23. Corrosion ceases when dissolution is in balance with deposition.

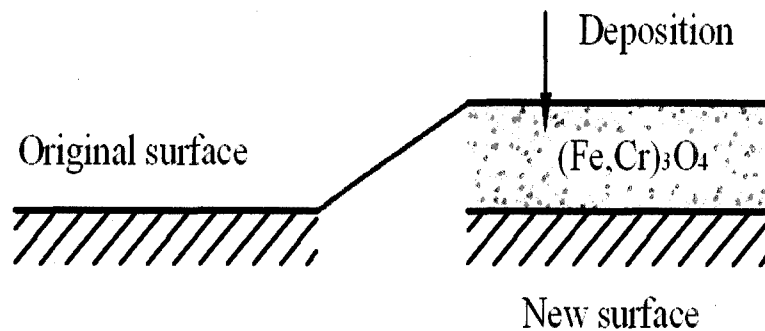


Figure 24. Deposition induces a single layer of  $(Fe,Cr)_3O_4$ .

The reaction will be different from the case shown in Figure 23 if the oxygen level is increased to a higher level. The protective oxide films will begin to form along the surface, if the oxygen concentration in lead or lead alloys is sufficient. The dissolved oxygen can react with the dissolved steel components and the insoluble oxide will be precipitated on the surface of the steel. At the beginning, a single layer oxide film will be



formed because all components of the stainless steel were pre-dissolved into the molten lead or LBE. Therefore, a deposition-induced single-layer structure of oxide layer, mainly  $(\text{Fe,Cr})_3\text{O}_4$ , can be observed as shown in Figure 24.

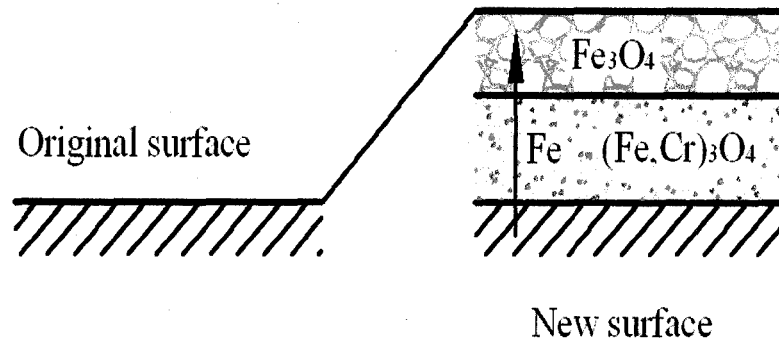


Figure 25. Duplex-layer structure without oxygen transported into the stainless steel.

If the oxygen concentration is controlled at a particular level, which is higher than zero and not high enough to diffuse into the oxide layer and the stainless steel structure, the concentration of dissolved steel components will become more and more dilute because of the reaction in the molten metal/alloy environment. Then, migration of the steel components into the lead and lead alloys starts again. Since the diffusion rates of Cr and other elements in the oxide layer are much lower than the diffusion rate of iron in the oxide layer, the oxide layer works as a good barrier for the diffusion of Cr and other elements. For Fe-Cr steels, the Fe-Cr spinel initially forming can retain Cr and other components such as Ni to stay their original location because they have a low diffusion rate through the scale, compared with Fe [46]. Therefore, the diffusion of Cr and other components into lead or lead alloy through the oxide layer will be neglected after the oxide film thickness reaches to 2-3 nm [46]. When all the dissolved Cr is consumed, a

new layer of the magnetite ( $\text{Fe}_3\text{O}_4$ ) will be formed on the top of the layer  $(\text{Fe,Cr})_3\text{O}_4$  via the surface reaction between the outward-diffused iron and oxygen, as illustrated in Figure 25 . The oxidation is controlled by the diffusion of iron in the oxide layer.

At a higher oxygen level, the surface reaction of the outwards diffused iron and oxygen cannot consume all the oxygen in the molten lead or LBE. The oxygen begins to migrate through the oxide layer and react with both Fe and Cr beneath the oxide film, increasing the thickness of the spinel. Obviously, the outwards diffused Fe reacts with oxygen at the outer surface and forms a porous outer layer of  $\text{Fe}_3\text{O}_4$  at the same time, which accounts for the growth of the outer oxide layer. As investigated previously, the transport of oxygen and iron both control the oxidation process. The duplex-layer oxide formation controlled by both the transport of oxygen and iron can be illustrated in Figure 26.

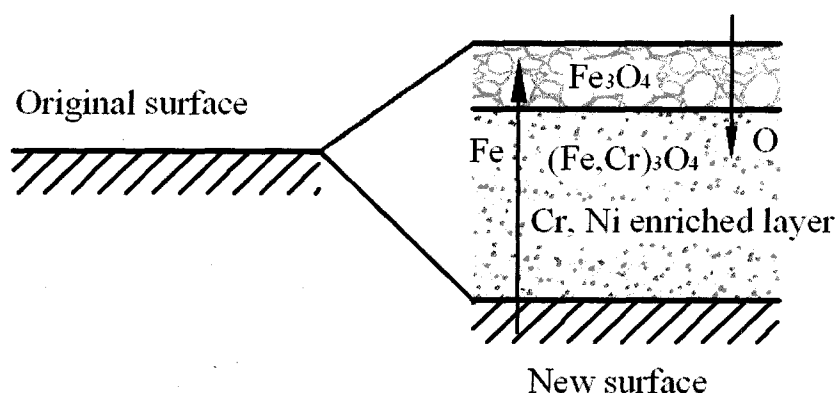


Figure 26. Duplex-layer structure oxide controlled by transports of iron and oxygen.

In fresh static LBE or lead which is clean and does not contain the steel components, surface oxide reaction occurs on the stainless steel surface if the oxygen level is high. Initially, in the molten LBE or lead, a very thin oxide layer of  $\text{Fe}_3\text{O}_4$  forms on the steel

surface quickly. This is different with the pre-corrosion case for a saturated LBE/lead alloys environment. The single layer is formed by the surface reaction of Fe and O instead of the deposition of  $\text{Fe}_3\text{O}_4$  and  $\text{Cr}_2\text{O}_3$  in the liquid. During the reaction, Fe is consumed in the material. Since iron is the main component in stainless steels, redistribution of the material and volume contraction take place because of the consumption of iron. Two directions in movement of the interface can be observed. One is the outwards movement of the oxide/liquid interface, and another one is the inwards movement of the oxide/steel interface. The single layer structure oxide induced by the surface reaction in clean static lead/LBE is illustrated in Figure 27.

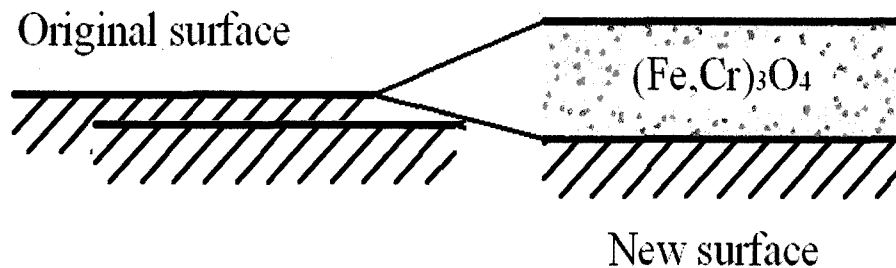


Figure 27. Single layer structure oxide induced by surface reaction in clean static lead/LBE.

With the increasing of the oxygen concentration in molten lead or LBE, oxygen begins to transport inwards to the material, which induces the reaction inside the material and on the interface of oxide/steel. The protective film impedes the oxidation process by slowing down the transport of oxygen and iron through the oxide layer when the film reaches 2-3 nm [46]. The oxidation is controlled by the transport of oxygen and iron. This transport will enhance the total reaction rate, together with the outer interface reaction. The oxygen transported inwards reacts with the iron and Cr and forms spinel of

(Fe,Cr)<sub>3</sub>O<sub>4</sub>. Beneath the inner spinel layer, there will be a layer with rich contents of Cr and other components since Fe diffuses out and forms the oxide layer. Therefore, a duplex-layer structure of oxide will be observed. And the inner interface of oxide/steel will move faster than the single layer case in Figure 27, since oxygen is now transported in. The duplex layer structure of oxide formation is shown in Figure 28.

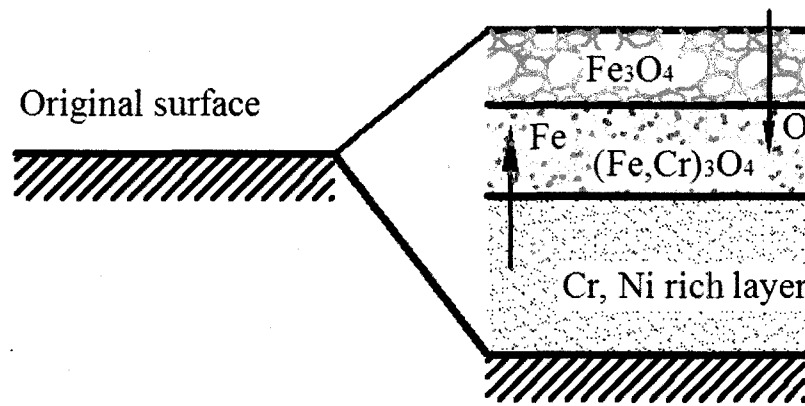


Figure 28. Duplex layer structure of oxide with oxygen transported in.

(b) For flowing lead or LBE

For cases of flowing lead and lead alloys environment, the corrosion and oxidation are different. First, the flowing solution (lead-alloys) can remove the oxide layer at the outer surface. Second, the non-isothermal condition may affect the corrosion and oxidation as well. These effects, of course, will make the corrosion and oxidation more complex. Simply, if the removal rate is greater than the diffusion rate of metal through the scale, no new oxide can be formed at the outer surface (liquid /oxide interface) and the oxide can be formed at the oxide/steel surface. Also, if the scale removal rate is large enough to remove the outer oxide layer, a single layer structure will be observed. If the scale removal rate is large enough to remove the total oxide layer, no oxide film will be

observed, and net removal of the structural material may occur, which is one kind of erosion corrosion.

Absent oxygen, or if the concentration of oxygen in lead or LBE is close to zero, the steel components will be dissolved in the molten lead and lead alloys. This case is similar to the first case in static lead/LBE. With the influence of the flowing conditions, the dissolved components can be transferred away quickly. Thus the dissolution corrosion rate is increased. Since there is no oxide film formed on the structural surface, net erosion on the structural material may occur, which will induce an erosion corrosion. (as shown in Figure 29)

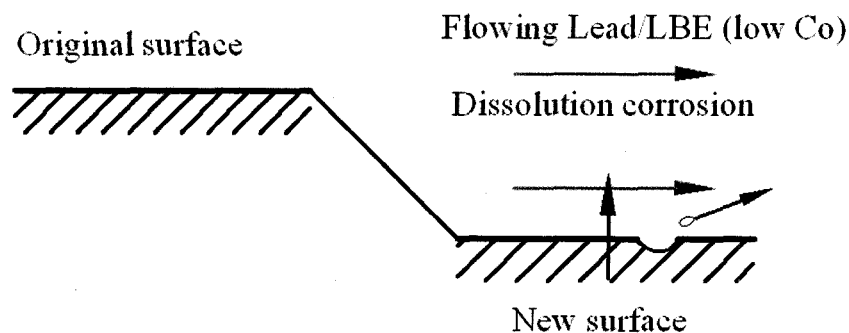


Figure 29. Dissolution corrosion in unsaturated flowing lead or LBE.

When the liquid is saturated with the steel components, the dissolution corrosion ceases at the balance between the dissolution and precipitation in an isothermal system. Only the scale removal process remains. This case is similar to the second case in static lead/LBE with pre-corrosion. And erosion corrosion may be observed because of the scale fragments in flowing lead/LBE and no film protection on the stainless steel surface (Figure 30).

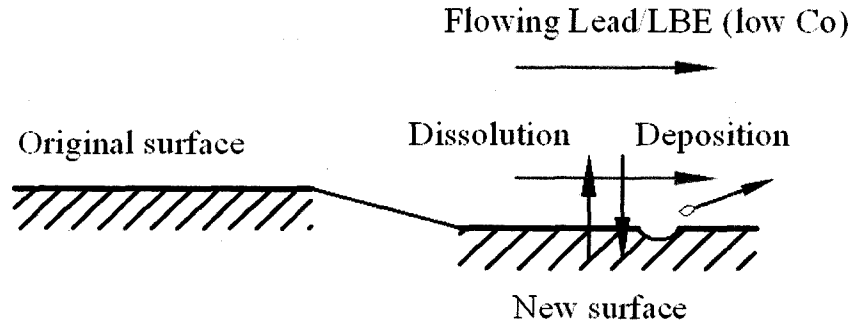


Figure 30. Dissolution is in balance with deposition (with scale removal).

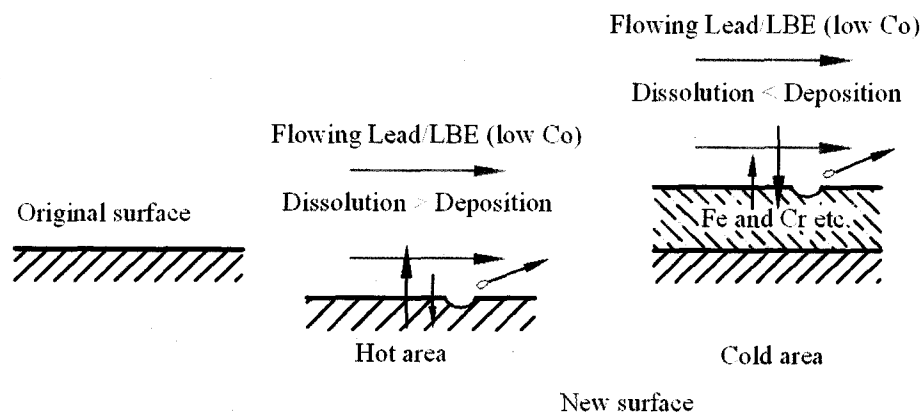


Figure 31. Corrosion and oxidation in a non-isothermal lead/LBE system with balance of dissolution and deposition in total quantity.

In a non-isothermal lead/LBE system, the corrosion and oxidation behaviors are different. Even the total deposition and dissolution are equal, and the net dissolution in the high temperature region and net deposition at the lower temperature region will occur, instead of the simple balanced reaction in the non-isothermal system, as shown in Figure 30. The corrosion/oxidation in an isothermal lead/LBE system with balance of dissolution and deposition in total quantity is shown in Figure 31. If the scale removal rate is larger than the maximum deposition rate (at the cold region), then the deposition may not be observed. Since the concentration of the dissolved components is beyond the saturated

concentration, solid phase particle or scale scrap will be found in the flowing lead and lead alloys. As mentioned earlier, the solid particle and solid scale scrap will enhance the erosion corrosion in turn.

With the increasing oxygen level in the flowing lead or lead alloys, the dissolved oxygen begins to react with the dissolved steel components and the insoluble oxide will precipitate on the surface of the steel. Except for the difference of scale removal effect and non-isothermal condition, the corrosion/oxidation results are similar to the cases in Figures 24-28. Simply, the effect of scale removal is that a small scale removal rate may only reduce the oxide growth rate at the outermost layer in a single layer or duplex layer structure of oxide. A higher scale removal rate may remove the outermost layer and reduce a duplex layer structure to a single layer structure, or remove the total single layer and induce erosion corrosion. A very high scale removal rate may remove the total duplex layer and induce erosion corrosion on the structural material. Similarly, the effect of the non-isothermal condition is that high corrosion occurs in a high temperature region and precipitation may occur in a cold temperature. Consequently, a duplex layer structure of magnetite and spinel ( $(\text{Fe,Cr})_3\text{O}_4$ ), a single layer of magnetite, a single layer of spinel ( $(\text{Fe,Cr})_3\text{O}_4$ ), or no oxide layer and erosion corrosion may be observed for stainless steel in flowing lead/LBE.

Since the corrosion/oxidation process is very complex, it depends on many parameters and conditions. For example, the stress effect is also an important factor in corrosion/oxidation, especially in a non-isothermal case. The stress can cause a crack in the protective oxide film, make a local penetration of corrosive lead/LBE, and even lead to breakage and scale off of the oxide layer. [27] As discussed above, that oxide layer

structure strongly depends on the steel composition, such as contents of Cr and Si. Discussions on the effects of Cr contents can be found in ref. [47] for aqueous environments, and of Si contents in ref. [48] for gaseous environments.

#### 1.3.4 Oxygen Control Technique

The main purpose for oxygen control in a liquid lead-alloy system is to create and maintain a protective film on the surface of the structural materials. The lower limit of the partial pressure of oxygen is the dissociation pressure of the oxide  $Fe_3O_4$  in equilibrium with the metal iron. However, when the oxygen partial pressure is too high and exceeds the saturation oxygen partial pressure,  $PbO$  begins to form and precipitate. The formation of  $PbO$  will contaminate the alloy coolant, change the composition, and thus change the properties of the coolant. Therefore, another goal of oxygen control is to prevent lead oxide precipitation. [36]

The saturation oxygen partial pressure can be determined according to the following reaction:



Therefore, the partial pressure of oxygen needs to be controlled in the range,

$$\frac{\Delta_f G_{Fe_3O_4}^0}{2RT} \leq \ln P_{O_2} \leq \frac{2\Delta_f G_{PbO}^0}{RT} \quad (1-11)$$

The oxygen concentration should be controlled in a proper range  $[C_{O,min}, C_{O,s}]$  [36, 42].

The oxygen solubility in liquid lead and LBE [36, 49] can be expressed in wt% as:



$$C_{O,s[Pb]}[wt\%] = 10^{3.2-5000/T} \quad (1-12)$$

$$C_{O,s[LBE]}[wt\%] = 10^{1.2-3400/T} \quad (1-13)$$

where  $T$  is the absolute temperature in K.

Assuming the bottom line for the concentration is to form  $Fe_3O_4$ ,  $C_{O,min}$  can be expressed as:

$$C_{O,min} = C_{O,s} a_{Pb} \exp\left(\frac{\Delta G_{Fe_3O_4} - 4\Delta G_{PbO}}{4RT}\right) \quad (1-14)$$

where  $\Delta G_{PbO}$  is the standard free energy of formation of PbO and in the temperature range from 400 to 1000 K,  $\Delta G_{PbO}(J/mol) = -218720 + 99.35T$  [50].  $a_{Pb}$  is the activity of Pb, and for liquid lead  $a_{Pb} = 1$  and for LBE  $a_{Pb} = 0.4232 \exp(-135.2/T)$  [36, 45].

For liquid lead:

$$C_{O,min[Pb]}[wt\%] = 10^{2.1012-8048/T} \quad (1-14)$$

and for LBE:

$$C_{O,min[LBE]}[wt\%] = 10^{-0.2722-6508/T} \quad (1-14)$$

In a typical flowing liquid lead/LBE coolant system, the temperature is not uniform and the flow is fully turbulent. The fully turbulent flow can mix the oxygen, leading to a nearly uniform oxygen concentration in the entire system. Because both  $C_{O,s}$  and  $C_{O,min}$  are functions of temperature, this uniform concentration should be less than  $C_{O,s}$  at the lowest temperature ( $T_{min}$ ) and greater than  $C_{O,min}$  at the highest temperature ( $T_{max}$ ). Then, in a non-isothermal system:

$$C_{O,\min}(T_{\max}) \leq C_O \leq C_{O,s}(T_{\min}) \quad (1-14)$$

A typical LBE coolant system has a temperature range from 350 °C to 550 °C, corresponding to a target oxygen range of  $6.63 \times 10^{-9} \text{ wt\%} \leq C_O[\text{LBE}] < 5.5 \times 10^{-5} \text{ wt\%}$ . The liquid lead system has a higher operating temperature range and is typically between 450 to 650°C, corresponding to a target oxygen concentration range of  $2.4 \times 10^{-7} \text{ wt\%} \leq C_O[\text{Pb}] < 1.9 \times 10^{-4} \text{ wt\%}$ . These typical oxygen ranges are shown in Figure 32. [36]

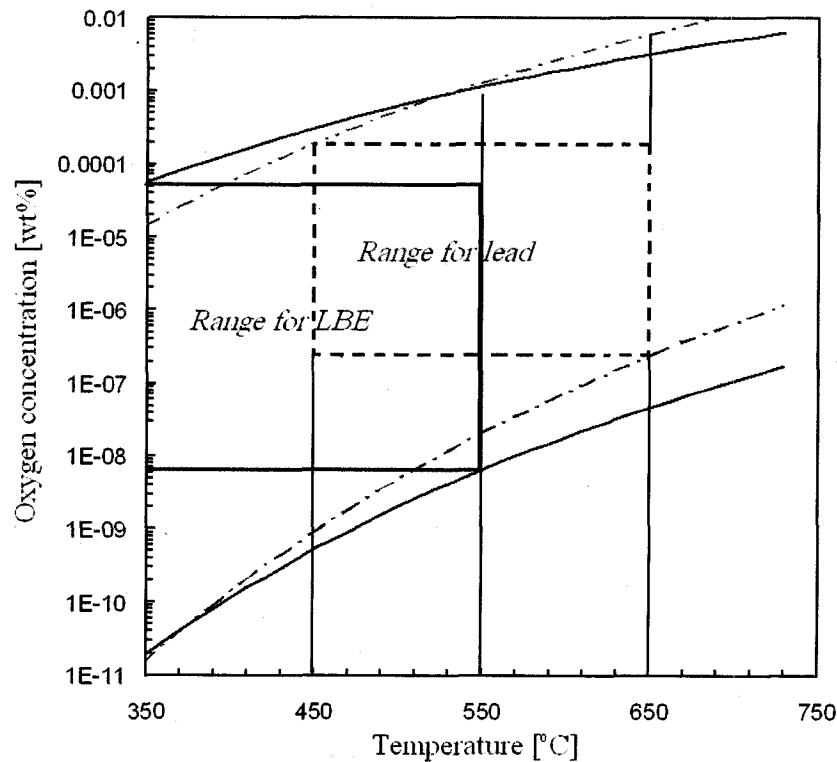


Figure 32. Typical oxygen control range in non-isothermal liquid lead and LBE flow systems. [36]

The methods for oxygen control include direct injection of oxygen and hydrogen gases, injection of hydrogen and steam mixture, and solid phase oxygen control. [36]

Since this topic is extensive, and not a goal of this research, the details will not be discussed in this dissertation.

#### 1.4 DELTA Loop

A test facility called DELTA (DEvelopment of Lead-Bismuth Target Applications) Loop was constructed at Los Alamos National Laboratory, U. S. The DELTA loop was designed in cooperation with the Institute of Physics and Power Engineering (IPPE) of Obninsk, Russia. The first run of DELTA loop took place on December 5th, 2001. The DELTA Loop was designed to study the long-term corrosive effects of LBE on structural materials at a high temperature. Moreover, the DELTA loop can also be used to study thermal and hydraulic properties of LBE flow in future spallation target designs. [51]

The main goals for the DELTA loop are [51]:

- Implementation of an oxygen measurement and control system in the LBE flow;
- Investigation of the long-term corrosive effects of LBE on a variety of materials;
- Implementation and investigation of natural convection flow in an LBE system; and
- Investigation of the thermal-hydraulic properties of LBE in prototype target designs.

The maximum designed temperature of the DELTA loop can reach up to 500°C, which is much higher than the melting points of both lead and LBE and lower than their boiling points. (see the values in Table 1)

Since the local temperature is important for the corrosion and deposition behaviors, a recuperator, a heater, and a heat exchanger are used to control the temperature distribution in DELTA loop.

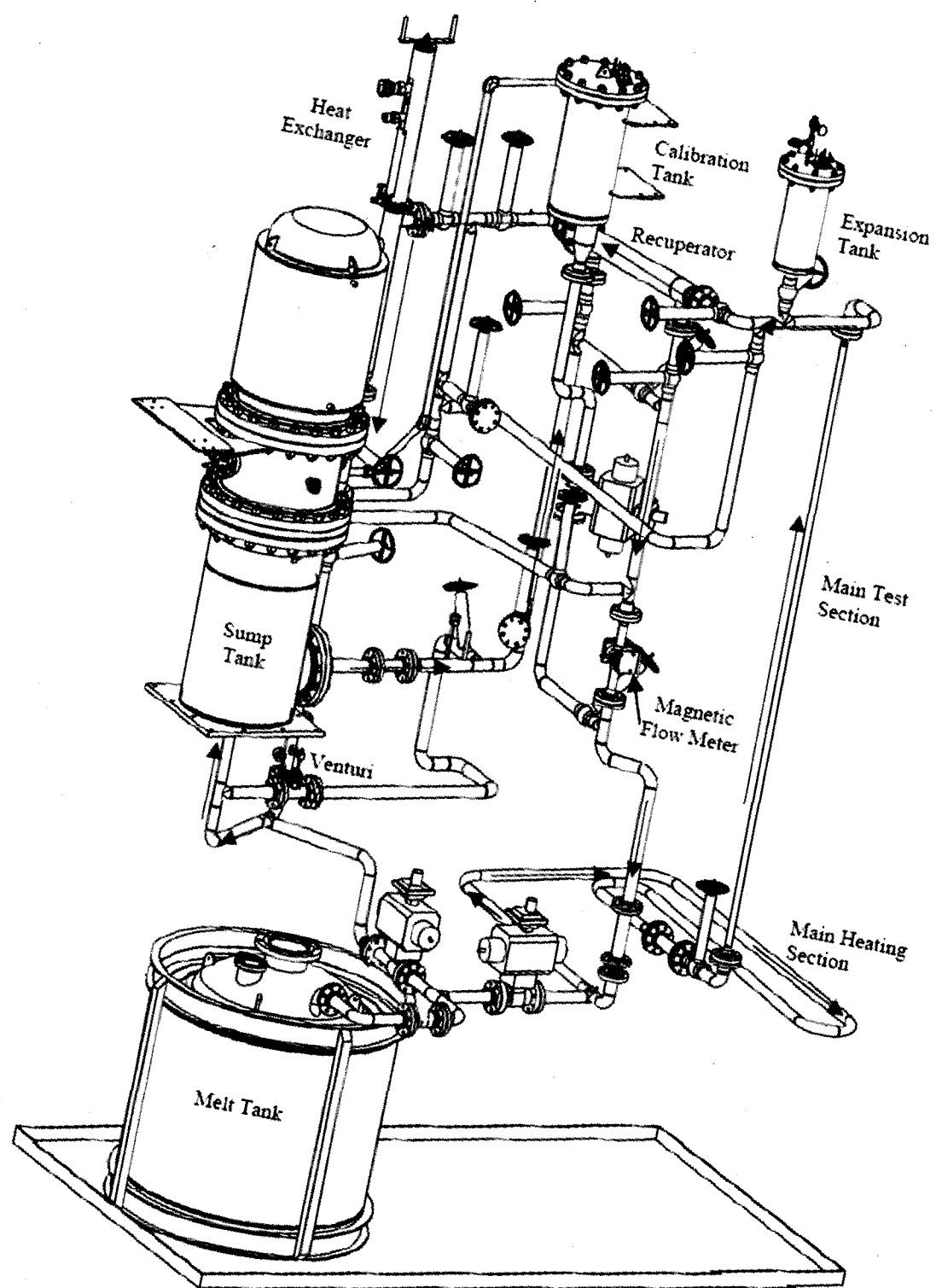


Figure 33. The schematic sketch of DELTA Loop. [51]

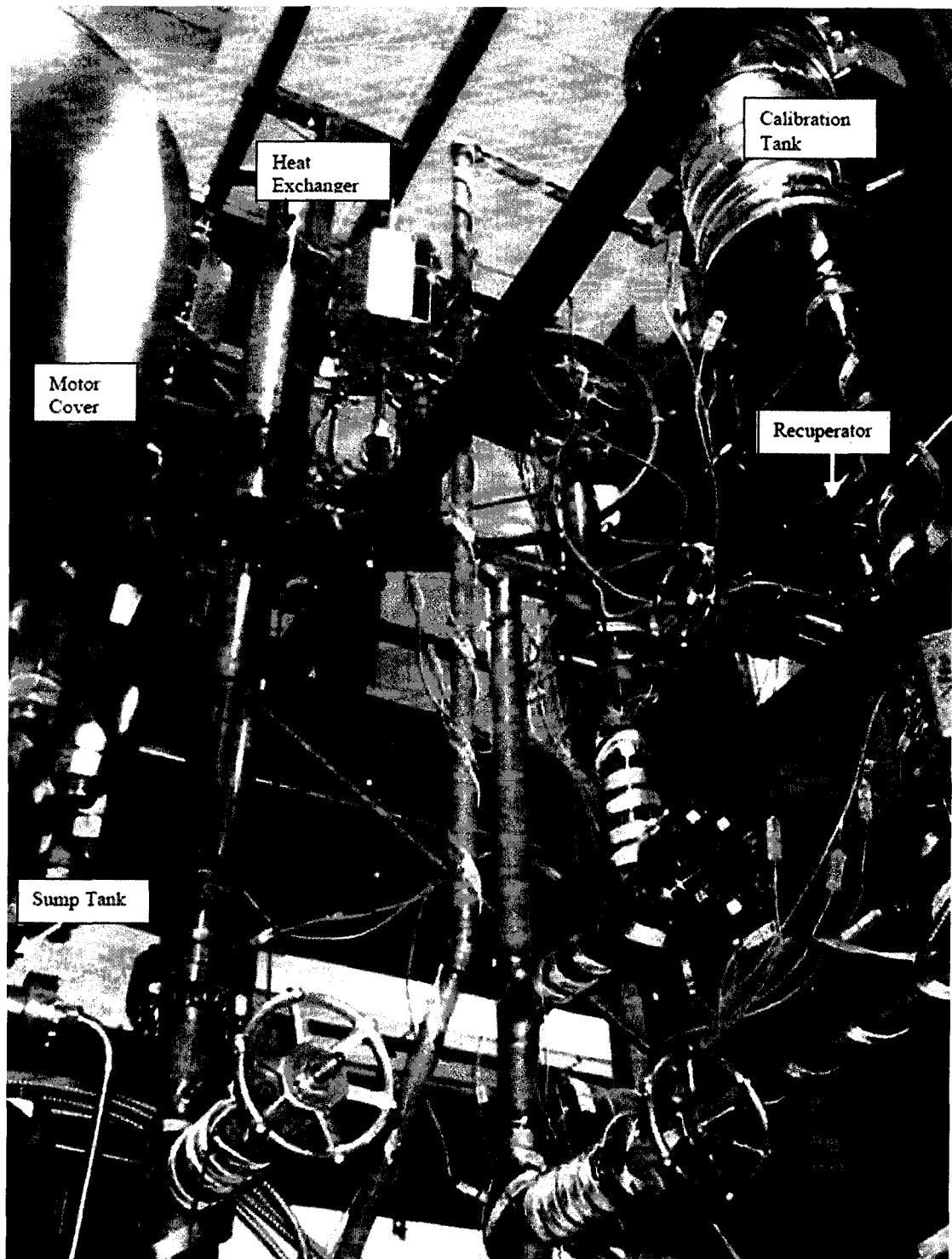


Figure 34. The DELTA Loop. Sump tank is visible on the left, heat exchanger next to sump tank, calibration tank is at the right top corner, and recuperator is underneath calibration tank, in the shadow. [51]

Briefly, LBE flow comes out of the pump at the lowest temperature section, passes through the recuperator shell side and the heater, and reaches the highest temperature at the test section. On the return path, the temperature decreases through the recuperator tube side and the heat exchanger, and drops to the lowest temperature.

The schematic sketch of the DELTA loop is shown in Figure 33. A photograph of the DELTA loop is shown in Figure 34. [51]

The DELTA loop is a closed system that is 6 meters high and is constructed primarily with 5.25 cm diameter pipe. The loop components include an 18.6 kW, variable-speed, sump-type, centrifugal pump capable of delivering LBE at a rate of 13 m<sup>3</sup>/hr; a magnetic flow meter with an attached calibration tank; a 60 kW heat input section for raising the fluid temperature during material testing; a 3.3 m long test section where various material sample coupons will be placed for corrosion testing in the LBE flow; an expansion tank that provides a free surface during natural convection operation; a shell-and-tube recuperator capable of providing a 50 °C fluid temperature change; a variable capacity, LBE-to-water heat exchanger; and a melt/drain tank that holds 3500 kg of LBE and is equipped with a 45 kW, radiant heater. Approximately 80 kW of tape heaters are mounted on the external surfaces of the loop piping and vessels to provide trace heating. All vessels and piping are designed according to the ASME Boiler and Pressure Vessel Code [52] and ASME Piping Code [53], and are built from 316L stainless steel. The DELTA loop was designed to minimize the stresses due to gravity, internal pressure, thermal expansion and seismic loads. Some of the supports are flexible, to allow for thermal expansion. The recuperator is an IPPE designed shell and tube heat exchanger with 19 1.43 cm diameter tubes enclosed in a 10.2 cm diameter shell. The heat

exchanger, designed by IPPE, is an annular, counter-flow design using water at room temperature and atmospheric pressure as the cooling fluid. The water is separated from the LBE by a closed, intermediate annulus containing lead-bismuth. This intermediate fluid can be moved up and down inside the annulus by sliding the inside cylinder like a piston. When the piston is brought all the way up, it leaves the intermediate lead-bismuth at the bottom of the annulus, thus reducing the heat exchanging capacity to a minimum. When the piston is lowered to the very bottom, the intermediate fluid is pushed up into the annulus, thus increasing the heat exchanging area and increasing the heat exchanger capacity. Turning a screw handle at the top of the heat exchanger moves the piston. [51]

Prior to operation, LBE is heated to 300 °C in the melt tank, the piping and vessels are heated to 250 °C using the trace heaters, and the loop is evacuated to a rough vacuum. The melt tank is then pressurized with helium to force the LBE up into the sump tank. The sump tank is then pressurized to force the LBE up into the rest of the piping. When the fill is complete, the pump can be started.

During operation, LBE leaves the sump tank and travels up to the recuperator's shell side where the fluid temperature is increased by 50 °C. LBE then flows to the magnetic flow meter through a long vertical pipe leading from the recuperator's shell side to the heated section at the bottom of the loop. The tubing in the heated section is covered with band heaters that are used to raise the fluid temperature another 50 °C. The heated fluid then enters the 2.65 cm diameter, vertical test section where material samples will be placed. Upon exiting the test section, the fluid then enters the tube side of the recuperator where the temperature is reduced by 50 °C. After leaving the recuperator, the fluid flows to the heat exchanger where its temperature is again reduced by 50 °C. The fluid leaves

the heat exchanger and returns to the sump tank through the bottom inlet. Several pipes are built into the loop to allow bypasses of the recuperator, the heat exchanger or the sump tank. In addition, a bypass of the primary piping exists to enable flow rate and pressure adjustment of the main flow. A venturi is located in this primary bypass where oxygen and hydrogen clean-up gases are injected. The temperature changes shown in this paragraph are nominal for the design flow speed of 1 m/s in the test section or about 6 kg/s mass flow rate. [51]

### 1.5 Transmutation Research Program

The University of Nevada, Las Vegas (UNLV) has entered into a partnership with the national laboratories through the Transmutation Research Program (TRP). The TRP projects are trying to establish a world-class program for transmutation technologies while building core competencies and facilities to promote UNLV's strategic growth goals. The central theme and purpose of this program is to involve UNLV students in research on the economically and environmentally sound refinement of spent nuclear fuel. The long-term goals of this program are to increase the University's research capabilities, attracting students and faculty of the highest caliber, while furthering the national program to address one of the nation's most pressing technological and environmental problems. [54]

Under the leadership of the program director, Dr. Anthony E. Hechanova, thirty projects are under scientific study, being researched in different departments at UNLV, together with the collaboration with other research groups and help from national laboratories. This research is the task #21 of the UNLV TRP program.



## 1.6 Purpose of Study

Liquid lead alloys have been considered as a prototype target and coolant candidate for the ADS systems because of their ideal thermal-physical and chemical properties. One of the main problems, as widely recognized, in using LBE is its adverse effect on structural materials, mostly stainless steels. This molten metal dissolves stainless steel components and causes severe corrosion during the application in the nuclear coolant systems

Initiated in Russia, one effective method to prevent corrosion in LBE systems is to create and maintain a protective oxide film on the surface of the metal/alloy structure. The so called “active oxygen control technique” can promote the formation of the “self-healing” oxide films on the structural material surface, drastically reducing steel corrosion and coolant contamination. The formation and longevity of the protective oxide layer depends on the oxygen concentration in the liquid metal. [3]

Many experiments on steels exposed to flowing lead-alloys have been carried out to study the corrosion rates and the protective oxide layer behaviors. [10, 17, 43] However, the experimental data are still very incomplete at present and cannot provide the dependence of the oxide behaviors on the system operating temperature, temperature profiles along the lead-alloys loop, oxygen concentration, flow velocity, etc. [10, 21] In addition, the mechanism of oxygen transport in the oxide layer and structural materials in a non-isothermal lead-alloys coolant system is not well understood. [27]

Precise studies and simulations of all hydrodynamics with thermal conditions encountered in practical coolant loop systems, by use of different flowing conditions in the laboratory, are difficult and expensive, if not impossible. Therefore, it is important

and necessary to develop theoretical models to predict the protective oxide layer behaviors at the design stage of a practical lead-alloys coolant system, to properly interpret and apply experimental results from test loops, and to provide guidance for optimization in lead-alloys nuclear coolant systems. The research project, therefore, is aimed at filling the gaps of protective oxide layer growth and the oxygen concentration level before lead-alloys nuclear coolant is ready for programmatic implementations and industrial applications.

As one task in TRP projects, the goal of the research is to provide basic understanding of the protective oxide layer behaviors, and to develop oxide layer growth models of steels in non-isothermal lead-alloys coolant systems. From the developed model, useful information and quantitative manipulating parameters are anticipated for an active oxygen control technique. [55]

This dissertation gives an introduction on the background and targets for this research project. The favorable properties of lead and LBE are reviewed as an ideal candidate of the nuclear coolant in ADS. Then, the mechanism of liquid metal/alloy corrosion and the factors, which influence the corrosion process, are studied. Based on the understanding of the lead and LBE corrosion and the identification of oxide structure from experiments, oxidation mechanism of stainless steel in both the static and flowing lead/LBE are studied. Then the active control technique is introduced. Later on, a brief introduction on the material test loop, DELTA loop, and UNLV TRP program are presented.

In Chapter 2, a theoretical kinetic model based on the boundary layer theory is presented. This model was developed to investigate the corrosion/precipitation in non-isothermal lead alloy coolant systems. The analytical expressions of the local

corrosion/precipitation rate and the bulk concentration of the corrosion products were obtained by considering a turbulent core region and a laminar sub-layer. Numerical solutions were also accomplished together with considering the effect of eddy mass diffusivity in lead alloy systems.

Chapter 3 proposes a diffusion controlling oxide layer growth model with scale removal in oxygen containing lead alloys. Scale removal effect was considered and the formation mechanism of duplex oxide layer structure was investigated in the model.

An improved stochastic mesoscopic cellular automaton (CA) model is developed in Chapter 4. In the CA model, the oxide layer growth process, together with the diffusion of oxygen and ionic metal, was studied at a mesoscopic level.

In Chapter 5, some useful conclusions are summarized based on the research results. Some results from the developed models were compared with the available experimental data and good agreement was attained. Moreover, the extended applications of the developed models were analyzed.

## CHAPTER 2

### CORROSION AND PRECIPITATION IN NON-ISOTHERMAL LIQUID LEAD OR LBE SYSTEMS

#### 2.1 Introduction

As discussed in the first chapter, the corrosion of steels by corrosive molten lead or LBE is a complex and important problem. The corrosion of stainless steel by molten lead or LBE presents the main challenge and leading obstacle to its nuclear application. Moreover, the precipitation in the cold region will block the flow of lead or LBE and cause severe safety problems as well. The experimental investigations on corrosion in LBE indicated that the flow-affecting corrosion depends strongly on exposure time, temperature distribution, flow velocity conditions, structural material, heat and surface treatment of material and many other factors. [2, 4, 10, 20, 21] In real operations, various values may be applied for each thermal and hydraulic parameter. It is impossible, expensive, time-consuming and not necessary to do experiments on each value for every variable parameter. Furthermore, experimental data on lead alloy corrosion are still very poor and scattered currently. [10, 15, 29, 56] Therefore, theoretical modeling is important and necessary to estimate corrosion and deposition behaviors in the LBE coolant systems.

A theoretical kinetic model based on the boundary layer theory was developed to investigate the corrosion/precipitation in non-isothermal lead alloy pipe/loop systems.

The analytical expressions of the local corrosion/precipitation rate and the bulk concentration of the corrosion products were obtained by considering a turbulent core region and a laminar sub-layer. Numerical solutions were also obtained, together with considering the effect of eddy mass diffusivity in lead alloy systems. [21] A parametric study will be conducted in order to illustrate the dependence on different thermal and hydraulic parameters, such as temperature distribution and inlet velocity, of the corrosion/precipitation rate and bulk concentration of the corrosion product. The present analytical model and numerical model will be benchmarked with some previous experimental data.

## 2.2 Literature Survey

Many scientists and researchers are devoted to building theoretic models for analytic calculations and numerical simulations for the corrosion problem of metallic material in molten lead or LBE environment. With the help of the built models, useful data are anticipated for predicting the corrosion and precipitation behaviors in a lead/LBE system.

As an example, Balbaud-Celerier and Barbier [15] applied the local corrosion models to calculate corrosion rates in liquid metal loops by assuming that the corrosion product bulk concentration was zero. However, the authors considered the local conditions only, such as the velocity and local temperature. Actually, the LBE pipe/loop systems are non-isothermal in most LBE coolant systems. Taking into account the effects of the axial temperature gradients, several kinetic corrosion models were developed. Assuming that the corrosion product concentration is equal to that in the cold zone, Epstein [29] developed a model that could predict the mean corrosion rate at the hottest zone in heat transfer loops. Applying this model, the corrosion and deposition zones could be

predicted, and good results were obtained that were consistent with the experimental results. However, their basic assumption that the mass transfer boundary layer is only a function of the liquid metal velocity, and remains constant in thickness along the loop is unreasonable for a loop system with large surface concentration or temperature gradient. In most of the existing corrosion models, only mean values were considered based on local conditions, in particular the velocity of the liquid and the local temperature. Another kinetic model incorporating the effects of the axial temperature profile was developed by He et al. [32]. The model demonstrated that the axial temperature profiles have significant effects on corrosion and precipitation phenomena in LBE loops. However, this model was limited to simple loop flows, and there was a missing term in the solution of the boundary layer concentration. In recent studies, Zhang and Li [2, 34] developed a kinetic model to investigate the dependence of corrosion/precipitation on the axial temperature profile for both closed pipe flow and open pipe flow. Basic concepts of chemical kinetics and thermal hydraulics of lead bismuth flow loops were studied and simulations were conducted by K. Dasika and S. Moujaes [57, 58] based on Zhang's model using a commercial Computational Fluid Dynamics code. Their studies showed that the corrosion/precipitation rates and their distributions in a LBE pipe/loop system depend on both the local temperature and the axial temperature profiles. However, the authors only considered the mass transfer in the boundary layer and did not consider that the boundary layer thickness effects play important roles on the corrosion product bulk concentration. Moreover, the eddy mass diffusivity was neglected because it was assumed that the turbulent boundary layer is so small that all the effects happen in the laminar sub-layer of the turbulent fluid flow.

The molecular diffusivity and the kinematic viscosity are both a function of local temperature. [10, 16, 30] Based on the analysis in Ref [36], the Schmidt number for the iron transport in liquid LBE is around 150. For the mass transport cases with high Schmidt numbers, the turbulent and molecular diffusions are of the same order of magnitude, so that it is very important to describe both of them with high accuracy. Rosen showed that even at the interface of the laminar sub-layer and buffer zones, the eddy mass diffusivity could be much larger than the molecular diffusivity in a solute with a Schmidt number of 5000 [59, 60]. Aravinth confirmed that the eddy mass viscosity plays an important role in the buffer regime and turbulent core region, especially in fluids with a high Schmidt number, e.g. liquid metals [61]. From Nelissen's calculations, the turbulent mass transfer model has a strong influence on the local concentration distribution, and all the models showed that the eddy mass diffusivity is important for a precise estimation [62]. To the best of knowledge, there was no work being done with consideration of eddy mass diffusivity in LBE corrosion models. One of the important reasons for this is the complexity in solving the convection-diffusion equation because of the non-linearity caused by the eddy mass diffusivity. Therefore, it is necessary to evaluate the influence of the eddy mass diffusivity in the LBE corrosion systems as well.

In the present study, the previous kinetic model [2, 34] was improved by considering the mass transfer effects in both turbulent core region and laminar boundary layer regions. The buffer zone was neglected in order to obtain analytical solutions. Systemic theories for predicting the corrosion/ precipitation rates in non-isothermal LBE pipe/loop systems were developed. The total mass transfer of corrosion products by the fluid towards the wall, as well as away from the wall, was studied in two regions respectively.

The developed model was applied to a materials test loop, the DELTA loop, at the Los Alamos National Laboratory, with specific axial temperature profiles. Following the model development, the corrosion/precipitation rate, together with bulk corrosion product concentration were calculated and discussed to illustrate the effects of the axial temperature profile. In the proposed numerical models, the eddy mass diffusivity effect was considered, coupling with the continuity equation and momentum equation in analyzing the corrosion/precipitation behaviors in non-isothermal lead alloy pipe/loop systems. Cases with different inlet velocity were studied in order to find the corrosion/precipitation dependence on flow conditions. The average Sherwood number at the highest temperature isothermal leg was also obtained and analyzed through numerical simulation of the corrosion and deposition rates in the DELTA loop. Both the analytical model and numerical model were benchmarked with a pure lead loop and attained good agreement with the available data.

## 2.3 Theory

The study on the dissolution corrosion and precipitation will be initiated from the investigating of the physical and mathematical model. By considering the boundary conditions, analytical and numerical algorithms will be applied to obtain solutions for the corrosion and precipitation rates, concentration of corrosion products, etc.

### 2.3.1 Assumptions and Governing Equations

The liquid lead alloy is considered to be incompressible, have constant thermal properties, and is a Newtonian fluid. These assumptions lead to the governing equations for the fluid flow of the continuity equation, the Navier-Stokes (momentum) equations,



and the mass transport equation. These equations in a steady state are shown as Equations (2-1 to 2-3).

$$\nabla \cdot \vec{u} = 0 \quad (2-1)$$

$$\rho(\vec{u} \cdot \nabla)\vec{u} = -\nabla \cdot \hat{p} + \mu \nabla^2 \vec{u} \quad (2-2)$$

$$(\vec{u} \cdot \nabla)c = -\nabla \cdot \vec{J} + R' \quad (2-3)$$

where  $\hat{p}$  is the effective pressure and  $\hat{p} = p + \rho gh$ ,  $\vec{J}$  is the diffusion flux of the corrosion product and  $R'$  is the net rate of production/consumption of the corrosion product.

Since the flow-induced corrosion/precipitation phenomena in the LBE system are very complex, more assumptions are needed to simplify this problem [10, 34]. The reaction near the wall is assumed to be in equilibrium. The wall surface is smooth, and corrosion and precipitation do not change the wall surface. The reaction term in the flow contributes little to mass transfer in the bulk flow. The flow is a fully developed turbulent flow. The physical properties of the liquid and the bulk flow velocity keep constant in axial direction. In the analytical solutions, the eddy mass diffusivity  $D_t$  can be neglected compared to the molecular mass diffusivity  $D_m$ , since the turbulent boundary layer is smaller and the mass transfer is governed mainly by the molecular diffusion in the laminar sub-layer. In order to obtain the analytical solutions, the hydraulic buffer zone is neglected.

Noticing that the molecular mass diffusivity of the corrosion product is much less than the kinematic viscosity of the liquid metal, and the Schmidt number is much greater

than 1, the mass diffusion boundary layer is submerged under the hydraulic boundary layer. Hence, it is reasonable to consider a turbulent core region and a laminar sub-layer region separately, as shown in Figure 35, where  $\delta$  is the thickness of hydraulic laminar sub-layer and it can be calculated by

$$\delta = y^+ \left( \frac{\nu}{u^*} \right) = y^+ \left( \frac{\nu}{\sqrt{\tau_w / \rho}} \right) = \frac{y^+ d}{Re} \sqrt{\frac{2}{f}} \quad (2-4)$$

where  $u^*$  is the friction velocity,  $y^+$  is the limit of laminar sub-layer,  $Re$  is the Reynolds number based on the average velocity, and  $\tau_w$  is the shear stress at the wall. The experimental results show that there is a layer of very small thickness  $y^+ = 1.6 \pm 0.4$ , in which a linear velocity gradient occurs virtually at all times [63]. In this research, the value of  $y^+$  is taken as 1.6 in all of the cases. The fanning-friction factor  $f$  is calculated by the simpler expression from the von Karman and Nikuradse theoretical equation [64, 65]

$$f = 0.046 Re^{-0.20} \quad (2-5)$$

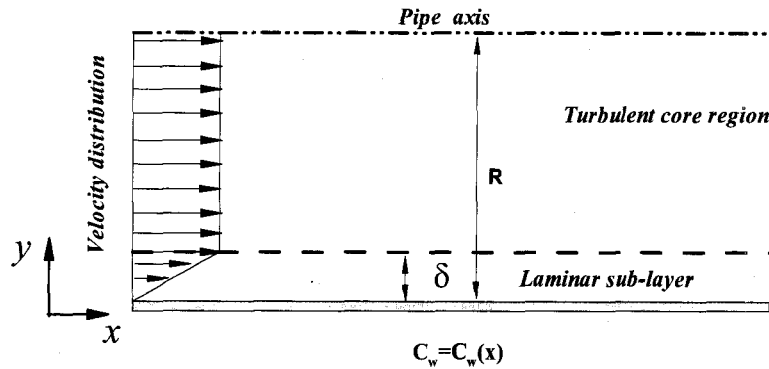


Figure 35. Scheme of the turbulent core region and laminar sub-layer near the wall.

In the laminar sub-layer region, according to the boundary layer theory, convection is dominant in the x-direction and diffusion is dominant in the y-direction. Thus, at a steady state, the convection-diffusion equation in Eq. (2-3) for corrosion product transport can be simplified as [66]:

$$\frac{\partial c_l}{\partial x} - \frac{D_m}{V_l} \frac{\partial^2 c_l}{\partial y^2} = 0 \quad (2-6)$$

where  $c_l$  is the concentration of corrosion product in the hydraulic laminar sub-layer.

In the analytical analysis, the flow velocity is set equal to a constant bulk flow velocity  $V_b$ . While in the hydraulic laminar sub layer, a linear velocity profile is assumed:

$$V_l = \frac{V_b y}{\delta} \quad (2-7)$$

Therefore, only the convection-diffusion equation needs to be considered in the analytical calculations. And Eq. (2-6) can be simplified to:

$$\frac{\partial c_l}{\partial \xi} - \frac{1}{\eta} \frac{\partial^2 c_l}{\partial \eta^2} = 0 \quad (2-8)$$

where the coordinate transforming variable is introduced,

$$\xi = \frac{x}{L}, \quad \eta = \left( \frac{V_b}{\delta D_m L} \right)^{1/3} y \quad (2-9)$$

and where  $L$  is the length of the loop/pipe. The concentration of corrosion product in the core region,  $c_b$ , is assumed to be independent of  $y$ , but a function of  $x$ . Therefore, the longitudinal diffusion terms are negligible, and it can be noticed that the mass flux of

turbulent core is equal to that of the laminar sub-layer at the interface. The following mass balance equation in the turbulent core region can be obtained by considering a control volume with an infinitesimal length in x direction, i.e.  $\Delta x \rightarrow 0$  [66]:

$$V_b \frac{dc_b}{dx} + \frac{2D_m}{R-\delta} \frac{\partial c_l}{\partial y} \bigg|_{y=\delta} = 0 \quad (2-10)$$

### 2.3.2 Boundary Conditions and Oxygen Control Technology

Thus, the governing equations (2-8) (2-10) are subject to the following boundary conditions:

$$c_l = c_w(\xi) \text{ at } \eta = 0 \quad (2-11)$$

$$c_l = c_b(\xi) \text{ at } \eta = \left( \frac{\delta^2 V_b}{D_m L} \right)^{1/3} \quad (2-12)$$

where  $c_w$  is the concentration of the corrosion product at the wall.

For a pipe,

$$c_l = c_b = 0 \text{ at } \xi = 0 \quad (2-13)$$

For a closed loop, periodic inlet conditions are employed,

$$c_l|_{\xi=0} = c_l|_{\xi=L} \text{ and } c_b|_{\xi=0} = c_b|_{\xi=L} \quad (2-14)$$

In a closed loop case, the liquid metal flow keeps cycling without renewal. At the steady state, as a consequence, the total amount of corrosion is equal to the total amount of precipitation in the entire loop [2],

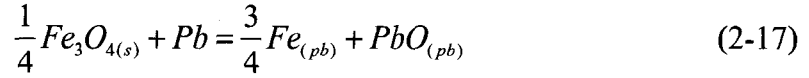
$$\int_0^L q dx = 0 \quad (2-15)$$

The concentration of the corrosion product at the wall  $c_w$  is a function of the local temperature. According to the oxygen control technique [32, 35, 36], the determination and the formation mechanisms for the concentration of corrosion product on the solid-liquid interface are very complex. The corrosion of structural materials such as steel in molten LBE occurs via dissolution at very low oxygen concentrations, and through surface oxidation and reduction of surface oxides at higher oxygen concentrations. No matter which way the corrosion proceeds, it is usually sufficiently fast and the corrosion is limited by the mass transfer process. Therefore, the corrosion products' concentrations are always at their saturated or equilibrium levels at the solid-liquid interface. When the oxygen concentration in LBE flow is low, the surface concentrations of the corrosion products in LBE equal their saturated concentrations, namely, the solubility in LBE

$$\log c_w = \log c_s \quad (2-16)$$

where  $c_w$  is the wall concentration, and  $c_s$  is the solubility which can be calculated from Eq. (1-4) with the coefficients from Table 3.

With the increase of oxygen concentration level in LBE alloy, an oxide layer of magnetite begins to form, since the free energy of formation for ferrous ferric oxide is lower than bismuth oxide and lead oxide. Among ferrous ferric oxide ( $\text{Fe}_3\text{O}_4$ ) □ bismuth oxide ( $\text{Bi}_2\text{O}_3$ ) and lead oxide ( $\text{PbO}$ ), the free energy of formation for bismuth oxide is the highest. It is thus possible to “passivate” the surface of the structural steels in contact with LBE with a protective magnetite film ( $\text{Fe}_3\text{O}_4$ ). The reactions for forming the oxide layer follow the Eq. (1-8) and (1-6). And the reaction on the protective magnetite film on structural surfaces submersed in LBE flow is (assuming magnetite  $\text{Fe}_3\text{O}_4$  is insoluble)



If the concentration of Fe in LBE is low and less than the equilibrium level, the reaction of Eq. (2-17) proceeds towards the right hand side and Pb begins to destroy the formed  $Fe_3O_4$  film. The reaction ceases at a dynamic balance until the Fe concentration near the interface reaches the equilibrium level. Therefore, only when the oxygen concentration is very high will the precipitants of bismuth oxide ( $Bi_2O_3$ ) contaminate the coolant. The equilibrium constant is for reaction in Eq. (2-17) as

$$K = \frac{a_{PbO(Pb)} a_{Fe(Pb)}^{3/4}}{a_{Pb} a_{Fe_3O_4(s)}^{1/4}} = \left( \frac{C_{Oxy}}{C_{s,Oxy}} \right) \left( \frac{C_{Fe}}{C_{s,Fe}} \right)^{3/4} = \exp \left( - \frac{\Delta F_{PbO}^0 - \frac{1}{4} \Delta F_{Fe_3O_4}^0}{RT} \right) \quad (2-18)$$

Where  $a$  is the activity, with  $a_{PbO(Pb)}$ ,  $a_{Fe(Pb)}$ ,  $a_{Pb}$ ,  $a_{Fe_3O_4(s)}$  for activity of lead oxide in LBE, atomic iron in LBE, atomic lead in LBE and solid magnetite respectively. The activity  $a_{Fe_3O_4(s)}$  is unity since  $Fe_3O_4$  is assumed to be non-soluble in LBE. According to Zhang [10] and Li [35], the difference between the oxygen partial pressure for LBE and that for lead is small, so that the activity of lead in LBE as unity is also reasonable.  $C_{Oxy}$  is the oxygen concentration in LBE flow which can be in a unit of wt% or wppm, and  $T$  is the local absolute temperature in Kelvin.

Therefore,

$$\log C_{Oxy} - C_{s,Oxy} + \frac{3}{4} \log C_{Fe} - \frac{3}{4} \log C_{s,Fe} = \frac{\frac{1}{4} \Delta F_{Fe_3O_4}^0 - \Delta F_{PbO}^0}{2.303RT} \quad (2-19)$$

and the solubility in LBE can be expressed in Eq. (1-4) . After substituting solubility from Eq. (1-4) for iron and oxygen,

$$\log C_{Fe} = -\frac{4}{3} \log C_{Oxy} + (A_1 + \frac{B_1}{T})_{Fe} + \frac{4}{3} (A_1 + \frac{B_1}{T})_O + \frac{4}{3} \frac{\frac{1}{4} \Delta F_{Fe_3O_4}^0 - \Delta F_{PbO}^0}{2.303RT} \quad (2-20)$$

The temperature dependence of the free energy formation can be generally expressed as

$$\Delta F^0 = A_F + B_F T \quad (2-21)$$

Therefore, for concentration of corrosion product in the solid-liquid interface in wt%

$$\log C_{Fe} = -\frac{4}{3} \log C_{Oxy} + 2.023 - \frac{12844}{T} \quad (2-22)$$

and for concentration of corrosion product in the solid-liquid interface in wppm

$$\log C_{Fe} = -\frac{4}{3} \log C_{Oxy} + 11.356 - \frac{12844}{T} \quad (2-23)$$

According to thermodynamic analysis, the equilibrium concentration of corrosion product in the solid-liquid interface in wt% can be expressed as

$$C_{Fe} = C_{Oxy}^{-4/3} 10^{2.023 - (12844/T)} \quad (2-24)$$

or, for concentration in wppm,

$$C_{Fe} = C_{Oxy}^{-4/3} 10^{11.35 - (12844/T)} \quad (2-25)$$

Obviously, the axial concentration of iron (the main dissolution corrosion product) at the wall is a function of axial temperature profile in a non-isothermal loop or pipe. As discussed above, the concentration of corrosion product at the solid-liquid interface is at its saturated level via dissolution at a low oxygen concentration, while the corrosion species concentration reaches and stops (dynamic balance) at the equilibrium level

through reduction reaction at the interface with the existence of the oxide layer at a higher oxygen concentration.

For a particular temperature, therefore, the corrosion production concentration at interface is given by the minimum of the saturation concentration from Eq. (2-16) and the chemical equilibrium concentration from Eq. (2-24) or (2-25). In formula, it can be expressed as the Eq. (2-26) or Eq. (2-27).

$$c_w = \text{Min}(10^{4.01-4380/T}, c_{Oxy}^{-4/3} 10^{2.023-(12844/T)}) \quad (2-26)$$

for concentrations in wt%, while

$$c_w = \text{Min}(10^{6.01-4380/T}, c_{Oxy}^{-4/3} 10^{11.35-(12844/T)}) \quad (2-27)$$

for concentration in wppm.

## 2.4 Methodology

The governing equations were listed above based on the proposed physical model. Considering the boundary conditions in section 2.2, the governing equations (2-8) and (2-10) for mass transfer can be solved analytically with Fourier series expansion. First, a similarity solution of the concentration of the dissolution corrosion product, mainly Fe, in the laminar boundary layer is calculated. The corrosion or precipitation rate is easy to obtain for regions with different temperatures, from the concentration of the dissolution corrosion product in the laminar boundary layer. Then, the concentration of the corrosion product in the bulk flow can be calculated from Eq. (2-10).

The continuity equation and the time-averaged Navier-Stokes equation (i.e. the so-called Reynolds equation) for a steady flow and the time-averaged conservation equation



for a species concentration of turbulent flow were solved numerically using Finite Volume Method (FVM). A structured mesh is created for the steady state numerical solutions. The standard k- $\epsilon$  model was selected to model the turbulent flow in the pipe/loop systems. The eddy mass diffusivity in the cases will be calculated from some empirical formulas and linked to the numerical simulations instead of the default Reynold's analogy. The corrosion product transport equation, together with the continuity and momentum equations, were then solved implicitly with a segregated iterative algorithm.

## 2.5 Analytical Solutions

### 2.5.1 Analytical Solutions for Open Pipe Flow

Using Fourier series to expand the bulk concentration  $c_l(\xi, \eta)$ :

$$c_l(\xi, \eta) = \hat{c}_l(\xi, \eta) + \sum_{k \neq 0} Y_k(\eta) e^{2\pi k i \xi} \quad (2-28)$$

where  $\hat{c}_l(\xi, \eta)$  is assumed to satisfy a partial differential equation (PDE)

$$\frac{\partial \hat{c}_l}{\partial \xi} - \frac{1}{\eta} \frac{\partial^2 \hat{c}_l}{\partial \eta^2} = 0 \quad (2-29)$$

and  $Y_k(\eta)$  satisfies the following ordinary differential equation (ODE)

$$2\pi k i \eta Y_k - \frac{d^2 Y_k}{d\eta^2} = 0 \quad (2-30)$$

Considering the boundary condition of the wall

$$c_l(\xi, 0) = c_w(\xi) = a_0 + \sum_{k \neq 0} a_k e^{2\pi k i \xi} \quad (2-31)$$

where  $a_0$  and  $a_k$  are Fourier's series coefficients,

$$a_k = \int_0^1 c_w(\xi) e^{2\pi k i \xi} d\xi \quad (2-32)$$

and

$$a_0 = \int_0^1 c_w(\xi) d\xi \quad (2-33)$$

Obviously,  $a_0$  accounts for the mean wall concentration. The PDE (2-29) can be transformed to an ODE by introducing  $\zeta = \eta / \xi^{1/3}$  in order to obtain a similarity solution,

$$\zeta^2 \frac{d\hat{c}_l}{d\zeta} + 3 \frac{d^2 \hat{c}_l}{d\zeta^2} = 0 \quad (2-34)$$

Taking into account boundary conditions, the ODEs (2-30) and (2-34) can be solved

$$Y_k(\eta) = \frac{a_k}{Ai(0)} Ai((2\pi k i)^{1/3} \eta) \quad (2-35)$$

$$\hat{c}_l(\xi, \eta) = \frac{a_0}{\Gamma\left(\frac{1}{3}\right)} \Gamma\left(\frac{1}{3}, \frac{\eta^3}{9\xi}\right) \quad (2-36)$$

where  $\Gamma$  stands for the Gamma function, while  $Ai$  is the Airy function with the cubic feet of the imaginary unit given by [34]:

$$\begin{cases} i^{1/3} = \sqrt{3}/2 + i/2 \\ (-i)^{1/3} = \sqrt{3}/2 - i/2 \end{cases} \quad (2-37)$$

After substituting,  $c_l$  is expressed as:

$$c_l(\xi, \eta) = \frac{a_0}{\Gamma\left(\frac{1}{3}\right)} \Gamma\left(\frac{1}{3}, \frac{\eta^3}{9\xi}\right) + \sum_{k \neq 0} \frac{a_k}{Ai(0)} Ai\left((2\pi ki)^{1/3} \eta\right) e^{2\pi ki \xi} \quad (2-38)$$

So the corrosion/precipitate rate  $q(\xi)$  at the wall into the fluid is equal to the diffusive flux given by Fick's law and applied at the wall, namely,

$$q(\xi) = \frac{a_0}{\Gamma(1/3)} \left( \frac{3D_m^2 V_b}{\delta \xi L} \right)^{1/3} + \left( \frac{2\pi D_m^2 V_b}{3\delta L} \right)^{1/3} \frac{1}{Ai(0)\Gamma(1/3)} \sum_{k \neq 0} (ki)^{1/3} a_k e^{2\pi ki \xi} \quad (2-39)$$

Plug the Eq. (2-38) into Eq. (2-10) and the expression of the concentration of corrosion product in the turbulent core region can be obtained as:

$$c_b(\xi) = c_0 + \frac{1}{R - \delta} \left( \frac{D_m^2 L^2}{\delta V_b^2} \right)^{1/3} \left\{ \frac{2a_0}{\Gamma(1/3)} \int \left( \frac{3}{\xi} \right)^{1/3} e^{\frac{\delta^3}{9\xi} \left( \frac{V_b}{\delta L} \right)} d\xi + \sum_{k \neq 0} \frac{ia_k}{\pi k Ai(0)} Ai\left(1, (2\pi ki)^{1/3} \left( \frac{V_b}{\delta L} \right)^{1/3} \delta\right) (2\pi ki)^{1/3} e^{2\pi ki \xi} \right\} \quad (2-40)$$

where  $c_0$  is a constant decided by the boundary condition Eq. (2-13)

### 2.5.2 Analytical Solution for Closed Loop Flow

In a closed loop case at a steady state, the total amount of corrosion is equal to the total amount of precipitation in the entire loop, as shown in Eq. (2-15). Substituting Eq. (2-39) into Eq. (2-15), it can be found that the mean concentration in the turbulent core region  $c_b^0 = a_0$  (the mean wall concentration) [10]. The corrosion production concentration in the laminar sub-layer region, therefore, can be expressed as

$$c_l(\xi, \eta) = a_0 + \sum_{k \neq 0} Y_k(\eta) e^{2\pi ki \xi} \quad (2-41)$$

The solution for the closed pipe loop flow is obtained by substituting Eq. (2-41) to Eq. (2-8) in the following form

$$c_l(\xi, \eta) = a_0 + \sum_{k \neq 0} \frac{a_k}{Ai(0)} Ai\left((2\pi ki)^{1/3} \eta\right) e^{2\pi ki \xi} \quad (2-42)$$

Consequently, the wall corrosion rate is given by

$$q(\xi) = \left( \frac{2\pi D_m^2 V_b}{3\delta L} \right)^{1/3} \frac{1}{Ai(0)\Gamma(1/3)} \sum_{k \neq 0} Q_k e^{2\pi ki \xi} \quad (2-43)$$

From Eq. (2-10), similarly, the concentration in the turbulent core region is obtained

$$c_b(\xi) = a_0 + \frac{1}{R - \delta} \left( \frac{D_m^2 L^2}{\delta V_b^2} \right)^{1/3} \sum_{k \neq 0} \frac{ia_k}{\pi k Ai(0)} Ai\left(1, (2\pi ki)^{1/3} \left( \frac{V_b}{\delta DL} \right)^{1/3} \delta\right) (2\pi ki)^{1/3} e^{2\pi ki \xi} \quad (2-44)$$

## 2.6 Numerical Model

The governing equations for velocity, momentum, and energy for a steady flow were solved numerically using FVM and a standard k- $\epsilon$  model. As pointed out by Nelissen [62], the algorithm to calculate the eddy mass diffusivity strongly influences the local concentration distribution. There are a number of theories to predict the value of eddy mass diffusivity. One typical model for turbulent diffusion is to assume turbulent diffusivity  $D_t$  is proportional to the turbulent viscosity  $\nu_t$ , i.e. turbulent Schmit number  $Sc_t$  is a constant. It is the straightforward extrapolation of what is generally done in turbulent heat transfer [11, 62, 67]. More elaborate models consider the dependence of  $Sc_t$  on some global quantities of the flow (Re, Sc, boundary layer thickness, etc.) [60]. Another type of method is to calculate  $D_t$  by an algebraic turbulence model. Several

different models have been developed [61, 68-70], most of them based on one set of measurements. A typical model proposed by Malang [71] for calculation of high Schmidt number liquid metal flow is

$$D_t = \begin{cases} 0 & 0 < y^+ \leq 5 \\ \nu(y^+ / 5 - 1) & 5 < y^+ \leq 30 \\ 0.005\nu Re^{0.875} & 30 \leq y^+ \end{cases} \quad (2-45)$$

As shown in Eq. (2-45), in the core region ( $y^+ > 30$ ),  $D_t$  is assumed to be zero, whereas in the mass transfer wall region ( $0 < y^+ < 30$ ),  $D_t$  is a function of  $y^+$  and molecular diffusivity. The eddy mass diffusivity in this study was calculated from Malang's model and linked to the numerical simulations instead of the default Reynold's analogy. The governing equations were solved implicitly with a segregated iterative algorithm.

## 2.7 Parameter Identification

The proposed model was applied to the DELTA test loop filling with flowing LBE. The parameters of DELTA loop adopted for the proposed models are [34]: Loop/pipe length  $L = 29.92 \text{ m}$ , hydraulic diameter  $d = 0.0525 \text{ m}$ , liquid LBE velocity  $V_b = 0.5 \text{ m/s}$ , oxygen concentration in LBE  $c_{oxy} = 0.01 \text{ ppm}$ .

The density of LBE is obtained from Eq. (1-1). From Figure 4, the kinematic viscosity of LBE is about a constant value at temperature from  $500^\circ\text{C} \sim 600^\circ\text{C}$ . For simplicity, it can be estimated as  $\nu = 1.5 \times 10^{-7} \text{ m}^2/\text{s}$  in the LBE loop. The molecular diffusivity of iron in LBE is approximated from Eq. (1-3). Therefore at  $823.15 \text{ K}$ , the

diffusion coefficient is calculated in the range  $D_m = 0.31 \sim 2.0 \times 10^{-9} m^2/s$ . As reported in Ref [34], a medium value  $D_m = 1.0 \times 10^{-9} m^2/s$  is usually employed for calculation of diffusion of iron in LBE flow.

The temperature profiles of DELTA loop with maximum temperature  $T_{max} = 550^\circ C = 823.15 K$  and temperature differences of  $\Delta T = 50 K$ ,  $\Delta T = 200 K$  and  $\Delta T = 350 K$  are shown in Figure 36. The maximum temperature locates at the test leg, and the temperature is linear in each subsection.

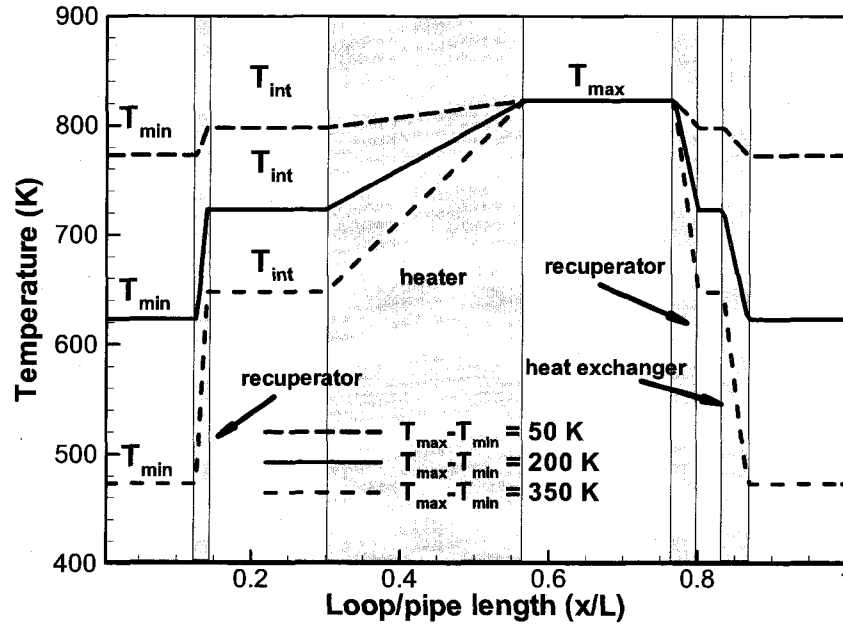


Figure 36. Temperature profile of the open pipe/DELTA loop, ( $T_{max} = 823.15 K$ ,

$$T_{int} = (T_{min} + T_{max}) / 2).$$

Three wall iron concentration profiles were obtained from Eq. (2-27) and are shown in Figure 37. The maximum value of the corrosion production concentration at the wall is 0.0257 ppm. The magnitude orders of the concentration at the wall are about  $10^{-4}$  ppm

or lower before the heater and after the second recuperator for a case with a temperature difference of or larger than 200 K.

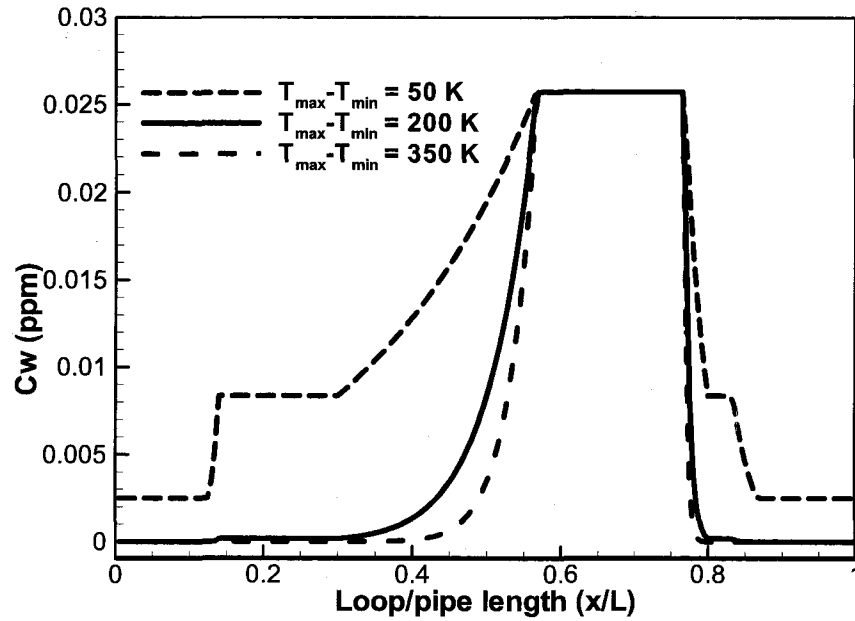


Figure 37. Wall concentration profile of the open pipe/DELTA loop.

In many real cases, it is difficult to keep the temperature distribution at a constant value or in a linear expression. Therefore, the corrosion/precipitation behaviors of open pipe/loop systems with a cosine axial temperature profile were also studied. The temperature profiles are expressed as Eq. (2-46):

$$T = T_{average} + \frac{\Delta T}{2} \cos\left(\frac{2\pi x}{L}\right) \quad (2-46)$$

The temperature profiles are shown in Figure 38. And the calculated wall corrosion production concentration profiles are shown in Figure 39. In these three cases, the average temperature was kept the same at  $T_{average} = 773.15K$ .

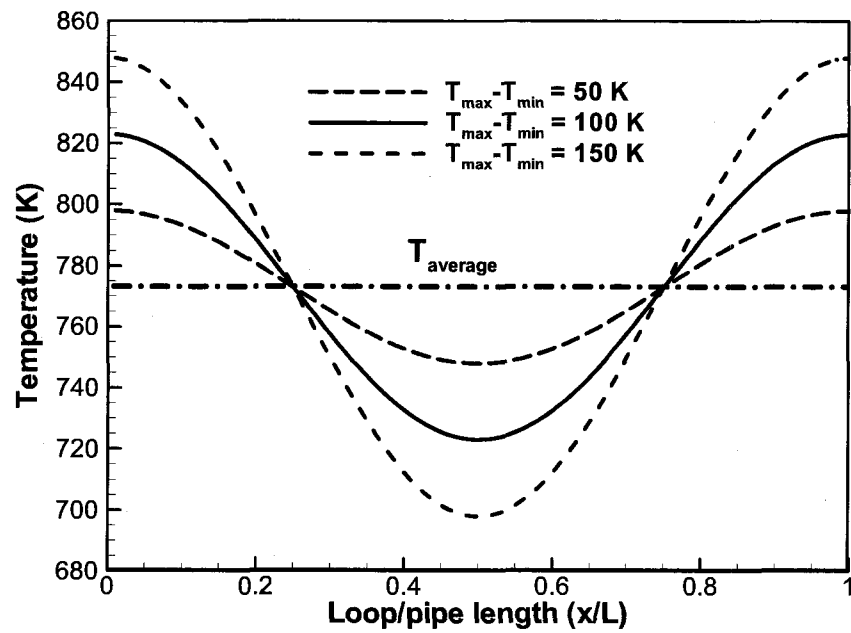


Figure 38. Cosine axial temperature profile of the pipe/loop.

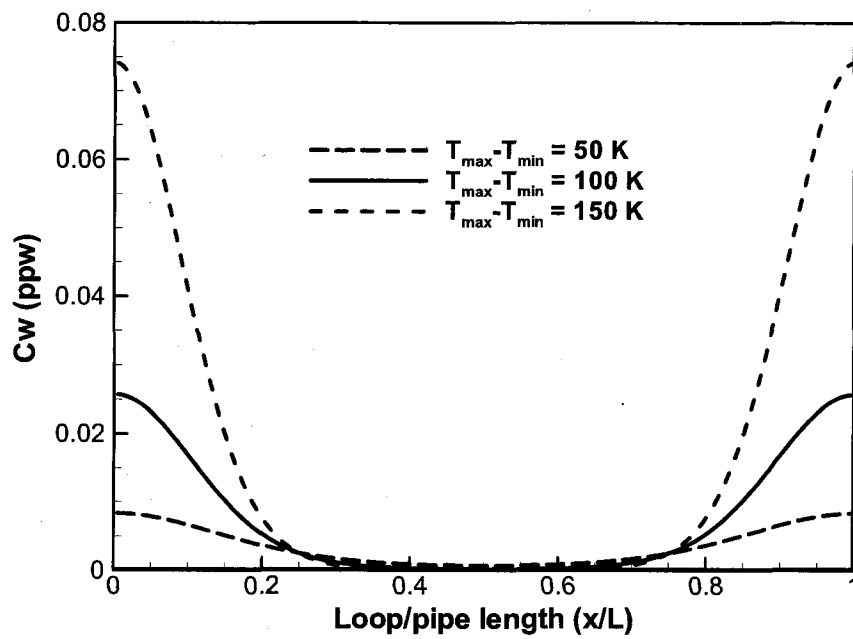


Figure 39. Wall concentration profile of a pipe/loop with a cosine axial temperature profile.



The maximum temperature of each case is no longer of the same value, which is different with the cases shown in Figure 36. Consequently, the maximum concentrations of the iron at the wall have a relatively larger difference, valued at 0.0083 ppm, 0.0257 ppm, 0.0749 ppm for temperature differences of 50 K, 100 K and 150K respectively. For a cosine temperature distribution case, the temperature increases or drops more slowly than a linear temperature distribution case. As a result, the wall concentration gradient along the pipe/loop is smaller and the profile looks smoother. This is the main difference between a cosine temperature distribution case and a linear temperature distribution case.

## 2.8 Results and Discussion

In the kinetic model, the corrosion/precipitation rates were calculated from Eq. (2-39) and Eq. (2-43) based on the different wall concentration distributions caused by the axial temperature distributions. The analytical solutions for both open pipe case and closed loop case are shown in Figure 40 and Figure 41. The positive values of the corrosion/precipitation rate correspond to corrosion, whereas the negative values correspond to precipitation. For the open pipe case, as shown in Figure 40, the corrosion/precipitation rate is different from the results in the Ref. [34], in which it assumed that the mean corrosion rate was linear with the transverse coordinate. For the open pipe flow case, the corrosion rate decreases, evidently, at the beginning section because of the entry effect. The maximal corrosion rate occurs at the beginning of the test leg, both in closed loop cases and in open pipe cases, as shown in Figure 41. Deposition occurs at the beginning part of the closed loop, which is different from the open pipe cases. At the test leg, a case with a larger temperature difference leads to a high corrosion rate even though the temperature at the test leg,  $T_{\max}$ , is the same.

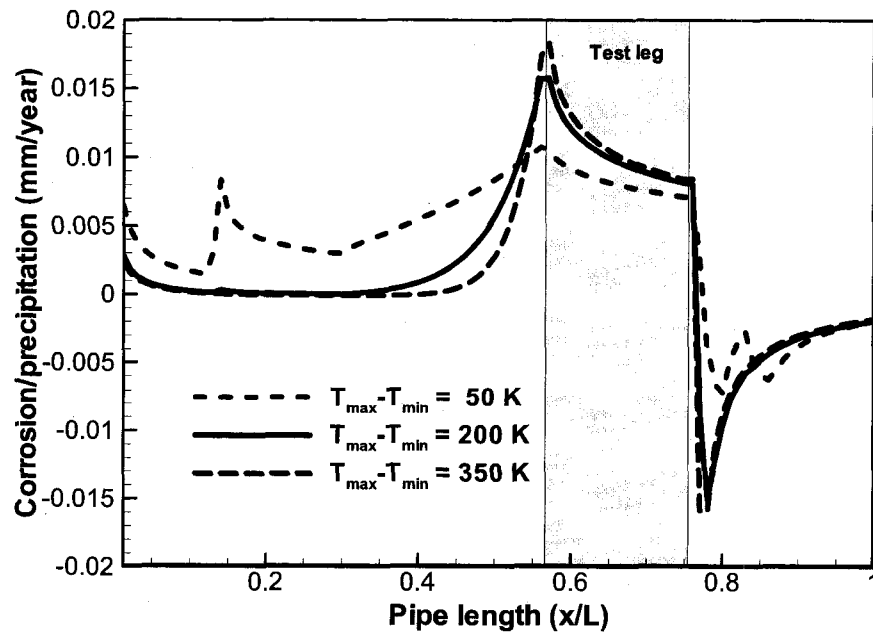


Figure 40. Corrosion/precipitation rates of an open pipe.

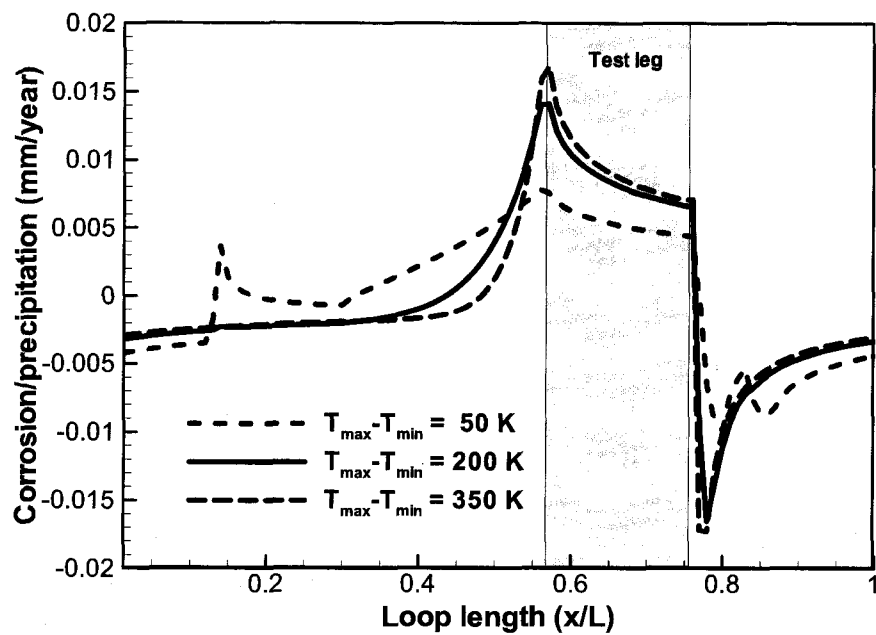


Figure 41. Corrosion/precipitation rates of a closed loop.

The reason is that both the local temperature and the global temperature profile of the pipe/loop can affect the corrosion/precipitation behaviors. A case with a smaller temperature difference leads to a higher corrosion rate at the beginning of open pipe systems for a given maximum temperature. However, at the beginning of a closed loop, a case with a smaller temperature difference leads to a higher precipitation rate for a given maximum temperature. For a particular  $\Delta T$ , the maximal corrosion rate and the maximal precipitation rate of an open pipe case is larger than that of a closed loop case.

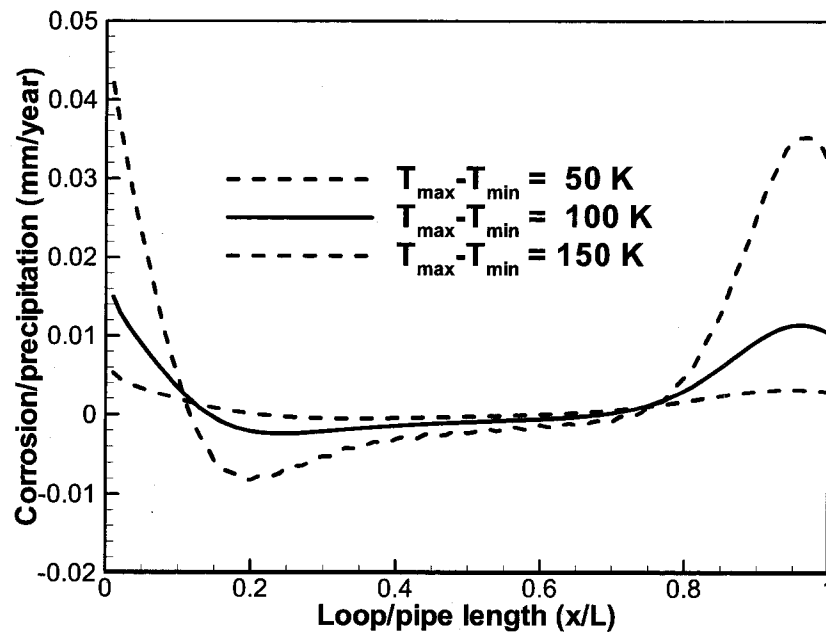


Figure 42. Corrosion/precipitation rates of an open pipe with a cosine axial temperature profile.

Figure 42 shows the corrosion or precipitation rate in an open pipe with an axial cosine temperature profile. While Figure 43 shows the corrosion/precipitation rate in a closed loop with cosine temperature distribution. Different from the cases of pipe/loop

systems with linear temperature profiles in each subsection, high corrosion was observed at the entrance of both cases. As shown in Figure 43, a maximum corrosion rate over 0.04 mm/year can be observed. First, this is because of the relatively high temperature at the beginning of the both cases. Second, the temperature and wall concentration drops more slowly after the maximum temperature in a cosine temperature profile case. In both cases of closed loop and open pipes with a cosine temperature distribution, the precipitation regions occur at the section after the corrosion part (the entrance region of the loop/pipe). And then, the precipitation rates keep decreasing until corrosion is observed again. The corrosion rates then keep increasing till they reach the maximum corrosion rate near the end part of the loop/pipe.

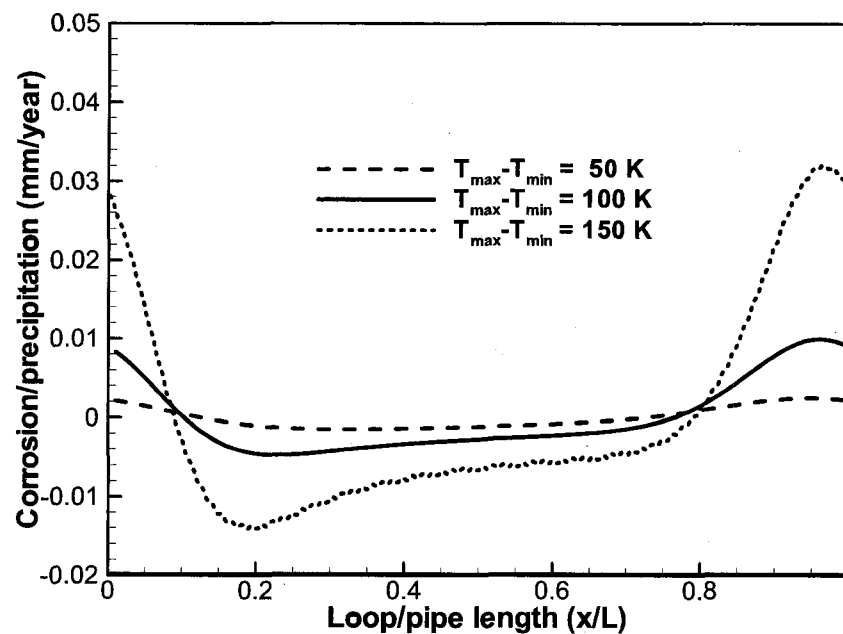


Figure 43. Corrosion/precipitation rates of a closed loop with a cosine axial temperature profile.

Also, it was found that a larger temperature difference corresponds to a higher corrosion/precipitation rate in the closed loop. At the entrance region, the corrosion rates of open pipes with a cosine temperature profile are higher than that of closed pipes with a cosine temperature profile because of the entrance effect. Moreover, it can be found that the corrosion rates have higher and steeper peaks, and the deposition rates have a relatively flatter profile in cases with cosine temperature distributions, compared with the cases of linear temperature distributions.

In order to predict the eddy mass diffusivity effect on the corrosion behaviors in turbulent flow, corrosion/precipitation processes are numerically simulated for open pipes with  $\Delta T=50$  K,  $\Delta T=200$  K, and  $\Delta T=350$  K with different inlet velocities, as shown in Figure 44 to Figure 46.

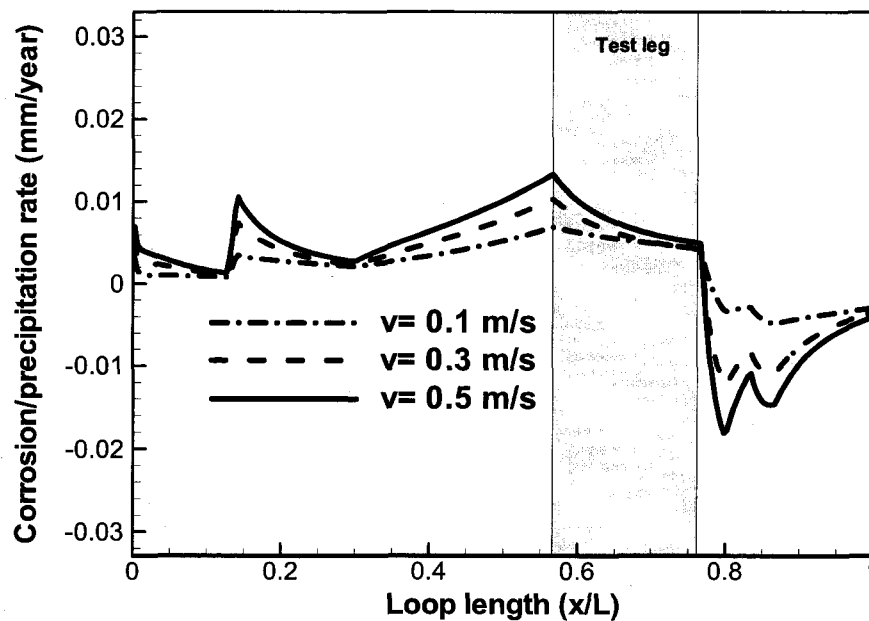


Figure 44. Corrosion/precipitation rates vs. inlet velocities of an open pipe with  $\Delta T=50$  K.

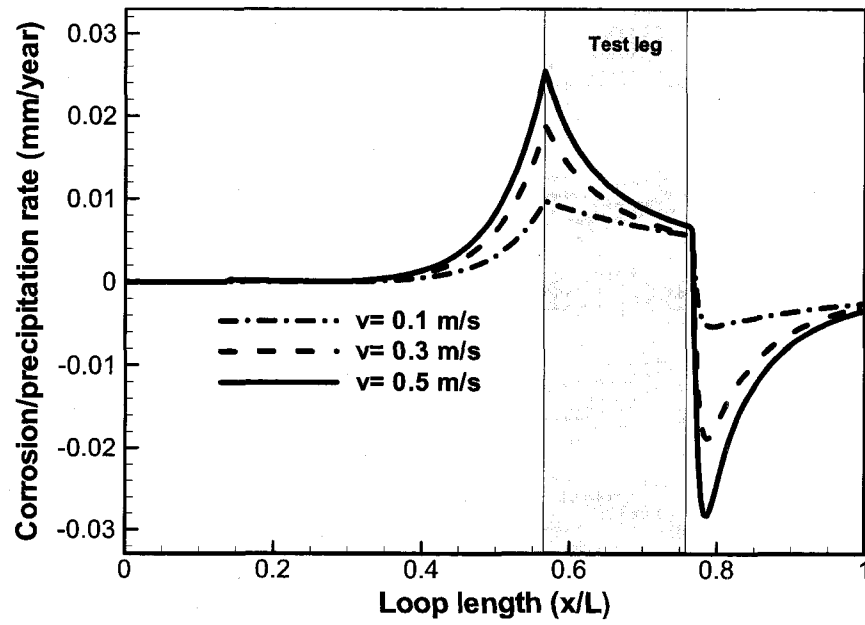


Figure 45. Corrosion/precipitation rates vs. inlet velocities of an open pipe with  $\Delta T=200$

K.

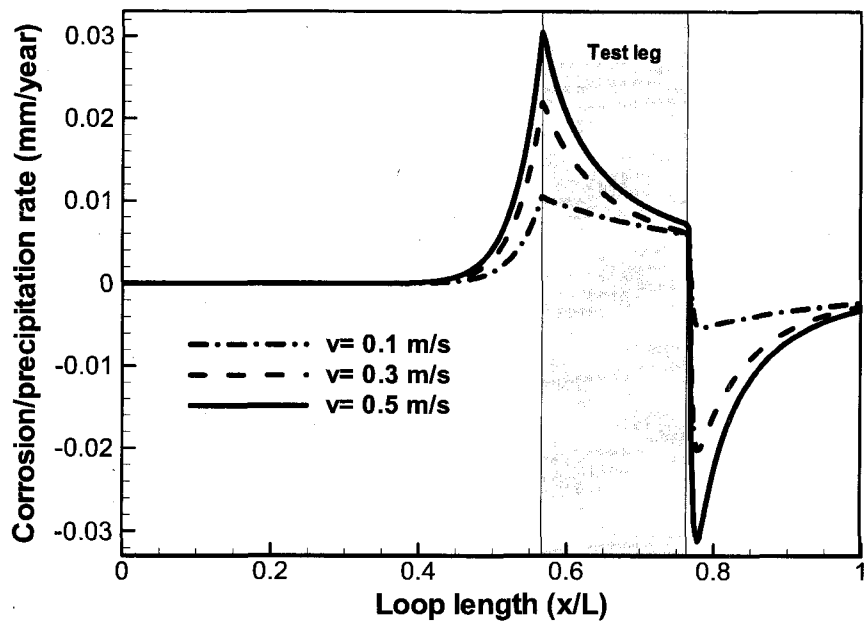


Figure 46. Corrosion/precipitation rates vs. inlet velocities of an open pipe with  $\Delta T=350$

K.

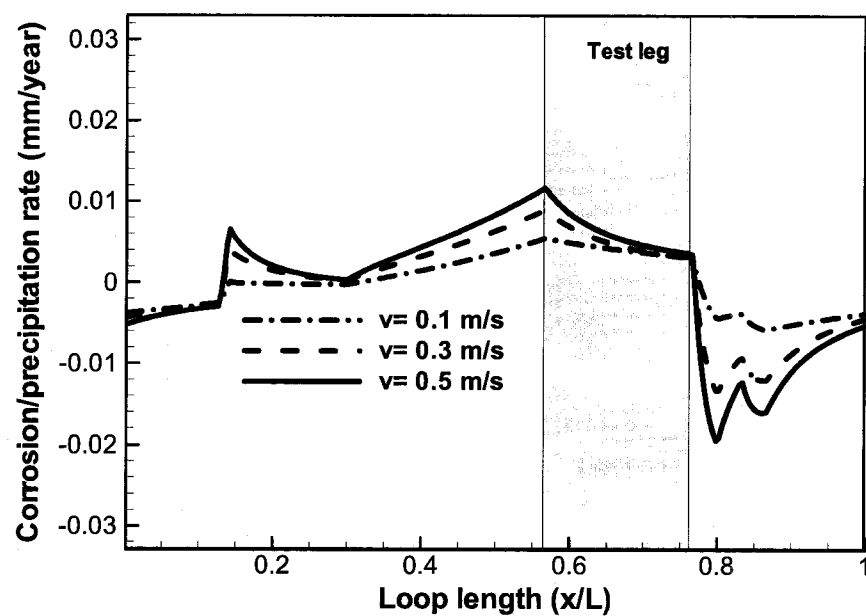


Figure 47. Corrosion/precipitation rates vs. inlet velocities of a closed loop with  $\Delta T=50$

K.

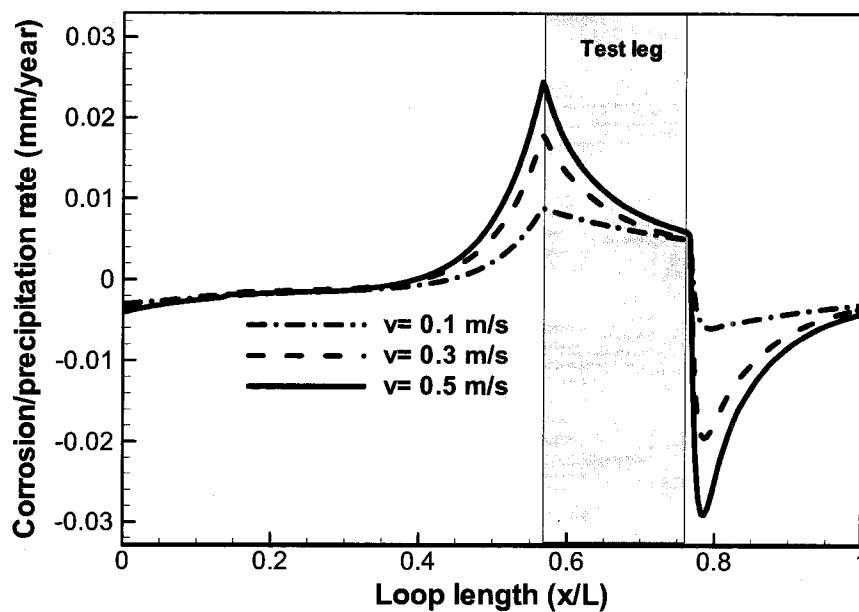


Figure 48. Corrosion/precipitation rates vs. inlet velocities of a closed loop with  $\Delta T=200$

K.

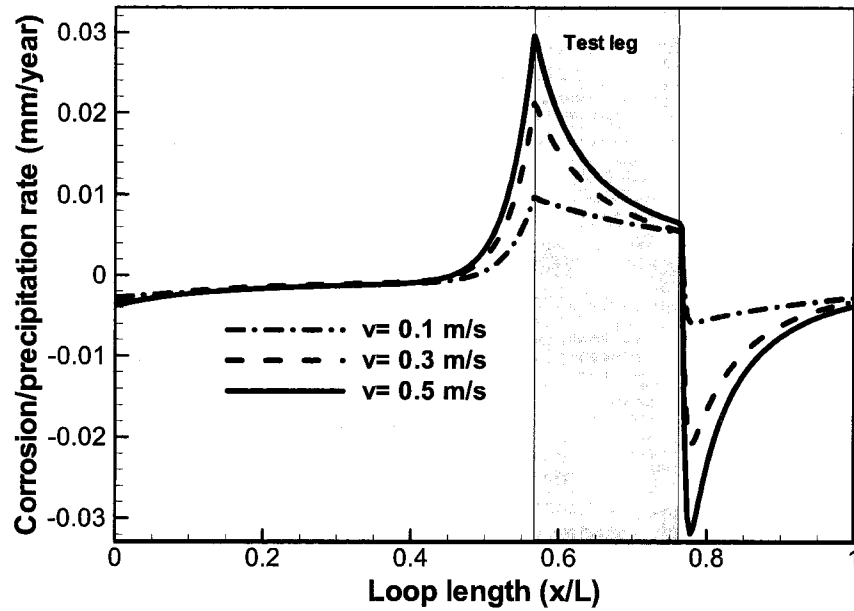


Figure 49. Corrosion/precipitation rates vs. inlet velocities of a closed loop with  $\Delta T=350$  K.

Figure 47 to Figure 49 show the numerical solutions of the corrosion/precipitation rates for closed loop cases  $\Delta T=50$  K,  $\Delta T=200$  K, and  $\Delta T=350$  K with different inlet velocities.

The eddy mass diffusivity, which was neglected in the analytical solutions, was considered in the numerical solutions. And the mass transfer equation was calculated together with the continuity and momentum equations. The eddy mass diffusivity is calculated using a typical S. Malang model [71] as in Eq. (2-38), in the numerical simulations. The profiles in Figure 44 to Figure 49 illustrate that a higher temperature difference leads to higher corrosion and precipitation rates, obviously, which agrees with the tendency from the analytical results. The maximum corrosion rates and deposition rates of cases with  $\Delta T=350$  K can be triple the values of cases with  $\Delta T=50$  K (Figure 46



vs. Figure 44, or Figure 49 vs. Figure 47). The figures also indicate clearly that the velocity can affect the corrosion/precipitation rate. A case with a higher inlet velocity tends to have a higher corrosion rate at the test leg and a higher precipitation rate after the test leg, although the relationship between the corrosion rate and the inlet velocity is not simply linear. Moreover, the momentum of the fluid flow influences the mass transfer behaviors. In the numerical simulations, the molecular diffusivity and eddy mass diffusivity were calculated at the same time, and these results also impact the corrosion/precipitation rates in the pipe/loop, since the eddy mass diffusivity is a function depending on the bulk velocity.

Later on, the analytical solution and numerical solutions were compared for a same inlet velocity, for example,  $V=0.5$  m/s. Figure 50 to Figure 52 show that the similar tendency of the corrosion/precipitation behaviors can be observed in the numerical solutions and analytical solutions. This means that the simplified kinetic model is reasonable and can be used to predict the corrosion/precipitation rates in an open pipe/loop LBE systems. However, differences were observed between the numerical and analytical solutions. The curves of the corrosion rates for the numerical solutions in the test leg region are steeper than those of the analytical solutions. At the beginning of the test leg, the calculated corrosion rates of the numerical solutions are higher. For a case with  $\Delta T=350$  K, the differences of the corrosion rates at the beginning of the test leg region are significant between the analytical solutions and the numerical solutions, valued at 0.017 mm/year and 0.030 mm/year respectively. Similarly, the maximal deposition rates have large differences between analytical solutions and numerical results, right after the test leg region. These differences are mainly caused by the eddy mass diffusivities

which were considered in the numerical models. With increasing temperature difference, this difference is found to be more obvious.

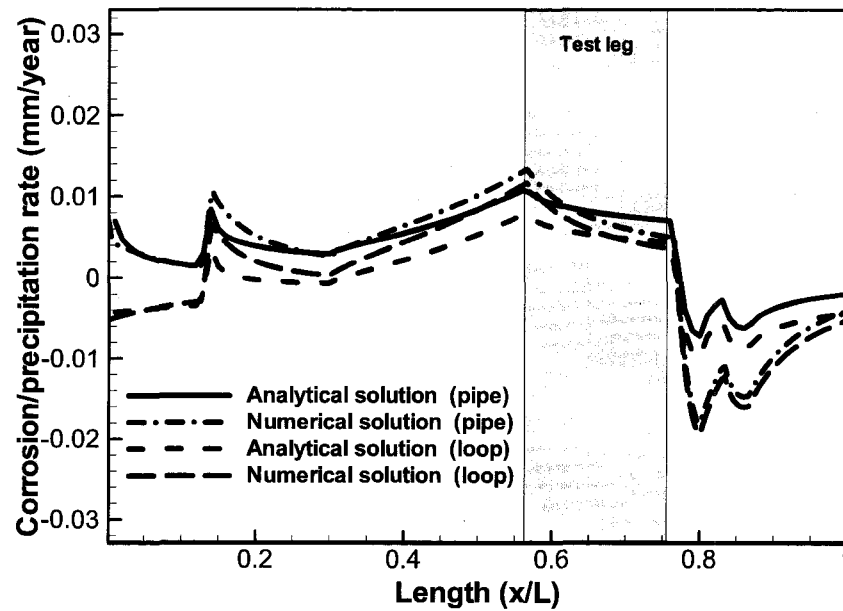


Figure 50. Comparison of analytical solution and numerical solutions for  $\Delta T=50$  K.

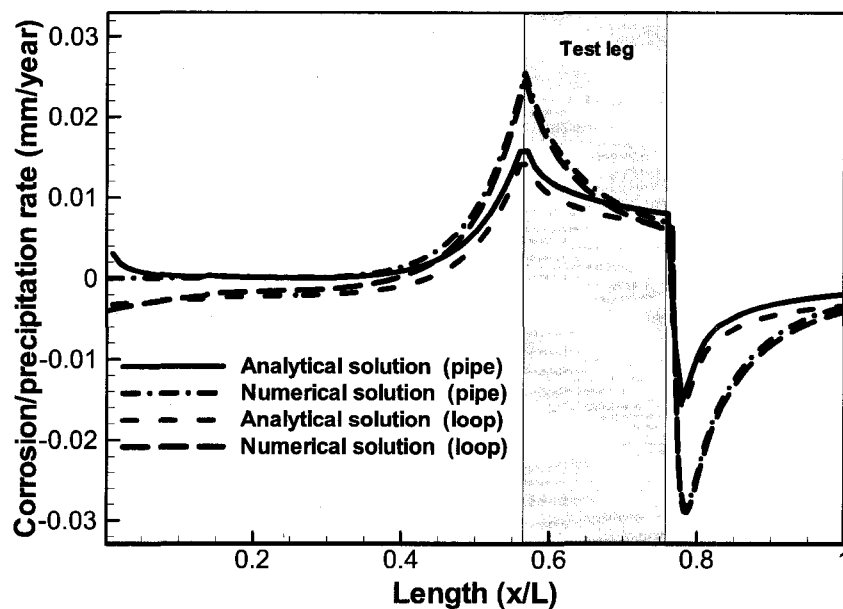


Figure 51. Comparison of analytical solution and numerical solutions for  $\Delta T=200$  K.

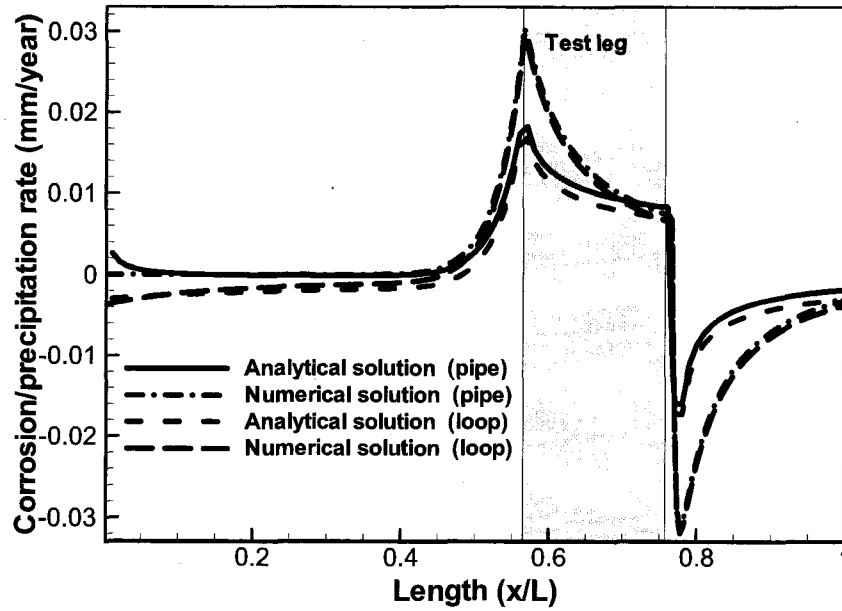


Figure 52. Comparison of analytical solution and numerical solutions for  $\Delta T=350$  K.

Therefore, the eddy mass diffusivities should be considered in order to calculate the corrosion rates more precisely, especially for a case with a large temperature difference.

For mass transfer controlled corrosion, the Sherwood number in a non-isothermal LBE pipe/loop system can be written as

$$Sh(\xi) = \frac{K(\xi)d}{D_m} = \frac{q(\xi)d}{D_m(c_w(\xi) - c_b(\xi))} \quad (41)$$

To capture the mass transfer characteristics at the isothermal test leg in a non-isothermal pipe/loop, the Sherwood number at the test leg was investigated. Figure 53 to Figure 55 show the variations of the Sherwood numbers at the test leg region for open pipe flows and with  $\Delta T=50$  K,  $\Delta T=200$  K, and  $\Delta T=350$  K. The Sherwood numbers at the test leg region for the closed loop cases with  $\Delta T=50$  K,  $\Delta T=200$  K, and  $\Delta T=350$  K are shown in Figure 56 to Figure 58.

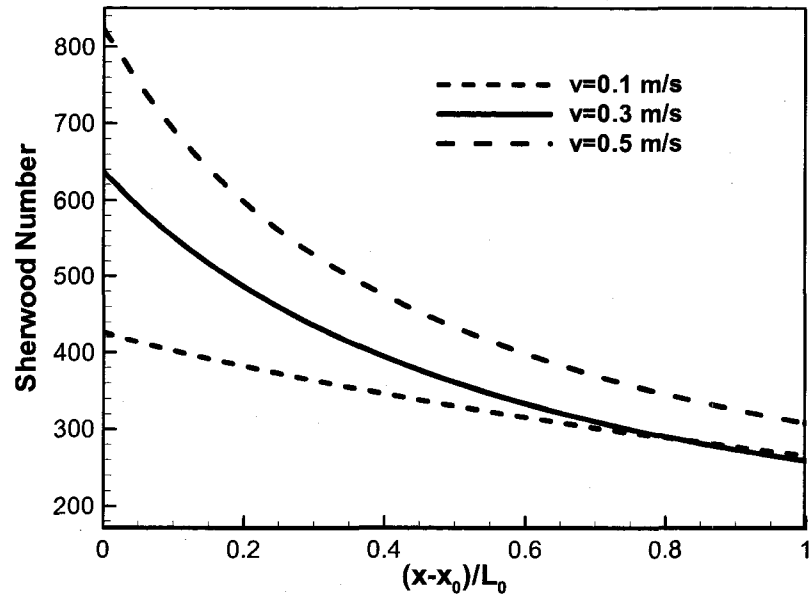


Figure 53. Sherwood number variations at the test leg for an open pipe,

$$T_{\max} = 823.15 K, \Delta T = 50 K.$$

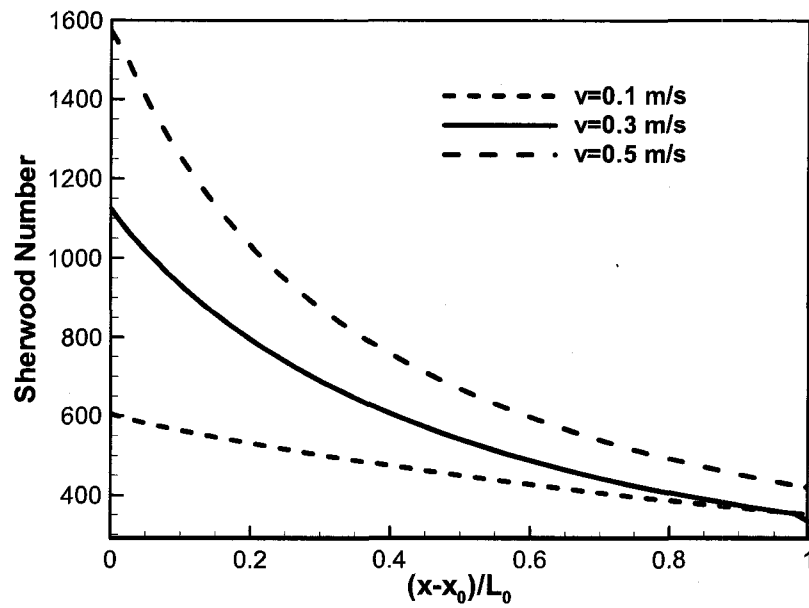


Figure 54. Sherwood number variations at the test leg for an open pipe,  $T_{\max} = 823.15 K$ ,

$$\Delta T = 200 K.$$

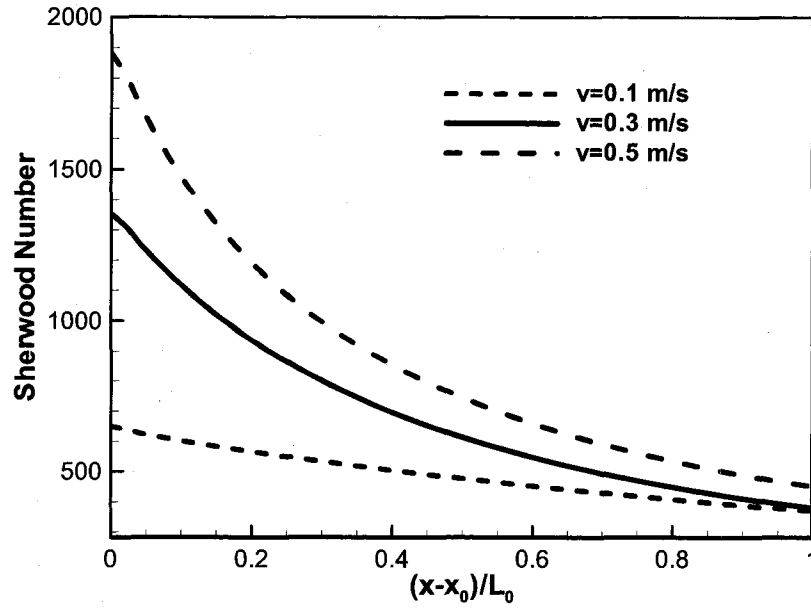


Figure 55. Sherwood number variations at the test leg for an open pipe,

$$T_{\max} = 823.15 K, \Delta T = 350 K.$$

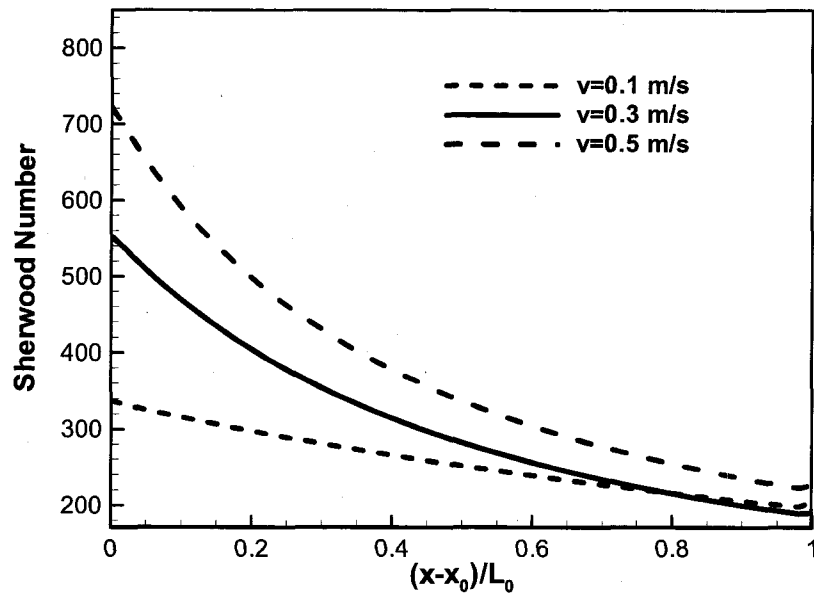


Figure 56. Sherwood number variations at the test leg for a closed loop,

$$T_{\max} = 823.15 K, \Delta T = 50 K.$$

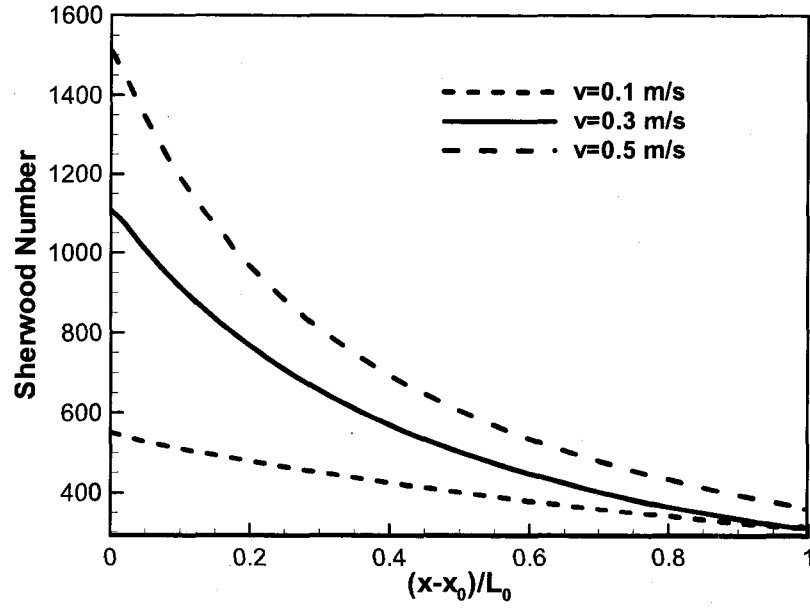


Figure 57. Sherwood number variations at the test leg for a closed loop,  $T_{\max} = 823.15 K$ ,  
 $\Delta T = 200 K$ .

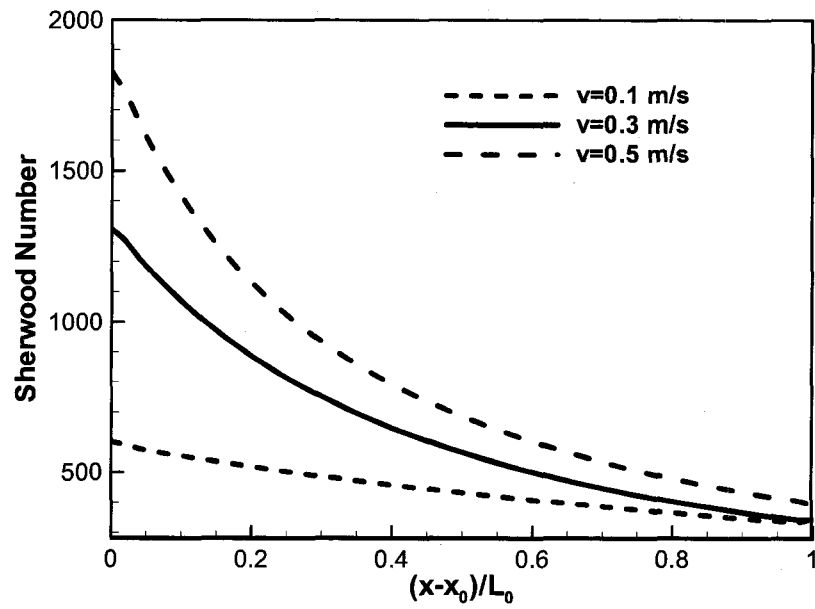


Figure 58. Sherwood number variations at the test leg for a closed loop,  
 $T_{\max} = 823.15 K$ ,  $\Delta T = 350 K$ .

For all of the cases, the Sherwood number decreases sharply from the beginning of the test leg to the minimum value at the end of the test leg. The figures show that the temperature difference affects the Sherwood number clearly. A larger temperature difference leads to a larger Sherwood number for both the open pipe cases and the closed loop cases. Comparing the cases of the open pipe and the cases of the closed pipe, it is easy to find that the Sherwood number is larger in the cases of the open pipe cases for a given temperature difference. The inlet velocity effect on the Sherwood number is also complex. At the beginning of the test leg, a larger inlet velocity tends to have a higher Sherwood number. However, some of the curves of the Sherwood number cross each other in the test leg region. This is because the relationship between the Sherwood number and the inlet velocity is not simply linear, and both the momentum and the eddy mass diffusivity of the fluid flow affect the mass transfer process.

To benchmark the proposed kinetic model and extend it to other non-isothermal liquid metal loop systems, the correlation for the closed loop flow to a non-isothermal pure lead loop built by Sanier and Santarini [72] is applied. In their experimental study, the oxygen level was assumed to be very low. The wall concentration of iron in pure lead is determined by the dissolution process at a low oxygen level, and thus is calculated by

$$C_w = 10^{4.34 - (3450/T)} \quad (42)$$

The following parameters are considered: the internal diameter of the tube is 0.0247 m and the length is 6 m; the highest temperature in the loop is 823.15 K (at the test leg) and the lowest temperature is 738.15 K; the flow velocity is 0.115 m/s. The kinematic viscosity of pure lead is estimated to be  $1.65 \times 10^{-7} \text{ m}^2/\text{s}$ . The density is obtained from

Eq (39), where  $A_p = 11.4478 \text{ kg/m}^3$ ,  $B_p = 0.00127 \text{ kg/K} \cdot \text{m}^3$  for pure lead. As reported in Ref [10], the molecular diffusivity of iron in pure lead is in the same order of that in LBE, and the molecular diffusivity is slightly higher, so  $D_m = 1.5 \times 10^{-9} \text{ m}^2/\text{s}$  is employed for calculating the pure lead loop.

The temperature distribution and corresponding wall concentration of iron is show in Figure 59.

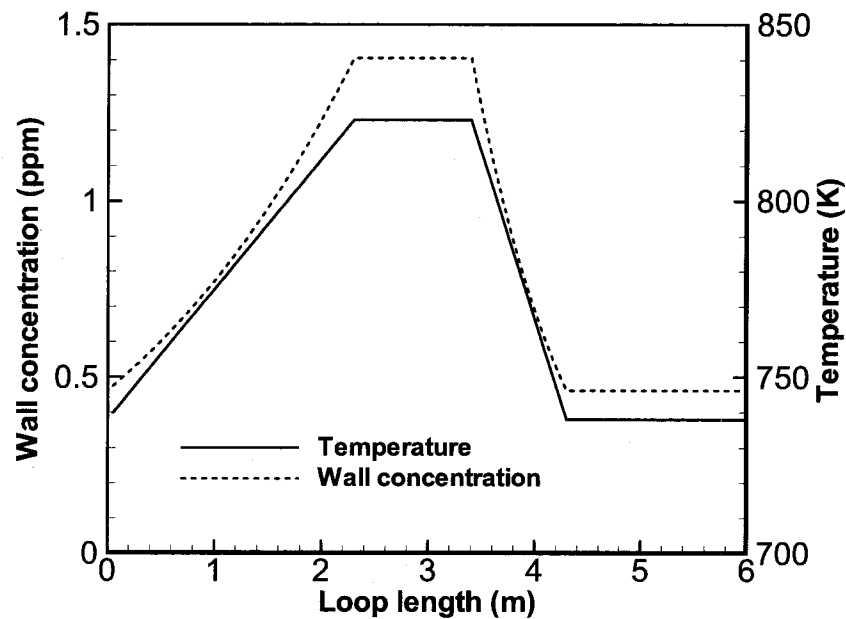


Figure 59. Wall temperature distribution and the wall concentration of iron of the experiment of the pure lead loop.

The experiments were carried out at three locations in the test leg. Two types of steel at the highest temperature were considered. For steel 10CD 9-10, the experimental corrosion rate was between  $75 \pm 20 - 110 \pm 20 \mu\text{m}$  after 3000 hours, and steel Z 10 CD Nb V92 was between  $25 \pm 20 - 40 \pm 20 \mu\text{m}$  after 2800 hours. The predicted corrosion rate



from the model of Balbaud-Celerier and Barbier was about  $239\ \mu\text{m}$  after 3000 hours, which was 2.1 times higher than the maximal experimental results [15].

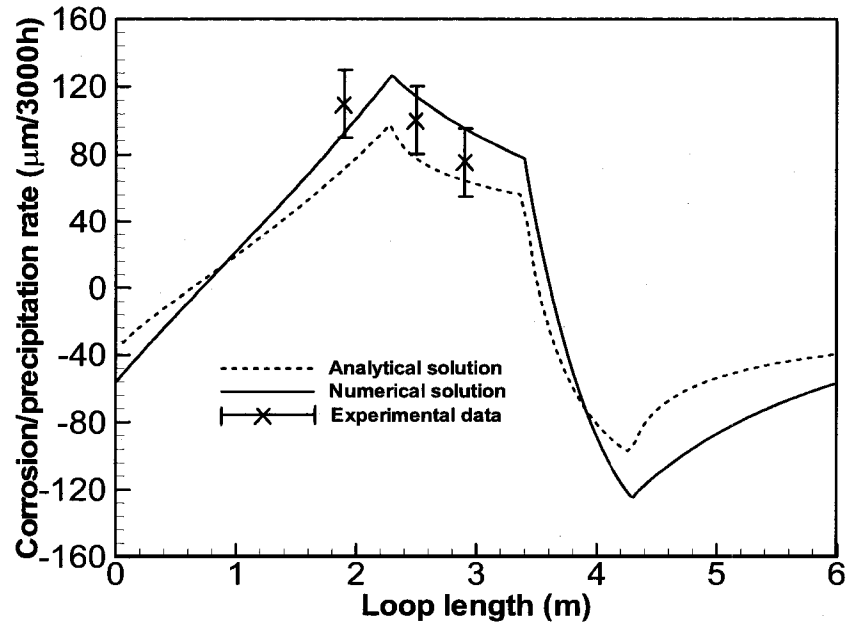


Figure 60. Comparisons between the experiment data [72], numerical and analytical results from the model for the pure lead loop.

Figure 60 shows the numerical solutions, analytical solutions from the proposed models and the comparison with the experimental data. As can be found, the corrosion rates of the numerical model in the three test locations are in the experimental data region. Therefore, the numerical model predicts the corrosion rate accurately. The analytical result also predicts the corrosion rate with an acceptable error, considering the test error and impact of the molecular diffusivity. Moreover, the numerical model predicts a higher corrosion rate in the test leg region and a higher precipitation rate right after the test leg than that in an analytical result, since the eddy mass diffusivity is considered. Those observations agree with the analysis of the proposed model above.

Thus, the analytical expression can be used to predict the corrosion/precipitation rates for lead and the lead alloy coolant system. The analytical prediction is precise, and the result is easy to obtain with explicit expressions. Compared with the results of Ref. [15], both the numerical simulation and the analytical calculation are more accurate. Hence, the proposed numerical model can calculate the corrosion/precipitation rates more precisely and accurately since the fluid condition and eddy mass diffusivity is considered.

## 2.9 Conclusions

A theoretical kinetic model based on the boundary layer theory was developed to predict the corrosion/precipitation in non-isothermal lead alloy pipe/loop systems. By considering a turbulent core region and a laminar sub-layer, the mass transport equations in both regions were solved. The analytical expressions of both the local corrosion/precipitation rate and the bulk concentration of the corrosion products were obtained. The present kinetic model is applied to the DELTA test loop with specific axial temperature distribution. Based on the present model, it was found that the maximal corrosion rate occurs at the beginning of the maximal temperature region both in the open pipe flow case and the loop flow case, and there is a precipitation region shortly after the high temperature leg. At the beginning region, the corrosion rate decreases sharply in the open pipe flow case. The temperature difference between the maximal and minimal temperatures affects the corrosion/precipitation rate significantly.

The corrosion or precipitation rates in an open pipe/closed loop with an axial cosine temperature profile were also investigated. High corruptions were observed at the entrance of the cases with an axial cosine temperature profile, which are different with the cases of the pipe/loop system with linear temperature profiles in each subsection. The reasons for

the difference are the relatively high temperature at the entrance and slower drops of the temperature and wall concentration after the maximum temperature in a cosine temperature profile case. Moreover, it can be found that the corrosion rates have higher and steeper peaks, and the deposition rates have relatively flatter profile in cases with cosine temperature distributions, compared with the cases of linear temperature distributions.

For the first time, the eddy mass diffusivity is coupled in the present numerical model in order to demonstrate the effect of the eddy mass diffusivity on the corrosion and precipitation in non-isothermal lead alloy pipe/loop systems. From the comparison of numerical and kinetic models, the eddy mass diffusivity has an obvious effect on the corrosion/precipitation behaviors, especially when the temperature difference is large. At the test leg, where temperature is at a maximum, the eddy mass diffusivity increases the corrosion rates. In addition, at the temperature dropping region right after the test leg, the eddy mass diffusivity leads to a much higher deposition rate. In the numerical model, the influence of flow conditions were also studied, such as the inlet velocity. For a higher inlet velocity, a higher corrosion rate can be found in the test leg region and a higher precipitation rate at the temperature dropping region right after the test leg. The average Sherwood number at the test leg section with the highest temperature for both open pipes and closed loops are also presented and analyzed.

In summary, both the analytical and the numerical solutions for a simple lead loop were compared to the experimental data and were in agreement. For a more precise and accurate prediction, the eddy mass diffusivities should be considered, especially for a case with a large temperature difference.

Finally, it should be noticed that the present model is only suitable for the high Schmidt number cases, which means the mass diffusion layer is submerged under the hydraulic boundary layer. Meanwhile, although the present solution is proposed for modeling the mass transfer corrosion in LBE pipe/loop systems, it can be extended to the other general problems of high Schmidt mass transfer for the developed turbulent wall-bounded shear flows in a non-isothermal system.

## CHAPTER 3

### A DIFFUSION CONTROLLING OXIDATION MODEL WITH SCALE REMOVAL IN OXYGEN-CONTAINING LIQUID FLOW

#### 3.1 Introduction

A diffusion controlling oxidation model considering scale removal is developed in an oxygen-containing liquid flow environment. Scale removal is implemented and the effect of scale removal rate on the formation mechanism of duplex oxide layer structure is analyzed in the model. The volume expansion effect caused by density difference is coupled with the weight gain during oxidation. A coordinate transform technique is employed to obtain the diffusion equations with an advection term. The governing equations are nondimensionalized and analogized with the Stefan problem and solved numerically by the finite difference method. The nondimensional parameters are studied and the model is extended to an oxide growth model with duplex layer structure and noble elements. The model is benchmarked with previous results and good agreement is obtained.

#### 3.2 Literature Survey

The study of the corrosion and oxidation of metals has been for many years a subject of considerable research effort because of its basic scientific interest as well as its technological importance. The severe corrosion of materials presents a critical barrier to

their industrial use in many cases. For example, it is widely recognized that the corrosiveness of the lead alloys is a critical challenge for safe applications as a potential coolant candidate in advanced reactors. [10, 19, 21, 36] In liquid flow, especially in liquid metal flow at high temperature, forming and maintaining a protective oxide layer by an oxygen controlling technique is one of the most efficient ways in protecting the containment and structural materials from critical corrosion. As reported, the main driving force for corrosion in liquid metal flow is the chemical potential for dissolution of all solid surfaces in contact with the liquids. [10, 19] The oxide layer separates the structural materials from the corrosive liquid flow and works as an effective solid-state diffusion barrier for oxygen and solid components.

The oxidation of metal in a liquid flow environment is very complex because many interactions are involved during the process. For example, the selective corrosion and/or oxidation occur because of the added alloying components and impurities. The flow conditions induce and enhance scale removal at the same time. Furthermore, the oxide layer and the remained components may restructure during the process. Among those phenomena, scale removal plays an important role, especially for high flow velocity at high temperature, through scale dissociation, volatilization, corrosion, erosion, etc. Therefore, scale removal can increase the corrosion rate and make the oxide layer unstable in structures easily broken away. [3] A duplex oxide layer structure can usually be observed in aqueous environments and liquid media. As a complex nonlinear process, the evolution of the oxide layer structure of steel, in a liquid environment containing oxygen, strongly depends on steel compositions, temperature and hydraulic factors. [10, 74]

Although studies were conducted and conclusions were drawn during the study of the oxidation process in liquid flows in many countries, convective results are still scarce and scattered. In order to interpret the existing data and to predict the oxidation and corrosion conditions in oxygen containing flowing liquid, it is necessary to develop kinetic oxidation models and study the oxidation process systemically. Several models assuming that the outer layer formation is due to the precipitation of dissolved metals have been presented in an aqueous environment. [27, 75-77] However, experimental results have shown that a porous outer layer can be formed on the gas/oxide interface even in a gaseous environment. Robertson [46, 78] developed an oxidation model for steel in steam and water at high temperature, in which he assumed the outer layer is formed due to the solid diffusion of iron and the inner layer is caused by the water reaching the inner surface through micro-pores. According to Robertson's model, the corrosion rate is independent of the liquid flow velocity and the partial oxygen pressure in the flow. However, studies and tests indicate that the oxide layer thickness depends strongly on the flow velocity and oxygen dissolved in the liquid. Actually, both the diffusion of metal and the diffusion of oxygen in liquid flow control the growth of the oxide layer. [27] The mechanism of duplex oxide films formation is very complex and not well understood at the present time. Stated simply, the porous outer layer is formed by the reaction of oxygen and the component element in metal which has a high mass diffusivity and is easily oxidized. The compact inner layer is formed by the remained components in metal material, together with the reactant of the active components and oxygen diffused inwards.

As stated by Wagner [47] and Coates et al. [79], the diffusion controlled oxidation problem is difficult to solve because it is a moving-boundary problem and complication arises from the change in density as metal is converted into oxide. By analogy with the Stefan problem, Wong and Caldwell et al. [80, 81] solved the oxygen diffusion controlling oxidation problem for pure zirconium using finite difference methods. Neither Wong nor Caldwell considered the weight of oxygen in the oxide and Caldwell even neglected the volume changes due to the density changes. Only a simple single layer structure oxide is formed for pure zirconium and no scale removal effect was studied because they developed the model for high-temperature steam. Ding [82] proposed a model for the oxidation of titanium in which the diffusion equation of oxygen was solved and the volume of titanium was replaced by the oxide simply. To the best knowledge, there is no model considering density change, oxygen weight absorption, and duplex oxide layer structure, together with scale removal effects in oxygen containing flowing liquid.

### 3.3 Theory

In the present study, an extensive diffusion-controlling oxidation model, with scale removal in oxygen containing liquid flow, is developed for metal or metal alloy materials. In oxygen containing liquid flows, the concentration of oxygen is assumed to be uniform so that the diffusion of oxygen in the fluid is not considered. The molar density of oxygen will be calculated in the oxidation process. On the interface of liquid flow and solid structure material, the molar density of oxygen is assumed to be at a constant value,  $C_{M0}$ . Assuming that only the component of element M in the metal materials has a high mass diffusivity in the oxide layer and only M reacts with oxygen.



Other components have relatively lower mass diffusivity, so their diffusion in the material and their reaction with oxygen are negligible. From time  $t=0$ , the active atomic oxygen begins to diffuse into the material and react with the active component M in the material via the following reaction:

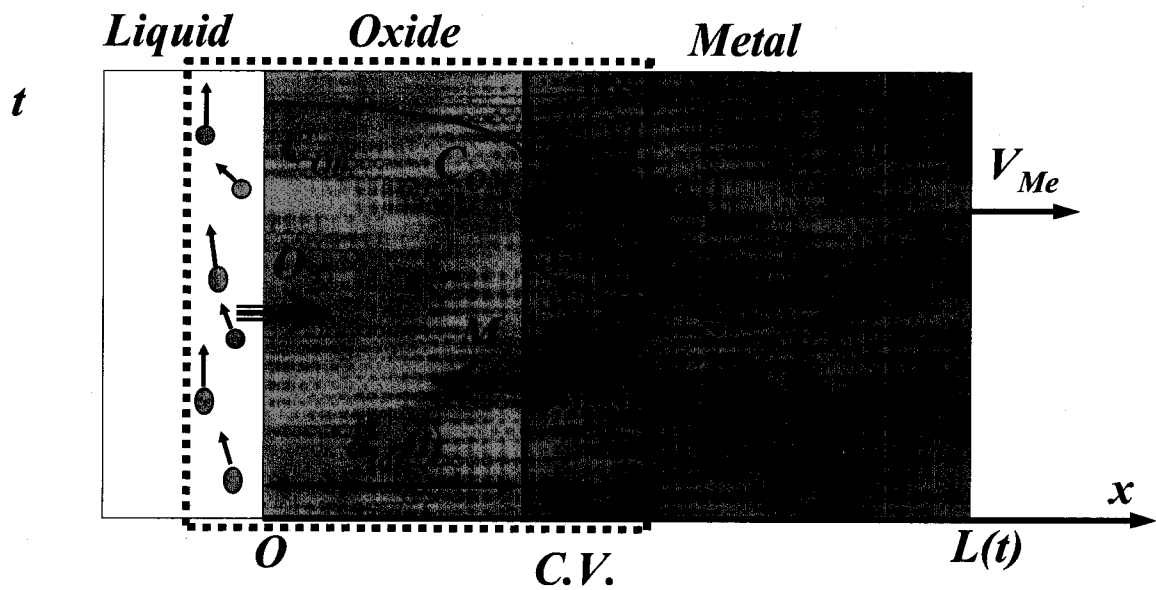


After the oxide layer, mainly  $M_xO_y$ , is formed on the surface of the metal, oxygen continues to diffuse inwards and M begins to diffuse outwards through this barrier. The oxygen which diffused inwards reacts with M behind the oxide layer and this part of the oxide forms the compact inner layer, together with all other remaining inert components of the structure materials. The reaction behind the oxide layer accounts for the inner volume expansion of the oxidation process. On the other hand, M keeps diffusing out and reacts with oxygen on the outer surface of the oxide layer and forms a new porous outer layer. This reaction may occur as well inside the oxide layer, partly, which will cause redistribution of the oxide structure during the process. At the same time, the oxide layer is undergoing a removal caused by the fluid flow. The reaction on the outer surface of the oxide layer, inside the oxide layer, and the removal of scale, all account for the outer volume expansion. The value of the outer volume expansion can be negative, which indicates a decrease in the thickness of the oxide layer. This decrease takes place especially in high turbulent flows, multi-phase flows with aggressive particles, or on the structure surface with a high shear stress. The consequent fast removal of the oxide layer results in a fast erosion on the outer surface of the oxide layer.

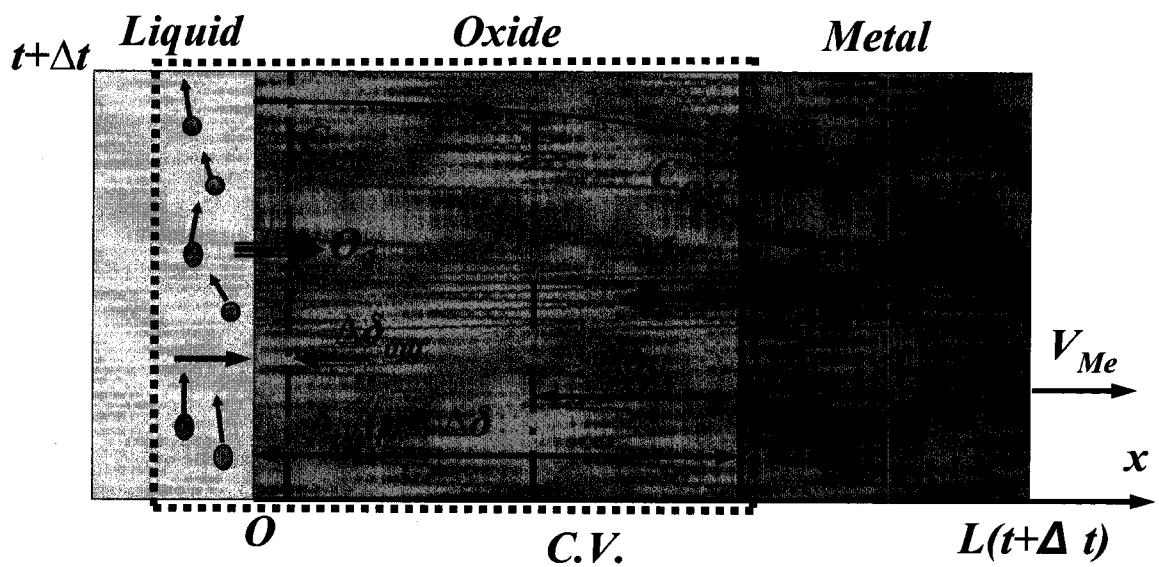
The diffusion of metallic element M is assumed to be faster than the diffusion of atomic oxygen. Thus, the oxidation is controlled by the diffusion of oxygen, and only the diffusion equation of atomic oxygen during the oxidation will be solved. However, the mass conservation of M is involved, which accounts for the diffusion result of M. As illustrated in Figure 61, the simplified oxidation process, considering the volume expansion effect, is illustrated from time  $t$  (a) to  $t+\Delta t$  (b). The atoms M from a layer of  $\Delta\lambda$  are assumed to be oxidized during this period. The weight ratio of M in the material,  $w$ , can be checked out from the material manuals. As analyzed above, the atomic M reacts behind the oxide layer, inside the oxide layer, and even on the outer surface of the oxide layer. Hereby, an important parameter is introduced,  $p$ , which stands for the ratio of inner reacted atomic M out of the total reacted atomic M. Thus,  $1-p$  of the reacted atomic M reacts inside the oxide layer or on the outer surface of the oxide layer. At time  $t+\Delta t$ , an inner layer of  $\Delta\delta_{in}$  is formed, and oxide of a thickness  $\Delta\delta_{out}$  is formed after the scale removal. Let  $K_r$  to be the scale removal rate constant.

The original point of the calculating coordinate is set at the outer surface of the oxide layer. The moving of the oxide layer as a whole sub-domain is neglected, since the oxidation occurs in the whole sub-domain, and there is a scale removal which causes a relatively small movement, compared with the movement of the metal. Consequently, the oxide-metal interface moves at a velocity of  $V_{OM}$ , and the coordinate changes from  $\delta(t)$  to  $\delta(t) + \Delta\delta_{tot}$ . The remaining metal is moving at a velocity of  $V_{Me}$ , since there is a volume substituting effect. The concentration of oxygen in the oxide phase satisfies the equation,

$$\frac{\partial C}{\partial t} - D_{ox} \frac{\partial^2 C}{\partial x^2} = 0 \quad \text{for } C_{o0} > C > C_{OM} \quad (\text{or } \delta_{tot}(t) > x > 0) \quad (3-2)$$



(a) at time  $t$



(b) at time  $t+\Delta t$

Figure 61. Illustration of the oxygen-controlling oxidation process.

And as a result of the moving of metal, the concentration of oxygen in the metal phase satisfies:

$$\frac{\partial C}{\partial t} + V_{Me} \frac{\partial C}{\partial x} - D_{Me} \frac{\partial^2 C}{\partial x^2} = 0 \quad \text{for } C_{MO} > C > 0 \text{ (or } L(t) > x > \delta_{tot}(t)) \quad (3-3)$$

where,  $L(t)$  is at the far end of the specimen away from the exposed end. Obviously,

$$L(t) = L_0 + V_{Me}t \quad (3-4)$$

where  $L_0$  is the original thickness of the specimen.

To find out the metal phase moving velocity  $V_{Me}$ , the mass conservation of element M is considered. For the reaction behind the oxide layer:

$$wp\rho_{Me}\Delta\lambda = r[\rho_{in}\Delta\delta_{in} - \rho_{Me}(1-w)\Delta\lambda] \quad (3-5)$$

where  $r$  is the fraction of mass of atomic M in the oxide molecular and,

$$r = \frac{xM_M}{yM_O + xM_M} \quad (3-6)$$

For the reaction other than behind the oxide layer:

$$w(1-p)\rho_{Me}\Delta\lambda = r\rho_{out}(\Delta\delta_{out} + K_r\Delta t) \quad (3-7)$$

So,

$$\Delta\delta_{tot} = \frac{wp + r - rw}{r} \frac{\rho_{Me}}{\rho_{in}} \Delta\lambda + \frac{w(1-p)}{r} \frac{\rho_{Me}}{\rho_{out}} \Delta\lambda - K_r\Delta t \quad (3-8)$$

$$V_{Me} = \frac{\Delta\delta_{tot} - \Delta\lambda}{\Delta t} = \frac{\Delta\delta_{tot}}{\Delta t} - \frac{\Delta\delta_{tot} + K_r\Delta t}{\Delta t \left( \frac{wp + r - rw}{r} \frac{\rho_{Me}}{\rho_{in}} + \frac{w(1-p)}{r} \frac{\rho_{Me}}{\rho_{out}} \right)} \quad (3-9)$$

which can be written as,

$$V_{Me} = \left(1 - \frac{1}{m}\right)V_{OM} - \frac{K_r}{m} \quad (3-10)$$

where,  $V_{OM}$  is the moving velocity of the oxide-metal interface

$$V_{OM} = \frac{\Delta \delta_{tot}}{\Delta t} \quad (3-11)$$

and,

$$m = \frac{wp + r - rw}{r} \frac{\rho_{Me}}{\rho_{in}} + \frac{w(1-p)}{r} \frac{\rho_{Me}}{\rho_{out}} \quad (3-12)$$

In Eq. (3-12),  $m$  is a complex factor. It consists of the densities of metal, inner oxide and outer oxide, the atomic mass fraction of mass of metallic element in its oxide molecular ( $r$ ), and the inner reaction ratio ( $p$ ), and weight ratio of element  $M$  in the material ( $w$ ).

Introduce

$$C^* = \frac{C}{C_{O0}} \quad (3-13.a)$$

$$x^* = \frac{x}{L_0} \quad (3-13.b)$$

$$t^* = \frac{t D_{Me}}{L_0^2} \quad (3-13.c)$$

$$V_{Me}^* = \frac{V_{Me} L_0}{D_{Me}} \quad (3-13.d)$$

and the Eq. (3-2) can be nondimensionalized to:

$$\frac{\partial C^*}{\partial t^*} - \frac{D_{Ox}}{D_{Me}} \frac{\partial^2 C^*}{\partial x^{*2}} = 0 \quad \text{for } 1 > C^* > C_{OM}^* \text{ (or } L^*(t^*) > x^* > \delta_{tot}^*(t^*)) \quad (3-14)$$

Similarly, Eq (3-3) follows the form,

$$\frac{\partial C^*}{\partial t^*} + V_{Me}^* \frac{\partial C^*}{\partial x^*} - \frac{\partial^2 C^*}{\partial x^{*2}} = 0 \quad \text{for } C_{Mo}^* > C^* > 0 \text{ (or } \delta_{tot}^*(t^*) > x^* > 0) \quad (3-15)$$

Let

$$V_{OM}^* = \frac{V_{OM} L_0}{D_{Me}} \quad (3-16.a)$$

$$K_r^* = \frac{K_r L_0}{D_{Me}} \quad (3-16.b)$$

Obviously, for a case with an initial condition of zero oxide layer thickness,

$$V_{OM}^* = \frac{\Delta \delta_{tot}^*(t^*)}{\Delta t^*} \quad (3-17)$$

Thus,

$$V_{Me}^* = \left(1 - \frac{1}{m}\right) V_{OM}^* - \frac{K_r^*}{m} \quad (3-18)$$

Where,

$$L^*(t^*) = \frac{L(t)}{L_0} \quad (3-19.a)$$

$$\delta_{tot}^*(t^*) = \frac{\delta_{tot}(t)}{L_0} \quad (3-19.b)$$

$$C_{OM}^* = \frac{C_{OM}}{C_{O0}} \quad (3-19.c)$$

$$C_{MO}^* = \frac{C_{MO}}{C_{O0}} \quad (3-19.d)$$

To simplify this problem, the coordinate is transformed by introducing,

$$y = \begin{cases} \frac{1}{m}(1 + \frac{K_r^*}{V_{OM}^*})x^* & \text{for } \delta_{tot}^*(t^*) \geq x^* \geq 0 \\ x^* - (1 - \frac{1}{m})\delta_{tot}^*(t^*) + \frac{K_r^*}{m}t^* & \text{for } L^*(t^*) > x^* > \delta_{tot}^*(t^*) \end{cases} \quad (3-20)$$

Even though the transformation differentiates between the oxide and metallic phase,  $y$  is continuous at the oxide-metal interface for a case with an initial condition of zero oxide layer thickness. Meanwhile,  $y$  is a dimensionless variable as well.

$$y(\delta_{tot}^{*-}(t^*)) = y(\delta_{tot}^{*+}(t^*)) = y_{OM}(t^*) = \frac{1}{m}\delta_{tot}^*(t^*) + \frac{K_r^*}{m}t^* \quad (3-21)$$

Another merit of this coordinate transformation is that the far end of the specimen is kept at a constant value  $L_0$ , in the new coordinate system.

$$y(x^* = L^*(t^*)) = 1 \quad (3-22)$$

Due to the transformation,

$$\frac{\partial C^*}{\partial x^*} = \begin{cases} \frac{1}{m}(1 + \frac{K_r^*}{V_{OM}^*})\frac{\partial C^*}{\partial y} & \text{for } \delta_{tot}^*(t^*) \geq x^* \geq 0 \\ \frac{\partial C^*}{\partial y} & \text{for } L^*(t^*) > x^* > \delta_{tot}^*(t^*) \end{cases} \quad (3-23)$$

$$(\frac{\partial C^*}{\partial t})_{x^*} = \begin{cases} (\frac{\partial C^*}{\partial t})_y & \text{for } \delta_{tot}^*(t^*) \geq x^* \geq 0 \\ (\frac{\partial C^*}{\partial t})_y + [\frac{K_r^*}{m} - (1 - \frac{1}{m})V_{OM}^*]\frac{\partial C^*}{\partial y} & \text{for } L^*(t^*) > x^* > \delta_{tot}^*(t^*) \end{cases} \quad (3-24)$$

After substituting, the governing equations become:

$$\frac{\partial C^*}{\partial t} - \frac{1}{m^2}(1 + \frac{K_r^*}{V_{OM}^*})^2 \frac{D_{Ox}}{D_{Me}} \frac{\partial^2 C^*}{\partial y^2} = 0 \quad \text{for } \delta_{tot}^*(t^*) \geq x^* \geq 0 \quad (3-25)$$

$$\frac{\partial C^*}{\partial t} - \frac{\partial^2 C^*}{\partial y^2} = 0 \quad \text{for } L^*(t^*) > x^* > \delta_{tot}^*(t^*) \quad (3-26)$$

Let

$$D_{Ox}^* = \frac{1}{m^2} \left(1 + \frac{K_r^*}{V_{OM}^*}\right)^2 \frac{D_{Ox}}{D_{Me}} \quad (3-27)$$

$$D_{Me}^* = 1 \quad (3-28)$$

Then the governing equation in all phases can be expressed in the same form:

$$\frac{\partial C^*}{\partial t} - D^* \frac{\partial^2 C^*}{\partial y^2} = 0 \quad (3-29)$$

The boundary conditions are analyzed as below. On the outer surface,

$$C^* = 1 \quad \text{at } y = 0 \quad (x^* = 0) \quad (3-30)$$

At the interface between the oxide and the metal material,

$$C^* = C_{OM}^* \quad \text{at } y(x^* = \delta_{tot}^{*-}(t^*)) = \frac{1}{m} \delta_{tot}^{*-}(t^*) + \frac{K_r^*}{m} t^* \quad (3-31)$$

$$C^* = C_{MO}^* \quad \text{at } y(x^* = \delta_{tot}^{*+}(t^*)) = \frac{1}{m} \delta_{tot}^{*+}(t^*) + \frac{K_r^*}{m} t^* \quad (3-32)$$

At the end of the specimen,

$$-D_{Me}^* \frac{\partial C^*}{\partial y} = 0 \quad \text{at } y(x^* = L^*(t)) = 1 \quad (3-33)$$

In order to solve the above equation numerically, the function  $D^*$  of  $C^*$  is extended from 0 to the maximum value of the concentration at the outer surface. The value of  $D^*$



is set to zero in the unphysical interval of  $C^*$  between  $C_{OM}^*$  and  $C_{MO}^*$ . By this extension, the Eq. (3-29) is now regarded as a nonlinear diffusion equation without restriction on the value of  $C^*$ . With this extension, the interface condition of the conservation of oxygen to join the governing Eqs. (3-2) and (3-3) now can be ignored.

A Kirchhoff transformation technique is applied by introducing [80],

$$Z = \int_0^{C^*} D^*(l) dl \quad (3-34)$$

The relation of  $Z$  and  $C^*$  can be shown in Figure 62. Therefore, a dimensionless equation can be obtained,

$$\frac{\partial C^*}{\partial t^*} = \frac{\partial^2 Z}{\partial y^2} \quad (3-35)$$

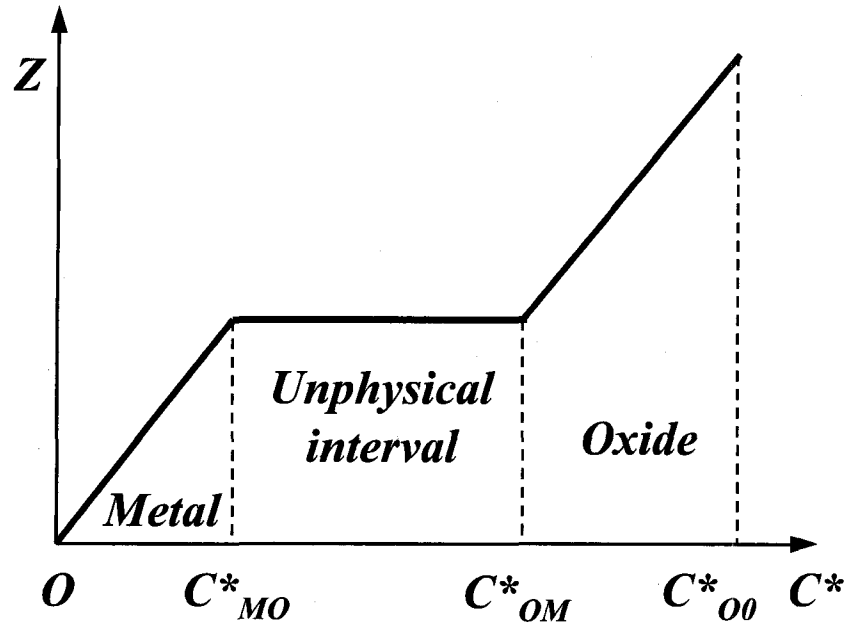


Figure 62. The function  $Z(C^*)$  with unphysical interval of  $D^* = 0$ .

In this form, the diffusion problem is analogous to the Stefan problem in the enthalpy formulation. [80]

$$\frac{\partial H}{\partial t} = \frac{\partial^2 T}{\partial y^2} \quad (3-36)$$

Where  $H$  is the specific enthalpy and  $T$  is the temperature. In the phase change region, the specific latent heat keeps the temperature at a constant value, which is analogous to the constant  $Z$  value during the unphysical interval where  $D^*$  is forced to be zero. Obviously, the functions  $Z(C^*)$  and  $T(H)$  have similar behaviors, and numerical methods can be used to solve the analogous Stefan problem.

### 3.4 Methodology

A forward-in-time, center-in-space, finite difference method is adopted for the numerical solutions of Eq. (3-35). An implicit method assures the unconditional stability of the numerical results along with the boundary conditions (3-31, 3-33). The Newton-Raphson's method is adopted for an iterating solution from  $C_{i,n+1}^k$  to  $C_{i,n+1}^{k+1}$ . After arrangement, a system of linear equations for  $C_{i,n+1}^{k+1}$  with tri-diagonal matrix coefficients is obtained and the Tri-Diagonal Matrix Algorithm (TDMA) is used to solve the matrix efficiently.

The normalized  $D^*$  is a function of  $V_{OM}^*$ , thus it is a function of time. The inter surface moving velocity  $V_{OM}^*$  is calculated at each step and is taken into account, together with  $C^*$ , in determining the value of  $D^*$ . Usually  $K_r^*$  is a very small value in real cases. When  $K_r^*$  is much smaller than  $V_{OM}^*$ , the scale removal effect can be neglected during the

calculating procedure of the diffusion equations for each time step. However, the scale removal effect impacts the solutions through the removal of oxide from a previous step to the next step, since the coordinate is adjusted each step after removal. This simplification is valid especially for a slow scale removal case or for a fast oxidation case. In these cases where  $D_{Ox}^*$  is not a function of time, the calculation time is decreased greatly by this simplification. In a simple inner oxidation model for pure metal materials,  $m = B/r$ , where B is the Pilling-Bedworth ratio.

### 3.5 Results and Discussions

To prove the validity of the proposed macroscopic model, simulations are conducted based on the diffusion controlling model. The calculated results are benchmarked with some previous work with a different metallic material. Also, the present model is benchmarked with experimental data on oxidation of stainless steel in LBE. In the end, duplex oxide layer growth will be studied from this model.

#### 3.5.1 Benchmark 1: Oxidation of Pure Zirconium without Scale Removal

This new oxidation model is benchmarked with both the experimental data and the numerical results from reference [80, 83]. In this simple model, the inner oxidation process is considered for pure zirconium without scale removal in a short time span of 460 seconds. The weight gain is calculated and a good agreement is obtained with the published results, as shown in Figure 63. Actually, the weight gain calculated by Moalem and Olander [83] using an integral approach with the real value of mass diffusivities of oxygen is much lower than the experimental data. The numerical results of Moalem and Olander [83] shown in Figure 63 were obtained by multiplying the diffusivities of oxygen

by four. Obviously, the present model and Wong's model [80] show advantages in estimating the weight gain of zirconium than Moalem and Olander's numerical model [83]. The weight gain increases quickly at the initial stage and slows down gradually during the oxidation process.

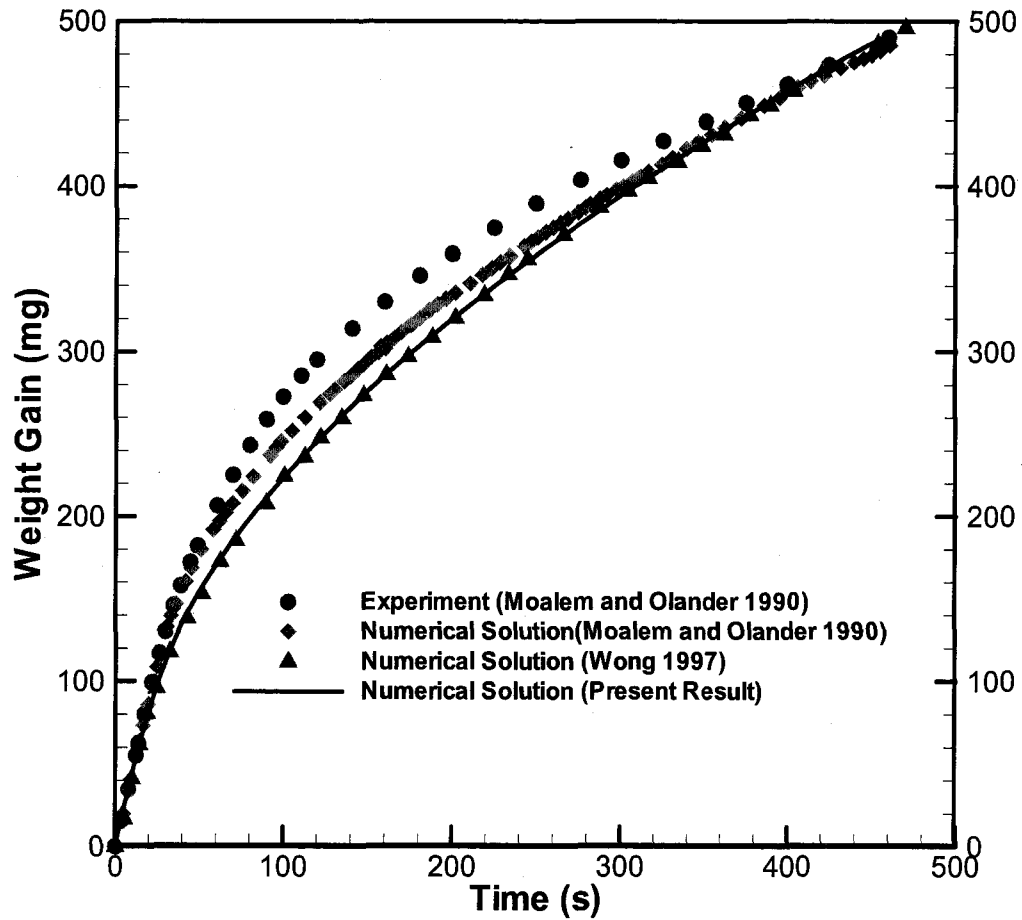


Figure 63. The weight gain with time for the oxidation of pure zirconium without scale removal.

### 3.5.2 Benchmark 2: Oxidation of Pure Titanium

Ding [82] proposed a model in which the oxidation of titanium was calculated. In Ding's model, only the diffusion equation of oxygen was solved and the volume of titanium will be replaced by the titanium dioxide simply.

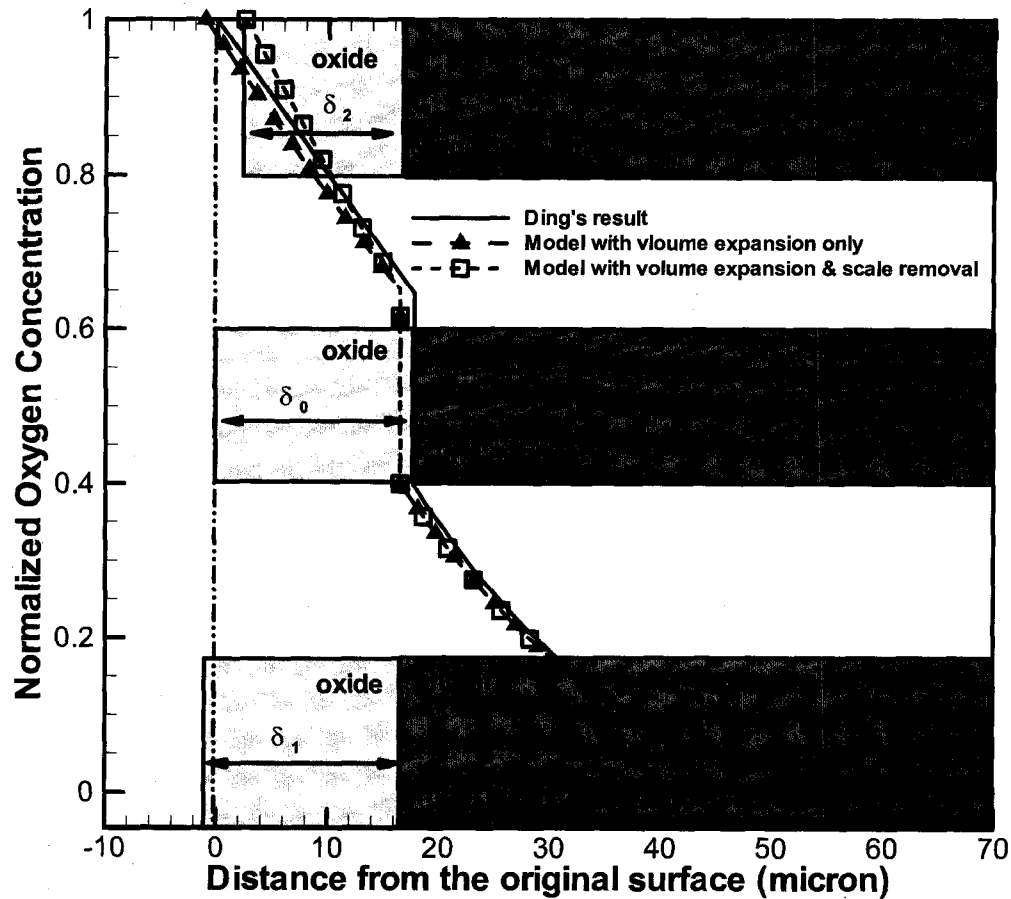


Figure 64. Distribution of the oxygen concentration at time  $t=0.5h$  ( $K_r=2 \times 10^{-9}$  m/s for the scale removal model).

Figure 64 shows the comparison of the model, considering both volume expansion and scale removal, the model considering volume expansion only, and Ding's model. In Ding's result, an oxide layer of thickness  $\delta_0$  is formed in a time interval of 0.5 hours. The

layer of titanium dioxide replaces the same thickness of the consumed titanium in volume. In the first new model that considers the volume expansion, the inward movement of the inner surface and the outward movement of the outer surface are observed in the oxide layer. The thickness of oxide layer  $\delta_1$  is larger than  $\delta_0$ , for the reason of volume expansion. In the model that considers both volume expansion and scale removal, a thickness decreasing in the oxide layer is observed. It should be noted, that the thickness of oxide layer  $\delta_2$  can be larger than  $\delta_0$ , when the oxide growth rate is larger than the scale removal rate. To benchmark the new model, input data for the oxidation of titanium were used from Ding's model, and the results were compared with Ding's solutions. From Figure 64, the calculated results agree very well with Ding's calculation, and the proposed models show advantages in considering volume expansion and scale removal effect.

### 3.5.3 Benchmark 3: Oxidation of Stainless Steel in LBE

The oxidation problem of stainless steel in LBE has been studied for years as a challenging research topic to mitigate the LBE corrosion on the stainless steel. [3, 10, 21, 26, 27, 43, 74] As reported in Ref [43], at a temperature of 743K, specimens of US martensitic steel, Batman 28, were tested in flowing LBE. The flow velocity was  $1.9 \pm 0.1 \text{ m/s}$ , and the oxygen concentration was maintained at  $(1-2) \times 10^{-6} \text{ wt\%}$ . The oxidation layer thickness was measured to be  $12 \mu\text{m}$ ,  $15 \mu\text{m}$ , and  $17 \mu\text{m}$  after 1,000, 2,000, and 3,000 h of exposure, respectively. Applying a constant scale removal rate  $K_r = 7.0 \times 10^{-13} \text{ m/s}$  [27], the oxide layer thickness is calculated and compared with the experimental data. From Figure 66, the numerical results from the present model agree with the experimental data.

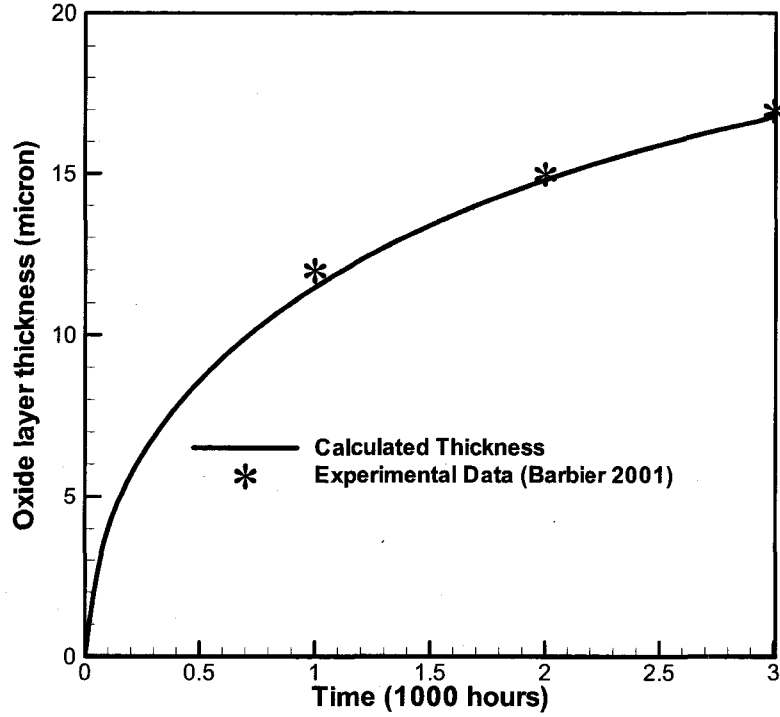


Figure 65. Benchmark with the experimental data.

#### 3.5.4 Parametric Study

The oxide layer thickness is studied for different values of normalized parameters  $D_{Ox}^*$ ,  $m$ , and  $K_r^*$ . From Eq. (3-13.c), the unity of  $t^*$  corresponds to a very large time scale, since  $D_{Me}$  has a much smaller value than  $L_0^2$  in the same unit system. So the cases are shown only for the normal time  $t^*$  from 0 to 0.1. Figure 6 shows that the oxide layer grows following a parabolic tendency, and the thickness increases faster with a smaller value of  $K_r^*$  with  $D_{Ox}^* = 0.5$  and  $m=1.5$ . The case of  $K_r^* = 0$  is for the oxidation process without scale removal. From figure 6, it is found that the oxide layer keeps growing unless a high scale removal exists. The growth rate of the normalized thickness is very high at the initial stage as well, which will drop down with time increases. For a case

with  $K_r^* = 1.0$ , the thickness of the oxide layer approaches a constant value after a long time. This means the oxidation is in a dynamic equilibrium with the scale removal, and a protective oxide film with a constant thickness will remain on the surface of the structural metal. In many applications of metal passivation, this is the expected result since erosion will damage the structure and a fast growth of the oxide layer will jam the fluid flow, especially in pipes.

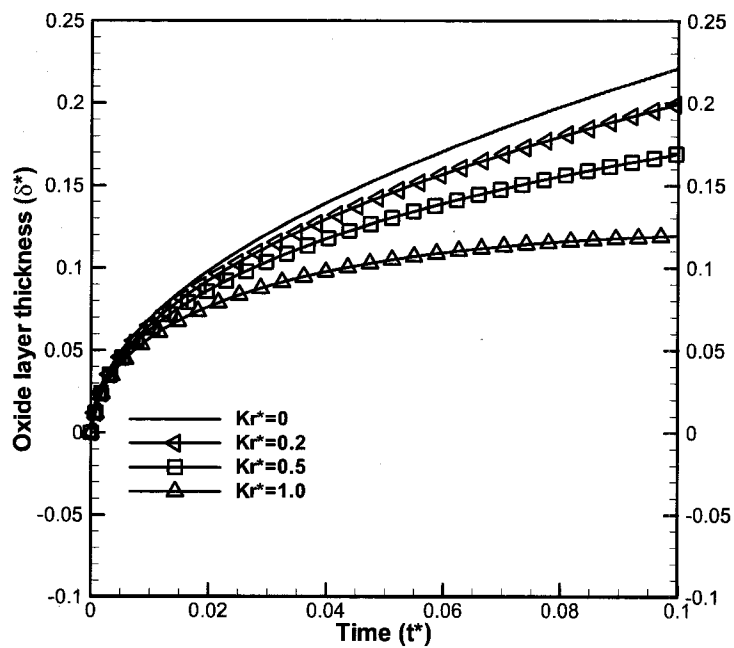


Figure 66. The impact of  $K_r^*$  ( $D_{ox}^* = 0.5$  and  $m=1.5$ ).

Physically  $m$  (expressed in Eq. (3-12)) is a factor which consists of the density change, oxygen absorbing, impurity of the material, etc. Usually,  $m$  is a value larger than unity. The parameter of  $m$  is very important and it controls the developing speed of the oxide layer and the ratio of inner oxide layer thickness to the outer oxide thickness. Figure 67 illustrates how the parameter  $m$  influences the oxide layer growth for cases of



$D_{Ox}^* = 0.5$  and  $K_r^* = 0.2$ . From the comparison, the oxide layer grows obviously faster with a larger value of  $m$ . From the expression of  $m$ , a larger value of the Pilling-Bedworth ratio and a smaller value of  $r$  both lead to a larger  $m$  and hereby cause a faster growth of the oxide layer.

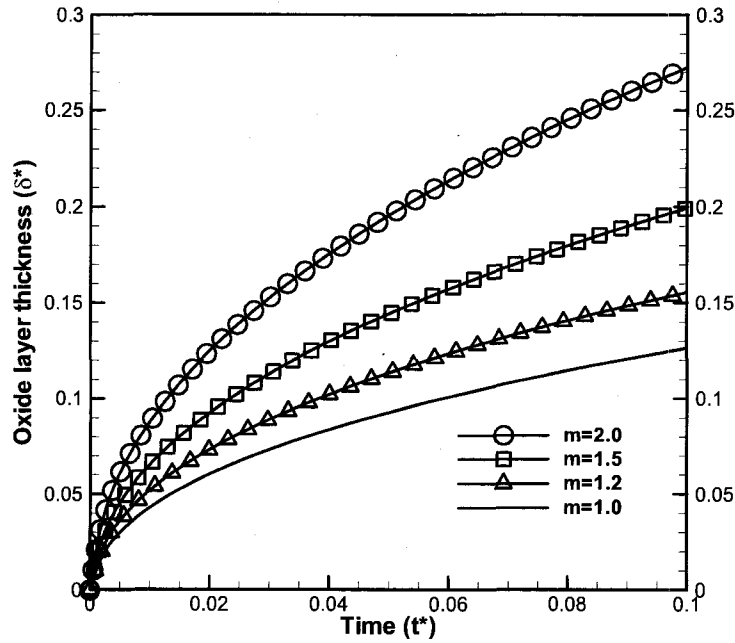


Figure 67. The impact of  $m$  ( $K_r^* = 0.2$  and  $D_{Ox}^* = 0.5$ )

The impact of  $D_{Ox}^*$  is shown in Figure 68, where  $K_r^* = 0.2$  and  $m=1.5$ . With a higher value of  $D_{Ox}^*$ , the oxide layer grows faster. This is understandable since the oxide layer is the main obstacle for the diffusion of oxygen during the oxidation process. With the given value of  $K_r^*$  and  $m$ , the thickness of oxide layer grows very slowly for the case of  $D_{Ox}^* = 0.1$ . When the value of  $D_{Ox}^*$  is enhanced to 0.8, the thickness of the oxide layer reaches about 7 times of the thickness for the case of  $D_{Ox}^* = 0.1$  at  $t^* = 0.1$ .

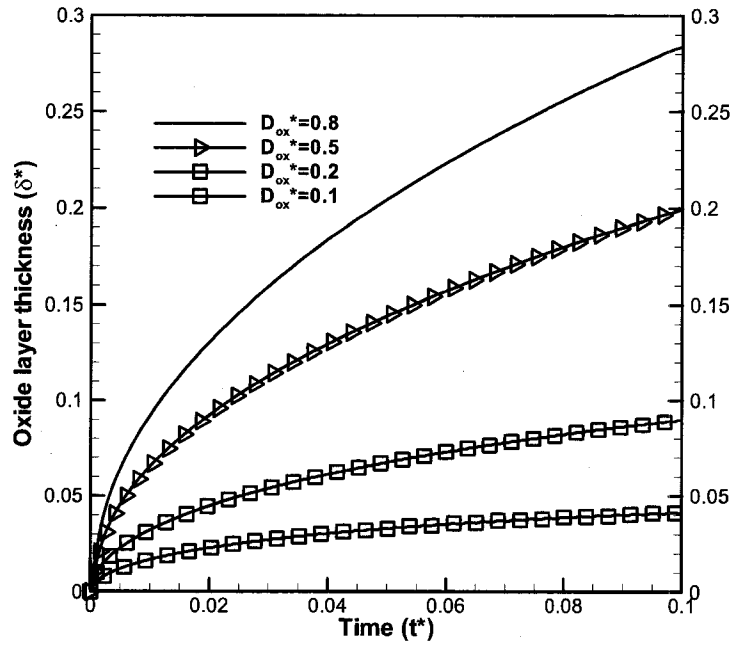


Figure 68. The impact of  $D_{ox}^*$  ( $K_r^* = 0.2$  and  $m=1.5$ ).

In reference [80], the weight of atomic oxygen in oxide was neglected during the derivation in the volume expansion. However, for many metals, the weight of atomic oxygen in oxide is a large proportion of the molecular weight, and it plays an important role during the oxide process. For example, the weight ratio of atomic oxygen quantitates at 0.276 for  $Fe_3O_4$ , 0.260 for  $ZrO_2$ , and 0.400 for  $TiO_2$ . In order to check the impact of the oxygen weight, the weight ratio of metal in its oxide,  $r$ , is studied for the oxidation of titanium. The cases with  $r=1$  neglect the atomic weight of oxygen in  $TiO_2$ . From Figure 69, it is found that the oxide layer keeps growing if there is no scale removal, or if the scale removal rate is low. Similar to the model for zirconium, the growth rate is very high at the initial stage and becomes slower with oxidation processing.

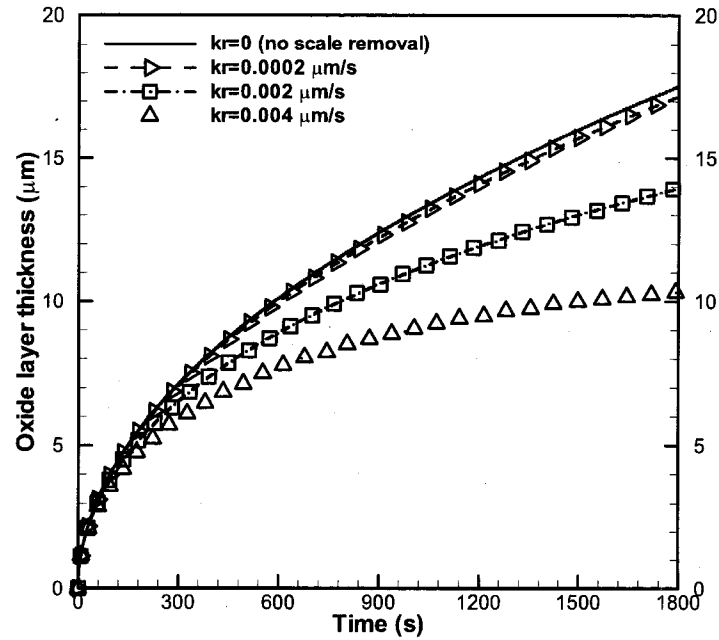


Figure 69. Total oxide layer thickness for  $r=1$ .

In Figure 70, all the cases neglect the atomic weight of oxygen in  $\text{TiO}_2$ . The oxide layer growth for  $r=0.6$ , which considers the impact of the atomic weight of oxygen in  $\text{TiO}_2$ , is examined and the results are shown in Figure 70. Compared with cases in Figure 69, a slower growth rate of oxide layer can be found. For the cases with high scale removal rates, the maximum thickness of the oxide layer is less than the results without considering the atomic weight of oxygen. And erosion occurs much earlier if the atomic weight of oxygen is considered. In Figure 71 and Figure 72, the net volume change of the specimen is shown. A positive value means a net increase of volume, whereas a negative value stands for a net decrease in the total volume. One interesting phenomenon is that the volume increases faster if the atomic weight of oxygen is considered even though the oxide layer thickness grows more slowly. This is because that the atomic weight of oxygen accounts for the volume expansion partly in the oxidation.

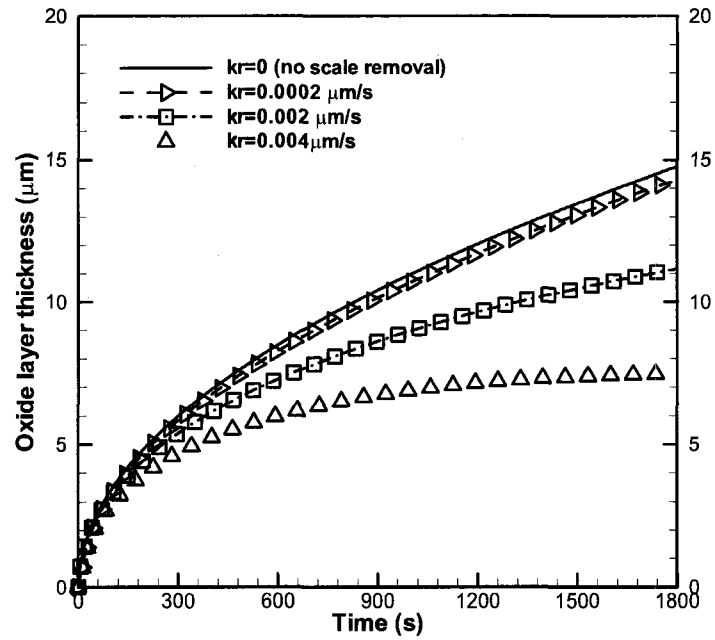


Figure 70. Total oxide layer thickness for  $r=0.6$ .

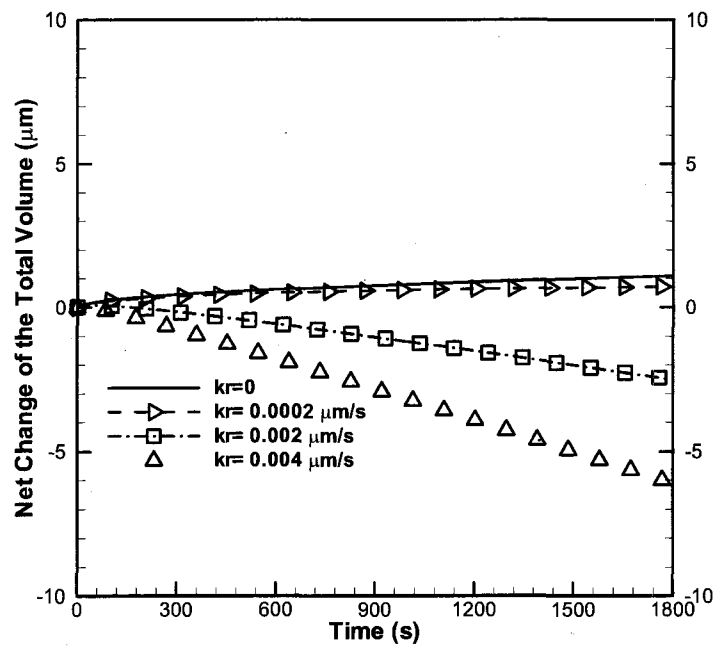


Figure 71. Net change in the total volume for  $r=1$ .

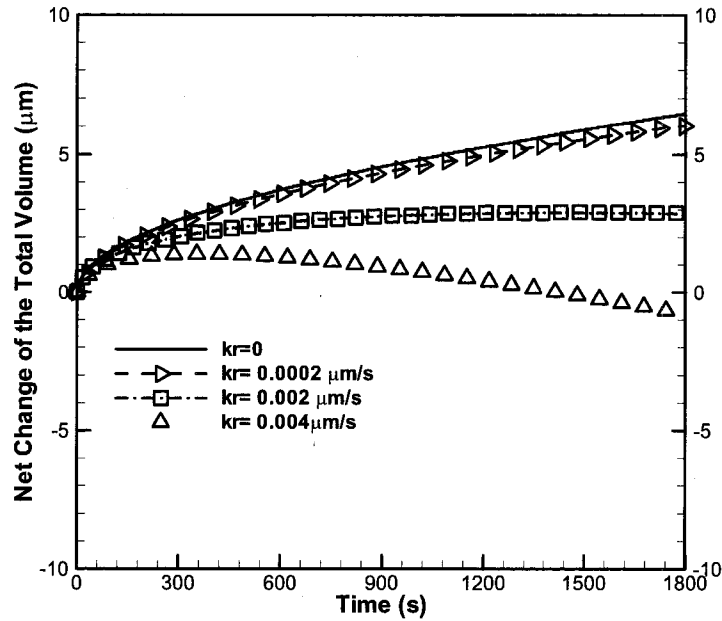
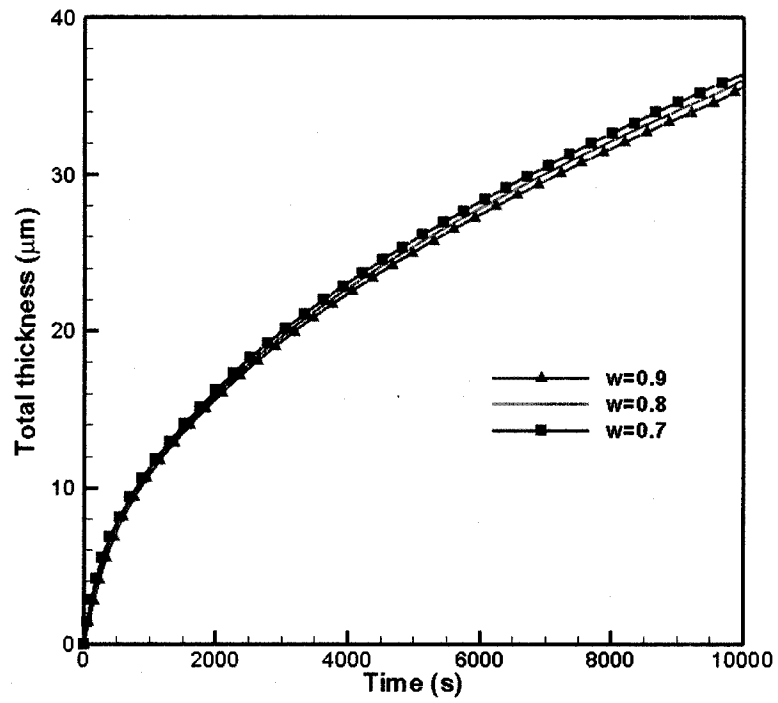


Figure 72. Net change in the total volume for  $r=0.6$ .

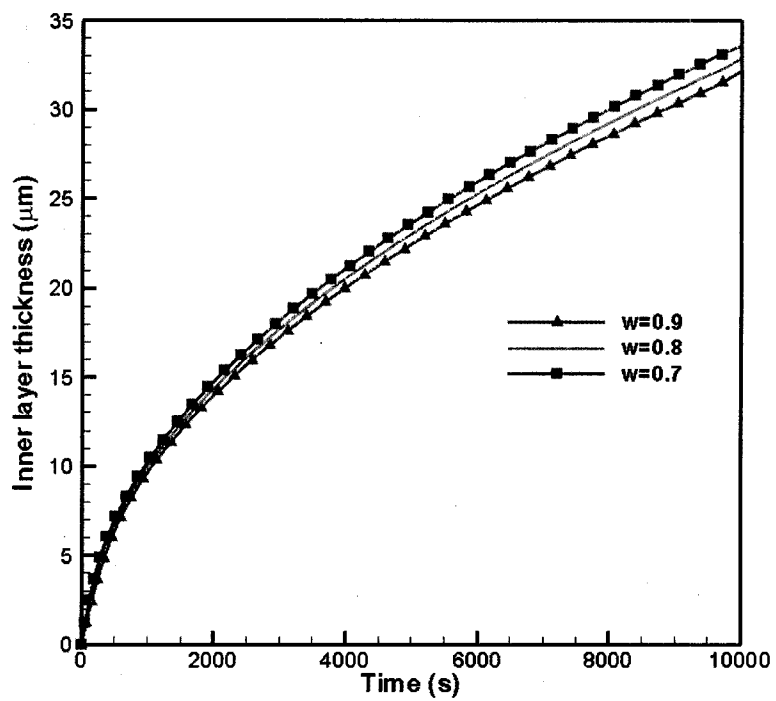
From the comparisons between Figure 69 and Figure 70, and Figure 71 and Figure 72, it can be concluded that the atomic weight of oxygen plays an important role during the oxidation, and it should be considered for a more accurate estimation.

### 3.5.5 Duplex Oxidation Simulation

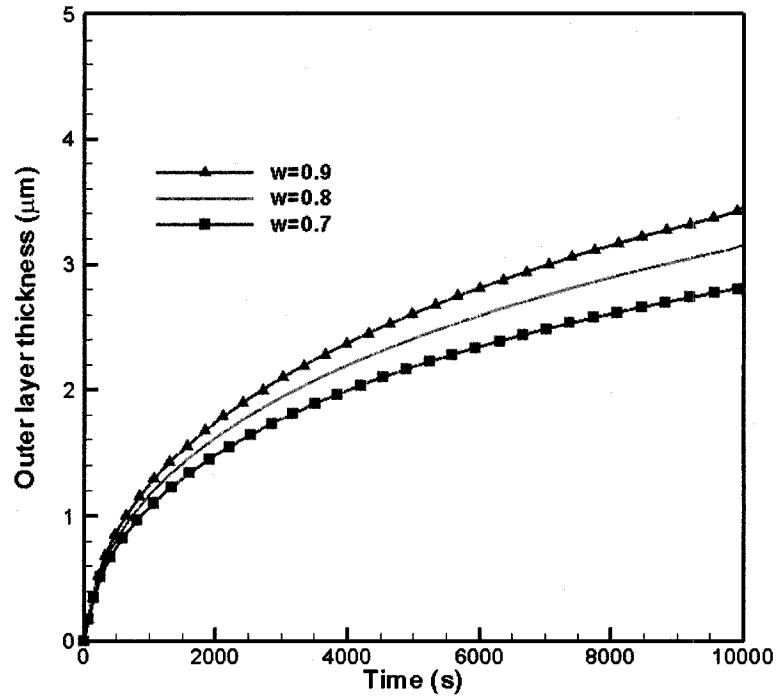
As mentioned earlier, this new model can be employed to estimate the duplex oxide layer growth for impure metal materials or alloys. By studying the two important parameters,  $w$  and  $p$  in Eq. (3-12), the total oxide layer can be analyzed as a sum of the compact inner layer and the porous outer layer after the total oxide layer thickness is calculated. The parameter  $w$  stands for the weight ratio of  $M$  in the structural material, and  $p$  is the ratio of reacted atomic  $M$  out of the total reacted atomic  $M$ .



(a) Total thickness



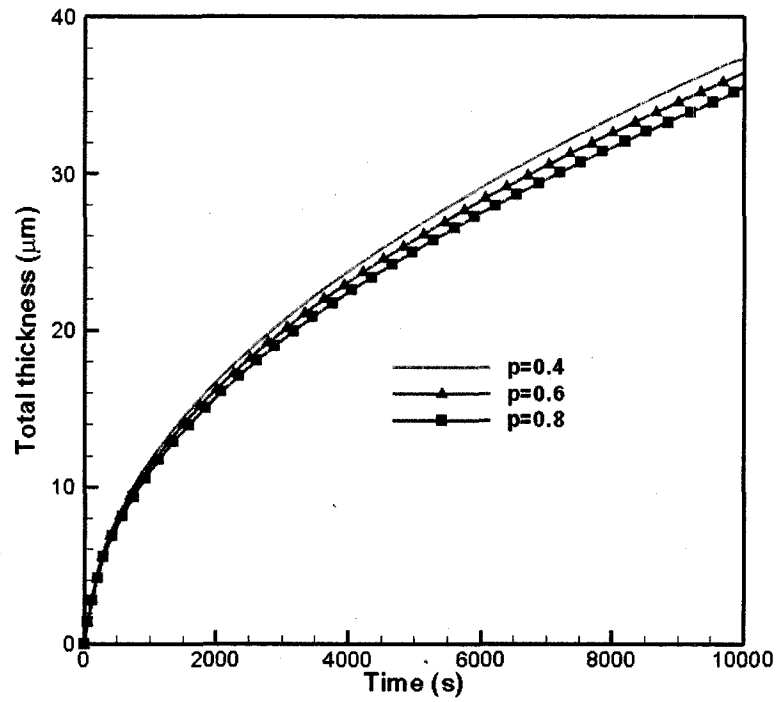
(b) Inner layer thickness



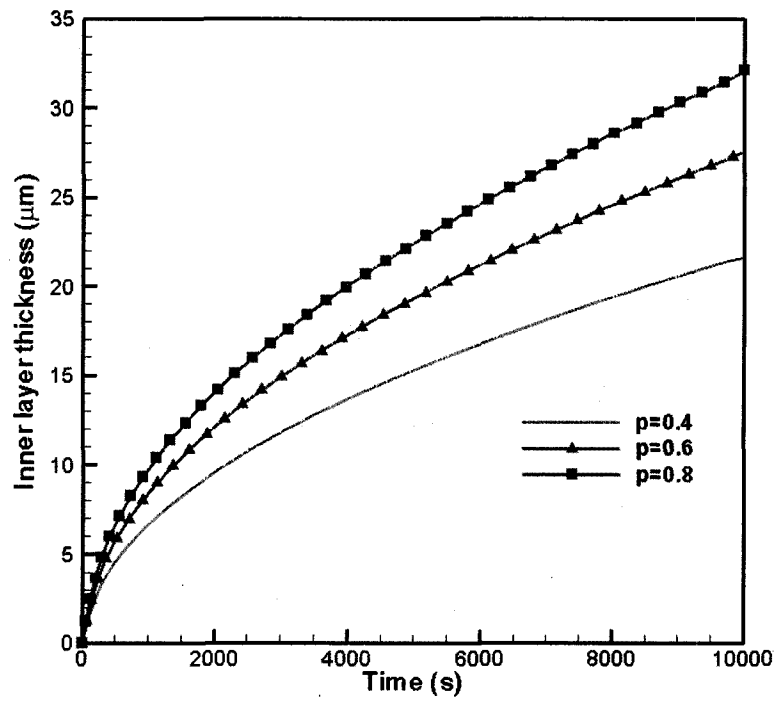
(c) Outer thickness

Figure 73. The thickness of the total oxide layer, the inner oxide layer and the outer oxide layer for different values of  $w$  ( $p=0.8$ ).

Figure 73 demonstrates the impact of  $w$  for the cases with same value of  $p=0.8$ . As it can be found, a high content of the reactive element will lead to a thinner thickness of the total oxide layer. This is because that the remainder of noble elements still occupies the inner layer, and more impurity leads to a faster growth of the inner oxide thickness, even though a high value of  $w$  will show a fast growth of the outer layer. Figure 74 shows the impact of the parameter  $p$  for the same  $w=0.9$ . A larger ratio of the inner action leads to a slower growth of the total oxide layer. Although a larger ratio of the inner action causes a faster increase of the inner oxide layer, a smaller ratio of the inner action accounts for a faster increase of the outer oxide layer. In all these cases, the growth of the oxide layer is observed to follow the parabolic law in both the inner and the outer directions.

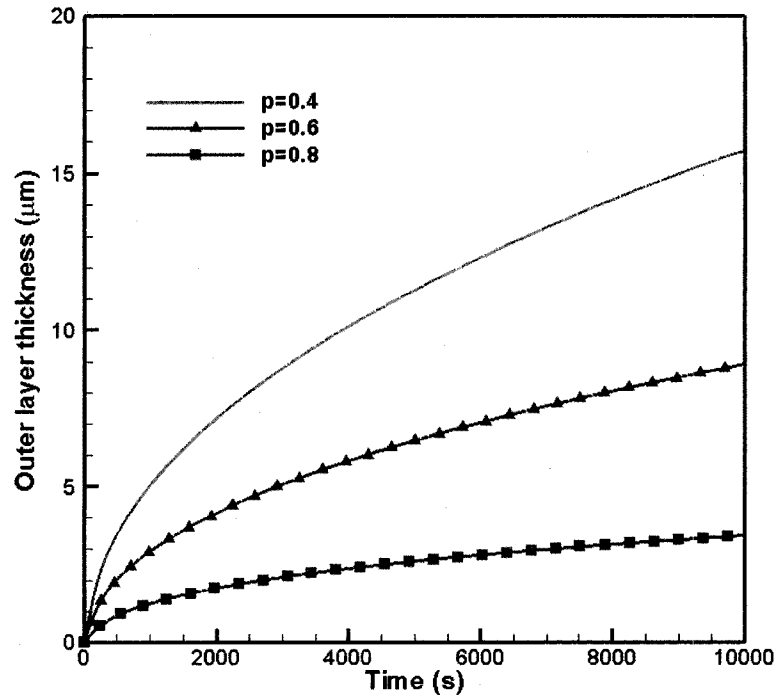


(a) Total thickness



(b) Inner thickness





(c) Outer thickness

Figure 74. The thickness of the total oxide layer, the inner oxide layer and the outer oxide layer for different values of  $p$  ( $w=0.9$ ).

### 3.6 Conclusions

A diffusion controlling oxidation model, with consideration of scale removal effect, is developed in oxygen containing liquid flow. In this new proposed model, the volume expansion effect caused by density difference, the weight gain caused by oxygen diffusion and chemical reaction were both taken into account. The governing equations are nondimensionalized and analogized with the Stefan problem in heat transfer, with phase change in the enthalpy formulation, and then solved numerically. The model is benchmarked with previous results and the experimental data, and good agreement is obtained. The dimensionless parameters were studied in order to check which one

accounts more for the oxide layer growth. Finally, the duplex oxide layer structure was analyzed for metal-containing impurity or metal alloys. The model demonstrates successfully the growth of oxide layer in two directions, following the parabolic law.

## CHAPTER 4

### AN IMPROVED MESOSCOPIC OXIDATION MODEL OF METALS IN MOLTEN LEAD OR LBE

#### 4.1 Introduction

Corrosion and oxidation of structure material in liquid lead or lead alloys have been the main challenge for the usage of lead or LBE, as an ideal coolant candidate and for other applications, in the nuclear industry [2-10]. In a high temperature liquid metal environment, the dissolution corrosion rate of stainless steels is controlled by the solid diffusion of iron into the molten metal/alloys. The oxidation process is controlled by both the outwards diffusion of iron and the inwards transport of oxygen, which may immigrate along the grain boundaries by some unclear mechanism. [21, 27]

The corrosion and oxidation of stainless steel in molten lead or LBE have been studied from a macroscopic level for years. Some significant results were obtained, and useful information was concluded. However, to study such a problem at a microscopic level, such as from an atomic or molecular point of view, has always been a dream for the scientists and researchers in the field of fluid mechanics, heat transfer, computational fluid dynamics (CFD), etc. However, to study so complex a macroscopic phenomenon at a microscopic level is difficult and time consuming. There is no perfect available microscopic theory to explain and calculate all macroscopic fluid mechanics phenomena.

With the development of modern computers, it becomes possible to simulate a simple fluid problem at a microscopic scale, but still not for such a complex problem in which fluid mechanics, heat transfer, mass transfer, chemical reactions and other phenomenon all are involved.

Therefore, to build a mesoscopic model for the oxidation of metal in lead or LBE environment will be significant and beneficial for the future study of oxidation problems at a mesoscopic scale. To the best of knowledge, there has been no such mesoscopic work yet done, with consideration of the diffusion of metal and transport of oxygen separately. Thus, this is one of the main motivations for this part of the research.

## 4.2 Literature Survey

Usually, the corrosion and oxidation involve several macroscopic processes, e.g., corrosion, precipitation, passivation/depasivation, growth of oxide layer, mechanical stress, etc. Each of these processes may be the result of several processes on a microscopic scale. In addition, all these phenomena take place in ill-defined conditions resulting from the environmental evolutions. [84] At the same time, the combination of these processes may generate different kinds of interfaces.

In the domain of interface growth, there has been much theoretical investigation based on numerical simulations. [85] The Eden model [86] and the Diffusion-Limited Aggregation (DLA or LDA) [87] model represent two basic starting points from which a theoretical description of the growth processes can be elaborated.

The Eden model is the simplest model, which describes a growing cluster of particles. It is a lattice model in which particles are added one at a time randomly to sites adjacent

to occupied sites. [86] A particle on the perimeter of the cluster acquires a new particle on its empty nearest-neighbor sites with equal probability. The DLA model was first proposed by Witten and Sander [87] and further explored in Ref [88, 89]. It is a variant of the Eden model. In the DLA model there are screening effects, which differentiate the exposed perimeter particles from the shadowed ones by assigning them different probabilities. The connection between the Eden model in finite dimensions and the DLA model has been discussed by Plischke and Racz. [90] The DLA model and the Eden model should coincide in infinite dimensions since the excluded-volume effects disappear in a DLA model. This conclusion was proved by Parisi and Zhang. [91] The Eden model was extended by Saunier [84] by introducing a feedback effect of the layer formed onto the corrosion rate, based on the concept of cellular automaton (CA) which has been proposed to study the effect of kinetic parameters involved in the corrosion mechanisms on the corroded surface roughness [84, 92, 93].

No matter how the Eden model and DLA model were explored, they were a simple way in which only the lattices were considered as the reaction sites and diffusion pathway. Thus, the Eden model and DLA model are in the range of “simple models”. For example, even in the extended model of Saunier, only the diffusion of iron was considered. The role of oxygen was neglected and no inner reaction by iron and the inward transported oxygen was considered. However, as discussed in Chapter 1, the transport of oxygen plays an important role in the oxidation of stainless steel in molten lead or LBE. The reactions take place on the oxide/liquid interface, on the steel/oxide interface, and even inside the oxide films as well. Moreover, the transport of oxygen is different from iron and other added alloying elements. The oxygen should be transported

along the grain boundaries, or some other pores and vacancies by some unclear mechanisms. [27] Zhou et al. studied the oxidation process using the improved random walk CA model in an atomic scale. [94-97] However, one of their models' bases is the dissociation of oxides, which takes place at a very high temperature and is not usually involved during oxidation of iron or steel in a molten lead or LBE environment. Moreover, whether the CA model is suit for simple application to atomic level was not proved, since the metal or alloys are usually in different crystal structure instead of simple atomic lattice. The difficulties of movement of each atom are different in a specific crystal. Also, the tendency of the moving direction for each atom is not the same in most real cases. That is, the microscopic movement is nonisotropic at an atomic scale and the random walk model may not be rational. Furthermore, the scale removal effect and fluid conditions were not touched in Zhou's models [94-97]. As reported, the hydraulic conditions, thermal conditions and even the mechanical and thermal stress all have important impact on the corrosion and oxidation of stainless steel in non-isothermal molten lead or LBE coolant systems.

Therefore, it is necessary to build a suitable mesoscopic model for estimating the long term behaviors of stainless steel in the nuclear coolant systems. The proposed improved mesoscopic oxidation model is trying to lay a new base for the future mesoscopic study of corrosion and oxidation of stainless steel in non-isothermal molten lead or LBE environments.

#### 4.3 Methodology

To interpret the transport of oxygen and iron and the reaction processes during oxidation, an improved stochastic CA model is built. In this CA model, four main

processes, the outwards diffusion of iron species across the oxide layer, the inwards transport of oxygen along the grain boundary, the reaction of ionization, and the oxidation reaction between oxygen and iron are simulated at a mesoscopic scale. The diffusion and transport process is simulated by a random walk model. As the beginning of this topic, the model is set up based on a pure metal material (not necessarily to be iron). Since the LBE or molten lead was reported to be turbulent flow, it is reasonable to assume that the concentration of oxygen in the turbulent flow is well mixed. The oxygen atom is assigned randomly at the interstitial sites in the fluid domain at each step of calculation.

In the simulation of random walk model, there are two schemes of sites selection. One is an asynchronous dynamics scheme, in which one random single particle moves at a time. Another one is the synchronous dynamics scheme, in which all particles move at each time. [98] In order to satisfy the physical phenomena, a synchronous dynamics scheme is applied. To make the model work randomly, a number of random selections will be conducted for the random walk model. The number of random selections equal to the total nodes of the calculating domain.

With the help of the present developed model, the research goals are to explore the gross features in the evolution of morphology of the structure material under the liquid lead or LBE environment. Also, the proposed model will lay a base for the further study considering the added alloying components in stainless steel and fluid conditions influence.

#### 4.4 An Improved CA Oxidation Model

Based on the analysis in Chapter 1, the morphology of pure iron under the mechanism of corrosion and oxidation in lead or lead-alloy environment is mimicked by an improved stochastic CA method. In the present proposed model, the simple mathematical model was used to investigate self-organization of oxide and metal in statistical mechanics. A global random walk method is included to characterize the diffusion process of iron and transport of oxygen. With this improved CA oxidation model, a duplex oxide layer growth model is simulated to explain the oxidation mechanism of steels in a high temperature corrosive liquid metal environment.

A cellular automaton is a mathematical idealization that describes the discrete spatial and temporal evolution of complex systems by applying local deterministic or probabilistic transformation rules to the cells of a lattice. [74] A CA model works in discrete time steps. The transport of iron or oxygen and the reactions of cells are governed by special rules. These local rules for many cellular automaton models in materials science can be derived through finite difference formulations of the underlying differential equations that govern the system dynamics at a mesoscopic level. [98] The state determined by the governing rules of a lattice point or an interstitial site is a function of its previous state and the state of its neighboring sites. After each time interval, the variables at each site are updated synchronously. [98]

In order to formulate the cellular automaton model for the simulation of corrosion/oxidation behavior of metal emerged in a liquid lead alloy system, several basic assumptions of the model are made as follows,



(a) In order to describe the gross features of this interface, many of the details at the microscopic level are assumed to be irrelevant [84].

(b) The metal is supposed to be pre-oxidized (only one layer of lattice on the surface of the metal). The direct dissolution of metal in a liquid lead alloy system for the initial stage is neglected.

(c) The LBE flow is turbulent so that the concentration of oxygen is uniform.

(d) The formed oxide layer is insoluble.

(e) There exist micropores or other routes along the grain boundary inside the oxide layer for the transport of oxygen.

(f) The diffusion of iron is in ionic form only, i. e., the atomic iron movement is neglected.

(g) The reaction rate is much faster than the transport rate of oxygen and metal.

The stochastic CA model for the evolution of the structure of an oxide layer with the intrinsic rules could be defined as follows:

(a) In the proposed improved CA model, a square lattice with a width “a (m)” represents a site which will be occupied by metal or oxide in solid phase, or be occupied by LBE in liquid phase. The interstitial sites are routes for oxygen to occupy and transport. (as shown in Figure 75)

(b) The state of each interstitial site can be represented by the site state variable  $Inte_{ij}(t)$  at the site (i, j) at time t. Two possible state values are involved in the present model:

$Inte_0$  denotes the site is not occupied by oxygen (a “vacancy” site);

$Inte_1$  denotes the site is occupied by oxygen (a “occupied” site).

Therefore,

$$Inte_{i,j}(t) \in \{Inte_0, Inte_1\} \quad (4-1)$$

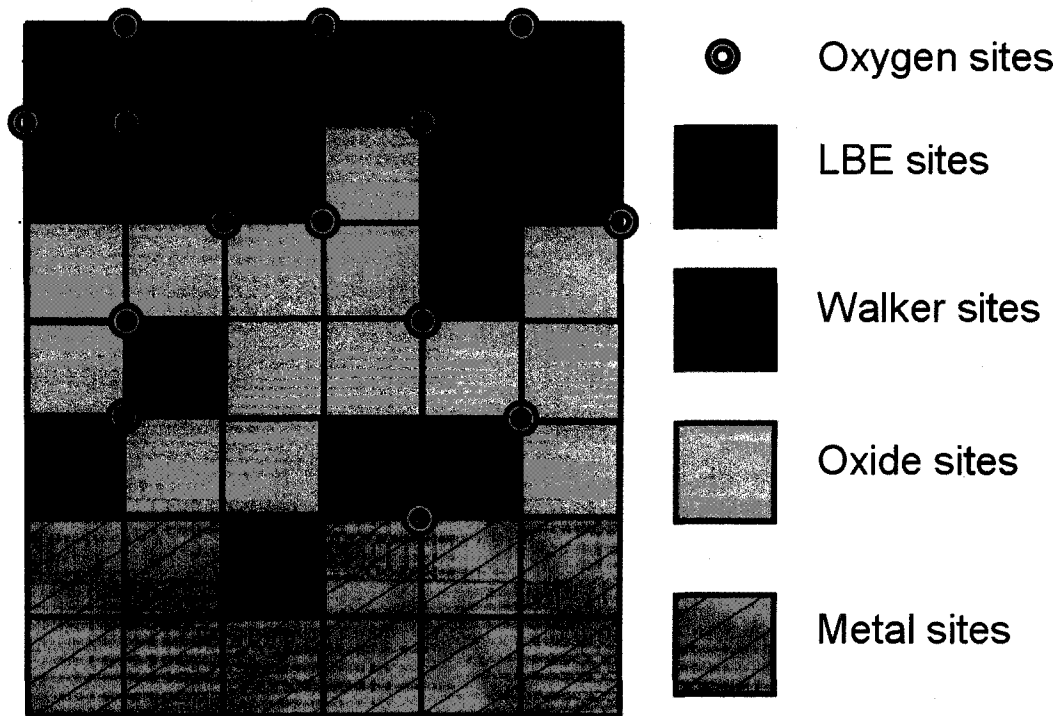


Figure 75. Schematic of CA model of corrosion/oxidation of metal in LBE.

(c) The state of each lattice can be represented by the site state variable  $Lat_{ij}(t)$ , which denotes a different component at the site (i, j) at time t. Four different state values are involved in the present 2-D model:

$Lat_2$  represents the atomic metal site (solid phase);

$Lat_3$  denotes the LBE site (liquid phase);

$Lat_4$  denotes the oxide site (solid phase).

$Lat_5$  denotes the site of oxide with overlapping with ionic metal (solid phase).

Similarly,

$$Lat_{i,j}(t) \in \{Lat_2, Lat_3, Lat_4, Lat_5\} \quad (4-2)$$

(d) Generally, the state of a given site in the next time step will be determined by the state of itself and its neighbors in the previous time step. The control variables can be formulated as follows

$$Inte_{i,j}(t + \delta t) = \Phi_{Inte}(Inte_{i,j}(t), \{Inte_{i,j}^{Nb}(t)\}, \{Lat_{i,j}^{Nb}(t)\}, \varphi_{Inte}) \quad (4-3)$$

$$Lat_{i,j}(t + \delta t) = \Phi_{Lat}(Lat_{i,j}(t), \{Lat_{i,j}^{Nb}(t)\}, \{Inte_{i,j}^{Nb}(t)\}, \varphi_{Lat}) \quad (4-4)$$

where  $\Phi_{Lat}$  and  $\Phi_{Inte}$  are the local evolution rules of cellular automaton for lattice sites and interstitial sites respectively.  $\varphi_{Lat}$ ,  $\varphi_{Inte}$  are the control variables, for lattice sites and interstitial sites respectively.  $\{Lat_{i,j}^{Nb}(t)\}$  are the neighbor lattices and  $\{Inte_{i,j}^{Nb}(t)\}$  are the neighbor interstitial sites of  $Inte_{i,j}(t)$  or  $Lat_{i,j}(t)$ .

For a 2-D square lattice CA model, the following three types of neighborhoods are usually used (as shown in Figure 76 to Figure 78). Figure 76 shows the Von Neumann neighborhood. The Von Neumann neighborhood is a common and popular neighborhood. The neighborhood takes its name from John Von Neumann. Only the northern, southern, eastern, western sites are considered during the simulation. The Moore neighborhood is another type of common neighborhood (Figure 77). The neighborhood takes its name

from the pioneer, Edward F. Moore. Four more neighbor sites, e.g. northwestern, southwestern, northeastern and southeastern, are included during the calculation.

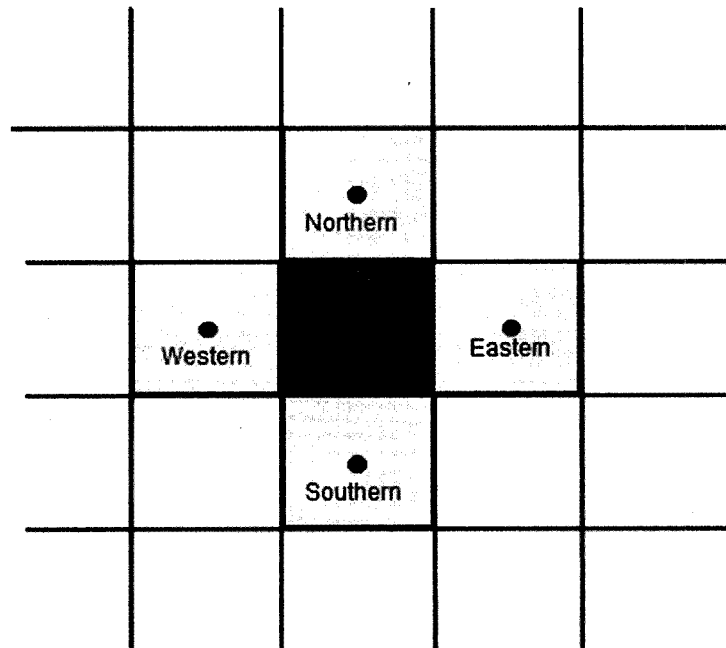


Figure 76. The Von Neumann neighborhood.

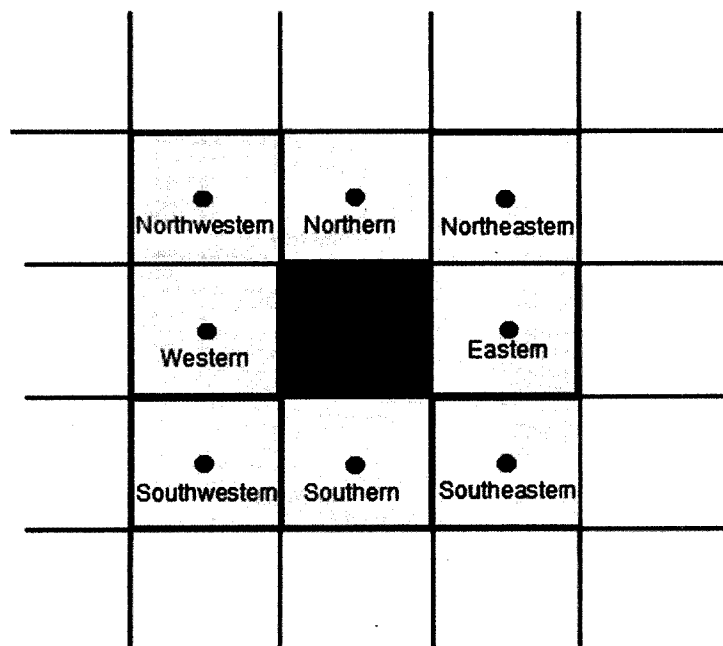


Figure 77. The Moore neighborhood.

The extended Moore neighborhood (Figure 78) takes sixteen more sites into account, which locate at one more lattices away from the objective site. [99]

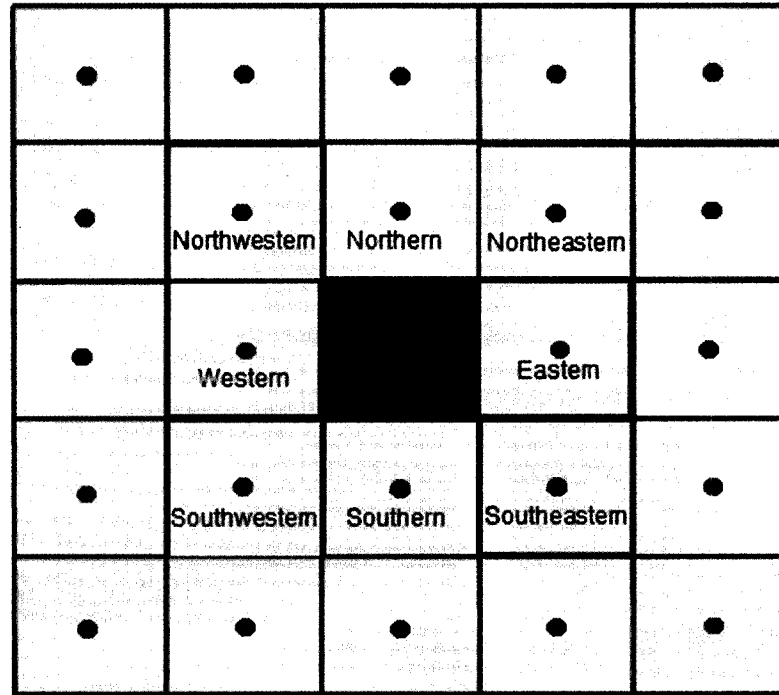


Figure 78. The extended Moore neighborhood.

In this improved oxidation CA model, a neighborhood system with Moore neighborhood system for lattice sites, coupling with four closest interstitial sites, will be applied. For each lattice  $Lat_{i,j}(t)$ , the status of eight neighbor lattices  $\{Lat_{i,j}^{Nb}(t)\}$  (northern, southern, eastern, western, northwestern, southwestern, northeastern and southeastern) and four interstitial sites  $\{Inte_{i,j}^{Nb}(t)\}$  (northwestern, southwestern, northeastern and southeastern) will influence its evolution for the next time step (as shown in Figure 79).

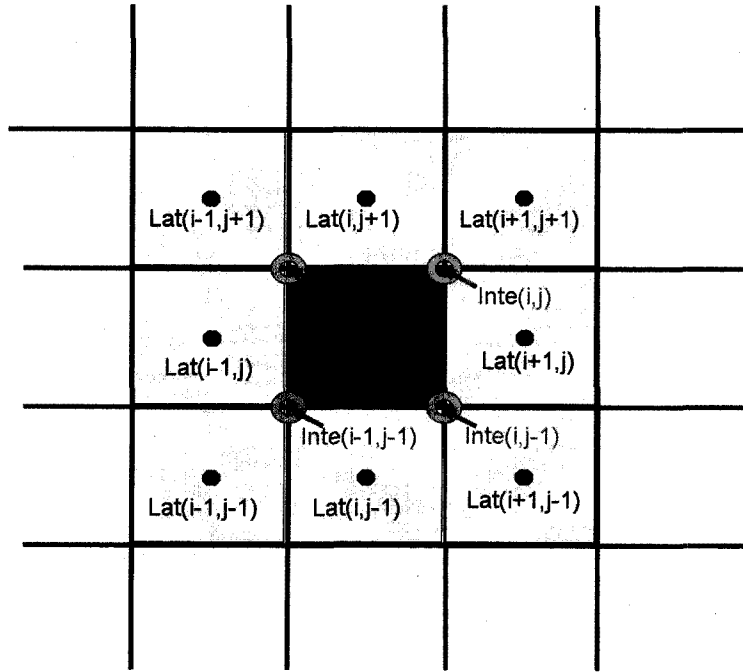


Figure 79. The neighbor lattices  $\{Lat_{i,j}^{Nb}(t)\}$  and interstitial sites  $\{Inte_{i,j}^{Nb}(t)\}$  for lattice  $Lat_{i,j}(t)$ .

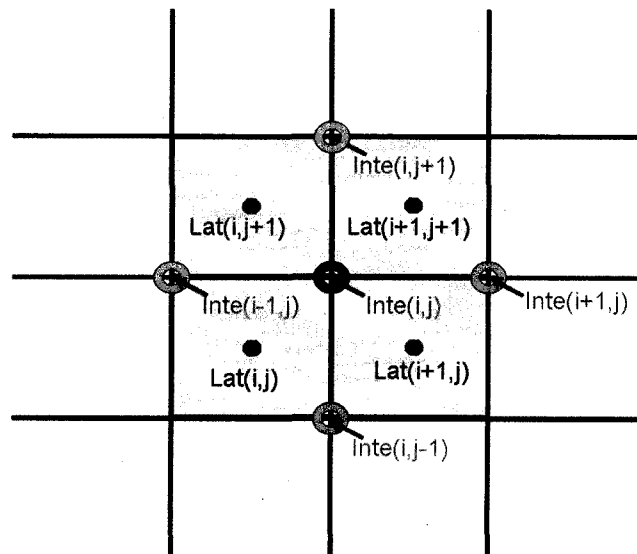


Figure 80. The neighbor lattices  $\{Lat_{i,j}^{Nb}(t)\}$  and interstitial sites  $\{Inte_{i,j}^{Nb}(t)\}$  for interstitial site  $Inte_{i,j}(t)$ .

With this neighborhood system, both the impact of the neighbor element and the close oxygen transported along the boundary will be considered. For each interstitial site  $Inte_{i,j}(t)$ , the status of four neighbor lattices  $\{Lat_{i,j}^{Nb}(t)\}$  (northwestern, southwestern, northeastern and southeastern) and four interstitial sites  $\{Inte_{i,j}^{Nb}(t)\}$  (northern, southern, eastern, and western) will influence its evolution for the next time step (see in Figure 80).

A metal lattice is assumed to contain a number of  $(\varepsilon + 1)$  of metal atoms (M). An occupied interstitial site contains  $\omega$  atoms of oxygen. When the metal lattice is involved in a reaction, one of the  $(\varepsilon + 1)$  metal atoms in the lattice site is consumed and a lattice site of oxide is formed. At the same time,  $\varepsilon$  metal atoms ionize and begin to diffuse outwards. The  $\varepsilon$  ionic metal (W), as a whole lattice overlapping with any oxide lattice site, diffuse through the oxide and react with oxygen when they meet at the oxide/LBE interface. Obviously, the value  $\varepsilon$  is connected to the Pilling and Bedworth factor that corresponds to the molar oxide volume/molar metal volume ratio. The basic rules for this improved oxidation CA model are listed below:

(a) In LBE, the oxygen concentration is kept constant and the oxygen distribution is uniform (randomly distributed for each step).

(b) For a metal site, if none of the four nearest interstitial sites (southwest, southeast, northwest, northeast as shown in Figure 79.) is occupied by oxygen, no oxidation will occur.

(c) For a metal site, if there is one or more of the nearest interstitial sites is occupied by oxygen, a reaction will occur possibly.

(c.1) If none of the eight neighbor sites (southwest, south, southeast, east, northeast, north, northwest, and west as shown in Figure 79) is oxide, no reaction occurs.

(c.2) If one or more of the eight neighbor sites is oxide, the oxidation reaction occurs immediately with a probability,  $P_{act}$ . As mentioned previously, the reaction speed is assumed to be much faster than the diffusion speed of oxygen. One of the oxygen sites is chosen randomly from the nearest interstitial sites for reaction and disappears. The site of metal disappears and an overlapping site of oxide and ionic metal substitutes. The ionic metal site always overlaps with an oxide site and the ionic metal site can diffuse in the oxide layer in any random direction and is called a “walker”. The higher is the value of  $P_{act}$ , the stronger the reactivity of the substrate in contact with oxygen.

(d) In each oxygen transport step, the atomic oxygen transports randomly in four possible directions along the interstitial edge of the lattices in the oxide layer or the metal zone. After each step of transport of all oxygen sites, the metal sites and their neighbors' status are checked again, and the calculation code takes actions following the procedure 3.

(e) After finite steps of transport of oxygen, for example,  $N_{OT}$ , the “walkers” diffuse  $N_{WD}$  steps in the oxide layer. The ratio of transport steps  $K_d = N_{OT} / N_{WD}$  depends on the mass transport rate of oxygen and ionic metal in the oxide layer. Usually the transport rate of oxygen is faster than the diffusion of ionic metal even though the self mass diffusivity of oxygen may be slower. In each calculating step,  $N_{WD}$  steps of “walkers”

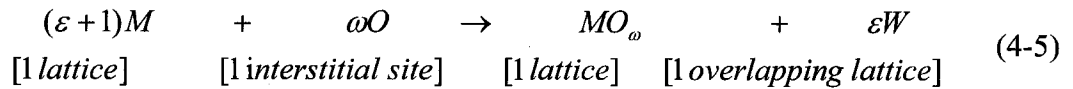


diffusion,  $N_{WD}$  steps of reaction between a walker site with oxygen on LBE/oxide interface,  $N_{OT}$  steps of transport oxygen, and  $N_{OT}$  steps of inner reaction of oxygen with metal will be involved.

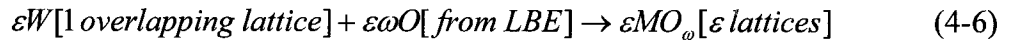
(f) When a “walker” meets LBE, oxidation occurs immediately, since it is assumed the oxygen diffuses very fast in LBE. By controlling the number of the newly formed oxide by an ionic metal lattice (walker), the volume expansion effect can be realized.

(g) The transported oxygen in the metal will walk randomly in the metal domain and cause “noise” in the simulation. They will be eliminated whenever the oxygen site reaches the far end of the calculating domain. Physically, it can be explained by the deposition of oxygen in some pores and vacancies during transport. Furthermore, it makes the far boundary satisfy the Dirichlet boundary conditions.

Therefore, the simulated oxidation reactions are,



and



Eq. (4-5) accounts for the oxidation and ionization at the inner interface of oxide/metal. Eq. (4-6) shows the result of outer surface reaction. The  $\varepsilon \omega$  product of oxygen is of no concern in the LBE domain, since it is assumed that the concentration of oxygen in LBE is constant and enough oxygen can be acquired from the LBE domain. The products  $\varepsilon W$  are in a lattice and overlap with any oxide lattice. If  $\varepsilon$  is assigned a

value of 2, the ideal volume is expanded by about 3 times, since a molecular  $MO_\omega$  is assigned in one lattice.

From the proposed rules, a continuous oxide layer will be formed. The ionization of metal will take place in the oxide/metal interface and oxidation occurs on both the liquid/oxide and oxide/metal interface, which accounts for outer oxidation and inner oxidation in the formation of a duplex oxide layer. The volume expansion effect can be realized by control the parameter of  $\varepsilon$ . The ideal volume expansion rate (the oxide layer volume by the consumed metal volume) is  $(\varepsilon + 1)$ .

In summary, the present model contains three explicit parameters:  $\varepsilon$ ,  $P_{act}$  and  $K_d$ . The volume control parameter  $\varepsilon$  is set to be unity in this dissertation, as an initial work of the mesoscopic model. The diffusion step number of “walkers”,  $N_{WD}$ , is set to be unity as well. Therefore, in each calculating step, one step diffusion of “walker” and  $K_d$  steps of transport of oxygen are involved.

#### 4.5 Results and Discussions

To save computational time, a two-dimensional domain with square lattices, considering the interstitial sites is employed for simulations. The mesoscopic model is first benchmarked with a pure diffusion problem. Later on, the chemical reactions and transport process of oxidation and iron are simulated and the results are mapped with some experimental data. A parametric study and result analyses are included as well.

#### 4.5.1 Benchmark the Pure Diffusion Process without Reaction

The first step of this work is to study the transport of oxygen, in which no reaction takes place. The transport of oxygen follows the diffusion equation. For a diffusion equation:

$$\frac{\partial u}{\partial t} = \frac{1}{2} \frac{\partial^2 u}{\partial x^2} \quad \text{with} \quad \begin{cases} u(0, t) = 0 \\ u(1, t) = 1 \\ u(x, t) = 0 \text{ (when } x \neq 1) \end{cases} \quad (4-7)$$

Eq. (4-7) can be solved analytically using Fourier series and the result is obtained as,

$$u(x, t) = x + \sum_{n=1}^{\infty} [(-1)^n \frac{2}{n\pi} \exp(-\frac{n^2 \pi^2}{2} t) \sin n\pi x] \quad (4-8)$$

And the steady state solution is expressed simply as,

$$u(x, t) = x \quad (4-9)$$

To benchmark this diffusion problem, the partial difference equation (4-7) was simulated in a square domain of 1000 by 1000 grids where the mesh is uniform. Since neither the diffusion of metal nor chemical reaction is involved in this simple problem,  $K_d$  is set to one to make the diffusion steps equal to the calculating steps ( $N_t$ ). The calculated particle concentration distributions for different time steps are show in Figure 81. As it can be found, the concentration distribution approaches to a steady solution with time steps increasing. After the calculation step exceeds 15,000 steps, no significant difference is observed.

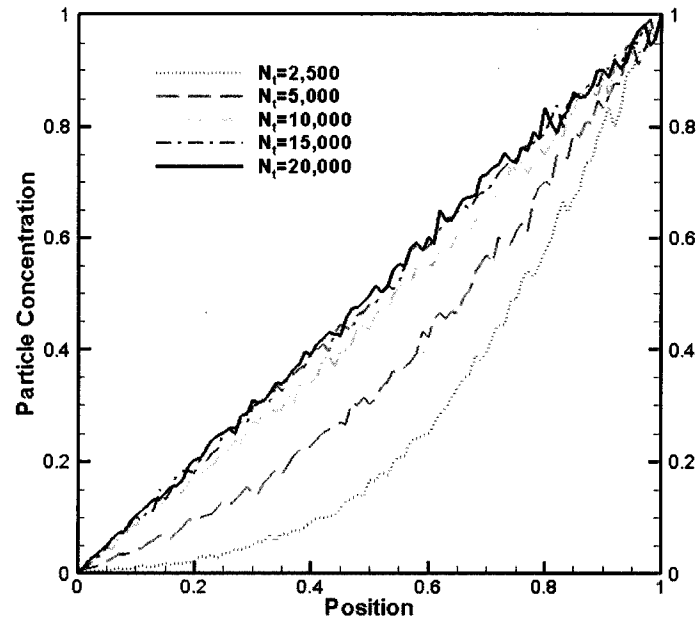


Figure 81. Particle concentration distributions for different time steps.

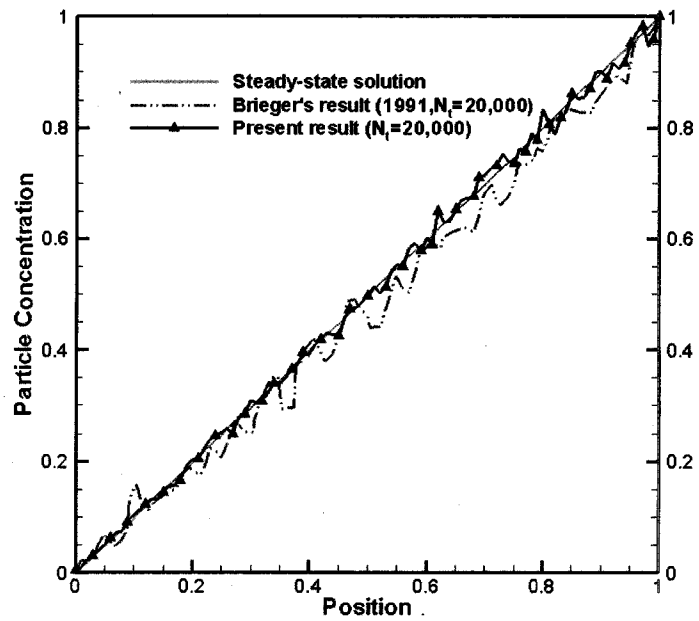


Figure 82. Benchmark of the results from the present model with the analytical solution and Brieger's result [98].

It was also proven that the concentration distribution profile of oxygen sites becomes smoother if the grids number of the calculation domain was increased. For benchmark, the calculated concentration of oxygen sites at 20,000 steps from the present model is compared with the steady-state solution and Brieger's result [98]. It can be seen that the result from the proposed model is in good agreement with the steady state solution and Brieger's solution (see Figure 82). The benchmark shows the proposed CA model satisfies the anticipated estimate of the transport of oxygen at a mesoscopic level.

#### 4.5.2 Oxidation Process with Transport of Oxygen and Metal

The whole oxidation process considering the ionization of metal, diffusion of ions, transport of oxygen along the grain boundaries, and oxidation reaction is simulated. First, the process is simulated with a square domain of 500 by 500 grids, with mesh size of  $a(m)$ . The concentration of oxygen in LBE is set at 0.2 and the reaction probability  $P_{act}$  is assigned a random value of 0.5. The mass transport ratio  $K_d$  is set at 2, in which oxygen sites transport 2 steps after each diffusion step of the ionic metal sites. Hence,  $N_{WD} = N_t$  and  $N_{OT} = 2N_t$  base on the input values for the parameters.

After  $N_t = 10,000$  steps (calculating steps), the snapshot of the simulated mesoscopic structure is shown in Figure 83. In order to make the snapshot clear, the interstitial oxygen sites are not shown here. It can be found that the oxide layer grows inwards and outwards at the same time, since the volume expansion effect is considered. After 10,000 steps, the consumption of the metal is about 45  $[a(m)]$  (45 lattice width) and the inner oxide layer front reaches the location of 215  $[a(m)]$  of the domain. At the same time, the outer oxide layer front reaches about 275  $[a(m)]$  and the outer oxide layer volume growth

is about 25 [a(m)]. The metal ions (the walkers) can be observed moving outwards and the concentration of the “walkers” are decreasing from the inner interface to the outer interface.

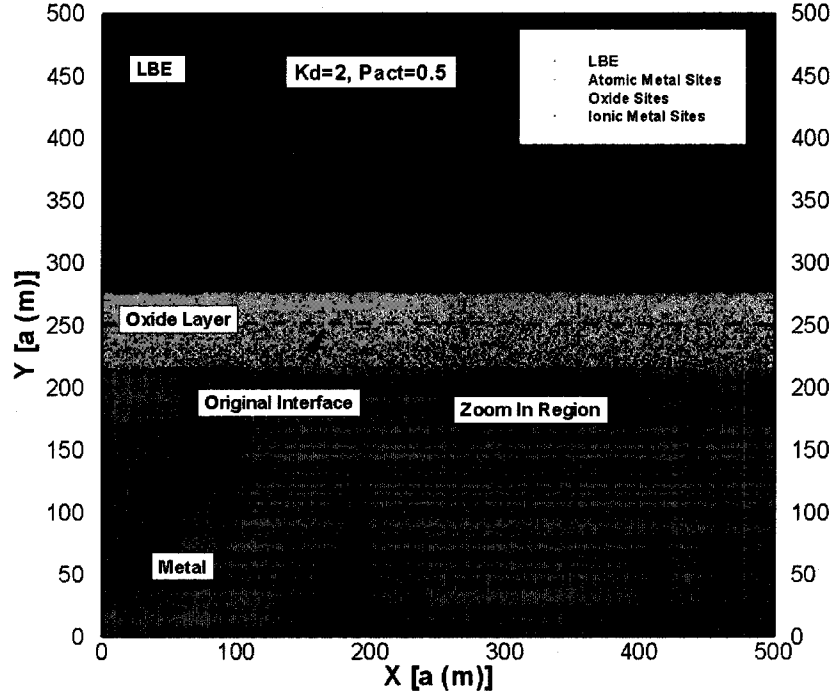


Figure 83. The snapshot of the simulated mesoscopic structure after  $N_t = 10,000$  steps.

However, as mentioned above, the volume control parameter  $\varepsilon$  is set to be unity. Therefore, the oxide layer volume after expansion should be equal to twice that of the consumption volume of the metal. But the volume expansion rate is less than 2, by observation. The reason for this interesting phenomenon is that the “walkers” do not occupy any volume during the process because they are assumed to overlap with oxide sites. The volume expansion effect is realized by the reaction of walkers and the oxide in LBE domain. Therefore, if a continuous oxidation (before the moment when the whole

metal is consumed) is considered, the volume expansion rate is always less than the ideal value ( $\varepsilon + 1$ ).

After zooming in for a small region from Figure 83, the transport processes of oxygen and ionic metal in the oxide layer can be observed more clearly. The oxygen sites transport towards the metal, since the concentration of oxygen in LBE is set at a constant value (0.2) and the metallic ions (“walkers”) diffuse outwards at the same time because ions are produced at the oxide/metal interface. The dashed line shown in Figure 83 and Figure 84 stands for the original location of the interface of metal and LBE.

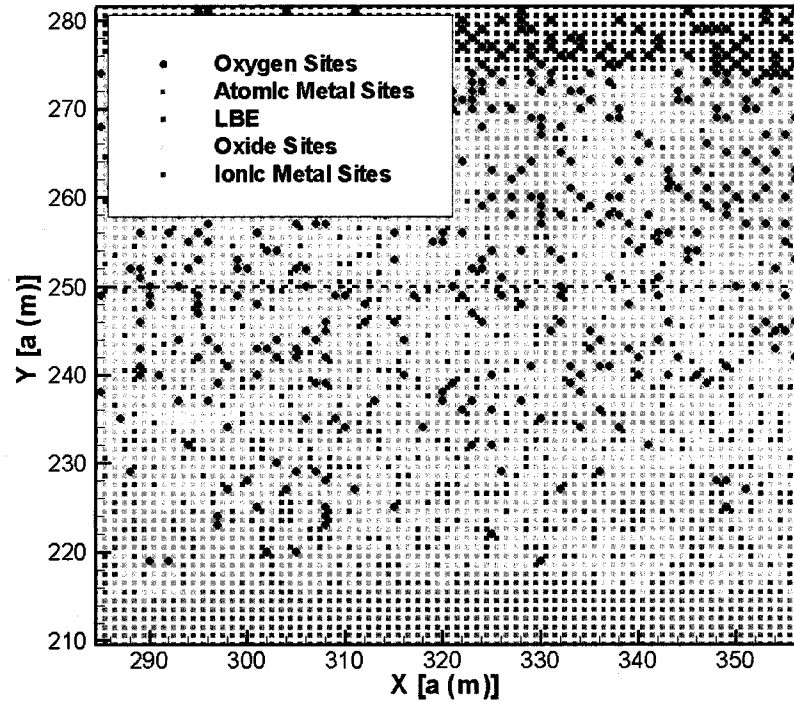


Figure 84. The zoom in view of the simulated mesoscopic structure of oxide layer after

$$N_t = 10,000 \text{ steps.}$$

The mean concentration of “walkers” in the oxide layer is calculated by,

$$\overline{C_{wa,j}} = \frac{1}{N} \sum_{i=1,N} IW_{i,j} \quad (4-10)$$

where,

$$IW_{i,j} = \begin{cases} 1 & \text{if } Lat_{i,j}(t) = Lat_s \\ 0 & \text{if } Lat_{i,j}(t) \neq Lat_s \end{cases} \quad (4-11)$$

N is the lattice number in x direction. The concentration distributions of “walkers” in the oxide layer for different calculating steps are shown in Figure 85.

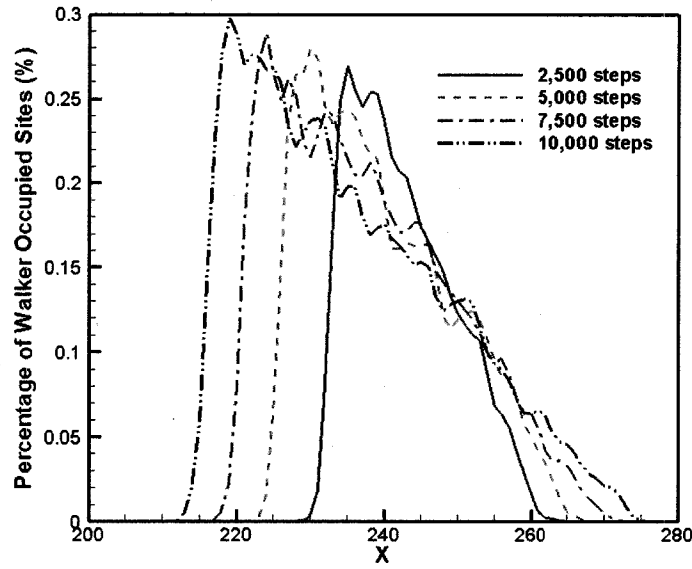


Figure 85. The walker concentration in the oxide layer.

The concentration of “walkers” in the oxide layer is calculated by,

$$\overline{C_{oxy,j}} = \frac{1}{N+1} \sum_{i=0,N} IO_{i,j} \quad (4-12)$$

where,



$$IO_{i,j} = \begin{cases} 1 & \text{if } Inte_{i,j}(t) = Inte_1 \\ 0 & \text{if } Inte_{i,j}(t) = Inte_0 \end{cases} \quad (4-13)$$

N+1 is the interstitial nodes number in x direction. The concentration distributions of oxygen sites in the oxide layer for different calculating steps are shown in Figure 86. From the figure, it can be found that the concentration of oxygen in LBE domain is fluctuating around 0.2, the set value, since this is a stochastic random model. If the mesh is refined to a very large number of lattices, a flatter curve will be observed in LBE domain. However, a finer mesh will increase the calculating time greatly. The concentration of oxygen decreases in the oxide layer and reaches a small value (close to zero) in the metal domain. Since the large value of concentration locates in the LBE domain and is around 0.2, and the small value locates in the metal domain and is close to zero, the cross of the concentration curves can be observed with the growth of the oxide layer in two directions.

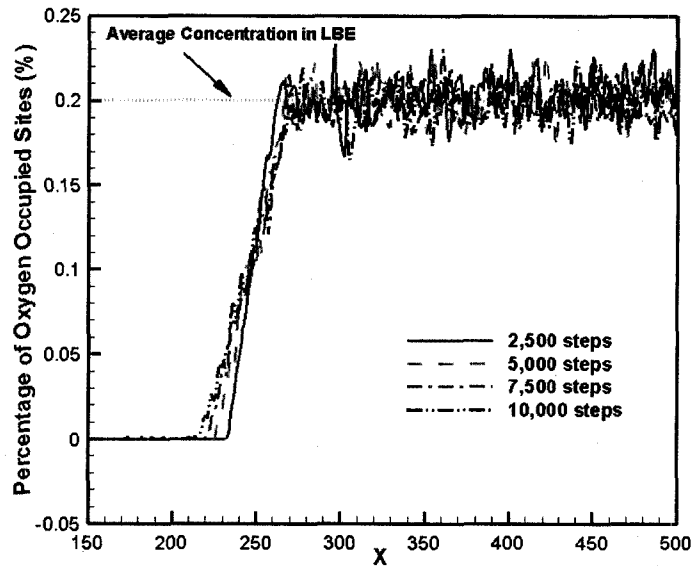


Figure 86. The oxygen concentration for different calculating steps.

To characterize the evolution of the front positions of oxide/metal interface, the inner layer thickness based on the mean position of the interface of oxide/metal interface is introduced,

$$\delta_{N,in} = \frac{1}{N} \sum_{i=1,N} (Y_0 - Y_{Ox\_Min}(i)) \quad (4-14)$$

where,  $Y_0$  is the original interface of metal/LBE, and  $Y_{Ox\_Min}(i)$  is the minimum position of the oxide site in Figure 83. Similarly, the outer layer thickness is defined as:

$$\delta_{N,out} = \frac{1}{N} \sum_{i=1,N} (Y_{Ox\_Max}(i) - Y_0) \quad (4-15)$$

where,  $Y_{Ox\_Max}(i)$  is the maximum position of the oxide site in Figure 83. The total thickness of the oxide layer is defined by,

$$\delta_{N,tot} = \delta_{N,in} + \delta_{N,out} \quad (4-16)$$

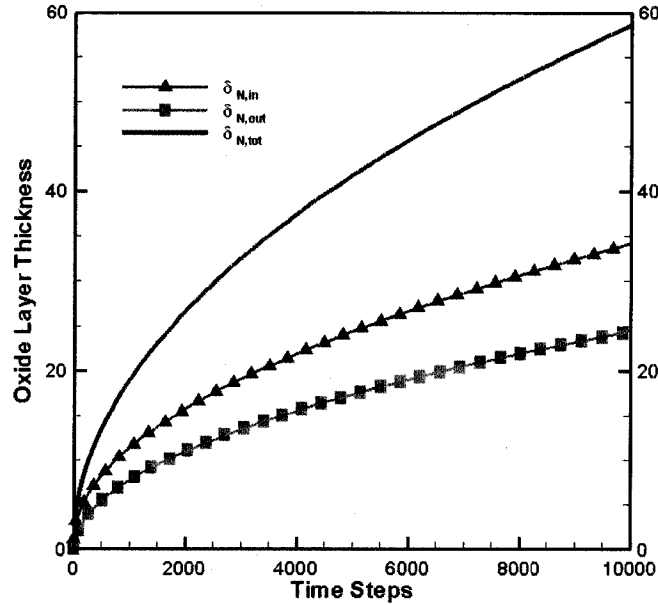


Figure 87. The oxide layer growth vs. time steps.

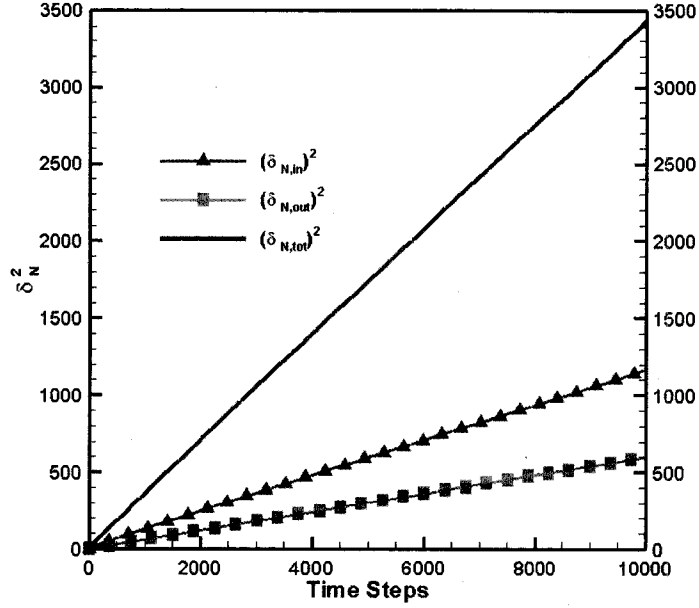


Figure 88. Values of  $(\delta_{N,in})^2$ ,  $(\delta_{N,out})^2$ , and  $(\delta_{N,tot})^2$  vs. time steps.

Figure 87 shows the oxide layer growth with calculating time steps. Figure 88 shows the values of  $(\delta_{N,in})^2$ ,  $(\delta_{N,out})^2$ , and  $(\delta_{N,tot})^2$  are close to straight lines. Therefore, the thickness of the inner oxide layer, outer oxide layer and the total oxide layer grow parabolically which accords with Wagner's theory [47].

#### 4.5.3 Mapping between the Mesoscopic Model and the Experimental Data

As discussed in the last section, the growth of the total thickness, inner layer thickness and outer layer thickness all follow the parabolic law. Therefore, the growth of the total thickness can be fitted in the following parabolic relation,

$$\delta_{N,tot}^2 = k_p^N N_t \quad (4-17)$$

where,  $k_p^N$  is the parabolic rate coefficient for the CA model with distance based on the lattice number. For the case of  $P=0.5$ ,  $\varepsilon = 1$ , and  $K_d = 2$ ,  $k_p^N$  can be fit to 0.3434 from Figure 87 and Figure 88.

According to the Wagner's theory [47], the real thickness of the oxide layer follows the relationship,

$$\delta_{tot}^2 = k_p t \quad (4-18)$$

where,  $k_p$  is the parabolic rate coefficient for real oxide layer growth. The time for forming thickness “a (m)” of oxide layer is assumed to be  $\Delta t$  (s). Then,

$$\delta_{tot} = \delta_{N,tot} a \quad (4-19)$$

$$t = N_t \Delta t \quad (4-20)$$

Substituting Eqs. (4-19) and (4-20) into Eq. (4-18),

$$(\delta_{N,tot} a)^2 = k_p N_t \Delta t \quad (4-21)$$

Comparing Eqs. (4-17) and (4-21),

$$\Delta t = k_p^N a^2 / k_p \quad (4-22)$$

From the Ref. [17], the fitted values of  $k_p$  from the experimental data for LBE loop at temperature 550 °C with oxygen concentration controlled at 0.03 ppm are estimated to be  $2.29 \times 10^{-17} m^2 / s$  for 316,  $2.35 \times 10^{-17} m^2 / s$  for D-9, and  $2.82 \times 10^{-17} m^2 / s$  for HT-9 respectively. Therefore, the time step spans equal to 0.3749 s, 0.3653 s and 0.3044 s for 316, D-9, and HT-9 with the above conditions respectively for a length  $a=5$  nm in the developed mesoscopic model.

#### 4.5.4 Parametric Study

The present stochastic mesoscopic model shows another way to predict the oxide layer growth at a mesoscopic level and the results was mapped with the experimental

data. It is necessary to conduct a parametric study for the proposed model in order to check the factors impacting the model in the simulations, for a longer term.

The mass transport ratio  $K_d$  is set at 1, and the oxygen concentration in LBE,  $C_{oxy}$ , is set at 0.2. The impact of the reaction probability  $P_{act}$  is examined. The snapshots of the simulated mesoscopic structures of cases with  $P_{act} = 0.0005$ ,  $P_{act} = 0.3$ ,  $P_{act} = 0.5$ , and  $P_{act} = 0.8$  after 200,000 calculating steps are shown in Figure 89 to Figure 92.

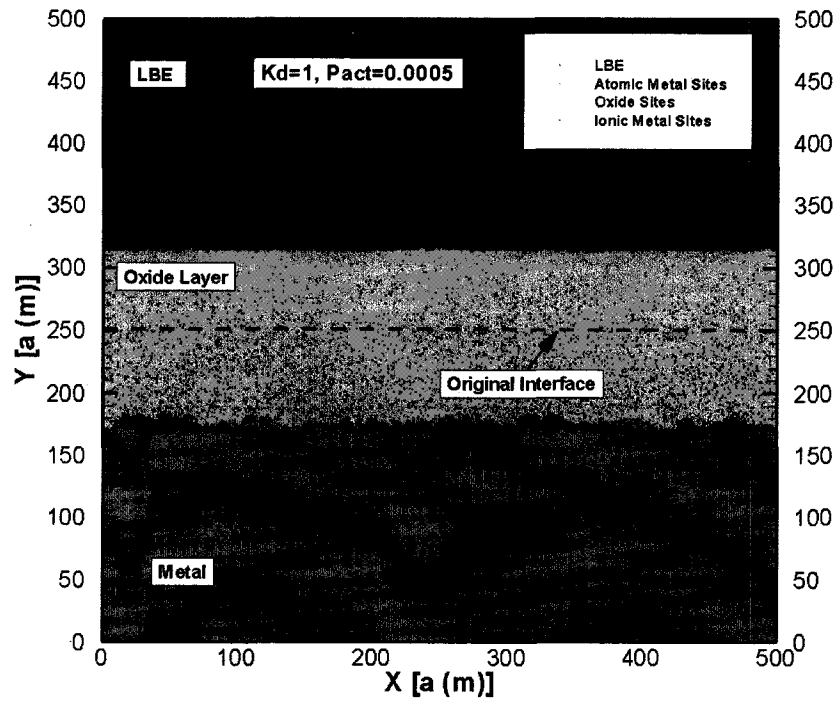


Figure 89. The snapshot of the mesoscopic structure for  $N_t = 200,000$ , with  $K_d = 1$ ,

$$C_{oxy} = 0.2 \text{ and } P_{act} = 0.0005.$$

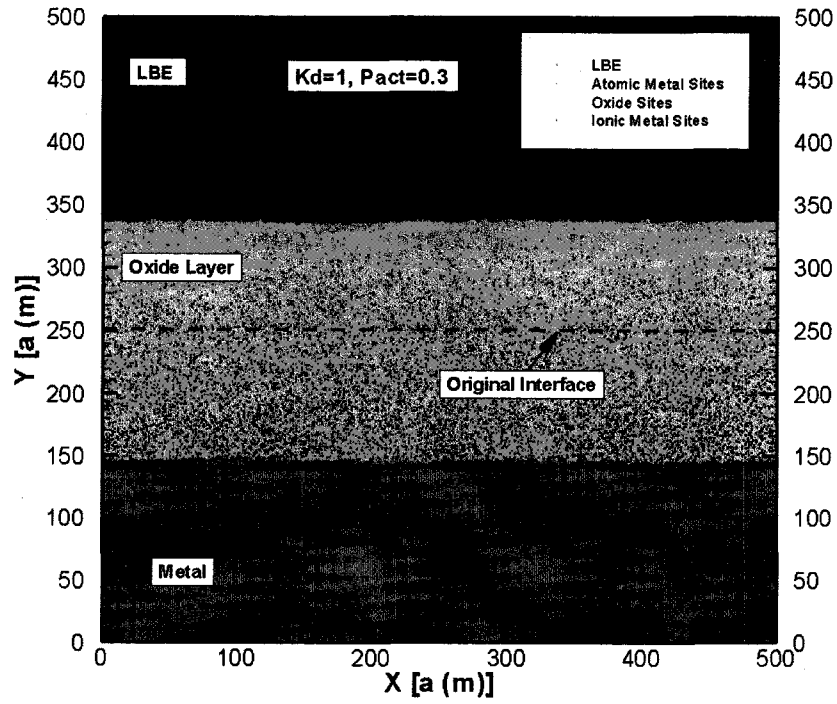


Figure 90. The snapshot of the mesoscopic structure for  $N_t = 200,000$ , with  $K_d = 1$ ,

$$C_{oxy} = 0.2 \text{ and } P_{act} = 0.3.$$

The increases in thickness of the inner oxide layer, outer oxide layer, and the total oxide layer with calculating steps are compared in Figure 93 to Figure 95. From the comparisons, a small change of the reaction probability (in the same order) does not impact the thicknesses of oxide layer too much on a long time scale. For example, the thicknesses of the inner oxide layers are estimated at about 102 [a(m)] for  $P_{act} = 0.3$ ,  $P_{act} = 0.5$ ,  $P_{act} = 0.8$ , and at about 68 [a(m)] for  $P_{act} = 0.0005$  at  $N_t = 200,000$ . The outer layer thicknesses are about 88 [a(m)] for  $P_{act} = 0.3$ ,  $P_{act} = 0.5$ ,  $P_{act} = 0.8$ , and 62 [a(m)] for  $P_{act} = 0.0005$  at  $N_t = 200,000$ . The total thicknesses are about 190(a) for  $P_{act} = 0.3$ ,  $P_{act} = 0.5$ ,  $P_{act} = 0.8$ , and 130 [a(m)] for  $P_{act} = 0.0005$  at  $N_t = 200,000$ . Between the cases of reaction probability in the same order (for example,

$P_{act} = 0.3$  and  $P_{act} = 0.8$  in Figure 94), the difference of the thickness are very small. Only a very small difference can be observed at the initial stage (see Figure 95). The reason is that such a high reaction probability will ensure most of the transported-in oxygen is consumed, sooner or later, in a long time. The oxygen keeps transporting randomly in four directions (some may go to and fro and react when they meet oxygen), and only a few of them will be transported to the far end of the specimen, to cause “noises” of the simulation.

The metal ions (“walkers”) concentration distributions for the cases with  $P_{act} = 0.0005$ ,  $P_{act} = 0.3$ ,  $P_{act} = 0.5$ ,  $P_{act} = 0.8$  after 200,000 calculating steps are shown in Figure 96 to Figure 99.

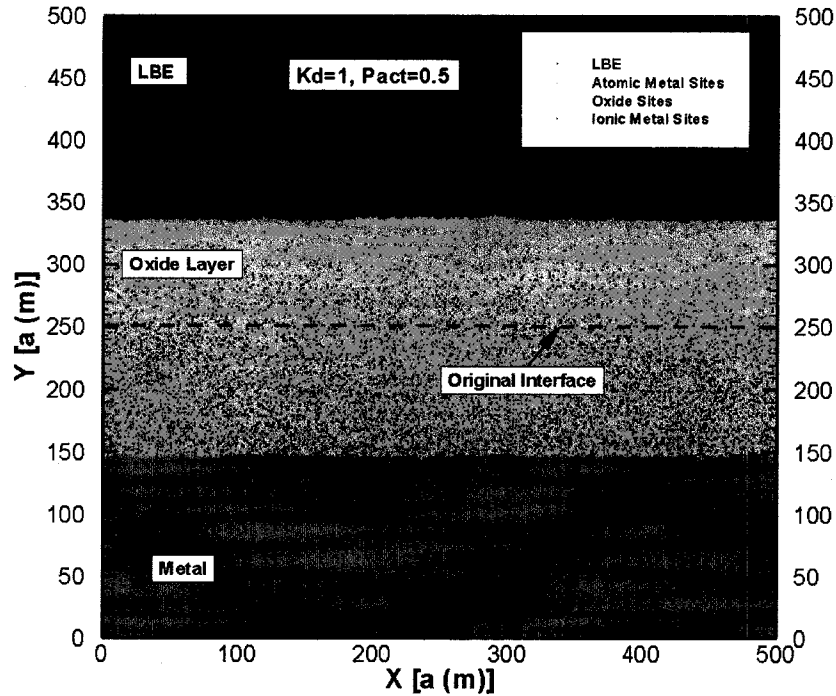


Figure 91. The snapshot of the mesoscopic structure for  $N_t = 200,000$ , with  $K_d = 1$ ,

$$C_{oxy} = 0.2 \text{ and } P_{act} = 0.5.$$

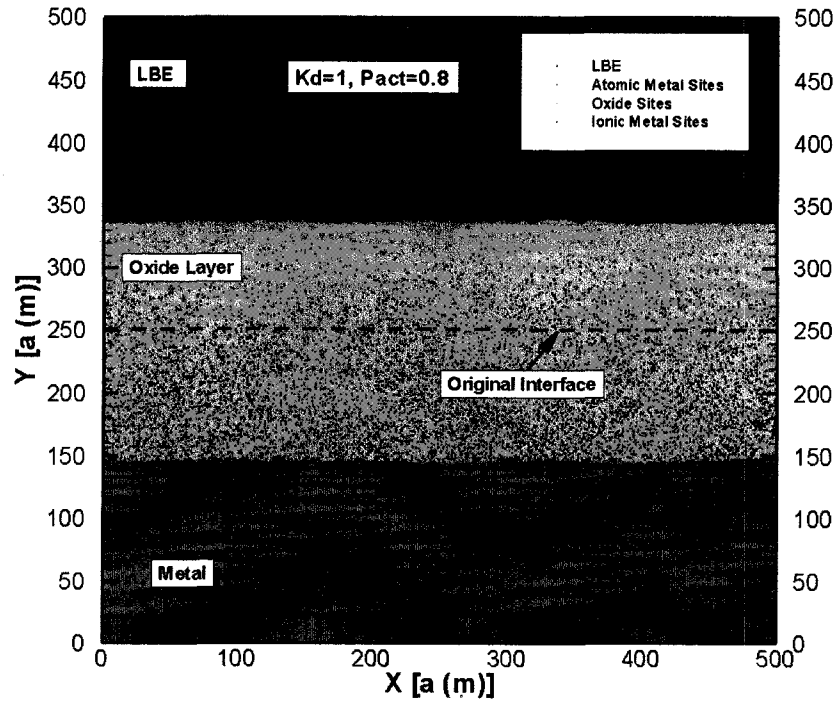


Figure 92. The snapshot of the mesoscopic structure for  $N_t = 200,000$ , with  $K_d = 1$ ,

$$C_{oxy} = 0.2 \text{ and } P_{act} = 0.8.$$

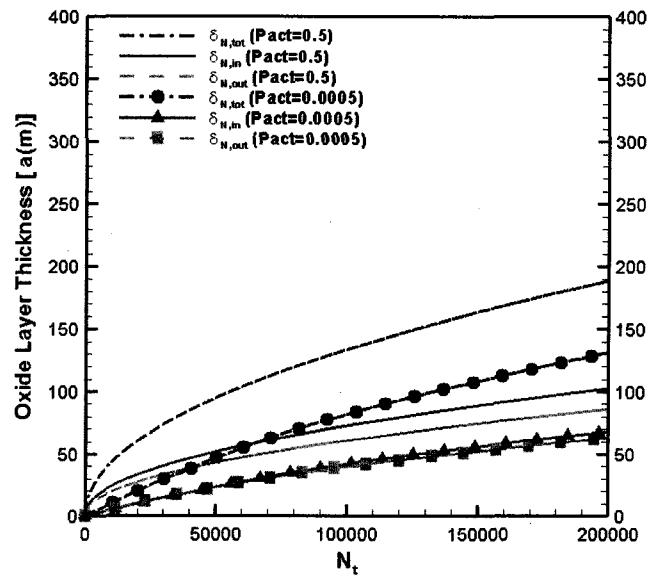


Figure 93. The comparison of the oxide layer thickness of cases with

$$P_{act} = 0.0005 \text{ and } P_{act} = 0.5 \text{ at } N_t = 200,000, \text{ with } K_d = 1, C_{oxy} = 0.2.$$



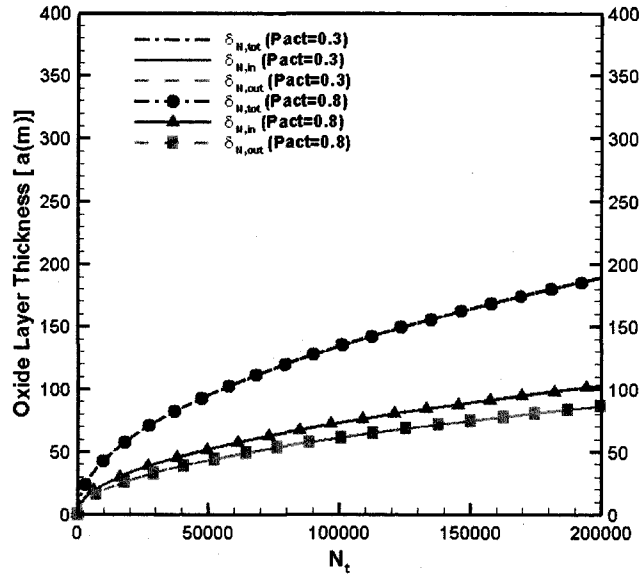


Figure 94. The comparison of the oxide layer thickness of cases with  $P_{act} = 0.3$  and  $P_{act} = 0.8$  at  $N_t = 200,000$ , with  $K_d = 1$ ,  $C_{oxy} = 0.2$ .

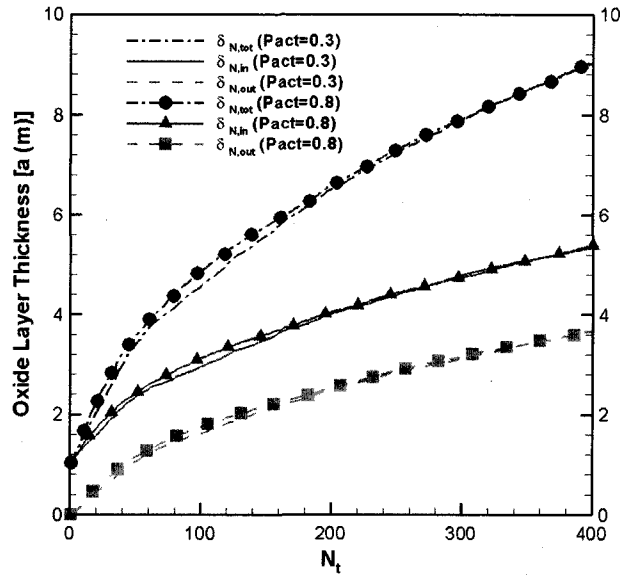


Figure 95. The comparison of the oxide layer thickness of cases with  $P_{act} = 0.3$  and  $P_{act} = 0.8$  at the initial stage, with  $K_d = 1$ ,  $C_{oxy} = 0.2$ .

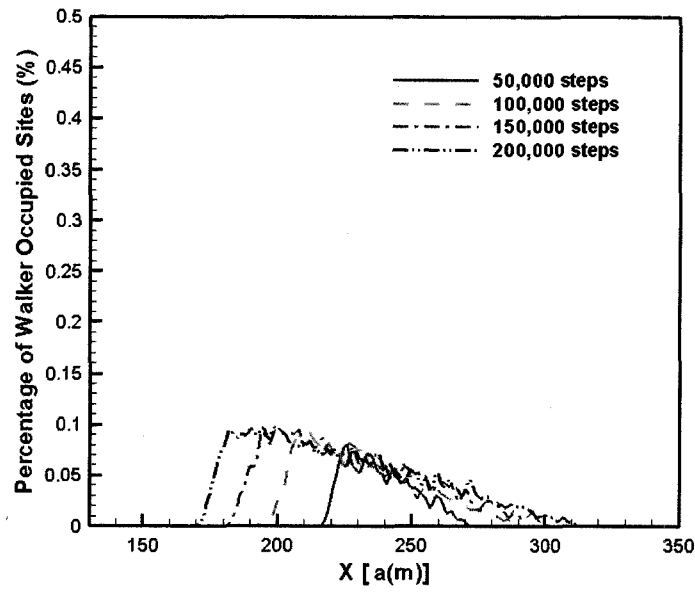


Figure 96. The walker distributions for  $N_t = 200,000$ , with  $K_d = 1$ ,

$$C_{oxy} = 0.2 \text{ and } P_{act} = 0.0005.$$

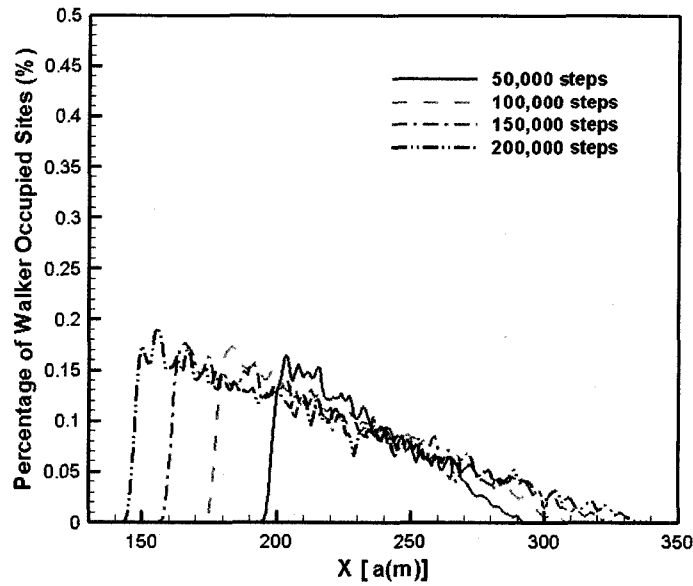


Figure 97. The walker distributions for  $N_t = 200,000$ , with  $K_d = 1$ ,

$$C_{oxy} = 0.2 \text{ and } P_{act} = 0.3.$$

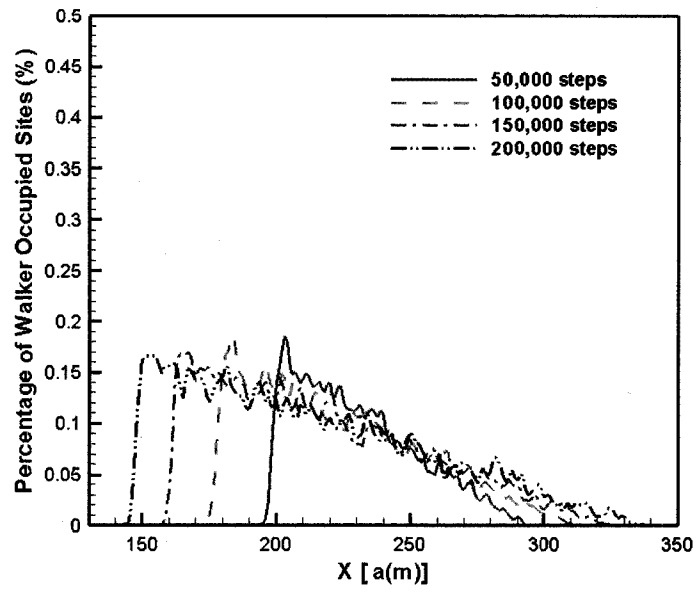


Figure 98. The walker distributions for  $N_t = 200,000$ , with  $K_d = 1$ ,  
 $C_{oxy} = 0.2$  and  $P_{act} = 0.5$ .

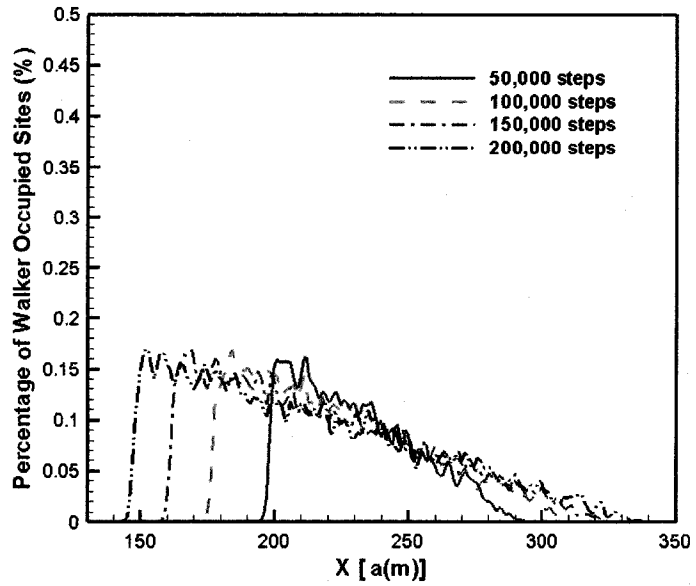


Figure 99. The walker distributions for  $N_t = 200,000$ , with  $K_d = 1$ ,  
 $C_{oxy} = 0.2$  and  $P_{act} = 0.8$ .

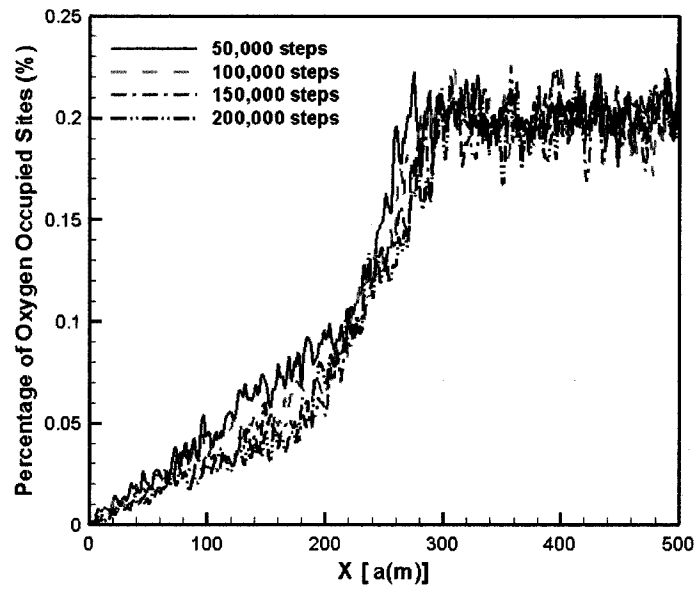


Figure 100. The oxygen distributions for  $N_t = 200,000$ , with  $K_d = 1$ ,  
 $C_{oxy} = 0.2$  and  $P_{act} = 0.0005$ .

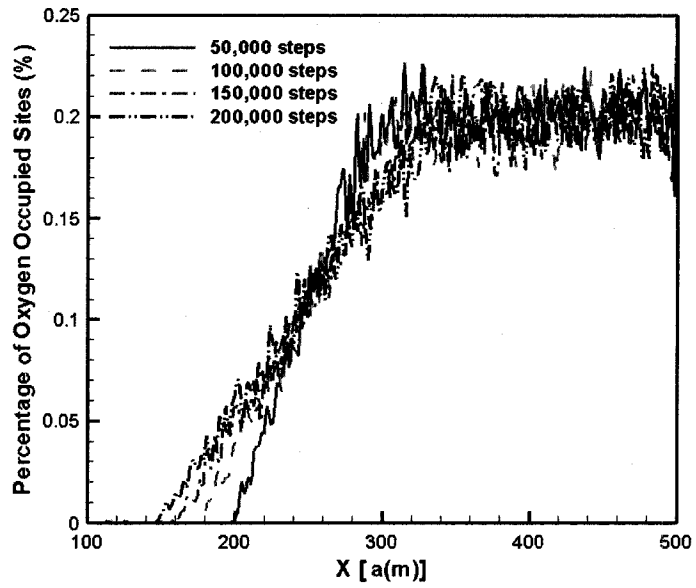


Figure 101. The oxygen distributions for  $N_t = 200,000$ , with  $K_d = 1$ ,  
 $C_{oxy} = 0.2$  and  $P_{act} = 0.3$ .

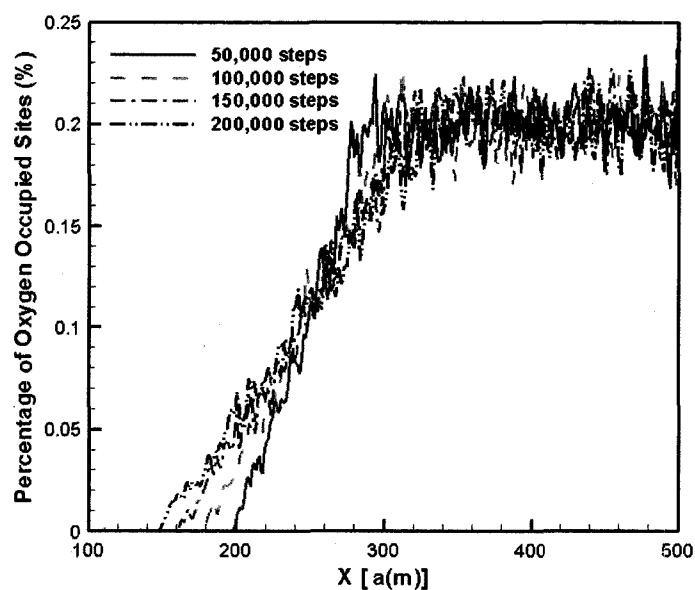


Figure 102. The oxygen distributions for  $N_t = 200,000$ , with  $K_d = 1$ ,

$$C_{oxy} = 0.2 \text{ and } P_{act} = 0.5.$$

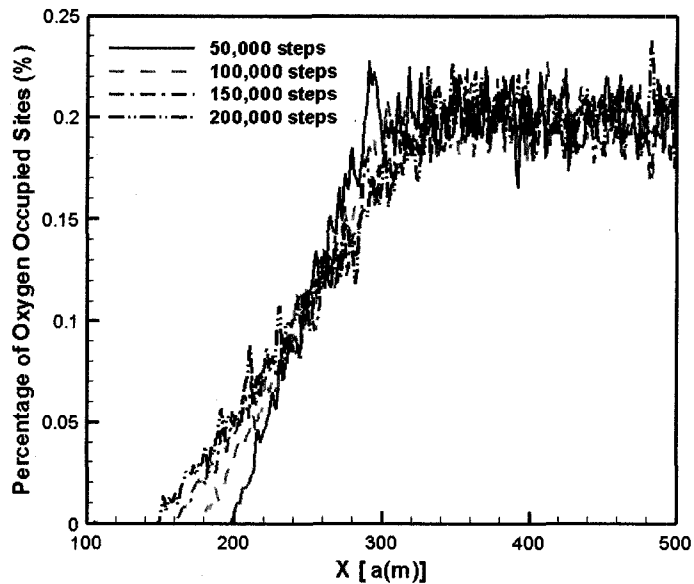


Figure 103. The oxygen distributions for  $N_t = 200,000$ , with  $K_d = 1$ ,

$$C_{oxy} = 0.2 \text{ and } P_{act} = 0.8.$$

The oxygen concentration distributions for the cases with  $P_{act} = 0.0005$ ,  $P_{act} = 0.3$ ,  $P_{act} = 0.5$ ,  $P_{act} = 0.8$  after 200,000 calculating steps are shown in Figure 100 to Figure 103.

From the comparisons, a small change of the reaction probability does not much affect the results of the concentration distributions of oxygen and “walkers” in a long time scale, either. The concentration distributions of oxygen and walkers look similar for cases of  $P_{act} = 0.3$ ,  $P_{act} = 0.5$ ,  $P_{act} = 0.8$ . The difference is mostly because that the model is a stochastic and the random walk and the random selection for each lattice or interstitial site. However, a much lower concentration distribution of metal ions can be observed in the case of  $P_{act} = 0.0005$ . The observation illustrates that a slower ionization process accompanies a slower oxidation reaction. One reason is the reaction rate is relatively lower, and another is that the extra oxygen is transported into the metal domain, as shown in Figure 100. By this model, the oxygen enriched substrate layer beneath the oxide layer is simulated. Another phenomenon observed is that a very low reaction probability (e.g.  $P_{act} = 0.0005$ ) will cause a coarse interface of the oxide and metal (as shown in Figure 89).

The comparison above shows the reaction probability does not impact the results markedly. The study will be conducted on cases of  $P_{act} = 0.0005$  and  $P_{act} = 0.5$  only with different values of  $K_d$ .

The snapshots at  $N_t = 200,000$  of the mesoscopic structure of oxide layer with  $K_d = 2$ ,  $C_o = 0.2$  and  $P_{act} = 0.0005$  is shown in Figure 104.

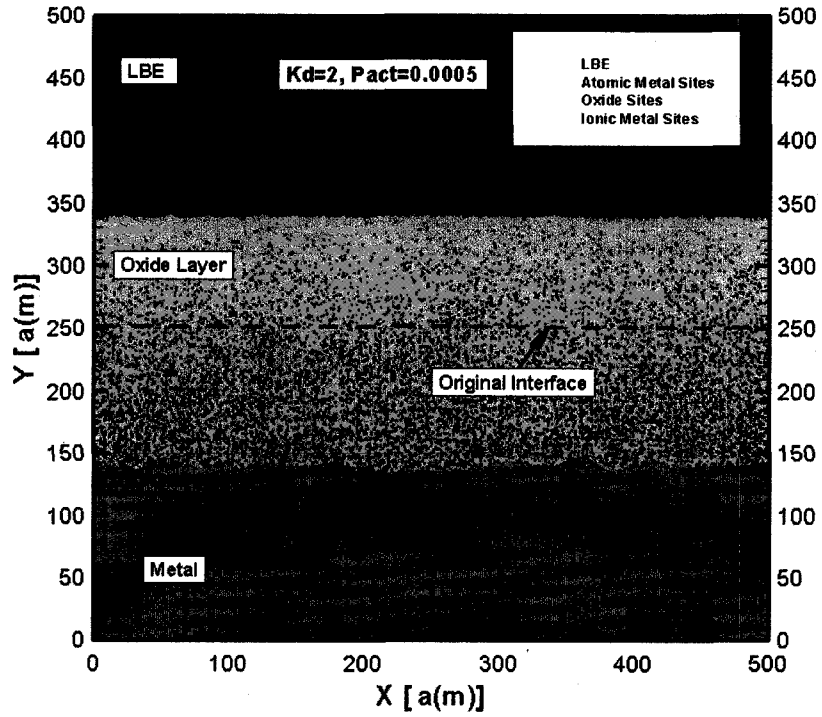


Figure 104. Snapshot of the mesoscopic structure with  $K_d = 2$ ,  $C_{oxy} = 0.2$

and  $P_{act} = 0.0005$  at  $N_t = 200,000$ .

Figure 105 shows the snapshot for case of  $P_{act} = 0.5$  with same parameters. Since the ratio of the transport steps  $K_d = 2$ , each of the “walkers” diffuses for an average step of  $N_{WD} = 200,000$  and each oxygen transports  $N_{OT} = 400,000$  steps in average, during the simulation.

Figure 106 shows the comparison of the oxide layer thicknesses for cases  $P_{act} = 0.0005$  and  $P_{act} = 0.5$  (both with  $K_d = 2$ ,  $C_{oxy} = 0.2$ ).

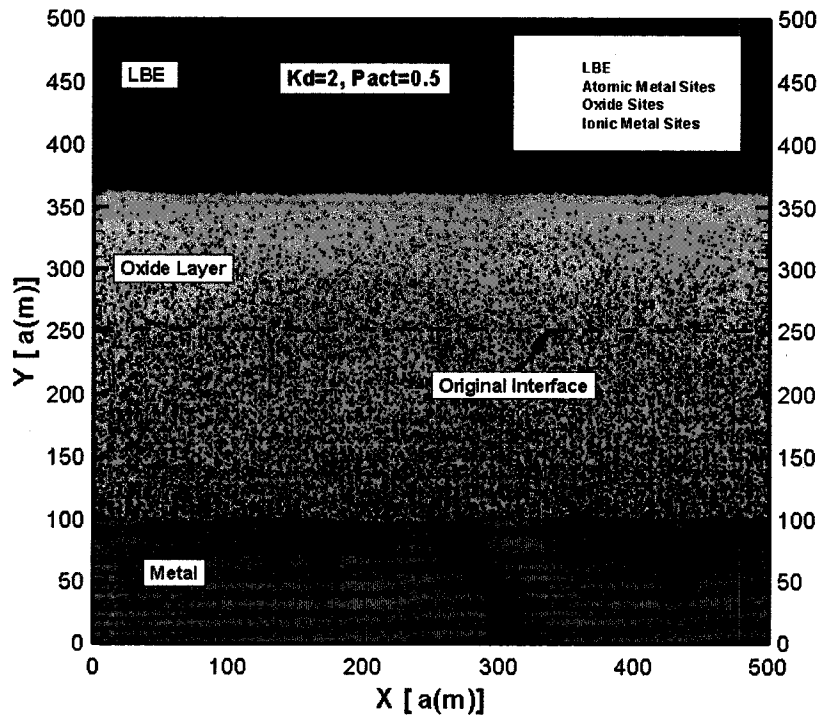


Figure 105. Snapshot of the mesoscopic structure with  $K_d = 2$ ,  $C_{oxy} = 0.2$  and  $P_{act} = 0.5$  at  $N_t = 200,000$ .

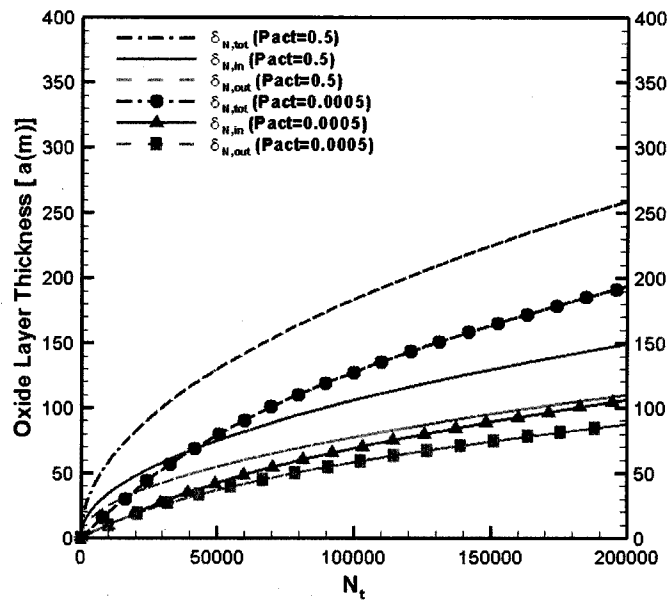


Figure 106. Comparison of the oxide layer thicknesses for cases  $P_{act} = 0.0005$  and  $P_{act} = 0.5$  (both with  $K_d = 2$ ,  $C_{oxy} = 0.2$ ).



A coarser interface can be observed in Figure 104, which agrees with the previous observation, in which a very low reaction probability causes a coarse interface of the oxide and metal (as shown in Figure 89). From Figure 104 to Figure 106, the thicknesses of the oxide layers grow faster significantly, with the value of  $K_d$  increasing from 1 to 2. The comparison of thicknesses for different value of  $K_d$  will be presented later. When  $K_d = 2$ , the difference between the thickness of cases  $P_{act} = 0.0005$  and  $P_{act} = 0.5$  are more obvious. For example, the thicknesses of the inner oxide layers are estimated at about 150 [a(m)] for  $P_{act} = 0.5$  and at about 105 [a(m)] for  $P_{act} = 0.0005$  at  $N_t = 200,000$ . The outer layer thicknesses are about 110 [a(m)] for  $P_{act} = 0.5$  and 88 [a(m)] for  $P_{act} = 0.0005$  at  $N_t = 200,000$ . The total thicknesses are about 260(a) for  $P_{act} = 0.5$  and 193 [a(m)] for  $P_{act} = 0.0005$  at  $N_t = 200,000$ .

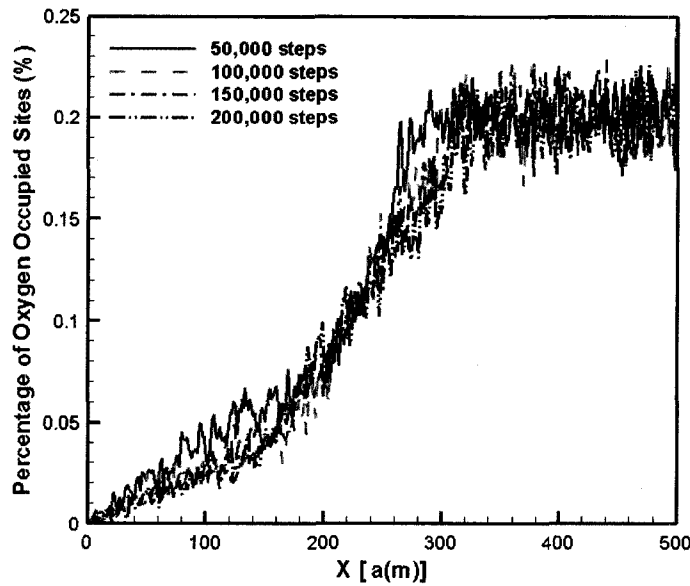


Figure 107. The oxygen distributions for  $N_t = 200,000$ , with  $K_d = 2$ ,

$$C_{oxy} = 0.2 \text{ and } P_{act} = 0.0005.$$

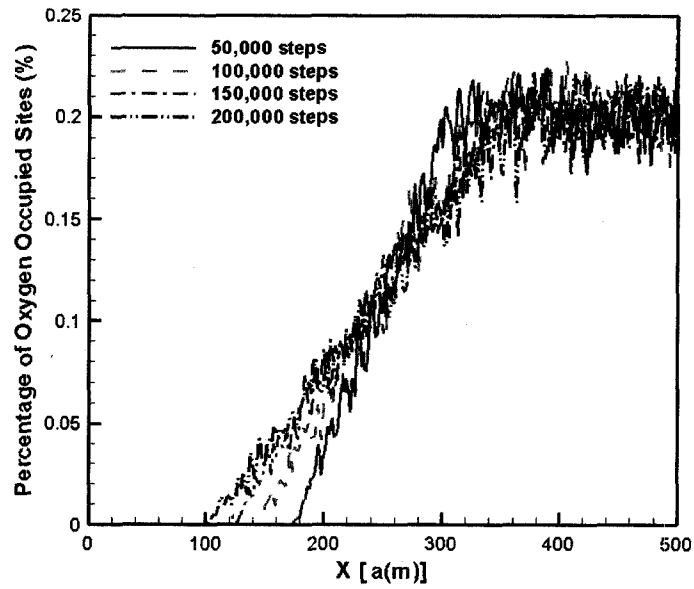


Figure 108. The oxygen distributions for  $N_t = 200,000$ , with  $K_d = 2$ ,

$$C_{oxy} = 0.2 \text{ and } P_{act} = 0.5.$$

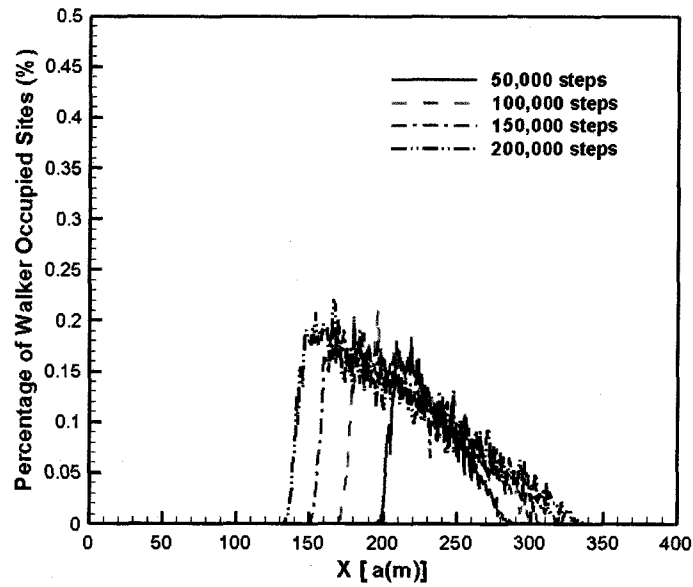


Figure 109. The walker distributions for  $N_t = 200,000$ , with  $K_d = 2$ ,

$$C_{oxy} = 0.2 \text{ and } P_{act} = 0.0005.$$

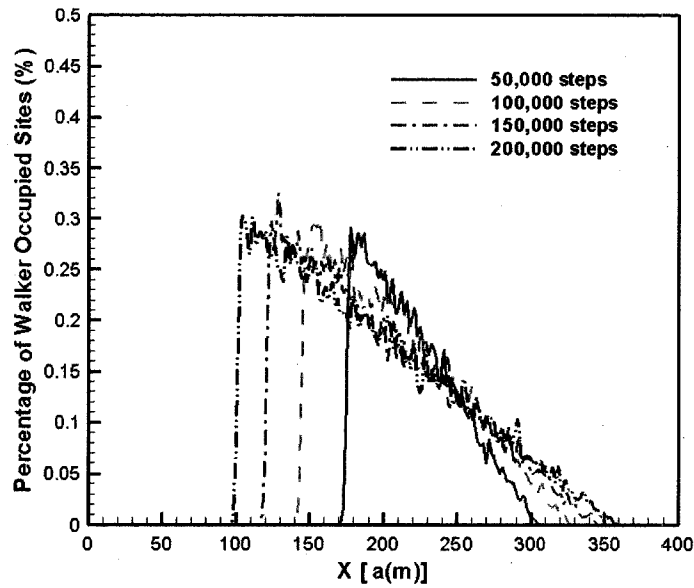


Figure 110. The walker distributions for  $N_t = 200,000$ , with  $K_d = 2$ ,

$$C_{oxy} = 0.2 \text{ and } P_{act} = 0.5.$$

The oxygen distributions for  $P_{act} = 0.0005$  and  $P_{act} = 0.5$  are shown in Figure 107 and Figure 108 respectively, both with  $K_d = 2$ ,  $C_{oxy} = 0.2$  and at  $N_t = 200,000$ . The distribution profiles of “walkers” for  $P_{act} = 0.0005$  and  $P_{act} = 0.5$  are shown in Figure 109 and Figure 110 respectively, both with  $K_d = 2$ ,  $C_{oxy} = 0.2$  and at  $N_t = 200,000$ .

Similarly, a very low reaction probability (e.g.  $P_{act} = 0.0005$ ) causes a deeper penetration of oxygen in the metal, which is because of a fast transport rate of oxygen and a lower reaction probability. The observation also illustrates a slower ionization process for a lower reaction probability. The concentration of “walkers” is much lower in the oxide layer in Figure 109 than that in Figure 110. The cases of  $K_d = 2$  have a larger value of “walker” concentration than that in cases of  $K_d = 1$ .

The oxidation process for  $K_d = 4$  is studied as well, in which each of the “walkers” diffuses for an average step of  $N_{WD} = 200,000$  and each oxygen site transports  $N_{OT} = 800,000$  steps in average during the simulation ( $N_t = 200,000$ ). The snapshots at  $N_t = 200,000$  of the mesoscopic structure of oxide layer with and  $P_{act} = 0.0005$  and  $P_{act} = 0.5$  are shown in Figure 111 and Figure 112 (both are of  $K_d = 4$  and  $C_{oxy} = 0.2$ ). Similarly, Figure 111 ( $P_{act} = 0.0005$ ) shows a coarser inner interface and Figure 112 ( $P_{act} = 0.5$ ) illustrates a much thicker oxide layer.

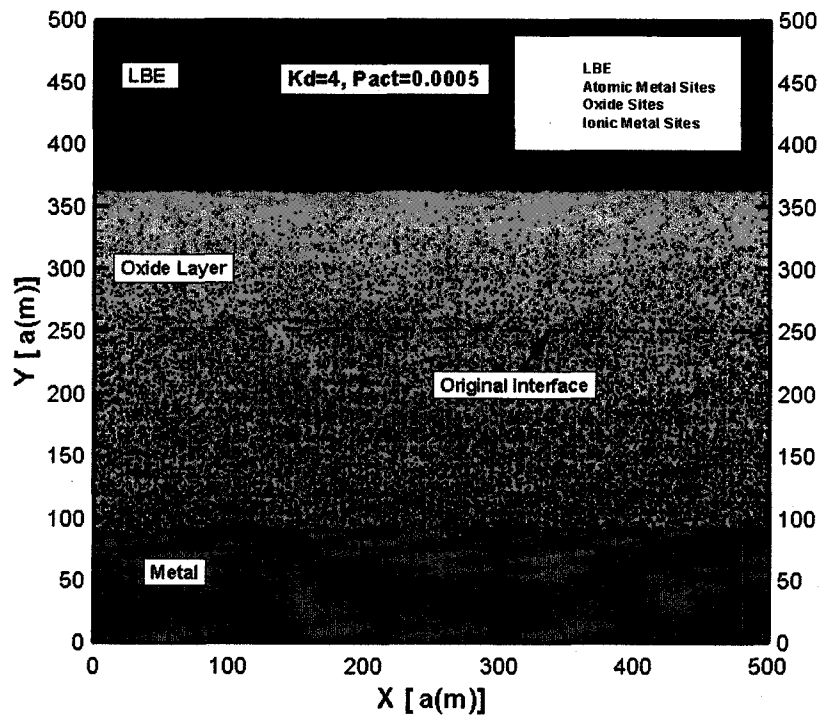


Figure 111. Snapshot of the mesoscopic structure with  $K_d = 4$ ,  $C_{oxy} = 0.2$

and  $P_{act} = 0.0005$  at  $N_t = 200,000$ .

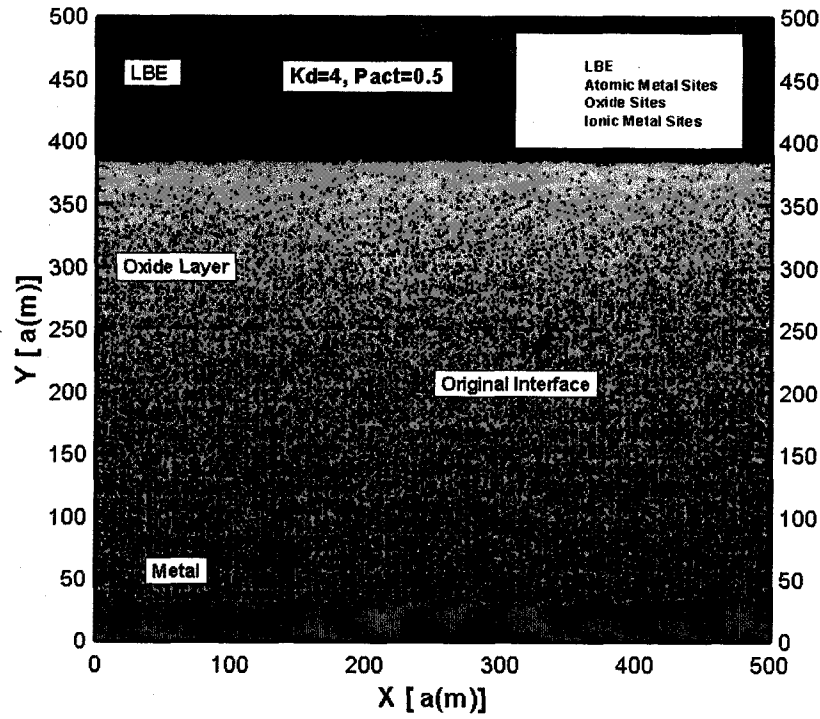


Figure 112. Snapshot of the mesoscopic structure with  $K_d = 4$ ,  $C_{oxy} = 0.2$  and  $P_{act} = 0.5$  at  $N_t = 200,000$ .

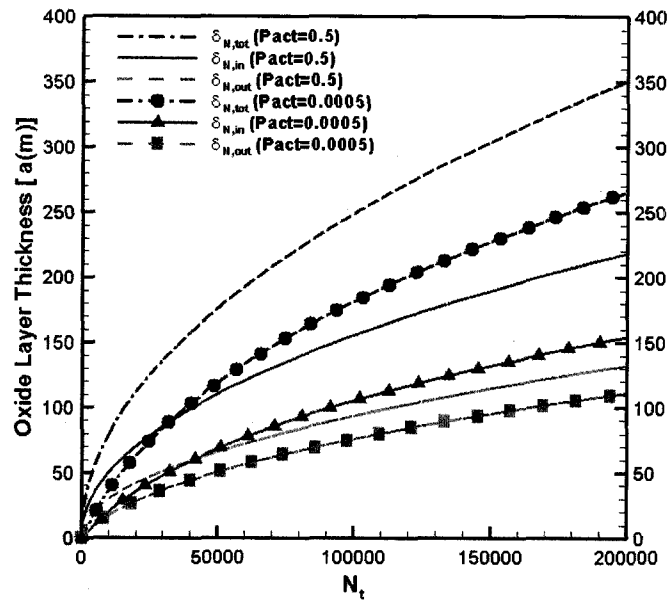


Figure 113. Comparison of the oxide layer thicknesses for cases  $P_{act} = 0.0005$  and  $P_{act} = 0.5$  (both with  $K_d = 4$ ,  $C_{oxy} = 0.2$ ).

Figure 113 shows the comparison of the oxide layer thicknesses for cases  $P_{act} = 0.0005$  and  $P_{act} = 0.5$  (both with  $K_d = 4, C_{oxy} = 0.2$ ). Much thicker oxide layers can be seen for both cases, and a more obvious difference can be observed between the cases of  $P_{act} = 0.0005$  and  $P_{act} = 0.5$ , since the value of  $K_d$  is much higher.

The distribution profiles of “walkers” for  $P_{act} = 0.0005$  and  $P_{act} = 0.5$  are shown in Figure 114 and Figure 115 respectively, both with  $K_d = 4$ ,  $C_{oxy} = 0.2$  and at  $N_t = 200,000$ . Figure 116 and Figure 117 show the oxygen distributions for  $P_{act} = 0.0005$  and  $P_{act} = 0.5$  respectively, both with  $K_d = 4$ ,  $C_{oxy} = 0.2$  and at  $N_t = 200,000$ .

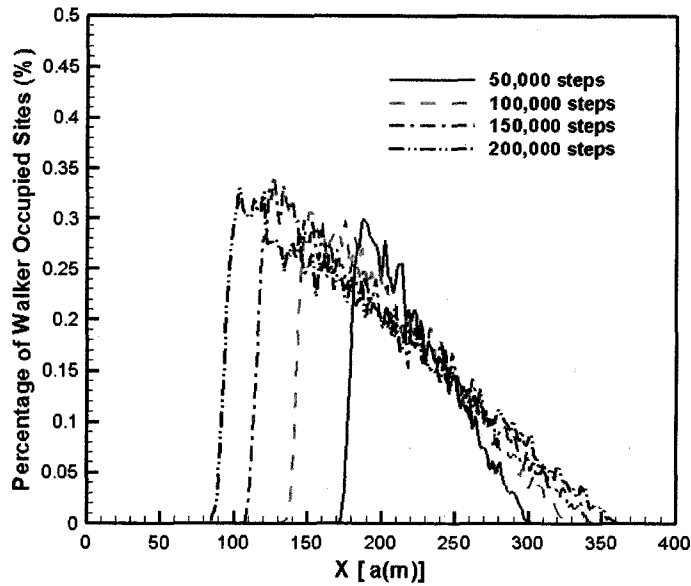


Figure 114. The walker distributions for  $N_t = 200,000$ , with  $K_d = 4$ ,

$$C_{oxy} = 0.2 \text{ and } P_{act} = 0.0005.$$

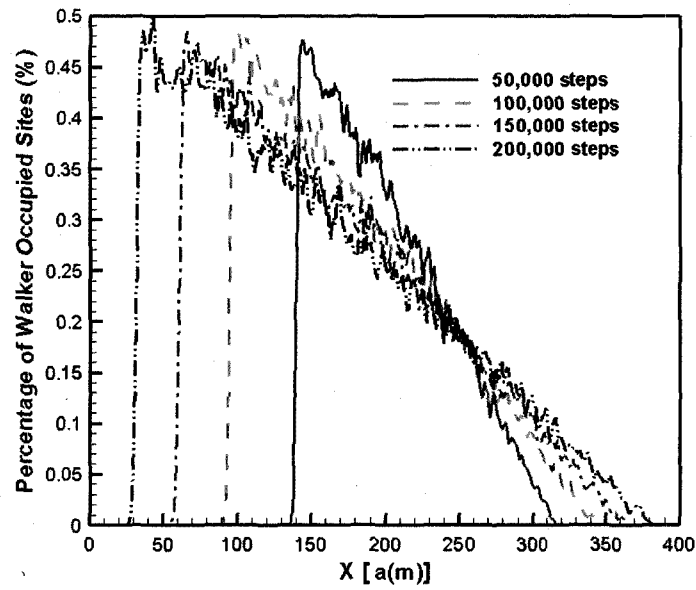


Figure 115. The walker distributions for  $N_t = 200,000$ , with  $K_d = 4$ ,

$$C_{oxy} = 0.2 \text{ and } P_{act} = 0.5.$$

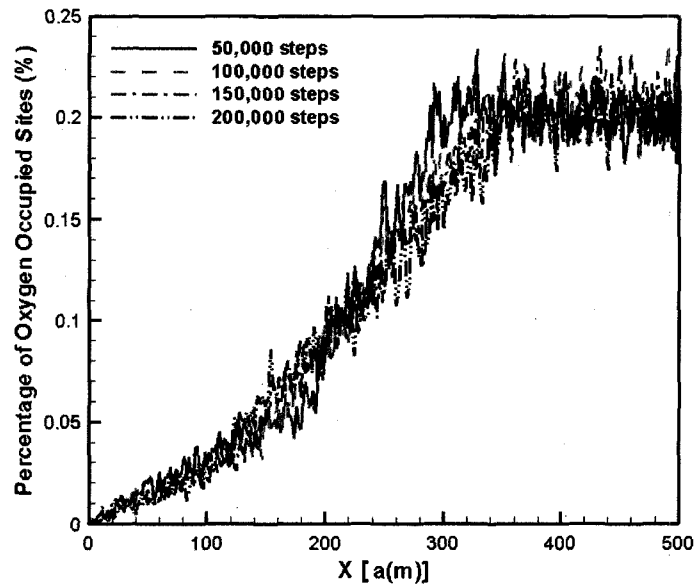


Figure 116. The oxygen distributions for  $N_t = 200,000$ , with  $K_d = 4$ ,

$$C_{oxy} = 0.2 \text{ and } P_{act} = 0.0005.$$

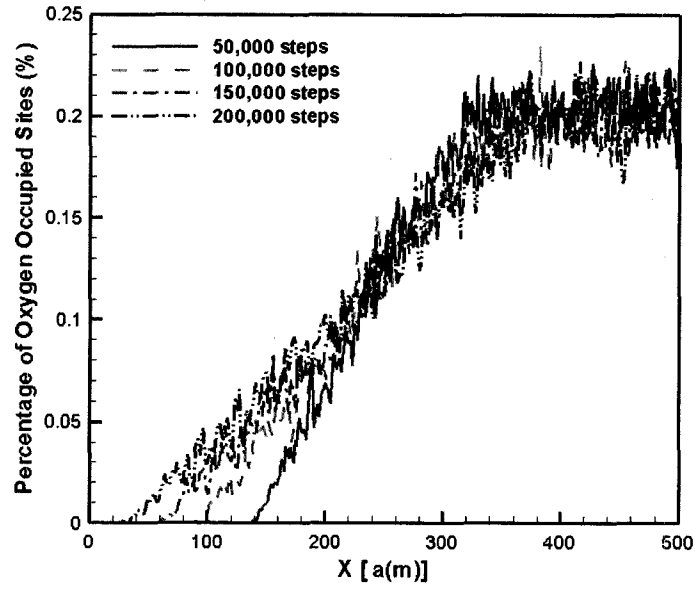


Figure 117. The oxygen distributions for  $N_t = 200,000$ , with  $K_d = 4$ ,

$$C_{oxy} = 0.2 \text{ and } P_{act} = 0.5.$$

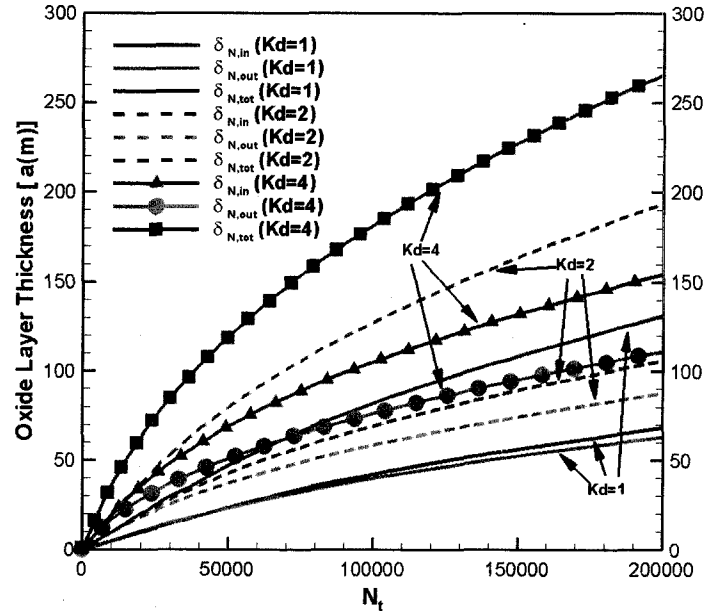


Figure 118. Comparison of thickness for different value of  $K_d$ , with  $C_{oxy} = 0.2$ ,

$$P_{act} = 0.0005.$$



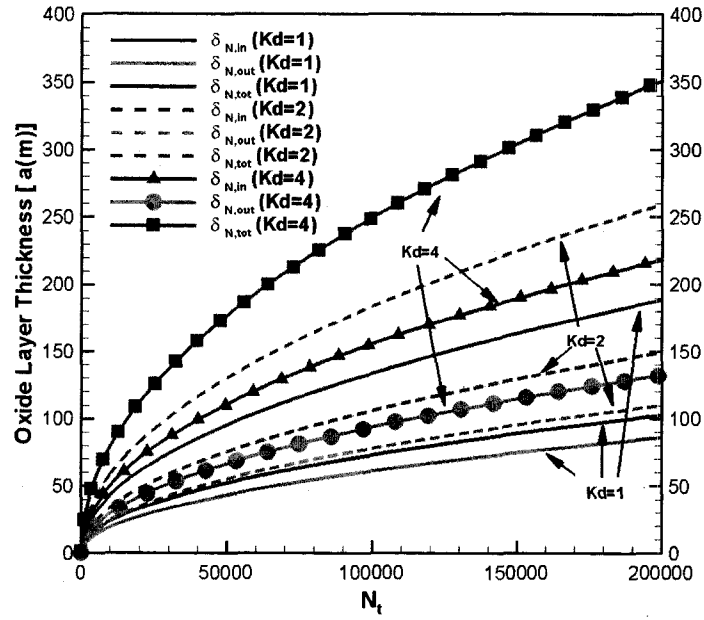


Figure 119. Comparison of thickness for different value of  $K_d$ , with  $C_{oxy} = 0.2$ ,

$$P_{act} = 0.5.$$

More evidently, a lower reaction probability (e.g.  $P_{act} = 0.0005$ ) causes a faster transport oxygen in the metal when the value of  $K_d$  is increased to 4. Also, a much slower ionization process was found since the “walker” concentrations are much lower in a case of  $P_{act} = 0.0005$ .

The comparison of thickness for different values of  $K_d$ , and with same values of  $C_{oxy} = 0.2$  and  $P_{act} = 0.0005$  at calculating time  $N_t = 200,000$  step, are shown in Figure 118. The comparison for  $P_{act} = 0.5$  with the same conditions are shown in Figure 119.

From the comparisons, the transport ratio  $K_d$  in the model has great impact on the thickness of the oxide layer, especially on the inner thickness. Increasing the value of the transport ratio  $K_d$  will increase the oxide film growth greatly for the same calculating

steps. The first reason is, the transport steps for oxygen sites are  $K_d$  times that of the metal ions for a particular calculating step number. The second reason is that a relatively fast transport will lead to more extra oxygen penetration into the metal, especially for a low reaction probability case.

#### 4.6 Conclusions

An improved stochastic mesoscopic model, based on cellular automaton, is proposed to investigate the development of a continuous oxide layer of metals.

The ionization of metal taking place in the oxide/metal interface, and oxidation occurring on both the liquid/oxide and oxide/metal interface, were simulated with consideration of the mesoscopic transport of oxygen along the grain boundary and the mesoscopic diffusion of metal ions. With this model, a duplex oxide layer growth is observed. The volume expansion effect can be realized by changing the volume control parameter,  $\varepsilon$ .

The model was benchmarked with a pure diffusion process, both with the analytical solution and with the previous work in Ref. [98]. Significant agreement was reached between the data, which shows the basic abilities of the present model for mesoscopic studies. From the present model, the thicknesses of inner oxide layer, outer oxide layer and the total oxide layer grow parabolically which accords with Wagner's theory [47]. The model is also mapped with the experimental data from an LBE loop, to show the developing of the oxide layer quantificationally.

A parametric study was conducted in order to check the importance of the three main explicit parameters of the mesoscopic model, the volume control parameter ( $\varepsilon$ ), reaction

probability ( $P_{act}$ ) and transport steps ratio of oxygen and metallic ions ( $K_d$ ). A small change of the reaction probability (in the same order) does not impact the thicknesses of oxide layer too much in a long time. A slower ionization process accompanies a slower oxidation reaction. A very low reaction probability will cause a coarse interface of oxide and metal. The transport ratio  $K_d$  in the model has great impact on the thickness of the oxide layer, especially on the inner thickness. To increase the value of the transport ratio,  $K_d$  will increase the oxide film growth greatly for the same calculating steps. One of the reasons is that the oxygen sites transport more steps than metallic ions sites for a particular calculating step number. Another reason is that a relatively fast transport leads to a deeper oxygen penetration into the metal, especially for a low reaction probability case. A large transport ratio  $K_d$ , and a small reaction probability, may cause an oxygen enriched substrate beneath the oxide layer.

## CHAPTER 5

### CONCLUSIONS AND RECOMMENDATIONS

#### 5.1 Conclusions

Based on the studies in the previous chapters on the corrosion and oxidation of steels in lead or lead alloys coolant systems, some conclusions can be summarized:

From the models for corrosion and precipitation:

1. The analytical solutions for corrosion model were obtained.

Analytical expressions were obtained for the local corrosion/precipitation rate and the bulk concentration of the corrosion products. The temperature difference between the maximal and minimal temperatures affects the corrosion/ precipitation rate significantly.

2. Numerical solutions were also accomplished. The eddy mass diffusivity is important.

From the comparison of numerical and kinetic models, the eddy mass diffusivity has obvious effect on the corrosion/precipitation behaviors, especially when the temperature difference is large. At the test leg, where temperature is at a maximum, the eddy mass diffusivity increases the corrosion rates. In addition, at the temperature dropping region, right after the test leg, the eddy mass diffusivity leads to a much higher deposition rate. For a higher inlet velocity, a higher corrosion rate can be found in the test leg region and a higher precipitation rate at the temperature dropping region right after the test leg.

From the diffusion controlling oxidation model:

The diffusion controlling oxidation model was benchmarked with experimental data and some previous study. Good agreement was obtained and advantages over the previous models were shown.

3. Scale removal effect was considered.

Scale removal plays an important role during the oxidation if the scale removal rate is relatively high comparing with the oxide layer growth rate. The present model shows the ability to estimate the scale removal effect during the simulation of oxide layer growth.

4. Volume expansion effect was studied.

The volume expansion effect, which is important for oxidation for many metals, due to the density change from metal to oxide was simulated successfully.

5. Duplex oxide layer structure was investigated.

Duplex oxide layer structure was simulated and the influence of important parameters was studied based on the present model.

From the mesoscopic CA model of oxidation:

6. The development of a continuous oxide layer of metals was investigated.

The oxide layer growth was studied successfully at a mesoscopic scale. The oxide layer grows in two directions which accounts for the outer interface reaction and inner interface reaction. Volume expansion effect was observed in the simulation.

7. The ionization of metal, oxidation reaction, and transport of oxygen and metallic ions were simulated.

The corrosion/precipitation model can be extended to corrosion cases for the developed turbulent wall-bounded shear flows in a non-isothermal system with a high Schmidt number, in which the mass diffusion layer is submerged under the hydraulic boundary layer. The diffusion controlling oxidation model is suitable for estimating the oxide layer growth of steels in oxygen containing liquid flow, not necessarily LBE or molten lead. The mesoscopic oxidation model can be used to simulate the oxidation growth of metals in a turbulent flow, except for molten lead or LBE, at a mesoscopic scale.

## 5.2 Recommendations for future work

For the corrosion/precipitation model, the analytical solutions coupling with the eddy mass diffusivity, and considering a buffer zone in the turbulent flow will be an interesting topic.

For the diffusion controlling oxidation model, how to couple it with the flow conditions is a new task.

In the mesoscopic oxidation model, the study of added alloying elements has not been done. To link the transport steps ratio with the real transport rate is another unfinished task. Finally, to study the oxidation of stainless steel in flowing LBE/lead considering the mesoscopic movement of liquid (fluid mechanics) at a mesoscopic scale, can be a meaningful research topic. How to link the mesoscopic with a real physical model is one of the most important future tasks for the present mesoscopic model.

## APPENDIX NOMENCLATURE

$a(m)$	the width of a square lattice in CA model
$a_0$	mean wall concentration
$a_k$	coefficient constant
$Ai$	Airy function
$A_1$	coefficient for solubility
$A_\rho$	coefficient for density of lead or lead alloy
$B$	Pilling-Bedworth ratio
$B_1$	coefficient for solubility
$B_\rho$	coefficient for density of lead or lead alloy
$c$	concentration of corrosion product (in Chapter 2)
$C$	concentration of oxygen (in Chapter 3)
$c_b$	bulk concentration of corrosion production
$c_l$	concentration of corrosion product in laminar sub-layer
$c_b^0$	mean concentration in the turbulent core region
$c_{Oxy}$	oxygen concentration in LBE liquid
$\hat{c}_l$	a part of the Fourier series of $c_l$
$c_s$	solubility of the corrosion product
$c_w$	wall concentration of the corrosion product
$C_{OO}$	concentration of oxygen at the oxide/liquid interface
$C_{OM}$	concentration of oxygen at the oxide/steel interface (on oxide side)
$C_{MO}$	concentration of oxygen at the oxide/steel interface (on steel side)
$\overline{C_{Oxy,j}}$	mean concentration of oxygen sites in j-th line for interstitial sites
$\overline{C_{wa,j}}$	mean concentration of “walkers” in j-th line for lattice sites
$D$	mass diffusivity
$D_m$	molecular diffusivity
$D_t$	eddy mass diffusivity
$D_{Me}$	mass diffusivity of oxygen in steels

$D_{Ox}$	mass diffusivity of oxygen in oxide layer
$f$	the Fanning friction factor
$H$	specific enthalpy
$i$	node number of the calculating domain
$Inte_{ij}(t)$	state variable of the interstitial sites
$Inte_{i,j}^{Nb}(t)$	state variable of the neighbor interstitial sites of the lattice (i, j)
$Inte_0$	a “vacancy” interstitial site
$Inte_1$	a “occupied” interstitial site by oxygen
$IO_{i,j}$	oxygen state value for an interstitial site
$IW_{i,j}$	walker state value for a lattice site
$J_y$	corrosion production flux in y-direction
$K$	mass transfer coefficient
$k$	iteration step number
$K_r$	scale removal rate constant
$k_p^N$	parabolic rate coefficient based on CA model
$k_p$	parabolic rate coefficient for real oxide layer growth
$K_d$	ratio of transport steps of an oxygen site and diffusion steps of a walker
$L$	reference length (loop/pipe)
$L(t)$	far end location of the specimen
$L_0$	original thickness of the specimen (in Chapter 3)
$L_0$	test leg length (in Chapter 2)
$Lat_{ij}(t)$	state variable of the lattice site
$Lat_{i,j}^{Nb}(t)$	state variable of the neighbor lattice sites of the lattice (i, j)
$Lat_2$	an atomic metal lattice site (solid phase)
$Lat_3$	a LBE lattice site (liquid phase)
$Lat_4$	an oxide lattice site (solid phase)
$Lat_5$	a lattice site of oxide with overlapping with ionic metal (solid phase)
$m$	combined volume expansion factor
$M_M$	atomic weight of metal element



$M_O$	atomic weight of oxygen
$N_{OT}$	transport steps of oxygen in a calculating step
$N_{WD}$	diffusion steps of walker in a calculating step
$N_t$	calculating steps
$N$	lattice number in x direction
$p$	ratio of inner reacted metallic atoms
$\hat{p}$	effective pressure, $p + \rho gh$
$Pr$	Prandtl number, $Pr = \nu / \alpha$
$P_{act}$	reaction probability of oxygen sites and metal sites
$q$	corrosion/precipitate rate at the wall
$r$	the fraction of mass of atomic M in the oxide molecular
$R$	radius of the pipe/loop
$R'$	net rate of production/consumption of the corrosion product
$R_g$	gas constant
$Re$	Reynolds number
$Sc$	Schmidt number $Sc = \nu / D_M$
$Sh$	Sherwood number $Sh = Kd_h / D_M$
$t$	time
$\Delta t$	a short time difference
$T$	temperature
$T_{average}$	average temperature
$T_{max}$	maximal temperature
$T_{min}$	minimal temperature
$T_{int}$	middle temperature $T_{int} = (T_{max} + T_{min}) / 2$
$\bar{u}$	velocity of the melt flow
$u^*$	the friction velocity
$V_{Me}$	the metal phase moving velocity
$V_{OM}$	the moving velocity of the oxide-metal interface
$V_l$	velocity in boundary layer
$V_b$	bulk velocity
$w$	the weight ratio of M in the material
$x$	coordinate in longitude direction
$x_0$	beginning coordinate of the test leg

$y^+$	limit of laminar sub-layer
$Y_k$	coefficients of the Fourier series of $c_i$
$y$	coordinate in transverse direction of x (in Chapter 2)
$y$	transformed coordinate of x (in Chapter 3)
$Y_0$	original interface of metal/LBE
$Y_{Ox\_Min}(i)$	minimum position of the oxide site at i-th column
$Y_{Ox\_Min}(i)$	maximum position of the oxide site at i-th column
$Z$	integral of normalized D and C

#### Greek Symbols

$\delta$	thickness of laminar sub-layer
$\delta_{N,in}$	mean inner layer thickness
$\delta_{N,out}$	mean outer layer thickness
$\delta_{N,tot}$	mean total thickness of the oxide layer
$\zeta$	variable for similarity solution
$\eta$	dimensionless coordinate of transverse direction
$\xi$	dimensionless coordinate of longitude direction
$\mu$	viscosity
$\rho$	density of fluid
$\rho_{Me}$	density of the steel
$\rho_{in}$	density of the inner oxide layer
$\rho_{out}$	density of the outer oxide layer
$\tau_w$	wall shear stress
$\nu$	kinematic viscosity
$\Gamma$	Gamma function
$\Delta$	difference
$\Delta t$ (s)	the time for forming thickness a(m) of oxide layer
$\Delta\lambda$	thickness of metal consumed for forming $\Delta\delta_{in}$ of inner oxide layer
$\Delta\delta_{in}$	increase of inner oxide layer
$\Delta\delta_{out}$	increase of outer oxide layer
$\Delta\delta_{tot}$	increase of the total oxide layer

$\Phi_{Lat}$	local evolution rules for a lattice site
$\Phi_{Inte}$	local evolution rules for an interstitial site
$\varphi_{Lat}$	control variables for an interstitial site
$\varphi_{Inte}$	control variables for a lattice site
$\varepsilon$	volume control parameter
$\omega$	number of oxygen atoms at an interstitial site
$\nabla$	gradient operator
$\nabla \cdot$	divergence operator

#### Subscript and superscript

*	normalized value
ave	average value
max	maximum value
min	minimum value
ini	medium value
0	beginning or initial value
oxy	properties of oxygen

## REFERENCES

- [1] B. F. Gromov, et al., "Use of lead-bismuth coolant in nuclear reactors and accelerator-driven systems", *Nucl. Eng. Des.*, 173, 207 (1997).
- [2] J. S. Zhang, N. Li, "Corrosion/precipitation in non-isothermal and multi-modular LBE loop systems", *Journal of Nuclear Materials*, 326 (2004), 201–210.
- [3] J. S. Zhang, N. Li, and Yitung Chen, "Dynamics of High Temperature Oxidation Accompanied by Scale Removal and Implications for Technological Applications", *Journal of Nuclear Materials*, 342 (2005), pp.1-7.
- [4] Taide Tan, Yitung Chen, Huajun Chen, and Hsuan-Tsung Hsieh, "Corrosion/precipitation in Non-isothermal Lead Alloy Coolant Systems", Proceedings of IMECE2006, November 5-10, 2006, Chicago, Illinois, USA.
- [5] J. J. Park, D.P. Butt, C.A. Beard, "Review of Liquid Metal Corrosion Issues for Potential Containment Materials for Liquid Lead and Lead-Bismuth Eutectic Spallation Targets as a Neutron Source", *Nucl. Eng. Des.*, 196 (2000) 315.
- [6] B. Spencer, "The rush to heavy liquid metal reactor coolants - gimmick or reasoned", ICONE-8729, (2000).
- [7] P. F. Tortorelli, O.K. Chopra, "Corrosion and compatibility considerations of liquid metals for fusion reactor applications", *J. Nucl. Mater.*, 103, 621 (1981).
- [8] Y. Kurata, M. Futakawa, K. Kikuchi, et al., "Corrosion studies in liquid Pb-Bi alloy at JAERI: R & D program and first experimental results", *J. Nucl. Mater.*, 301, 28 (2002).
- [9] G. Muller, et al., "Results of steel corrosion tests in flowing liquid Pb/Bi at 420–6000C after 2000 h", *J. Nucl. Mater.*, 301, 40 (2002).
- [10] J. S. Zhang, N. Li, J. S. Elson, "Review of Studies on Fundamental Issues in LBE Corrosion", *J. Nucl. Mater.*, in press, 2007.
- [11] Y. I. Orlov, "Stages of Development of Lead-bismuth as a Coolant for Nuclear Reactors in Russia", International Workshop on Physics of Accelerator-Driven

Systems for Nuclear Transmutation and Energy Production, Trento, Italy, Sept. 29-Oct. 3, 1997.

- [12] J. R. Weeks, "Lead, Bismuth, Tin and Their Alloys as Nuclear Coolants", *Nuclear Engineering and Design*, Volume 15, 1971, Pages 363-372.
- [13] V. Sobolev, "Thermophysical Properties of Lead and Lead-Bismuth Eutectic", *J. Nucl. Mater.* (2007), doi:10.1016/j.jnucmat.2007.01.144.
- [14] S. S. Kutateladze, V. M. Borishanskii, I. I. Novikov, O. S. Fedynskii, *Liquid Metal Heat Transfer Media*, Consultants Bureau, Inc., New York (1959).
- [15] F. Balbaud-Celerier, F. Barbier, "Investigation of Models to Predict the Corrosion of Steels in Flowing Liquid Lead Alloys", *Journal of Nuclear Materials*, 289 (2001) 227.
- [16] W. M. Robertson, "Diffusion of Cobalt and Iron in Liquid Lead Measured by Grain Boundary Grooving", *Trans. TMS-AIME*, 242, 2139 (1968).
- [17] J. S. Zhang, N. Li, Yitung Chen, A.E. Rusanov, "Corrosion Behaviors of US Steels in Flowing Lead-Bismuth Eutectic (LBE)", *Journal of Nuclear Materials*, 336 (2005) 1-10.
- [18] G. Y. Lai, "High Temperature Corrosion of Engineering Alloys", *ASM Int.*, Materials Park, OH 44073, 1990.
- [19] J. R. Weeks, "Mechanisms of Liquid Metal Corrosion", 4th NASA-AEC Liquid Metal Corrosion Meeting, CONF-428, October 2, 1963.
- [20] Taide Tan, Yitung Chen and Huajun Chen, "Corrosion and Precipitation Process in Non-isothermal LBE Pipe/loop Systems", Proceedings of ICAPP '06, Paper 6305, Reno, NV, USA, June 4-8, 2006.
- [21] Taide Tan, Yitung Chen and Huajun Chen, "Theoretical Modeling and Numerical Simulation of the Corrosion and Precipitation in Non-isothermal Liquid Lead Alloy Pipe/loop Systems", *Heat and Mass Transfer*, accepted: 8 February 2007.
- [22] E. M. Lyutiy, "Problems of High-Temperature Liquid-Metal Corrosion of Refractory Metals and Alloys", *Soviet Union Materials Science*, Vol. 24 (1988) 441.

- [23] H. Glasbrenner, F. Barbagallo, D. Viol, Spallation Neutron Source Division, Paul Scherrer Institut, PSI Villigen, Switzerland, NUM Report 2002 - ISSN 1423-7326.
- [24] F. N. Remy and M. Bouchacourt, "Flow-Assisted Corrosion: A Method to Avoid Damage", *Nuclear Engineering and Design*, 133 (1992) 23-30.
- [25] J. Weber, "Flow Induced Corrosion: 25 Years of Industrial Research", *Brit. Corros. J.*, Vol. 27, No. 3, pp. 193-199, (1992).
- [26] E. Heitz, "Chemo-Mechanical Effects of Flow on Corrosion", *Corrosion*, Vol. 47(2), (1991) 135.
- [27] J. S. Zhang, "Oxidation Mechanism of Steels in Liquid-Lead Alloys", *Oxidation of Metals*, Vol. 63, Nos. 5/6, June 2005 (. 2005).
- [28] R. Dieckmann, H. Schmalzried, Ber. Bunsenges. "Defects and Cation Diffusion in Magnetite (II)", *Phys. Chem.*, 81, 414 (1977).
- [29] L. F. Epstein, "Static and Dynamic Corrosion and Mass Transfer in Liquid Metal Systems", *Liquid Metal Technology*, 20 (1957) 67.
- [30] G. Ilinev, "Research Results on the Corrosion Effects of Liquid Heavy Metals Pb, Bi and Pb-Bi on Structural Materials with and without Corrosion Inhibitors", *Nuclear Engineering and Design*, 217 (2002) 167.
- [31] T. Y. Chen, A. A. Moccari, D.D. Macdonald, "Development of Controlled Hydrodynamic Techniques for Corrosion Testing", *Corrosion*, 48 (1992) 239.
- [32] X. He, N. Li, M. Mineev, "A Kinetic Model for Corrosion and Precipitation in Non-Isothermal LBE Flow Loop", *Journal of Nuclear Science*, 297 (2001) 214.
- [33] J. S. Zhang, N. Li, "Improved Application of Local Models to Steel Corrosion in Lead-Bismuth Loops", *Nuclear Technology*, 144 (2003) 379.
- [34] J. S. Zhang, N. Li, "Parametric study of a corrosion model applied to lead-bismuth flow systems," *J. Nucl. Mater.*, 321, 184 (2003).
- [35] N. Li, "Active control of oxygen in molten lead-bismuth eutectic systems to prevent steel corrosion and coolant contamination," *J. Nucl. Mater.*, 300, 73 (2002).

- [36] J. S. Zhang, N. Li, and Yitung Chen, "Oxygen Control Technique in Molten Lead and Lead-bismuth Eutectic Systems," *Nuclear Science and Engineering*, 2006, 154 (2), pp. 223-232.
- [37] N. Li, "Active Control of Oxygen in Molten Lead-Bismuth Eutectic Systems to Prevent Steel Corrosion and Coolant Contamination", Los Alamos National Laboratory, LA-UR-99-4696 (1999).
- [38] J. Weeks, A. J. Romano, "Liquidus Curves and Corrosion of Fe, Ti, Zr, and Cu in Liquid Bi-Pb Alloys", *Corrosion*, 25(3), (1969) 131.
- [39] Y. A. Chang, K. Fitzner and Min-Xian Zhang, "The Solubility of Gases in Liquid Metals and Alloys", *Progress in Materials Science*, 32 (1988) 97.
- [40] D.C. Firth, *Elementary Chemical Thermodynamics*, ISBN-13: 978-0199140015, 1969.
- [41] Zhongqi Cui, *Metal and Heat Treatment*, Mechanical Industry Publishing Company, P. R. China, ISBN 7-111-01796-X, (2000).
- [42] G. Müller, G. Schumacher, F. Zimmermann, "Investigation on Oxygen Controlled Liquid Lead Corrosion of Surface Treated Steels", *Journal of Nuclear Materials*, 278 (2002) 85.
- [43] F. Barbier, G. Benamati, C. Fazio, A. Rusanov, "Compatibility Tests of Steels in Flowing Liquid Lead-bismuth", *Journal of Nuclear Materials*, 295 (2001).
- [44] F. Balbaud-Celerier, A. Terlain, P. Fauvet, C. Richet, "Corrosion of Steels in Liquid Lead Alloys Protected by an Oxide layer Application to the MEGAPIE target and to the Russian Reactor Concept BREST 300", Report Technique RT-SCCME 630, CEA Report (2003).
- [45] F. Balbaud-Celerier, P. Deloffre, A. Terlain, A. Rusanov, "Corrosion of Metallic materials in flowing liquid lead-bismuth", *J. Phys. IV France*, 12, Pr8-177 (2002).
- [46] J. Robertson, "The Mechanism of high Temperature Aqueous Corrosion of Stainless Steels", *Corrosion Science*, 32, 443 (1991).
- [47] C. Wagner, "The Distribution of Cations in Metal Oxide and Metal Sulphide Solid Solutions Formed during the Oxidation of Alloys", *Corrosion Science*, 9, 91 (1969).

- [48] A. Atkinson, "A theoretical Analysis of the Oxidation of Fe-Si Alloys", *Corrosion Science*, 22, 87 (1982).
- [49] B. F. Gromov, Y. I. Orlov, P. N. Martynov, V. A. Gulevsky, "The problems of technology of the heavy liquid metal coolants (lead-bismuth, lead)". In proceeding: Heavy liquid metal coolants in nuclear technology (HLMC-98), Vol.1, 87 (1998).
- [50] I. Barin, *Thermochemical Data of Pure Substances*, VCH, Weinheim, 1989.
- [51] Valentina Tcharnotskaia, Curtt Ammerman, Keith Woloshun, "Results from the Initial Operation of the LANL DELTA Loop", Los Alamos National Laboratory, P.O. Box 1663, Los Alamos, NM 87545.
- [52] ASME Boiler and Pressure Vessel Code, 2000.
- [53] ASME B31.1, Power Piping, 1998.
- [54] <http://aaa.nevada.edu/>
- [55] Yitung Chen, J. S. Zhang, and N. Li, "Theoretical Modeling of Protective Oxide Layer Growth in Non-isothermal Lead-Alloys Coolant Systems", TRP-UPP proposal 2004.
- [56] G. Benamati, et al., "Temperature effect on the corrosion mechanism of austenitic and martensitic steels in lead-bismuth", *J. Nucl. Mater.*, 301, 23 (2002).
- [57] S. Moujaes, Y. Chen, K. Dasika, C. Wu, N. Li, J. Zhang, "Simulation Considerations in Lead-Bismuth Transmutation Loops: Corrosion Concentration, velocity and Temperature Profiles of LBE Loops", NURETH10-conf. S. Korea Oct. 5-9. 2003.
- [58] Kanthi Kiran Dasika, *Chemical Kinetics and Thermal Hydraulics of Lead Bismuth Flow Loops*, MS thesis 2003, University of Nevada, Las Vegas (call number in UNLV library: QD502 .D37 2003a ).
- [59] C. Rosen and C. Tragardh, "The  $\overline{u'v'}$  Reynolds stress in the viscous sublayer over a wide range of Reynolds numbers", *AIChE. J.*, 40 (1994) 29-39.
- [60] C. Rosen, et al., "Prediction of turbulent high Schmidt number mass transfer using a low Reynolds number  $k - \varepsilon$  turbulence model", *Chem. Eng. J.*, Vol. 59, Issue 2, October 1995, Pages 153-159.



- [61] S. Aravinth, "Prediction of heat and mass transfer for fully developed turbulent fluid flow through tubes", *International Journal of Heat and Mass Transfer*, 43 (2000), 1399-1408.
- [62] Gert Nelissen, et al., "Multi-ion transport and reaction simulation in turbulent parallel plate flow", *Journal of Electroanalytical Chemistry*, 563 (2004) 213-220.
- [63] A. T. Popovich, R. L. Hummel, "Experimental study of the viscous sub-layer in turbulent pipe flow", *AIChE Journal*, 13, 854 (1967).
- [64] V. Karman, "The Analogy between Fluid Friction and Heat Transfer", *Trans. Amer. Soc. Mech. Engrs*, Vol. 61, pp. 705-710, 1939.
- [65] Nachrichten, Mechanische Ahnlichkeit und Turblenz, Ges.der Wiss. Zu Gott., Math.-Phys. Kl. pp. 58-76, 1930.
- [66] C. R. Huang, A.F. Denny, et al., "Molecular Diffusion in the Laminar Sub-Layer during Turbulent Flow in a Smooth Tube", *Chem.Eng. Sci.*, 59, 1191 (2004).
- [67] Y. Wang, J. Postlethwaite, "The Application of Low Reynolds Number  $k - \epsilon$  Turbulence Model to Corrosion Modeling in the Mass Transfer Entrance Region", *Corros. Sci.* 39 (1997) 1265.
- [68] R.H. Notter, A. Sleicher, "The Eddy Diffusivity in the Turbulent Boundary Layer near a Wall", *Chem. Eng. Sci.*, 26 (1971) 161.
- [69] S. Martemyanov, E. Skurygin, J. Legrand, "Turbulent Mass Transfer in the Developing Diffusion Layer at large Schmidt Numbers", *Int. J. Heat Mass Transfer*, 42 (1999) 2357.
- [70] T. Mizushima, F. Ogino, Y. Oko, H. Fuduka, "Turbulent Heat and Mass Transfer between Wall and Fluid Streams of Large Prandtl and Schmidt Numbers", *Int. J. Heat Mass Transfer*, 14 (1971) 1705.
- [71] S. Malang and D. L. Smith, "Modeling of Liquid-Metal Corrosion/Precipitation in a Fusion Reactor Blanket", ANL/FPP/TM—192 (4. 1984).
- [72] J. Sannier, G. Santarini, "Study of the Corrosion of 2 Ferric Steels by Liquid Lead in a Thermosiphon-Research of a Model", *J. Nucl. Mater.*, 107, 196 (1982).
- [73] Yitung Chen, Huajun Chen, Jin. S. Zhang, "Numerical Investigation on Enhancement of Oxygen Transfer by Forced Convection in Liquid Lead-Bismuth

- Eutectic System”, *International Journal of Heat and Mass Transfer*, 50 (2007) 2139–2147.
- [74] Huajun Chen and Yitung Chen, “Cellular Automaton Modeling on the Corrosion/Oxidation Mechanism of Steel in Liquid Metal Environment”, the 2nd COE-INES International Symposium on Innovative Nuclear Energy Systems Yokohama, Japan, November 26-30, 2006.
  - [75] J. E. Castle, H. G. Masterson, “The Role of Diffusion in the Oxidation of Mild Steel in High Temperature Aqueous Solutions”, *Corrosion Science*, Vol. 6, 93 (1966).
  - [76] R. Winkler, F. Huttner, F. Michel, “Reduction of Corrosion Rates in PWR Primary Circuits in order to Limit Radioactive Deposits”, *VGB Kraftwerkstechnik* (1989), Vol. 69(5), 527-31 CODEN: VGBKB5; 0372-5715, German.
  - [77] D. H. Lister, R. D. Davidson, E. McAlpine, “The Mechanism and Kinetics of Corrosion Product Release from Stainless Steel in Lithiated High Temperature Water”, *Corrosion Science*, Vol. 27, 113 (1987).
  - [78] J. Robertson, “The Mechanism of High Temperature Aqueous Corrosion of Steel”, *Corrosion Science*, Vol. 29, 1275 (1989).
  - [79] D. E. Coates and A. D. Dalvi, “An Extension of the Wagner Theory of Alloy Oxidation and Sulfidation”, *Oxid. Met.*, 2, 331 (1970).
  - [80] S. K. Wong, et al, “An Improved Formulation of the Oxygen-Diffusion Problem and its Application to Zircaloy Oxidation by Steam”, *Oxidation of Metals*, Vol. 47, Nos. 5/6, 1997.
  - [81] J Caldwell, C. C. Chan and S. K. Wong, “An Implicit Enthalpy Formulation for Oxidation of Nuclear Reactor Fuel Cladding by Steam”, *Communication in Numerical Methods in Engineering*, 2000; 16:205-214.
  - [82] Zhonghai Ding, “A Domain Transformation Technique in Oxygen Diffusion Problems with Moving Oxidation Fronts on Unbounded Domains”, *Int. J. Numer. Meth. Engng.* 42, 361-384 (1998).
  - [83] M. Moalem and D. R. Olander, “Oxidation of Zircaloy by Steam”, *Journal of Nuclear Materials*, 182 (1991) 170-194.

- [84] J. Saunier, A. Chausse, J. Stanfiej, J. P. Badiali, "Simulations of Diffusion Limited Corrosion at the Metal/Environment Interface", *J. Electroanal. Chem.*, 563 (2004), 239-247.
- [85] A.L. Barabasi, H.E. Stanley, *Fractal Concepts in Surface Growth*, Cambridge University Press, Cambridge, 1995.
- [86] Eden, M., "A two-dimensional growth process, in: Biology and Problems of Health", Proc. 4th Berkeley Symposium on Mathematics, Statistics and Probability, Vol. 4, F. Neyman, ed., University of California Press, Berkeley, pp. 223–239 (1961).
- [87] T. A. Witten, Jr. and L. M. Sander, "Diffusion-Limited Aggregation, a Kinetic Critical Phenomenon", *Phys. Rev. Lett.*, 47, 1400 (1981).
- [88] T. A. Witten, Jr. and L. M. Sander, "Diffusion-Limited Aggregation", *Phys. Rev. B.*, 27, 5686 (1983).
- [89] E. Somfai, L.M. Sander, R.C. Ball, "Scaling and Crossovers in Diffusion Limited Aggregation", *Phys. Rev. Lett.*, 83, 5523 (1999).
- [90] M. Plischke and Z. Racz, "Active Zone of Growing Clusters: Diffusion-Limited Aggregation and the Eden Model", *Phys. Rev. Lett.*, 53, 415 (1984).
- [91] Giorgio Parisi, Yi-Cheng Zhang, "Eden Model in Many Dimensions", *Phys. Rev. Lett.*, 53, 1791 (1984).
- [92] D. Sazou, C. Georgolios, "Morphological Surface Changes of the Fe Electrodeposition in 2M H<sub>2</sub>SO<sub>4</sub> During Bursting Oscillations Induced by Br", *Electrochim. Acta*, 41 (1996) 147.
- [93] J. W. Schultze, M. Schweinsberg, "From Pm to Km: Scaling up and Scaling down of Electrochemical Systems with TiO<sub>2</sub> and ZrO<sub>2</sub> Passive Films as an Example", *Electrochim. Acta*, 43 (1998) 2761.
- [94] L. Zhou and X Wei, "A Random Walk-Cellular Automaton Model of Precipitation of Internal Oxides", *Scripta Materialia*, Vol. 37, No. 10, pp. 1483-1489, 1997.
- [95] L. Zhou and X Wei, "A Random Walk- Cellular Automaton Simulation of Internal Oxidation and its Transition to External Oxidation", *Scripta Materialia*, Vol. 40, No. 3, pp. 365–374, 1999.

- [96] L. Zhou, "A Monte Carlo Simulation Study of the Minimum Time Required for Formation of Stable Oxide Scale in Oxidation of Alloys", *Computational Materials Science*, 7 (1997) 336-342.
- [97] N. Zhou, L. Zhou, "A Fusion-Crystalization Mechanism for Nucleation of Misfit Dislocations in FCC Epitaxial Films", *Journal of Crystal Growth*, 289 (2006) 681-685.
- [98] Leesa Brieger and Ernesto Bonomi, "A Stochastic Cellular Automaton Model of Non-Linear Diffusion and Diffusion with Reaction", *Journal of Computational Physics*, Volume 94, Issue 2, June 1991, Pages 467-486.
- [99] <http://cell-auto.com/neighbourhood/index.html>

VITA

Graduate College  
University of Nevada, Las Vegas

Taide Tan

Local Address:

1600 E. University AVE., Apt #149  
Las Vegas, NV 89119

Degrees:

Master of Science  
University of Nevada, Las Vegas, 2004

Bachelor of Science  
Machinery and Facilities in Chemical Engineering, 1996  
Nanchang University, Nanchang, Jiangxi, People's Republic of China

Publications and Conference Presentations:

1. Taide Tan, Yitung Chen, Huajun Chen, "An Improved Mesoscopic Oxidation Model of Metals in Molten Lead or LBE", (Results are ready, paper under preparing).
2. Taide Tan, Yitung Chen, Huajun Chen, Hsuan-Tsung Hsieh, "Modeling of a Diffusion Controlling Oxidation Process with Scale Removal in Oxygen-containing Liquid Flow", Proceedings of the ASME IMECE '07, Nov 11-15, 2007, Seattle, WA, USA (IMECE2007-42322, submitted June 12).
3. Taide Tan, Yitung Chen, Huajun Chen, "A Diffusion Controlling Oxidation Model with Scale Removal in Oxygen Containing Liquid Flow", submitted to Oxidation of metals, Received May 3, 2007.
4. Taide Tan, Yitung Chen, Huajun Chen, "Theoretical Modeling and Numerical Simulation of the Corrosion and Precipitation in Non-isothermal Liquid Lead Alloy Pipe/loop Systems", Heat and Mass Transfer, Accepted: 8 February 2007 (in press).
5. Taide Tan, Yitung Chen, Huajun Chen, and Hsuan-Tsung Hsieh, "Corrosion/precipitation in Non-isothermal Lead Alloy Coolant Systems," Proceedings of IMECE2006, November 5-10, 2006, Chicago, Illinois, USA.
6. Xianfang Tan, Yitung Chen, Huajun Chen, Taide Tan, Hsuan-Tsung Hsieh, "Numerical Analysis of Natural Convection Induced Oxygen Transport in Liquid Lead Bismuth Eutectic", IMECE2006 -15459, Chicago, Illinois, Nov. 5-10, 2006.

7. Xianfang Tan, Yitung Chen, Taide Tan, Huajun Chen, "Oxygen Transport in Liquid Lead Bismuth Eutectic Filled Cavity by Natural Convection", ICONE 14-89069, Miami, Florida, Jul. 17-20, 2006.
8. Taide Tan, Yitung Chen and Huajun Chen, "Corrosion and Precipitation Process in Non-isothermal LBE Pipe/loop Systems", Proceedings of ICAPP '06, Paper 6305, Reno, NV, USA, June 4-8, 2006.
9. Taide Tan, Yitung Chen, Huajun Chen, "Theoretical Modeling and Numerical Simulation of the Corrosion/precipitation Process in Non-isothermal Pipe Systems", ASME IMECE'05, November 5-11, 2005 - Orlando, Florida, USA.
10. Xianfang Tan, Taide Tan, Huajun Chen, Yitung Chen, "A Kinetic Corrosion/Precipitation Model in Non-isothermal LBE Systems", ANS Student Conference, Columbus, Ohio, April. 13-16, 2005.
11. Taide Tan, Yitung Chen, Randy Clarksean, and Hsuan-Tsung Hsieh, "Numerically Simulating the Solidification Process of A Melt Casting Metallic Fuel Pin Mold Using FIDAP", ANS Student Conference, Berkeley, CA, April 2-6, 2003. (abstract and presentation)
12. Taide Tan, Yitung Chen, Randy Clarksean, and Hsuan-Tsung Hsieh, "Simulation and Analysis of the Filling and Solidification Process for A Melt Casting Metallic Fuel Pin Mold Incorporating Volatile Actinides", ASME International Mechanical Engineering Congress and R&D Expo, Washington, DC, November 16-21, 2003.
13. Taide Tan, Yitung Chen, Randy Clarksean, and Hsuan-Tsung Hsieh, "Numerical Simulation of an Induction Heating Process in An Induction Skull Melting Furnace ", CHT-04-200, ICHMT International Symposium on Advances in Computational Heat Transfer, Norway, April 19-24, 2004.
14. Taide Tan, Yitung Chen, Randy Clarksean, and Hsuan-Tsung Hsieh, "Simulating an Induction Heating Process in the Induction Skull Melting Furnace With a CFD Code", ICONE12-49385, 12th International Conference on Nuclear Engineering, "Nuclear Energy- Powering the Future", Hyatt Regency Crystal City, Arlington, Virginia (Washington, D. C.), USA-April 25-29, 2004.
15. Taide Tan, Yitung Chen, Randy Clarksean, and Hsuan-Tsung Hsieh, "Numerical Simulation of the Casting Process of a Mold for Casting a Metallic Fuel Pin Using FIDAP", ICONE12-49386, 12th International Conference on Nuclear Engineering, "Nuclear Energy- Powering the Future", Hyatt Regency Crystal City, Arlington, Virginia (Washington, D. C.), USA-April 25-29, 2004.
16. Taide Tan, Yitung Chen, Randy Clarksean, and Hsuan-Tsung Hsieh, "Design and Numerical Simulation of an Induction Skull Melting Process", 2004 ANS Student Conference, Madison, WI, Apr 1-3, 2004. (abstract and presentation)
17. Taide Tan, Yitung Chen, Randy Clarksean, and Hsuan-Tsung Hsieh, "Analyzing a Process for Casting Volatile Actinides", NUTHOS-6-000261, Oct 4-8, 2004, Japan.
18. Taide Tan, Yitung Chen, Randy Clarksean, and Hsuan-Tsung Hsieh, "Numerical Simulation of an Induction Heating Process for Casting Volatile Actinides", IMECE2004-59654, ASME 2004, Nov 13-19, 2004, Anaheim, California, USA.

Thesis Title:

MODELING OF THE PROTECTIVE OXIDE LAYER GROWTH IN NON-  
ISOTHERMAL LEAD-ALLOYS COOLANT SYSTEMS

Dissertation Examination Committee:

Chairperson, Dr. Yitung Chen, Ph. D.  
Committee Member, Dr. Robert Boehm, Ph. D., P. E.  
Committee Member, Dr. Samir F. Moujaes, Ph. D., P. E.  
Committee Member, Dr. Hsuan-Tsung Hsieh, Ph. D.  
Committee Member, Dr. Huajun Chen, Ph. D.  
Graduate College Representative, Dr. Jichun Li, Ph. D.